Universitat Politècnica de Catalunya
Programa de Doctorat en Matemàtica Aplicada

Facultat de Matemàtiques i Estadística

Ejection-collision orbits in the Restricted Three-Body Problem

by

Óscar Rodríguez del Río

PhD dissertation
Advisors: Mercè Ollé Torner[1] and Jaume Soler Villanueva[2]
Barcelona, June 2021

[1] Departament de Matemàtiques
[2] Departament d'Enginyeria Civil i Ambiental

Tot per dir

Agraïments

En primer lloc m'agradaria donar les gràcies als meus directors de tesi, la Mercè i el Jaume, per la seva inestimable ajuda, suport i dedicació que no es limiten només a aquestes pàgines. Sense vosaltres aquesta dissertació no hauria sigut possible i considero que aquesta dissertació és tan meva com vostra. Sens dubte em sento un privilegiat per haver pogut gaudir de dos magnífics investigadors, i sobretot de dues magnífiques persones, durant aquests anys. Moltíssimes gràcies per tot.

En segon lloc vull agraïr al Grup de Sistemes Dinàmics de la Universitat Politècnica de Catalunya per haver pogut formar part d'ell i no trobar-me mai cap porta tancada. En especial a la Tere per tot el temps que m'ha dedicat i la seva genial col·laboració. Aquest agraïment també es fa extensibles als membres del Grup de Sistemes dinàmics de la Universitat de Barcelona i de tota Catalunya en general. En concret vull donar les gràcies a l'Esther i el Pitu pels seus consells/comentaris d'ençà que vaig començar aquesta aventura i els quals s'han mantingut durant tot el doctorat.

Per altra banda vull fer un reconeixement especial als companys doctorands no només de la UPC durant aquests anys, sobretot als membres del Chaotic Seminar. En particular, vull agrair amb més efusió a la Begoña per tot el seu suport, ajut i les vivències al llarg d'aquests anys, i també vull fer una menció especial del Gladston i el Marco, dels quals m'enduc una magnífica amistat i moltes anècdotes.

També agraeixo als meus amics de tota la vida i a la meva família que, tot i no entendre ben bé el que feia, sempre s'han preocupat per saber com anava la cosa.

Finalment, vull donar les gràcies als meus pares i a la meva germana per haver-me recolzat en tot moment. Aquesta tesi també és vostra.

Summary

The main objective of this dissertation is the study of the ejection-collision (EC) orbits in the circular and planar Restricted Three Body Problem (RTBP from now on). In particular, we will focus on the analytical and numerical study of a very specific type of EC orbits, that we denote as n-EC orbits. An n-EC orbit is an orbit such that the particle ejects from one primary and reaches n times a relative maximum in the distance with respect to the primary from which it ejected before colliding with it. In this way, we will study numerically in depth this kind of orbits and we will show analytically that for a sufficiently large value of the Jacobi constant (for which we will give an expression in terms of the mass parameter and the value of n) there exist exactly four n-EC orbits with well-defined characteristics. These results generalize and improve the previous results for the particular case of $n = 1$, and we will see that they can be easily extrapolated to the Hill problem. Besides, we will observe numerically that the evolution of these four original families of n-EC orbits present a very rich dynamics.

It is well-known that the system that defines the motion of the particle is not well defined at the points where the primaries are located. For this reason, we have used two different techniques to regularize the collision, the McGehee regularization and the Levi-Civita regularization. Thus, in this dissertation we have analyzed the advantages and disadvantages of each regularization and the different methods that can be used to detect collisions. Since this dissertation will be mainly focused on values of the Jacobi constant greater than those associated to the equilibrium point L_1, these two local regularizations will be enough. For less restrictive values of the Jacobi constant we will see that there exist other global regularizations or alternatively, we can simply work with local regularizations in a neighbourhood of each primary.

On the other hand, from the numerical point of view we have analyzed the global behaviour of the ejection orbits in the RTBP. We have studied the relation between the family of Lyapunov periodic orbits around the equilibrium point L_1 and the ejection orbits for values of the Jacobi constant such that the associated Hill regions only allow a bounded motion for these orbits. In particular, we have seen that a chaotic infinity of heteroclinic connections between one primary and the Lyapunov periodic orbits around the equilibrium point L_1 are obtained. As a consequence a chaotic infinity of ejection-collision orbits is also derived. Besides, we will see that we can construct colour diagrams that allow to describe the global dynamics of the ejection orbits given a range of time. These colour diagrams provide a very precise understanding of the dynamics of these orbits.

Finally, we have made a first exploration of the spatial case of the circular restricted three body problem (RTBP 3D). In this first approach we have not used the classical Kustaanheimo–Stiefel regularization, instead we have decided to use a 3D version of the McGehee regularization. This presents some problems that we have analyzed and addressed, but this approximation is sufficient to obtain a first numerical result on 1-EC orbits and to illustrate the complexity of the 3D case.

Resum

L'objectiu principal d'aquesta dissertació és l'estudi de les òrbites d'ejecció-col·lisió (EC) al problema restringit de tres cossos circular i pla (RTBP a partir d'ara). En particular, ens centrarem en l'estudi analític i numèric d'unes òrbites d'EC molt particulars, a les quals hem anomenat òrbites de n-EC. Aquestes òrbites d'n-EC, són òrbites tal que la partícula ejecta d'un primari, assoleix n màxims en la distància respecte al primari del qual han ejectat per a continuació tornar a col·lisionar amb ell. D'aquesta forma numèricament estudiarem en profunditat aquest tipus d'òrbites i analíticament demostrarem que per un valor prou gran de la constant de Jacobi (per la qual donarem una expressió en termes del paràmetre de masses i el valor de n) existeixen exactament quatre òrbites d'n-EC amb unes característiques ben determinades. Aquests resultats generalitzen i milloren els resultats previs pel cas particular de $n = 1$, i veurem que es poden extrapolar fàcilment al problema de Hill. A més, numèricament veurem que l'evolució d'aquestes quatre famílies d'òrbites de n-EC originals presenta una dinàmica molt rica.

És ben sabut, que el sistema que defineix el moviment de la partícula no està ben definit als punts on es troben situats els primaris. Per aquest motiu hem utilitzat dues tècniques de regularització de la col·lisió, la regularització de McGehee i la regularització de Levi-Civita. D'aquesta forma, en aquesta memòria hem analitzat els avantatges i els inconvenients de cada regularització, i els diferents mètodes que es poden utilitzar per detectar col·lisions. Com que gran part d'aquesta memòria es focalitzarà en valors de la constant de Jacobi més grans que l'associat al punt d'equilibri L_1 aquestes dues regularitzacions de caràcter local seran suficients. Per valors menys restrictius de la constant de Jacobi veurem que existeixen altres regularitzacions de caràcter global o que simplement podem treballar amb regularitzacions locals a l'entorn de cada primari.

Per altra banda, numèricament hem analitzat el comportament global de les òrbites d'ejecció al RTBP. Hem estudiat la relació entre la família de les òrbites periòdiques de Lyapunov al voltant del punt d'equilibri lineal L_1 i les òrbites d'ejecció que es duu a terme al rang de valors de la constant de Jacobi tals que les regions de Hill associades només permeten un moviment fitat per a aquestes òrbites. En particular, hem vist que s'obté una infinitat caòtica de connexions heteroclíniques entre un primari i l'òrbita periòdica de Lyapunov al voltant del punt d'equilibri lineal L_1. Com a conseqüència, també es deriva una infinitat caòtica d'òrbites d'ejecció-col·lisió. A més, veurem que podem construir uns diagrames de color que ens permeten descriure la dinàmica global de les òrbites d'ejecció donat un interval de temps. Aquests diagrames proporcionen una comprensió molt precisa de la dinàmica d'aquestes òrbites.

Finalment, hem fet una primera exploració del cas espacial del problema restringit de tres cossos circular (RTBP 3D). En aquesta primera aproximació no hem utilitzat la clàssica regularització de Kustaanheimo–Stiefel i hem decidit utilitzar una versió 3D de la regularització de McGehee. Això presenta alguns problemes, que hem analitzat i abordat, però aquesta aproximació és suficient per obtenir un primer resultat numèric sobre òrbites de 1-EC i per il·lustrar la complexitat del cas 3D.

Contents

Introduction

The restricted three-body problem (RTBP) has been extensively studied as an inspiration for many theoretical analysis and numerical simulations, even as a first approximation model in different real missions. This problem is very rich from the dynamics point of view and it is still far from being well understood. Among all this rich dynamics of the problem we will focus on the study of an specific type of orbits, the ejection/collision orbits and, in particular, the case of the ejection-collision orbits.

As is well known, the RTBP describes the motion of an infinitesimal body P under the attraction of two bodies called primaries, P_1 and P_2 of masses $m_1 = 1 - \mu$ and $m_2 = \mu$, for $\mu \in (0, 1)$, which describe circular orbits around their common center of mass, located at the origin. In particular, a solution of the RTBP has a collision (ejection) with one of the two massive primaries (P_1 or P_2) at the instant t_0 if the distance between the particle and P_1 or P_2 tends to zero when $t \to t_0^-$ ($t \to t_0^+$). In this way, an orbit defined on the interval (t_0, t_1) is called an ejection-collision (EC) orbit if it has an ejection when $t \to t_0^+$ and a collision when $t \to t_1^-$.

The definition of ejection or collision as a limit can be easily understood if we consider Newton's law of gravitation, according to which the gravitational forces that act between the particles tend to infinity when the distance between them tends to zero. In this way, the equations that govern the motion of the particle P are not well defined when the distance to one of the two primaries is 0, i.e. when there is a collision.

It is important to note that in celestial mechanics the orbits do not pass through the singularity points, as before reaching the singularity the celestial bodies collide, because they are not point masses. Understanding the dynamics at and near the collision is important, but the direct study of the motion around these singularities in the RTBP (and other problems of Celestial Mechanics) is practically impossible in an analytical and numerical way. However, this problem can be solved through regularization techniques, which allow us to study the solutions -both analytically and numerically- before, at, and after collision, and on the other hand to treat close approaches with numerical and analytical precision.

The Theory of Regularization had a great interest at the end of the 19th century and in the first half of the 20th century applied to theoretical aspects. The development of computers and the space age made these methods acquire a new relevance in the numerical aspects since the 1960's and 70's.

We could say with no doubt that the theory of regularization began to acquire great importance with Tullio Levi-Civita's work on the study of singular trajectories of the RTBP [LC03, LC04]. These works were based on the results of Paul Painlevé[1] and allowed Levi-Civita to remove the singularity due to the collision only few years later [LC06]. Finally, the ideas introduced by Karl F. Sundman[2] led

[1] Paul Painlevé (1863-1933) was a french mathematician and Prime Minister of the French Third Republic. He proved that all the singularities in the three body-problem correspond to collisions and that the problem could be solved using convergent power series if the initial conditions excluded all the possible collision between them [Pai97]. The problem, however, was how to find these conditions corresponding to collision and he conjectured that they must satisfy two analytic relations.

[2] Karl Frithiof Sundman (1873 - 1949) was a finnish mathematician who, among other works, proved the existence of

Levi-Civita [LC20] to write a canonical regularization of the three-body problem in the neighborhood of a binary collision.

Trying to collect all the different techniques and methods that have been developed for the regularization of the equations of motion would be an unaffordable task, due to the vast number of existing works dealing with this topic. However, among these works it is worth highlighting the global regularization of Thiele-Burrau [Thi95, Bur06], the global regularization of Birkhoff [Bir15] and Lemaître's global regularization [Lem55]. It is also important to highlight the work of McGehee [McG74, McG78] for the regularization of the triple collision through a blowup of this one. This technique is very useful to understand the internal dynamics of the collision.

Regarding to the analytical studies of EC orbits in the *planar* RTBP, Llibre [Lli82] proved the existence of at least two EC orbits for $\mu > 0$ small enough and the Jacobi constant C big enough, or equivalently when the energy or the Hamiltonian H (to be defined later on) is small enough. In Lacomba and Llibre [LL88] the authors used the existence of such transversal EC orbits to prove that both the Hill problem and the RTBP have no C^1-extensible regular integrals. Chenciner and Llibre [CL88] proved the existence of four EC orbits for *any* value of the mass parameter μ and H small enough. Concerning to the *spatial* RTBP Llibre and Martinez Alfaro [LMA85] extended the existence of EC orbits for small enough values of the mass parameter and in [LP90, Piñ95], the authors considered the *planar elliptic* RTBP and proved the existence of EC orbits for both the mass parameter and the eccentricity small enough.

There are other results related to the analytical study of EC orbits in different problems. Delgado [DF89] proved the existence of four EC in the Hill's problem when the energy is sufficiently small. Alvarez and Vidal [ARV13] studied the behavior of the binary collision in a planar restricted $(n+1)$-body problem and proved the existence of four EC orbits when the energy is small enough. In a similar way, Maranhão and Llibre [ML98] proved the existence of four EC orbits in a restricted four-body problem for any value of $\mu \in (0, 1/2]$ and energy small enough.

All the previously mentioned analytical results correspond to a very particular case of EC orbit, since they are orbits that eject from a primary and reach a relative maximum in the distance with respect to the primary from they have been ejected before colliding with it. In this dissertation, we will generalize this concept to the case of n-EC orbit, which in the particular case of the restricted problem can be defined as the orbit that ejects from the first primary and reaches n times a relative maximum in the distance with respect to the first primary before colliding with it.

Concerning numerical results, we mention Henon's paper about the computation of EC orbits obtained along the continuation of some families of symmetric periodic –non-collision– orbits in the Copenhagen problem (that is $\mu = 0.5$, see [Hén65]) and also for Hill's problem (see [Hén69]). Finally, the evolution of 16 particular collision periodic orbits obtained from the $\mu = 0.5$ case was numerically studied for different values of the mass ratio μ in [Boz70].

From the point of view of astronomical applications, a great variety of papers dealing with ejection orbits appear. Typically such papers consider just a particular value of the mass parameter. Just to mention a few, ejection orbits allow to explain a mechanism of transfer of mass in binary stars systems (see [HTP02], [MK80], [PW85] and [WDT95]), to analyze regions of capture of irregular moons by giant planets (see [ABWF03]) to study temporary capture (see most recently [PG20] and references therein), or the formation of Kuiper belt binaries by means of multiple encounters with low-mass intruders (see [ALF05]).

A different approach regarding the probability of crash motion when taking into account a big set of initial conditions and a particular range of time for a given μ and varying C is analyzed in [Nag04] and [Nag05]. We observe that ejection/collision orbits also play an important role in other physical

a convergent infinite series solution for the three-body problem [Sun07, Sun09] and published a very appreciated paper on a regularization method for the three-body problem [Sun13].

problems rather than astronomy or celestial mechanics. For example in atomic physics, we mention the hydrogen atom submitted to a circularly polarized microwave field, where the ejection collision orbits (in this case between the electron and the nucleus) allow to explain a mechanism for ionization. See [BUF97] and [Oll18].

The main goal of this dissertation is to study the n-EC orbits in the *planar* RTBP (denoted from now on as simply RTBP). This study has been accomplished through numerical simulations as well as with analytical techniques. In addition, the dynamics of ejection orbits, mechanisms for generating new ejection-collision orbits and a first approach to the *spatial* problem (3D RTBP) have also been studied. In this way, and in more detail, the structure of this dissertation is as follows:

In Chapter 1 the RTBP and the properties that will be useful throughout the dissertation will be presented. It is important to note that the Jacobi constant C will play a fundamental role both in the study and in the structure of the thesis. In particular, two ranges of C have been considered mainly: the values that allows bounded motion and there is no possible transit from moving in a neighborhood of one primary to a neighborhood around the other one (considered mainly in Chapters 3, 4 and 5) and the values of C that allow bounded motion and there is possible transit to move around both primaries (Chapter 6). In addition, the following two problems will be introduced: the Hill's problem as a limit case of RTBP (Chapter 5) and the case of the 3D RTBP (Chapter 7).

In Chapter 2, the two regularization techniques that have been used to deal with the collision will be presented in detail: the McGehee regularization and the Levi-Civita regularization. These two regularizations are local, since they only regularize the collision with one of the two primaries but this will be sufficient when we restrict ourselves to values of $C \geq C_{L_1}$ since only collision with a primary will be allowed. It is important to remark that in this dissertation we will consider values of the mass parameter $\mu \in (0, 1)$ so that we consider that the ejection always occurs from the first primary (and in the case of $C \geq C_{L_1}$ also the collision). However, as we have said, we will also study values of C that do allow collision with the second primary. For these cases we have two strategies: use local regularizations around both primaries or use global regularizations, some of which we will introduce in the final section of this chapter.

In Chapter 3 the numerical study of the n-EC orbits will be presented and different methods that will be useful for us to calculate these orbits will be explained. These methods will not only be used from a numerical point of view, as we will use them in the following chapters to study n-EC orbits analytically. Using these methods we will see numerically that there exist exactly four n-EC orbits for values of $C \geq \hat{C}(\mu, n)$. In this chapter we will also make a comparison between the various methods and the regularizations of McGehee and Levi-Civita that have been used to compute these orbits.

In Chapter 4 we will explain the first analytical result and we will prove the existence of exactly four n-EC orbits given a $n \in \mathbb{N}$ for values of μ sufficiently small and C large enough. The main idea of this proof will be to compute the angular momentum of the ejection orbits working directly with the equations obtained from the Levi-Civita regularization.

In Chapter 5 we will present the strong analytical result and we will show that there exists a constant $\hat{C}(\mu, n)$ such that for all $C \geq \hat{C}(\mu, n)$ with $\mu \in (0, 1)$ and $n \in \mathbb{N}$ there exist exactly four n-EC orbits. The proof of this theorem is based on the computation of the angular momentum with a rescaling of the Levi-Civita variables. In addition, we will see that this result can easily be extrapolated to Hill's problem.

Although Chapters 4 and 5 have an analytical character, they will also be supplemented with some numerical results in order to deepen and illustrate the results obtained.

In Chapter 6 a discussion on the relation between the Lyapunov periodic orbit around the collinear equilibrium point L_1 (LPO_1) and the ejection orbits is carried out in the range of values of the Jacobi constant such that the associated Hill regions permit a bounded motion. Furthermore, we will see that

there are infinite heteroclinic connections between LPO_1 and the first primary and, as a consequence, there is a chaotic infinity of ejection-collision orbits. To conclude this chapter, 2D plots, called colour code diagrams, allow to describe the global dynamics of the ejection orbits given a range of time. Such diagrams provide a very accurate understanding of the dynamics of the orbits under discussion.

Finally in Chapter 7, a first exploration of the 3D RTBP case will be made. In this first approximation we will not use the classic, Kustaanheimo–Stiefel regularization and we will focus on using a 3D version of the McGehee regularization. This presents some problems, which we will analyze and grapple with, but it will be sufficient for a first exploration of the 1-EC orbits.

It is important to note that all the computations have been done using double precision and the numerical integration of the systems of ODE has been done using an own implemented Runge-Kutta (7)8 (see [Feh68]) and Runge-Kutta (8)9 (see [Ver78]) integrators with an adaptive step size control described in [DP05] and a Taylor method implemented on a robust, fast and accurate software package in [JZ05].

To conclude we remark that this thesis is made up of the following articles:

[ORS18] M. Ollé, O. Rodríguez and J. Soler. Ejection-collision orbits in the RTBP. *Commun Nonlinear Sci Numer Simulat*, 55:298–315, 2018.

[ORS20b] M. Ollé, O. Rodríguez and J. Soler. Regularisation in Ejection-Collision Orbits of the RTBP. *Recent Advances in Pure and Applied Mathematics*, 35–47, 2020.

[ORS20a] M. Ollé, O. Rodríguez and J. Soler. Analytical and numerical results on families of n-ejection-collision orbits in the RTBP. *Commun Nonlinear Sci Numer Simulat*, 90:105294, 2020.

[ORS21b] M. Ollé, O. Rodríguez and J. Soler. Transit regions and ejection/collision orbits in the RTBP. *Commun Nonlinear Sci Numer Simulat*, 94:105550, 2021.

[MSORS21] T. Martínez-Seara, M. Ollé, O. Rodríguez and J. Soler. Generalised analytical results on n-ejection-collision orbits in the RTBP. Analysis of bifurcations, *Preprint*

[ORS21a] M. Ollé, O. Rodríguez and J. Soler. McGehee regularization in the 3D Restricted three-body problem. Application to Ejection-collision orbits, *Preprint*

Chapter 1

The Restricted Three-Body Problem

Only a few years after formulating the law of universal gravitation Newton and other contemporaries realized that it was not enough to know the position and velocities of a planet to determine its orbit exactly. Some orbits computed considering only the mutual attraction of the Sun and the planet were very different from those observed. Newton realized that this was because the planets also interacted with each other, which gave rise to the now famous n-body problem. In particular, Newton published in the Principia the preliminary steps for the study of the case $n = 3$.

The three-body problem consists in determining the motion of three bodies subjected to a mutual gravitational attraction at any instant of time and under certain initial conditions. Under the assumptions that the three bodies P_1, P_2 and P_3 are symmetrically spherical and mutually isolated, the general problem of the three bodies of masses m_1, m_2 and m_3 in a reference system that has its origin fixed is given by:

$$\begin{aligned} m_1\ddot{\boldsymbol{r}}_1 &= \frac{Gm_1m_2}{||\boldsymbol{r}_1-\boldsymbol{r}_2||^3}(\boldsymbol{r}_2-\boldsymbol{r}_1)+\frac{Gm_1m_3}{||\boldsymbol{r}_1-\boldsymbol{r}_3||^3}(\boldsymbol{r}_3-\boldsymbol{r}_1),\\ m_2\ddot{\boldsymbol{r}}_2 &= \frac{Gm_1m_2}{||\boldsymbol{r}_1-\boldsymbol{r}_2||^3}(\boldsymbol{r}_1-\boldsymbol{r}_2)+\frac{Gm_2m_3}{||\boldsymbol{r}_2-\boldsymbol{r}_3||^3}(\boldsymbol{r}_3-\boldsymbol{r}_2),\\ m_3\ddot{\boldsymbol{r}}_3 &= \frac{Gm_1m_3}{||\boldsymbol{r}_1-\boldsymbol{r}_3||^3}(\boldsymbol{r}_1-\boldsymbol{r}_3)+\frac{Gm_2m_3}{||\boldsymbol{r}_2-\boldsymbol{r}_3||^3}(\boldsymbol{r}_2-\boldsymbol{r}_3), \end{aligned} \tag{1.1}$$

where G is the gravitational constant, $\boldsymbol{r}_i \in \mathbb{R}^3$ is the position of P_i and $\dot{} = d/dt$ denotes the time derivative. This is a problem of dimension 18 and we can only reduce 10 fixing the center of masses (6) and using the conservation of the energy (1) and the angular momentum (3). However, we will focus on a particular case of the three-body problem, where the mass of the third object will be considered infinitesimally small, i.e. $m_3 \to 0$. This problem is called the restricted three-body problem.

1.1 The RTBP

In particular we will focus on the planar and circular restricted three-body problem (RTBP) that consists in the study of the motion of a particle of infinitesimal mass, that moves on the same plane (X, Y) and under the gravitational influence of two massive bodies P_1 and P_2, called primaries, that are assumed to describe circular orbits around their common center of mass.

In order to simplify the notation of the problem it is usual to normalize the units of mass, length and time imposing that:

$$m_1 + m_2 = 1, \ ||\boldsymbol{r}_1 - \boldsymbol{r}_2|| = 1,$$

and that the period of the orbit of the two primaries is 2π. If we also impose the center of mass at the origin and we introduce the mass parameter $\mu \in (0,1)$, such that $m_2 = \mu$ (and $m_1 = 1-\mu$), the motion of the two primaries is given by: $\boldsymbol{r}_1 = \mu(\cos t, \sin t)$ and $\boldsymbol{r}_2 = (\mu - 1)(\cos t, \sin t)$.

Equations in the sidereal system

Under these assumptions the equations of motion for the particle in this *sidereal* system are given by

$$\begin{aligned} \ddot{X} &= -\frac{(1-\mu)(X - \mu\cos t)}{r_1^3} - \frac{\mu(X + (1-\mu)\cos t)}{r_2^3}, \\ \ddot{Y} &= -\frac{(1-\mu)(Y - \mu\sin t)}{r_1^3} - \frac{\mu(Y + (1-\mu)\sin t)}{r_2^3}, \end{aligned} \tag{1.2}$$

where $r_1 = \sqrt{(X - \mu\cos t)^2 + (Y - \mu\sin t)^2}$ and $r_2 = \sqrt{(X - (\mu-1)\cos t)^2 + (Y - (\mu-1)\sin t)^2}$.

Equations in the synodical system

In order to deal with an autonomous system of ordinary differential equations, it is quite common to consider a system of coordinates (x, y) that rotates with the primaries (called *rotating* or *synodical* system). We can obtain these coordinates from the previous system via:

$$\begin{pmatrix} X \\ Y \end{pmatrix} = \begin{pmatrix} \cos t & -\sin t \\ \sin t & \cos t \end{pmatrix} \begin{pmatrix} x \\ y \end{pmatrix}.$$

The equations of motion for the particle in the synodical system are given by

$$\begin{cases} \ddot{x} - 2\dot{y} = \Omega_x(x, y), \\ \ddot{y} + 2\dot{x} = \Omega_y(x, y), \end{cases} \tag{1.3}$$

where

$$\begin{aligned} \Omega(x,y) &= \frac{1}{2}(x^2 + y^2) + \frac{1-\mu}{\sqrt{(x-\mu)^2 + y^2}} + \frac{\mu}{\sqrt{(x-\mu+1)^2 + y^2}} + \frac{1}{2}\mu(1-\mu) \\ &= \frac{1}{2}\left[(1-\mu)r_1^2 + \mu r_2^2\right] + \frac{1-\mu}{r_1} + \frac{\mu}{r_2}, \end{aligned} \tag{1.4}$$

with $r_1 = \sqrt{(x-\mu)^2 + y^2}$ and $r_2 = \sqrt{(x-\mu+1)^2 + y^2}$.

Hamiltonian formulation

The RTBP also admits a hamiltonian formulation (see [Sze67]), and it can be obtained easily via the relation

$$\begin{cases} p_x = \dot{x} - y, \\ p_y = \dot{y} + x. \end{cases}$$

In that way, the Hamiltonian is given by

$$H(x, y, p_x, p_y) = \frac{1}{2}(p_x^2 + p_y^2) + yp_x - xp_y - \frac{1-\mu}{r_1} - \frac{\mu}{r_2} + \frac{1}{2}\mu(1-\mu), \tag{1.5}$$

and the equations of motion are given by the well known formulas

$$\dot{x} = \frac{\partial H}{\partial p_x}, \qquad \dot{p}_x = -\frac{\partial H}{\partial x},$$
$$\dot{y} = \frac{\partial H}{\partial p_y}, \qquad \dot{p}_y = -\frac{\partial H}{\partial y}.$$

For our purposes it is important to note that all the previous formulations of the problem have 2 singularities that correspond to $r_1 = 0$ and $r_2 = 0$.

In order to study the ejection/collision orbits in the next chapters we will use some well-known properties of the RTBP. To describe these useful properties of the problem, we will consider (if not stated otherwise) the synodical formulation of the problem. It is important to remark than these and other interesting properties can be found in [Sze67].

1.1.1 The symmetry of the problem

The first important property is that system (1.3) has the symmetry

$$(t, x, y, \dot{x}, \dot{y}) \to (-t, x, -y, -\dot{x}, \dot{y}). \tag{1.6}$$

A geometrical interpretation of it is that given an orbit in the configuration plane (x, y), the symmetrical orbit with respect to the x axis will also exist (see Figure 1.1).

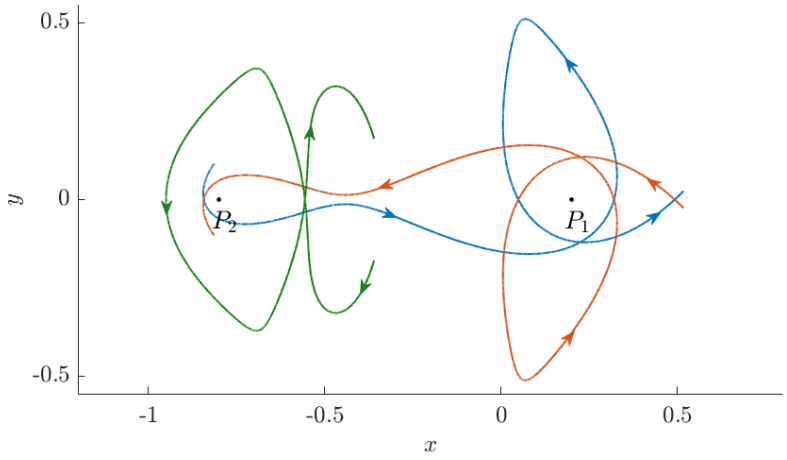

Figure 1.1: Symmetrical orbits to each other (blue and red) and a symmetrical orbit itself (green) for $\mu = 0.2$

This property will be crucial for studying and characterizing the ejection/collision orbits.

1.1.2 Equilibrium points

The second important property is that the system (1.3) has five trivial solutions that correspond to the five equilibrium points of the system, also known as the Lagrangian points: the so called collinear ones L_i, $i = 1, 2, 3$, located on the x axis and the triangular ones L_i, $i = 4, 5$. On the plane (x, y), the collinear points are located on the x axis, with $x_{L_2} < \mu - 1 < x_{L_1} < \mu < x_{L_3}$ and $L_{4,5}$ forming an equilateral triangle with the primaries (see Figure 1.2).

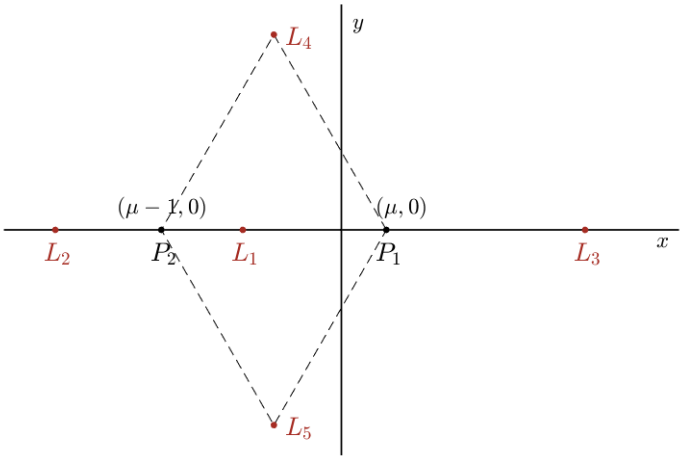

Figure 1.2: Equilibrium points for $\mu = 0.2$

The values of x_{L_i} for $i = 1, 2, 3$ are solution of a polynomial of degree 5 called the Euler's quintic equation. These values can be computed numerically through a very simple iterative process, but they also admit an expansion in power series. For our purpose we will be interested in the expression for L_1 and it is well known that x_{L_1} admits an expansion in terms of $\mu^{1/3}$ (when μ is near 0), or $(1-\mu)^{1/3}$ (when μ is near 1)

$$\begin{aligned} x_{L_1}(\mu) &= -1 + \frac{3^{2/3}}{3}\mu^{1/3} - \frac{3^{1/3}}{9}\mu^{2/3} + \frac{26}{27}\mu + \mathcal{O}\left(\mu^{4/3}\right), \\ x_{L_1}(\mu) &= 1 - \frac{3^{2/3}}{3}(1-\mu)^{1/3} + \frac{3^{1/3}}{9}(1-\mu)^{2/3} - \frac{26}{27}(1-\mu) + \mathcal{O}\left((1-\mu)^{4/3}\right). \end{aligned} \tag{1.7}$$

The stability of the Lagrangian points is also well known and we will only make a small observation regarding their stability. The 3 collinear points are of center $\times$ saddle type. We can see this easily by rewriting the system (1.3) as a system of first order (in the variables $(x, y, \dot{x}, \dot{y})$). The differential of the system is given by

$$DF(x,y) = \begin{pmatrix} 0 & 0 & 1 & 0 \\ 0 & 0 & 0 & 1 \\ \Omega_{xx} & \Omega_{xy} & 0 & 2 \\ \Omega_{xy} & \Omega_{yy} & -2 & 0 \end{pmatrix}, \tag{1.8}$$

and the eigenvalues of DF at the collinear points give us the center $\times$ saddle type.

The case of the triangular points is quite different:

- $L_{4,5}$ are of center $\times$ center type if $\mu < \mu_R$ or $\mu > 1 - \mu_R$
- $L_{4,5}$ are degenerate centers if $\mu = \mu_R$ or $\mu = 1 - \mu_R$
- $L_{4,5}$ are of complex saddles type if $\mu \in (\mu_R, 1 - \mu_R)$

where $\mu_R = \frac{1}{2}\left[1 - \frac{\sqrt{69}}{9}\right] \approx 0.03852089650455137181950$ is the Routh value (see [Sze67]).

1.1.3 Jacobi Constant and Hill regions

The system (1.3) has a first integral, the so-called Jacobi integral, defined by

$$C = 2\Omega(x, y) - \dot{x}^2 - \dot{y}^2, \tag{1.9}$$

that is related with the Hamiltonian (1.5) by $H = -C/2$.

From the Jacobi integral and taking into account that $2\Omega(x, y) - C \geq 0$, given a value of the Jacobi constant C, the motion can only take place in the Hill's region defined by

$$\mathcal{R}(C) = \left\{(x, y) \in \mathbb{R}^2 \,|\, 2\Omega(x, y) \geq C\right\}. \tag{1.10}$$

We denote by C_{L_i} the value of C at L_i, $i = 1, ..., 5$, and it is also known that the topology of the Hill's regions varies with C_{L_i} (see Figure 1.3). As for the x-coordinate of the collinear points, the values of C_{L_i}, $i = 1, 2, 3$, admit an expansion in power series. In particular, for our purpose we will be interested in the value of C_{L_1} when μ is near 1. This value is given by

$$C_{L_1}(\mu) = 3 + 9\left(\frac{1-\mu}{3}\right)^{2/3} - 7\frac{1-\mu}{3} + \mathcal{O}\left((1-\mu)^{4/3}\right). \tag{1.11}$$

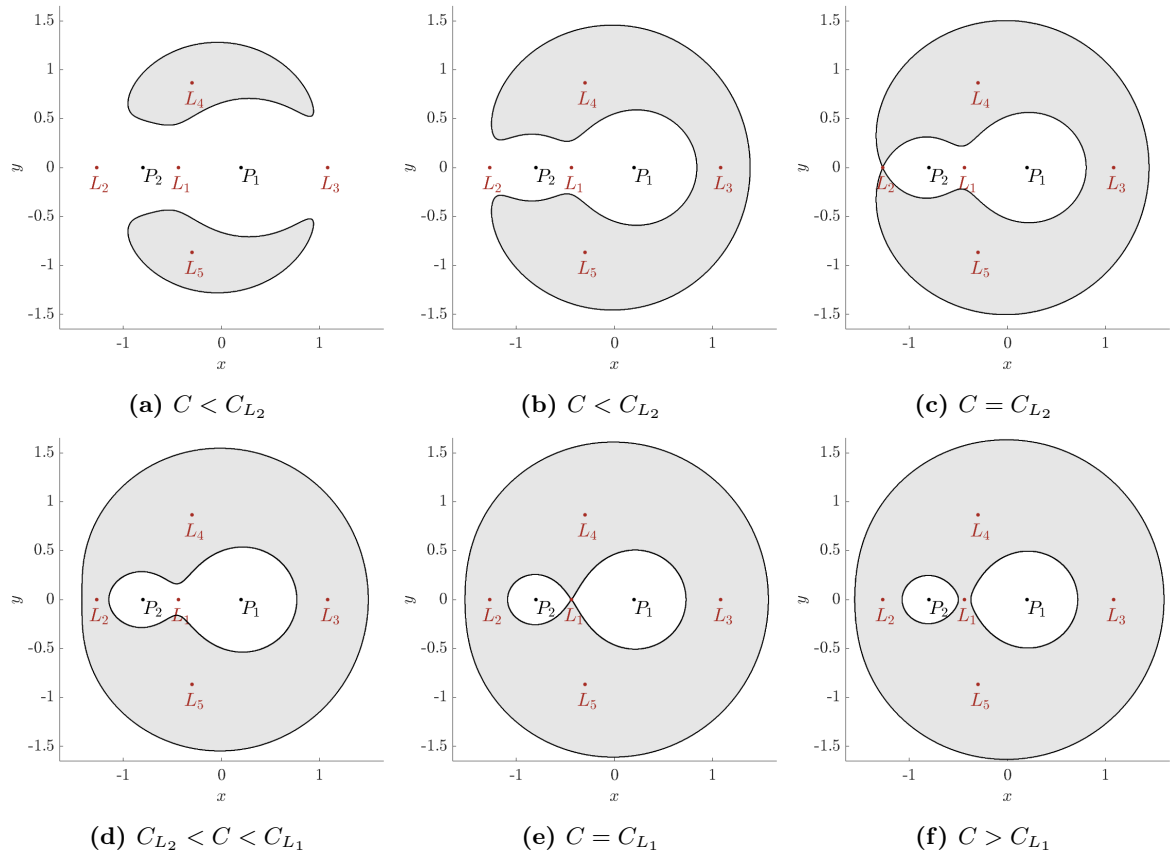

(a) $C < C_{L_2}$ **(b)** $C < C_{L_2}$ **(c)** $C = C_{L_2}$

(d) $C_{L_2} < C < C_{L_1}$ **(e)** $C = C_{L_1}$ **(f)** $C > C_{L_1}$

Figure 1.3: Hill regions associated to different values of C for $\mu = 0.2$.

Before concluding this subsection it is important to note two points:

- For values of $C \geq C_{L_1}$ we have bounded motion and there is no possible transit from moving in a neighborhood of one primary to a neighborhood around the other one (see Figures 1.3e 1.3f).

- For values of $C \in [C_{L_{2,3}}, C_{L_1})$, (where $C_{L_{2,3}} = C_{L_2}$ when $\mu \leq 0.5$ and $C_{L_{2,3}} = C_{L_3}$ otherwise) we have bounded motion in a neighborhood of the primaries with a possible transit to move around both primaries due to the shape of the Hill region (see Figures 1.3c 1.3d).

Finally, we remark that in this dissertation we will consider only $C \geq C_{L_{2,3}}$.

1.1.4 Lyapunov periodic orbits

As we have explained previously, the collinear points are equilibrium points of center×saddle type. This has two main consequences:

- L_i $i = 1, 2, 3$ are unstable and there exists a $1D$ unstable manifold ($W^u(L_i)$) and a $1D$ stable manifold ($W^s(L_i)$) associated to these points.

- Applying Lyapunov's center theorem (see [MO17]), it is well known that for $C < C_{L_i}$, $i = 1, 2, 3$ there exists a one parameter family of periodic orbits, called Lyapunov periodic orbits around L_i, $i = 1, 2, 3$, respectively, and parametrized by C. We will denote by LPO_i, $i = 1, 2, 3$ the associated Lyapunov periodic orbit for a given suitable C.

It is also well known that the LPO_i are unstable (the eigenvalues of the monodromy matrix are 1, 1, λ, $1/\lambda$, with $\lambda > 1$) at least for a suitable range of C close to C_{L_i}, $i = 1, 2, 3$. Applying the theorem of stable/unstable manifolds (see for example [MO17]), the existence of $2D$ invariant manifolds associated with each LPO_i is guaranteed.

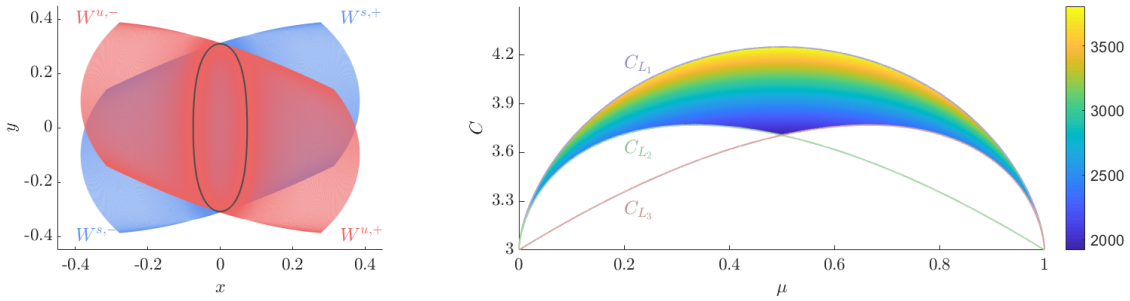

Figure 1.4: *Left.* Branches $W^{u,\pm}$ and $W^{s,\pm}$ of a LPO_1 for $\mu = 0.5$ and $C = C_{L_2}$. *Right.* Maximum eigenvalue of the monodromy matrix (in colour) when varying $\mu \in (0, 1)$ and $C \in [C_{L_{2,3}}, C_{L_1})$.

We will focus on the LPO_1 because we will consider $C \geq C_{L_{2,3}}$, and the only LPO_i that exists for those values of C is LPO_1 and will discuss in Chapter 6 how the associated 2D invariant manifolds explain why orbits that eject from one primary remain on the same region or visit a region around the other primary. We will denote by $W^{u,+}$, $W^{u,-}$ (similarly $W^{s,+}$, $W^{s,-}$) the branches of the unstable (stable) manifolds that *start* asymptotically forward (backward) in time on the right or left hand side of the periodic orbit respectively (see Figure 1.4); we will call them positive and negative branch respectively.

Finally, it is important to remark that the LPO_1 are highly unstable; we plot in Figure 1.4 the maximum real eigenvalue $\lambda > 1$ of the LPO_1 for any value of $\mu \in (0, 1)$ (on the x axis) and the range $C \in [C_{L_{2,3}}, C_{L_1})$ (on the y axis). We remark that such eigenvalue is large (approximately between 2000 and 4000) for all $\mu \in (0, 1)$.

1.2 The Hill problem

The *Hill problem* or *Hill's lunar problem* (see [MS82]) is a simplified limiting case of the RTBP that focusses on the vicinity of the small primary. This approximation to the RTBP is valid only if the mass parameter μ is very small (or very close to 1). In fact, we can obtain the equations of Hill problem making a translation of the small primary to the origin and rescaling the coordinates by a factor of $\mu^{1/3}$ if $\mu \to 0$ or $(1-\mu)^{1/3}$ if $\mu \to 1$. The typical construction of the Hill's equations of motion is in the case when $\mu \to 0$ but in our context we consider the case when $\mu \to 1$, because in Chapter 5 we will see that we can extend the analytical results obtained for the RTBP to the Hill problem if we consider it as the limit case $\mu \to 1$.

The first step as we said is to make the translation and the scaling of the variables. For this purpose we introduce new variables (x_h, y_h) defined by the relation

$$x = \mu + (1-\mu)^{1/3} x_h, \qquad y = (1-\mu)^{1/3} y_h. \tag{1.12}$$

With these new variables the expression (1.4) becomes

$$\frac{1}{(1-\mu)^{2/3}}\left(\Omega - \frac{3}{2}\right) = \frac{3}{2}x_h^2 + \frac{1}{\sqrt{x_h^2+y_h^2}} + \mathcal{O}\left((1-\mu)^{1/3}\right). \tag{1.13}$$

In this way, taking the limit $\mu \to 1$ we obtain the Hill's potential

$$\Psi(x_h, y_h) = \frac{3}{2}x_h^2 + \frac{1}{\sqrt{x_h^2+y_h^2}}, \tag{1.14}$$

and the equations of motions are

$$\begin{cases} \ddot{x}_h - 2\dot{y}_h = \Psi_{x_h}(x_h, y_h), \\ \ddot{y}_h + 2\dot{x}_h = \Psi_{y_h}(x_h, y_h). \end{cases} \tag{1.15}$$

Like the RTBP, Hill's problem has a number of useful properties for our purposes:

Symmetries of the problem

Hill's problem not only inherits the symmetry of the RTBP, that is a symmetry with respect to the x_h-axis, but also has an extra one with respect to the y_h-axis. In this way the system (1.15) has the symmetries

$$(t, x_h, y_h, \dot{x}_h, \dot{y}_h) \to (-t, x_h, -y_h, -\dot{x}_h, \dot{y}_h), \tag{1.16a}$$
$$(t, x_h, y_h, \dot{x}_h, \dot{y}_h) \to (-t, -x_h, y_h, \dot{x}_h, -\dot{y}_h). \tag{1.16b}$$

These two symmetries can be combined into

$$(t, x_h, y_h, \dot{x}_h, \dot{y}_h) \to (t, -x_h, -y_h, -\dot{x}_h, -\dot{y}_h), \tag{1.17}$$

that corresponds to a symmetry with respect to the origin.

Equilibrium points

As mentioned, the Hill problem is a limit case of RTBP that aims at studying the movement around the small primary. In this way, it makes sense that only two equilibrium points are preserved, which are those that are in the vicinity of the small primary. These points would be the equivalent of L_1 and L_2 if we consider the case $\mu \to 0$ or L_1 and L_3 if we consider the case $\mu \to 1$. For historical consistency, we will call these equilibrium points L_1 and L_2, which have positions $(\pm 1/3^{1/3}, 0)$ (see Figure 1.5).

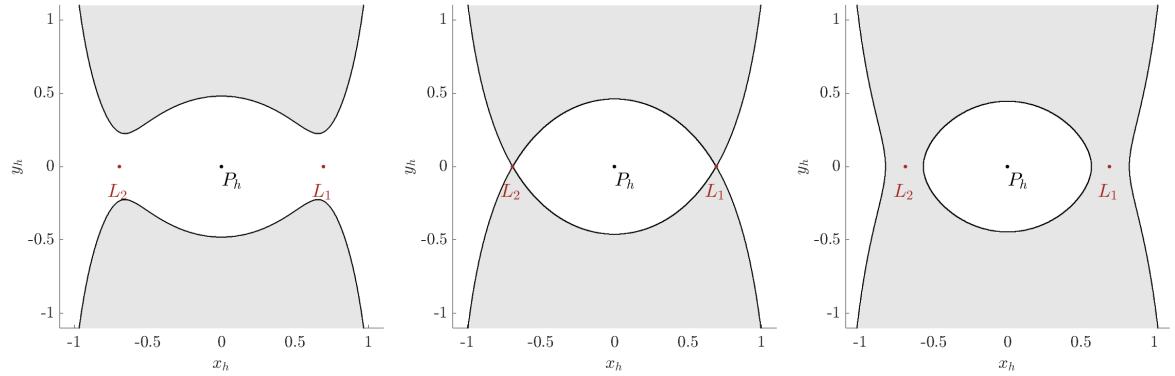

(a) $K < K_L$ **(b)** $K = K_L$ **(c)** $K > K_L$

Figure 1.5: Hill regions associated to different values of K.

Constant of the motion and Hill regions

The system (1.15) has a first integral defined by

$$K = 2\Psi(x_h, y_h) - \dot{x}_h^2 - \dot{y}_h^2, \tag{1.18}$$

where K is related with the Jacobi integral by

$$C(x, y) = 3 + (1 - \mu)^{2/3} K(x_h, y_h). \tag{1.19}$$

From the first integral and taking into account that $2\Psi(x_h, y_h) - K \geq 0$, given a value of K, the motion can only take place in the Hill's region defined by

$$\mathcal{R}_h(K) = \left\{(x_h, y_h) \in \mathbb{R}^2 \,|\, 2\Psi(x_h, y_h) \geq K\right\}. \tag{1.20}$$

We denote by $K_L = 3^{4/3}$ the value of K at L_1 and L_2 and again it is also known that the topology of the Hill's regions varies with K_L: for $K \geq K_L$ we have that all the possible motion in a neighborhood of the primary is bounded but for $K < K_L$ we have also possible unbounded motion (see Figure 1.5). In our case we will only consider values of $K \geq K_L$.

1.3 The 3D RTBP

Although in most of this dissertation we will consider the circular and planar version of the restricted three-body problem, in the last chapter we will explore the 3D case, which we will denote by the 3D RTBP. The equations of motion in a *synodical* system where the primary of mass $1 - \mu$ is located at $(\mu, 0, 0)$ and the primary of mass μ is located in $(\mu - 1, 0, 0)$ are given by

$$\begin{cases} \ddot{x} - 2\dot{y} = \Omega_x(x, y, z), \\ \ddot{y} + 2\dot{x} = \Omega_y(x, y, z), \\ \ddot{z} = \Omega_z(x, y, z), \end{cases} \tag{1.21}$$

where

$$\Omega(x, y, z) = \frac{1}{2}(x^2 + y^2) + \frac{1 - \mu}{r_1} + \frac{\mu}{r_2} + \frac{1}{2}\mu(1 - \mu), \tag{1.22}$$

with $r_1 = \sqrt{(x - \mu)^2 + y^2 + z^2}$ and $r_2 = \sqrt{(x - \mu + 1)^2 + y^2 + z^2}$.

By introducing the variables $p_x = \dot{x} - y$, $p_y = \dot{y} + x$ and $p_z = \dot{z}$ the 3D RTBP can be written in a Hamiltonian form with Hamiltonian

$$H(x, y, z, p_x, p_y, p_z) = \frac{1}{2}(p_x^2 + p_y^2 + p_z^2) + yp_x - xp_y - \frac{1-\mu}{r_1} - \frac{\mu}{r_2} + \frac{1}{2}\mu(1-\mu), \tag{1.23}$$

and the equations of motion are given by

$$\begin{cases} \dot{x} = p_x + y, \\ \dot{y} = p_y - x, \\ \dot{z} = p_z, \\ \dot{p}_x = p_y - \dfrac{1-\mu}{r_1^3}(x-\mu) - \dfrac{\mu}{r_2^3}(x-\mu+1), \\ \dot{p}_y = -p_x - \dfrac{1-\mu}{r_1^3}y - \dfrac{\mu}{r_2^3}y, \\ \dot{p}_z = -\dfrac{1-\mu}{r_1^3}z - \dfrac{\mu}{r_2^3}z. \end{cases} \tag{1.24}$$

The properties that will be of interest for us in this problem are basically: the symmetries, the equilibrium points, the Jacobi constant and the Hill region, which, as we will see, have expressions almost analogous to those already commented for the planar case:

1. The equations of motion satisfy the symmetries

$$\begin{aligned} (t, x, y, z, \dot{x}, \dot{y}, \dot{z}) &\longrightarrow (-t, x, -y, z, -\dot{x}, \dot{y}, -\dot{z}), \\ (t, x, y, z, \dot{x}, \dot{y}, \dot{z}) &\longrightarrow (-t, x, -y, -z, -\dot{x}, \dot{y}, \dot{z}). \end{aligned} \tag{1.25}$$

   This means that, given any solution on the configuration space $(x(t), y(t), z(t))$ of system (1.21), there exists its symmetrical one with respect to the (x, y) plane and with respect to the (x, z) plane.

2. The system has the same five equilibrium point than in the planar case.

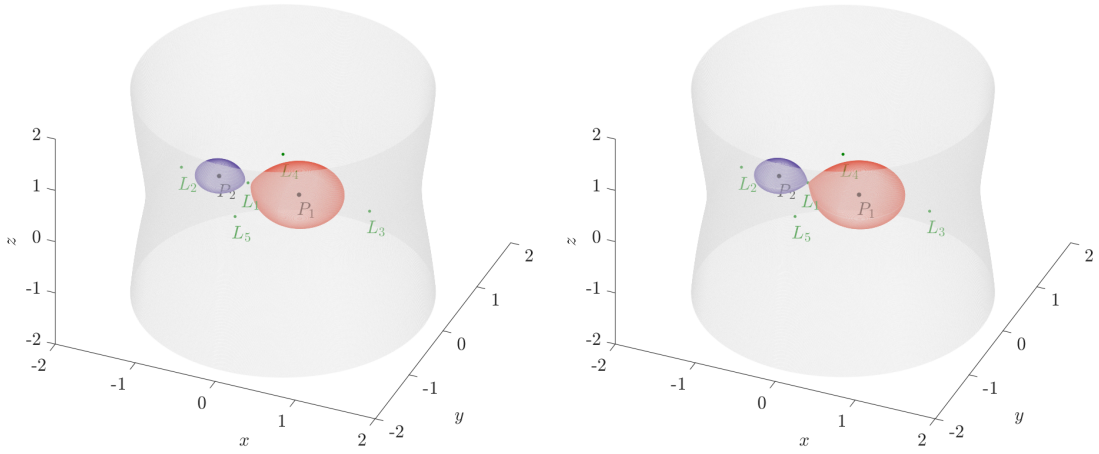

Figure 1.6: Hill region of motion for $C > C_{L_1}$ (left), $C = C_{L_1}$ (right). The forbidden region of motion is limited between the red and blue surfaces and the grey one.

3. The Jacobi integral in this case is defined by

$$C = 2\Omega(x, y, z) - \dot{x}^2 - \dot{y}^2 - \dot{z}^2, \tag{1.26}$$

and we have the same relation $H = -C/2$. In the same way, fixed a value of the Jacobi constant C (or the Hamiltonian H), the motion is allowed to take place in the Hill's region (see Figure 1.6) defined by

$$\mathcal{R}(C) = \{(x, y, z) \in \mathbb{R}^2 \mid 2\Omega(x, y, z) \geq C\}.$$

For the 3D case we will restrict the range of values of C to $C \geq C_{L_1}(\mu)$ ($H \leq H_{L_1}(\mu)$).

Chapter 2

Local regularization of the RTBP

The goal of this dissertation is to study the ejection-collision orbits, that is, orbits that eject and collide with a primary but the RTBP system (1.3) is singular at $r_1 = 0$ and $r_2 = 0$ (i.e. when the infinitesimal mass particle collides with one of the two primaries). So we have to regularize these points. In this chapter we will explain the basics of the most known *local regularizations* of the RTBP: The McGehee regularization and the Levi-Civita regularization.

These regularizations are local because they only regularize the collision with one of the two primaries (i.e. $r_1 = 0$ or $r_2 = 0$). But this will be enough for Chapters 3, 4 and 5 since we will restrict ourselves mainly to $C \geq C_{L_1}$ values and therefore the collision with the other primary cannot occur.

However, there are other global regularizations that deal with the two singularities of the RTBP system (1.3) at the same time. We will not go into much detail about them because it has been more convenient for us to work with local regularizations.

2.1 McGehee regularization

The first regularization that we will consider follows the ideas introduced by McGehee in [McG74, McG78] and consists in a blowup of the collision. In this section we will explain the procedure for the regularization of the ejection/collision with the first primary (remember that we consider $\mu \in (0, 1)$) but the procedure is analogous for the regularization of the ejection/collision with the other primary. Therefore, the first step is to translate the position of the primary that we want to regularize to the origin. To do it, we will consider the hamiltonian formulation introduced in (1.5) and we will introduce new variables:

$$\begin{aligned} \bar{x} &= x - \mu, & p_{\bar{x}} &= p_x = \dot{x} - y = \dot{\bar{x}} - \bar{y}, \\ \bar{y} &= y, & p_{\bar{y}} &= p_y = \dot{y} + x = \dot{\bar{y}} + \bar{x} + \mu. \end{aligned}$$

In this way, the Hamiltonian (1.5) becomes:

$$H(\bar{x}, \bar{y}, p_{\bar{x}}, p_{\bar{y}}) = \frac{1}{2}(p_{\bar{x}}^2 + p_{\bar{y}}^2) + \bar{y}p_{\bar{x}} - \bar{x}p_{\bar{y}} - \mu p_{\bar{y}} - \frac{1-\mu}{r_1} - \frac{\mu}{r_2} - \frac{1}{2}\mu(1-\mu), \tag{2.1}$$

where $r_1 = \sqrt{\bar{x}^2 + \bar{y}^2}$ and $r_2 = \sqrt{(\bar{x}+1)^2 + \bar{y}^2}$. The next step is to consider the symplectic change to polar coordinates

$$\begin{aligned} \bar{x} &= r\cos\vartheta, & p_{\bar{x}} &= p_r\cos\vartheta - \frac{p_\vartheta}{r}\sin\vartheta, \\ \bar{y} &= r\sin\vartheta, & p_{\bar{y}} &= p_r\sin\vartheta + \frac{p_\vartheta}{r}\cos\vartheta. \end{aligned}$$

With this change of coordinates the Hamiltonian (2.1) is given by

$$H(r,\vartheta,p_r,p_\vartheta) = \frac{1}{2}\left(p_r^2+\frac{p_\vartheta^2}{r^2}\right) - p_\vartheta - \frac{1-\mu}{r} - \frac{\mu}{r_2} - \mu\left(p_r\sin\vartheta + \frac{p_\vartheta}{r}\cos\vartheta\right) - \frac{1}{2}\mu(1-\mu), \tag{2.2}$$

with $r_2 = \sqrt{r^2+2r\cos\vartheta+1}$.

The associated system of ODE is given by

$$\begin{cases} \dot r = p_r - \mu\sin\vartheta, \\ \dot\vartheta = \dfrac{p_\vartheta}{r^2} - 1 - \dfrac{\mu\cos\vartheta}{r}, \\ \dot p_r = \dfrac{p_\vartheta^2}{r^3} - \dfrac{1-\mu}{r^2} - \mu\left(\dfrac{r+\cos\vartheta}{r_2^3} + \dfrac{p_\vartheta\cos\vartheta}{r^2}\right), \\ \dot p_\vartheta = \mu\left(\dfrac{r\sin\vartheta}{r_2^3} + p_r\cos\vartheta - \dfrac{p_\vartheta\sin\vartheta}{r}\right). \end{cases} \tag{2.3}$$

Introducing the new variables

$$v = \dot r r^{1/2}, \qquad u = r^{3/2}\dot\vartheta,$$

that are the components of the velocity in polar coordinates multiplied by $r^{1/2}$ the system (2.3) becomes

$$\begin{cases} \dot r = \dfrac{v}{r^{1/2}}, \\ \dot\vartheta = \dfrac{u}{r^{3/2}}, \\ \dot v = \dfrac{v^2}{2r^{3/2}} + \dfrac{u^2}{r^{3/2}} - \dfrac{1-\mu}{r^{3/2}} + 2u + r^{3/2} + \mu r^{1/2}\left(\cos\vartheta - \dfrac{r+\cos\vartheta}{r_2^3}\right), \\ \dot u = -\dfrac{uv}{2r^{3/2}} - 2v - \mu r^{1/2}\sin\vartheta\left(1-\dfrac{1}{r_2^3}\right). \end{cases} \tag{2.4}$$

Finally, introducing a change of time $dt/d\tau = r^{3/2}$ and denoting by $'$ the time derivative with respect the new time variable, the equations of motion are given by

$$\begin{cases} r' = vr, \\ \vartheta' = u, \\ v' = \dfrac{v^2}{2} + u^2 - (1-\mu) + 2ur^{3/2} + r^3 + \mu r^2\left(\cos\vartheta - \dfrac{r+\cos\vartheta}{r_2^3}\right), \\ u' = -\dfrac{uv}{2} - 2vr^{3/2} - \mu r^2\sin\vartheta\left(1-\dfrac{1}{r_2^3}\right). \end{cases} \tag{2.5}$$

We remark that the singularity $r=0$ has been removed and this system has just one singularity –the collision with the second primary $r=1$, $\vartheta=\pi$. If we consider the Hamiltonian (2.2) in these variables, which is a first integral, the relation $H=\mathfrak{h}$ becomes

$$0 = -\mathfrak{h}r + \frac{1}{2}\left(u^2+v^2\right) - (1-\mu) - \frac{r^3}{2} - \mu r\left(\frac{1}{2} + \frac{1}{r_2} + r\cos\vartheta\right). \tag{2.6}$$

2.1.1 The collision manifold

System (2.5) has an invariant manifold Λ defined by $r = 0$, called the collision manifold. From (2.6) we conclude that Λ is a torus (see Figure 2.1),

$$\Lambda = \{u^2 + v^2 = 2(1-\mu), \quad \vartheta \in [0, 2\pi]\}, \tag{2.7}$$

and the dynamics on this torus is given by

$$\begin{cases} \vartheta' = u, \\ v' = \dfrac{v^2}{2} + u^2 - (1-\mu) = \dfrac{u^2}{2}, \\ u' = -\dfrac{uv}{2}. \end{cases} \tag{2.8}$$

We want to point out that this torus is on the boundary of each energy level of the constant Hamiltonian relation (2.6).

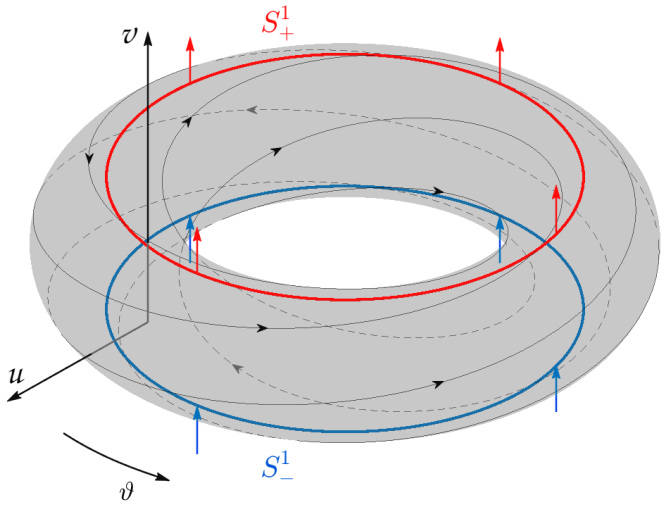

Figure 2.1: Collision manifold.

For our purposes we remark that on Λ there exist two circles of equilibrium points defined by $S^1_+ = \{r = 0, \vartheta, v = v_0, u = 0, \vartheta \in [0, 2\pi]\}$ and $S^1_- = \{r = 0, \vartheta, v = -v_0, u = 0, \vartheta \in [0, 2\pi]\}$ with $v_0 = +\sqrt{2(1-\mu)}$. We also observe that the tangent vector to both circles of equilibria is given by $(0, 1, 0, 0)$.

Let us define the matrices $M^{\pm}$ as the linearization of system (2.5) at the corresponding equilibrium points $S^1_{\pm}$; they are given by

$$M^{\pm} = \begin{pmatrix} \pm v_0 & 0 & 0 & 0 \\ 0 & 0 & 0 & 1 \\ 0 & 0 & \pm v_0 & 0 \\ 0 & 0 & 0 & \mp v_0/2 \end{pmatrix}.$$

The matrix $M^{\pm}$ has eigenvalues:

$$\lambda_1 = \lambda_2 = \pm v_0, \quad \lambda_3 = 0, \quad \lambda_4 = \mp v_0/2,$$

and corresponding eigenvectors:

$$\boldsymbol{v}_1 = (0,0,1,0), \quad \boldsymbol{v}_2 = (1,0,0,0), \quad \boldsymbol{v}_3 = (0,1,0,0), \quad \boldsymbol{v}_4 = (0,-2/v_0,0,1). \tag{2.9}$$

So for each equilibrium point $P_+ \in S^1_+$ we have a 2D unstable manifold $W^u(P_+)$ and a 1D stable one $W^s(P_+)$. Similarly, for each equilibrium point $P_- \in S^1_-$, we have a 2D stable manifold $W^s(P_-)$ and a 1D unstable one $W^u(P_-)$.

At this point we distinguish between 3 types of orbits: ejection, collision and ejection-collision orbits.

1. The set of *ejection orbits* –those which are ejected from collision with the first primary– is the set of orbits on the unstable manifold $W^u(P_+)$, for any $P_+ = (0, \vartheta, v_0, 0) \in S^1_+$. So each ejection orbit may be regarded as an orbit such that $r > 0$ for all finite time τ and asymptotically tends to an equilibrium point $P_+ \in S^1_+$ as $\tau \to -\infty$.

2. The set of *collision orbits* –those which arrive at collision with the first primary– is the set of orbits on the stable manifold $W^s(P_-)$, for any $P_- = (0, \vartheta, -v_0, 0) \in S^1_-$. So each collision orbit may be regarded as an orbit such that $r > 0$ for all finite time τ and asymptotically tends to an equilibrium point $P_- \in S^1_-$ as $\tau \to +\infty$.

3. The set of *ejection-collision orbits* –those which eject from/arrive at collision with the first primary– is the set of orbits obtained from the intersection $W^u(S^1_+) \cap W^s(S^1_-)$. So they may be regarded as heteroclinic connections between $P_+ \in S^1_+$ and $Q_- \in S^1_-$.

2.1.2 Particular case $\mu = 0$.

In order to have a first insight of such type of orbits, let us consider the particular case $\mu = 0$.

As it is well known, an ejection/collision orbit in this case is characterized by the angular momentum $M = r^2(d\vartheta/dt + 1)$ equal to 0 (see [Sze67]) that is $M = 0$, or equivalently, using the u variable, by $u = -r^{3/2}$. So, the manifold of ejection/collision orbits at the energy level $H = \mathfrak{h}$ defined by (2.6) now becomes

$$r\mathfrak{h} = \frac{1}{2}v^2 - 1. \tag{2.10}$$

We plot in Figure 2.2 the associated level curves and in Figure 2.3 we visualize the corresponding manifolds in variables (r, ϑ, v). In particular, for $H = \mathfrak{h} < 0$ we obtain the coinciding manifolds of ejection-collision orbits. If $H = \mathfrak{h}$ is either equal to 0 or positive, we obtain the manifolds consisting of the ejection-parabolic escape orbits (and parabolic escape-collision ones) and the ejection-hyperbolic escape orbits (and hyperbolic escape-collision ones) respectively, in the sense that they arrive at (depart from) infinity with zero or positive velocity.

We are particularly interested in this dissertation in ejection-collision orbits. We have just shown that for $\mu = 0$ the ejection manifold and the collision one coincide for $H < 0$. Thus any orbit ejecting from the primary ends colliding with it. However when μ is different from zero, the influence of the small primary somewhat deforms the ejection and collision manifolds and these manifolds do not coincide any more. The dynamics is much richer and intricate in this case and the subject of the next chapters is to study, from a numerical and an analytical point of view, this dynamics.

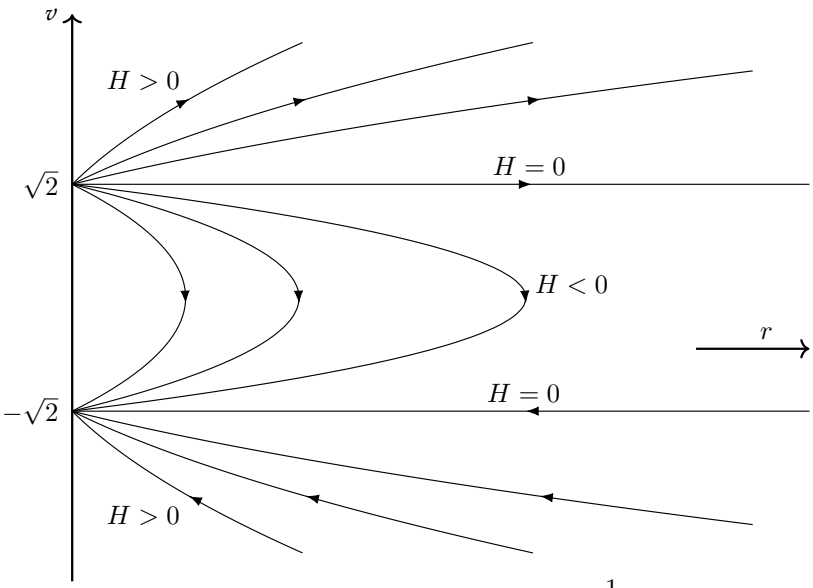

Figure 2.2: $\mu = 0$. Level curves of $rH = \frac{1}{2}v^2 - 1$.

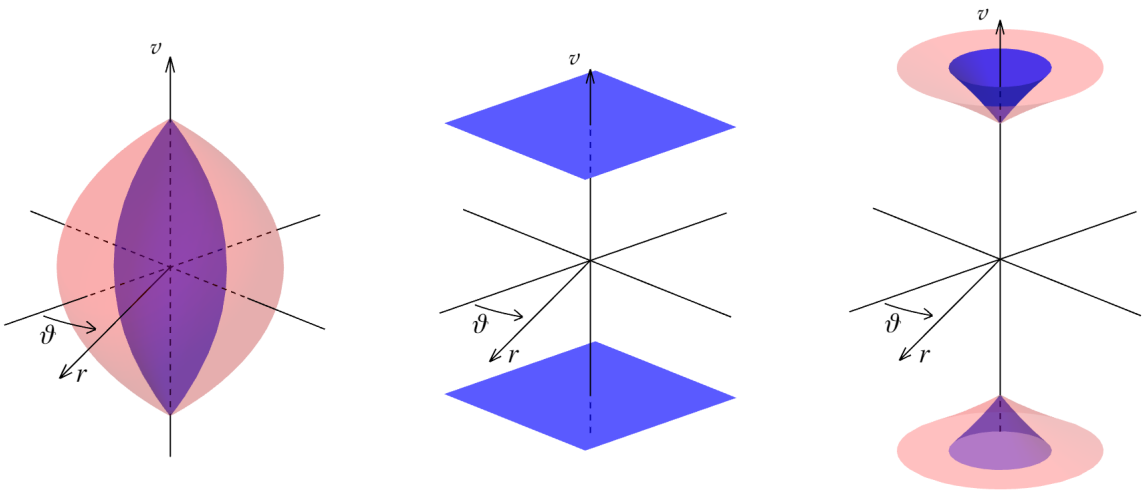

Figure 2.3: $\mu = 0$. Ejection-collision manifold for $H < 0$ (left). Ejection and collision manifolds for $H = 0$ (middle) and $H > 0$ (right).

2.2 Levi-Civita regularization

The other local regularization that we will consider is the Levi-Civita regularization [LC06] because it is conceptually simple, suitable for our theoretical purposes and efficient for numerical simulations as we will see in the next chapters. It is important to note that this regularization can be generalized in the 3D case through the Kustaanheimo – Stiefel regularization which can be found in [SS71].

The Levi-Civita regularization consists in two steps: first a change of time and then a coordinate change. We will see this regularization for problems of the form

$$\ddot{\boldsymbol{x}} + B\dot{\boldsymbol{x}} = \nabla_{\boldsymbol{x}}\Omega(\boldsymbol{x}), \tag{2.11}$$

with B a given matrix and

$$\boldsymbol{x} = \begin{pmatrix} x \\ y \end{pmatrix},$$

where the singularity of Ω, located at $\boldsymbol{x} = \boldsymbol{p}$, that we want to regularize has the form of a gravitational potential (as for example (1.4) or (1.14)) and we have a constant of motion given by

$$C = 2\Omega(\boldsymbol{x}) - (\dot{\boldsymbol{x}}, \dot{\boldsymbol{x}}). \tag{2.12}$$

Change of time

First, we will introduce the change of time $dt = ar\, ds$ with a constant, and we will denote by $' = \frac{d}{ds}$. Thus, we have

$$\dot{\boldsymbol{x}} = \frac{d\boldsymbol{x}}{dt} = \frac{d\boldsymbol{x}}{ds}\frac{ds}{dt} = \frac{\boldsymbol{x}'}{ar},$$
$$\ddot{\boldsymbol{x}} = \frac{d\dot{\boldsymbol{x}}}{dt} = \frac{d\dot{\boldsymbol{x}}}{ds}\frac{ds}{dt} = \frac{d}{ds}\left(\frac{\boldsymbol{x}'}{ar}\right)\frac{1}{ar} = \frac{r\boldsymbol{x}'' - r'\boldsymbol{x}'}{a^2 r^3}.$$

So we obtain

$$\ddot{\boldsymbol{x}} + B\dot{\boldsymbol{x}} = \frac{r\boldsymbol{x}'' - r'\boldsymbol{x}'}{a^2 r^3} + B\frac{\boldsymbol{x}'}{ar} = \nabla_{\boldsymbol{x}}\Omega(\boldsymbol{x}),$$

or, similarly

$$r\boldsymbol{x}'' - r'\boldsymbol{x}' + ar^2 B\boldsymbol{x}' = a^2 r^3 \nabla_{\boldsymbol{x}}\Omega(\boldsymbol{x}). \tag{2.13}$$

Change of coordinates

The next step is to introduce new coordinates $\boldsymbol{u} = (u, v)$

$$\boldsymbol{x} = L(\boldsymbol{u})\boldsymbol{u} + \boldsymbol{p}, \tag{2.14}$$

where

$$L(\boldsymbol{u}) = \begin{pmatrix} u & -v \\ v & u \end{pmatrix}, \tag{2.15}$$

and recall that $\boldsymbol{p}$ is the position that we want to regularize.

It is easy to see that

$$\begin{aligned} &\boldsymbol{x}' = L(\boldsymbol{u})\boldsymbol{u}' + L(\boldsymbol{u}')\boldsymbol{u} = 2L(\boldsymbol{u})\boldsymbol{u}', \\ &\boldsymbol{x}'' = 2L(\boldsymbol{u})\boldsymbol{u}'' + 2L(\boldsymbol{u}')\boldsymbol{u}', \\ &r = (\boldsymbol{u}, \boldsymbol{u}), \\ &r' = 2(\boldsymbol{u}, \boldsymbol{u}'), \end{aligned} \tag{2.16}$$

where $(\boldsymbol{a}, \boldsymbol{b})$ denotes the scalar product of the vectors $\boldsymbol{a}$ and $\boldsymbol{b}$, so we can rewrite (2.13) as

$$(\boldsymbol{u}, \boldsymbol{u})\left(2L(\boldsymbol{u})\boldsymbol{u}'' + 2L(\boldsymbol{u}')\boldsymbol{u}'\right) - 4(\boldsymbol{u}, \boldsymbol{u}')L(\boldsymbol{u})\boldsymbol{u}' + a(\boldsymbol{u}, \boldsymbol{u})^2 B 2L(\boldsymbol{u})\boldsymbol{u}' = a^2(\boldsymbol{u}, \boldsymbol{u})^3 \nabla_{\boldsymbol{x}}\Omega. \tag{2.17}$$

Using that

$$2(\boldsymbol{u}, \boldsymbol{u})L(\boldsymbol{u}')\boldsymbol{u}' - 4(\boldsymbol{u}, \boldsymbol{u}')L(\boldsymbol{u})\boldsymbol{u}' = -2(\boldsymbol{u}', \boldsymbol{u}')L(\boldsymbol{u})\boldsymbol{u},$$

we have that (2.17) becomes

$$2(\boldsymbol{u}, \boldsymbol{u})L(\boldsymbol{u})\boldsymbol{u}'' - 2(\boldsymbol{u}', \boldsymbol{u}')L(\boldsymbol{u})\boldsymbol{u} + 2a(\boldsymbol{u}, \boldsymbol{u})^2 BL(\boldsymbol{u})\boldsymbol{u}' = a^2(\boldsymbol{u}, \boldsymbol{u})^3 \nabla_{\boldsymbol{x}}\Omega. \tag{2.18}$$

Multiplying by $\frac{1}{2}L^{-1}(\boldsymbol{u}) = \frac{1}{2(\boldsymbol{u},\boldsymbol{u})}L^T(\boldsymbol{u})$ and dividing by $(\boldsymbol{u}, \boldsymbol{u})$ we obtain

$$\boldsymbol{u}'' - \frac{(\boldsymbol{u}', \boldsymbol{u}')}{(\boldsymbol{u}, \boldsymbol{u})}\boldsymbol{u} + aL^T(\boldsymbol{u})BL(\boldsymbol{u})\boldsymbol{u}' = \frac{a^2}{2}(\boldsymbol{u}, \boldsymbol{u})L^T(\boldsymbol{u})\nabla_{\boldsymbol{x}}\Omega, \tag{2.19}$$

and by the chain rule $\nabla_{\boldsymbol{u}}\Omega = 2L^T(\boldsymbol{u})\nabla_{\boldsymbol{x}}\Omega$, so

$$\boldsymbol{u}'' - \frac{(\boldsymbol{u}', \boldsymbol{u}')}{(\boldsymbol{u}, \boldsymbol{u})}\boldsymbol{u} + aL^T(\boldsymbol{u})BL(\boldsymbol{u})\boldsymbol{u}' = \frac{a^2}{4}(\boldsymbol{u}, \boldsymbol{u})\nabla_{\boldsymbol{u}}\Omega. \tag{2.20}$$

Using the expression of the constant of motion (2.12) we can see that

$$2\Omega - C = (\dot{\boldsymbol{x}}, \dot{\boldsymbol{x}}) = \frac{4}{a^2(\boldsymbol{u}, \boldsymbol{u})^2}(L(\boldsymbol{u})\boldsymbol{u}', L(\boldsymbol{u})\boldsymbol{u}') = \frac{4(\boldsymbol{u}', \boldsymbol{u}')}{a^2(\boldsymbol{u}, \boldsymbol{u})},$$

so we obtain

$$\boldsymbol{u}'' - \frac{a^2}{4}\left(2\Omega - C\right)\boldsymbol{u} + aL^T(\boldsymbol{u})BL(\boldsymbol{u})\boldsymbol{u}' = \frac{a^2}{4}(\boldsymbol{u}, \boldsymbol{u})\nabla_{\boldsymbol{u}}\Omega,$$

or similarly

$$\boldsymbol{u}'' + aL^T(\boldsymbol{u})BL(\boldsymbol{u})\boldsymbol{u}' = \frac{a^2}{4}\left[\left(2\Omega - C\right)\boldsymbol{u} + (\boldsymbol{u}, \boldsymbol{u})\nabla_{\boldsymbol{u}}\Omega\right]. \tag{2.21}$$

Finally, denoting by $U = \Omega - \frac{C}{2}$ and observing that

$$\nabla_{\boldsymbol{u}}\left[(\boldsymbol{u}, \boldsymbol{u})U\right] = 2\boldsymbol{u}U + (\boldsymbol{u}, \boldsymbol{u})\nabla_{\boldsymbol{u}}U = 2\left(\Omega - \frac{C}{2}\right)\boldsymbol{u} + (\boldsymbol{u}, \boldsymbol{u})\nabla_{\boldsymbol{u}}\Omega,$$

we have

$$\boldsymbol{u}'' + aL^T(\boldsymbol{u})BL(\boldsymbol{u})\boldsymbol{u}' = \frac{a^2}{4}\nabla_{\boldsymbol{u}}\left[(\boldsymbol{u}, \boldsymbol{u})U\right]. \tag{2.22}$$

It is important to note that the Levi-Civita regularization can be generalized to the 3D case through the linear operator

$$L(\boldsymbol{u}) = \begin{pmatrix} u_1 & -u_2 & u_3 & u_4 \\ u_2 & u_1 & -u_4 & -u_3 \\ u_3 & u_4 & u_1 & u_2 \\ u_4 & -u_3 & u_2 & -u_1 \end{pmatrix}, \tag{2.23}$$

although the proof of the 3D case is more laborious, because the vector field is non-orientable on the sphere. This implies that the required properties of the L operator are not so obvious and it is necessary to increase the dimension of the system (see [SS71]).

There is a compact formulation of the Levi-Civita regularization (see [Sze67]) for the particular case of

$$B = \begin{pmatrix} 0 & -2 \\ 2 & 0 \end{pmatrix}.$$

Using the complex notation we can rewrite the equation (1.3) as

$$\ddot{x} + i\ddot{y} + 2i(\dot{x} + i\dot{y}) = \Omega_x + i\Omega_y \Longleftrightarrow \ddot{z} + 2i\dot{z} = \nabla_z\Omega, \tag{2.24}$$

where $z = x + iy$ and $\nabla_z\Omega = \Omega_x + i\Omega_y$.

In order to regularize (2.24) we have to consider the previous equivalent transformations:

$$\begin{cases} z = f(w), \\ \dfrac{dt}{ds} = g(w) = \left|f'(w)\right|^2, \end{cases} \tag{2.25}$$

with $w = u + iv$ and, similarly, defining $U = \Omega - C/2$ and using the Jacobi integral (1.9), the transformed equation of (2.24) becomes

$$w'' + 2i\left|f'\right|^2 w' = \nabla_w(U\left|f'\right|^2).$$

In this way, the transformation $z = f(w) = p_1 + p_2 i + w^2$ regularizes the singularity at $(x, y) = (p_1, p_2) = \boldsymbol{p}$.

2.2.1 Regularization of the RTBP

In order to regularize the RTBP we only have to select $\boldsymbol{p} = (\mu, 0)$ in (2.14) to regularize the position of the first primary and $\boldsymbol{p} = (\mu - 1, 0)$ for the second primary. In addition, we will choose $a = 4$. The system (1.3) regularized at $P_1 = (\mu, 0)$ becomes

$$\begin{cases} u'' - 8(u^2+v^2)v' = \left(4\mathcal{U}(u^2+v^2)\right)_u \\ \qquad\qquad = 4\mu u + 16\mu u^3 + 12(u^2+v^2)^2 u + \dfrac{8\mu u}{r_2} - \dfrac{8\mu u(u^2+v^2)(u^2+v^2+1)}{r_2^3} - 4Cu, \\ v'' + 8(u^2+v^2)u' = \left(4\mathcal{U}(u^2+v^2)\right)_v \\ \qquad\qquad = 4\mu v - 16\mu v^3 + 12(u^2+v^2)^2 v + \dfrac{8\mu v}{r_2} - \dfrac{8\mu v(u^2+v^2)(u^2+v^2-1)}{r_2^3} - 4Cv, \end{cases} \tag{2.26}$$

where $' = d/ds$ and

$$\mathcal{U} = \frac{1}{2}\left[(1-\mu)\left(u^2+v^2\right)^2 + \mu\left((1+u^2-v^2)^2 + 4u^2v^2\right)\right] + \frac{1-\mu}{u^2+v^2} + \frac{\mu}{r_2} - \frac{C}{2},$$

with $r_2 = \sqrt{(1+u^2-v^2)^2+4u^2v^2}$. The system of ODE is now regular everywhere except at the collision with the primary P_2 ($r_2 = 0$).

In this new system of variables, the previous properties of the RTBP are translated as:

1. Since the Levi-Civita transformation duplicates the configuration space (see Figure 2.4) the equations of motion satisfy two symmetries, (2.27a) in consequence of the duplication of space and (2.27b) due to (1.6)

$$(s, u, v, u', v') \to (-s, u, -v, -u', v'), \tag{2.27a}$$
$$(s, u, v, u', v') \to (-s, -u, v, u', -v'). \tag{2.27b}$$

2. The equilibrium points are now duplicated and they are located on the plane (u, v). In particular, the collinear points now are located in the u axis and in the v axis. See Figure 2.4.

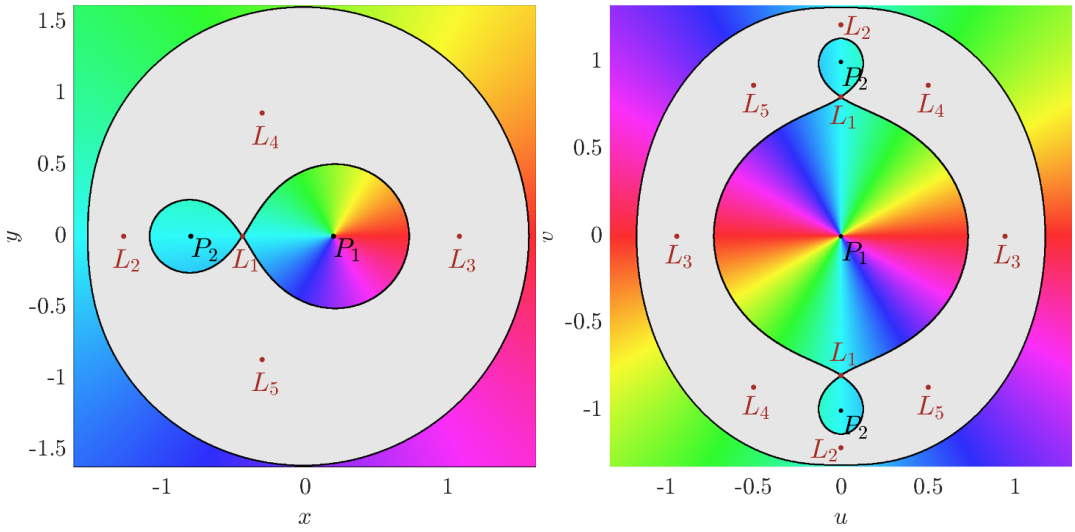

Figure 2.4: Levi-Civita transformation. Hill's region for $\mu = 0.2$ and C_{L_1}. Left. Synodic (x, y) coordinates. Right. Levi-Civita ones (u, v). In grey the forbidden region.

3. Jacobi Integral

$$u'^2 + v'^2 = 8\left(u^2 + v^2\right)\mathcal{U}, \tag{2.28}$$

which is regular at the collision with the primary P_1. In particular, the velocity at the position of the first primary $(u = 0, v = 0)$ satisfies

$$u'^2 + v'^2 = 8(1 - \mu). \tag{2.29}$$

4. Similarly, given a value of the Jacobi constant C, the Hill's region in variables (u, v) now becomes

$$\mathcal{R}(C) = \left\{(u, v) \in \mathbb{R}^2 \,|\, (u^2 + v^2)\mathcal{U} \geq 0\right\}. \tag{2.30}$$

If we restrict to the case $C \geq C_{L_1}$ it is enough to consider a local regularization, because the Hill region does not allow motion around the singularity of the other primary. However in Chapter 6 we will consider values of $C \in [C_{L_{2,3}} C_{L_1})$ and to deal with possible transits between both primaries we have two options:

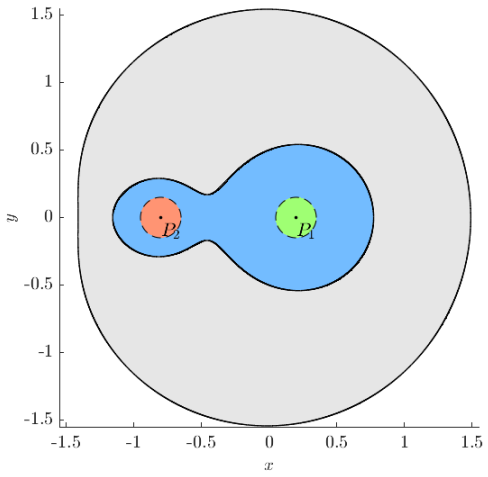

Figure 2.5: $\mu = 0.2$, $C = 3.8$. The motion will be considered on the blue region and in synodical (x, y) coordinates, except in a neighborhood of each primary (green and red areas) where the corresponding Levi-Civita regularization is carried out.

1. To consider global regularizations (see Section 2.3).

2. To use local regularizations around each primary. In particular in Chapter 6 we will use this strategy using the Levi-Civita regularization (see Figure 2.5): Outside a small neighborhood of each primary, we use synodical coordinates (x, y) and the usual time t. Whenever we are inside a small neighborhood of one primary, we consider the suitable Levi-Civita coordinates (u, v) and the corresponding local time s (see Figure 2.5). Thus, we consider 3 different times, a global time t when working with synodical coordinates (x, y) and a variable s when dealing with the Levi-Civita coordinates, (so actually two different times depending on which local regularization we are considering). This will be specially useful in Chapter 6, when describing a global evolution of ejection orbits.

2.2.2 Regularization of the Hill problem

In order to regularize the Hill problem we only have to select $\boldsymbol{p} = (0, 0)$ in (2.14) to regularize the position of the primary and, in a similar way, we will choose $a = 4$. The system (1.15) becomes:

$$\begin{cases} u_h'' - 8(u_h^2 + v_h^2)v_h' = \left(4\mathcal{U}_h(u_h^2 + v_h^2)\right)_{u_h} \\ \qquad\qquad = -4Ku_h + 12\left(2(u_h^4 - 2u_h^2v_h^2 - v_h^4) + (u_h^2 + v_h^2)^2\right)u_h, \\ v_h'' + 8(u_h^2 + v_h^2)u_h' = \left(4\mathcal{U}_h(u_h^2 + v_h^2)\right)_{v_h} \\ \qquad\qquad = -4Kv_h + 12\left(2(v_h^4 - 2u_h^2u_h^2 - u_h^4) + (u_h^2 + v_h^2)^2\right)v_h, \end{cases} \tag{2.31}$$

with

$$\mathcal{U}_h = \frac{3(u_h^2 - v_h^2)^2}{2} + \frac{1}{u_h^2 + v_h^2} - \frac{K}{2}, \tag{2.32}$$

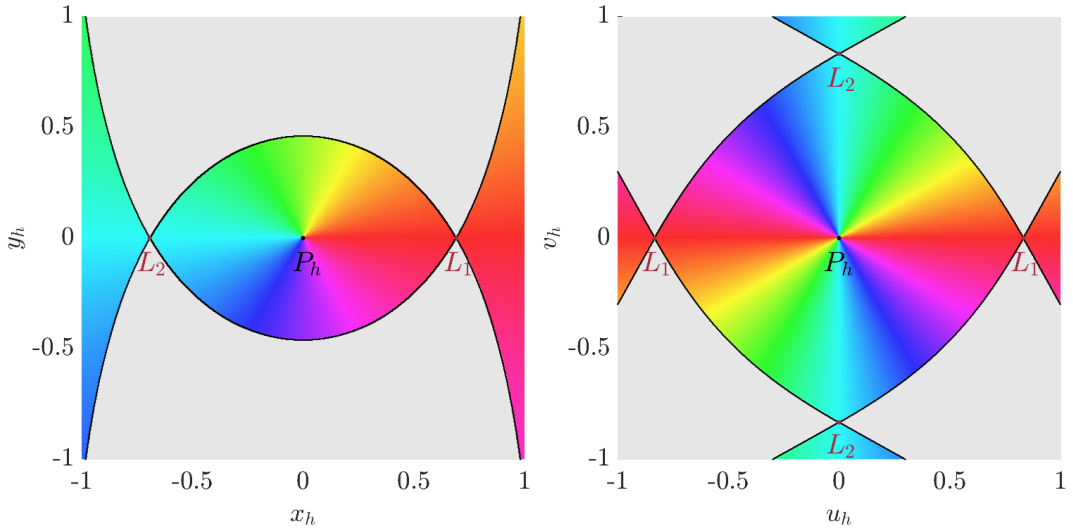

Figure 2.6: Levi-Civita transformation. Hill's region for $K = K_L = 3^{4/3}$. Left. Synodic (x_h, y_h) coordinates. Right. Levi-Civita ones (u_h, v_h). In grey the forbidden region.

With this transformation the previous properties of the Hill problem are translated as:

1. As the transformation duplicates the configuration space (see Figure 2.6), the system (2.31) satisfies the symmetries:

$$(s, u_h, v_h, u_h', v_h') \to (-s, u_h, -v_h, -u_h', v_h'), \tag{2.33a}$$
$$(s, u_h, v_h, u_h', v_h') \to (-s, -u_h, v_h, u_h', -v_h'), \tag{2.33b}$$
$$(s, u_h, v_h, u_h', v_h') \to (-s, v_h, u_h, -v_h', -u_h'). \tag{2.33c}$$

2. For the same reason, the equilibrium points are duplicated, and we have $L_1 = (\pm 3^{-1/6}, 0)$ and $L_2 = (0, \pm 3^{-1/6})$.

3. The first integral of (2.31) is given by:

$$u_h'^2 + v_h'^2 = 8(u_h^2 + v_h^2)\mathcal{U}_h, \tag{2.34}$$

which is regular at the collision with P_h. In particular the velocity at the position of the primary $(u_h = 0, v_h = 0)$ satisfies:

$$u_h'^2 + v_h'^2 = 8. \tag{2.35}$$

4. Depending on the value of the first integral of the system K we can define the valid region of motion (see Figure 2.6) in the plane (u_h, v_h) as:

$$\mathcal{R}(K) = \left\{(u_h, v_h) \in \mathbb{R}^2 \,|\, (u_h^2 + v_h^2)\mathcal{U}_h \geq 0\right\}. \tag{2.36}$$

2.3 Global regularizations of the RTBP

There exist transformations that can regularize the position of both primaries simultaneously. In this section we will present the three most famous global regularizations: the Thiele-Burrau, the Birkhoff and the Lemaitre transformation and we will conclude with a formulation that can generalize the formulae of all these transformations.

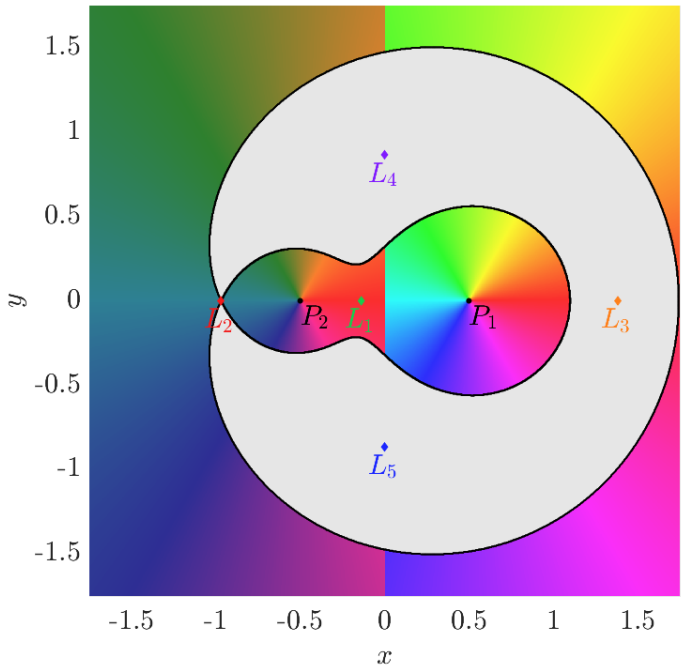

Figure 2.7: Synodic reference system where the primaries are in the positions $(\pm 1/2, 0)$, Hill region and equilibrium points for $\mu = 0.2$ and C_{L_2}.

In order to present these global regularizations, it is more convenient to use a reference system (see Figure 2.7) where the primaries are equidistant from the origin, that is, the position of the first primary is $(1/2, 0)$ and the position of the second primary is $(-1/2, 0)$. In this way, using the complex notation and introducing the variable $q = z + 1/2 - \mu$ we can rewrite system (2.24) as

$$\ddot{q} + 2i\dot{q} = \nabla_q \Omega, \tag{2.37}$$

Let us emphasize that now $r_1 = |q - 1/2|$ and $r_2 = |q + 1/2|$ and the regularizations are given by an analogous formula to (2.25):

$$\begin{cases} q = f(w), \\ \dfrac{dt}{ds} = |f'(w)|^2. \end{cases} \tag{2.38}$$

The Thiele–Burrau transformation

The Thiele-Burrau transformation was introduced by Thiele [Thi95] for the particular case $\mu = 0.5$ and was generalized by Burrau [Bur06] for any μ. This transformation is given by

$$\begin{aligned} q = f(w) &= \frac{1}{2}\cos w \\ &= \frac{1}{2}\cos(u+iv) = \frac{1}{2}\left(\cos u \cosh v - i \sin u \sinh v\right). \end{aligned} \tag{2.39}$$

This regularization (see Figure 2.8) is 2π-periodic (in u) and the primaries are now located at $P_1 = (2k\pi, 0)$ and $P_2 = ((2k+1)\pi, 0)$ for $k \in \mathbb{Z}$ but we can also restrict ourselves to the interval $u \in [0, \pi]$ thanks to the symmetry $\cos(w) = -\cos(\pi - w)$.

From the transformation (2.39) it is easy to see that $u = ctt$ corresponds to hyperbolas and $v = ctt$ corresponds to ellipses in the physical plane (x, y), since

$$\frac{x^2}{\cos^2 u} - \frac{y^2}{\sin^2 u} = \frac{1}{4} \qquad \text{and} \qquad \frac{x^2}{\cosh^2 v} + \frac{y^2}{\sinh^2 v} = \frac{1}{4}.$$

Before proceeding it is also important to note that the distances of the third particle from P_1 and P_2 become $r_1 = \frac{1}{2}(\cosh v - \cos u)$ and $r_2 = \frac{1}{2}(\cosh v + \cos u)$.

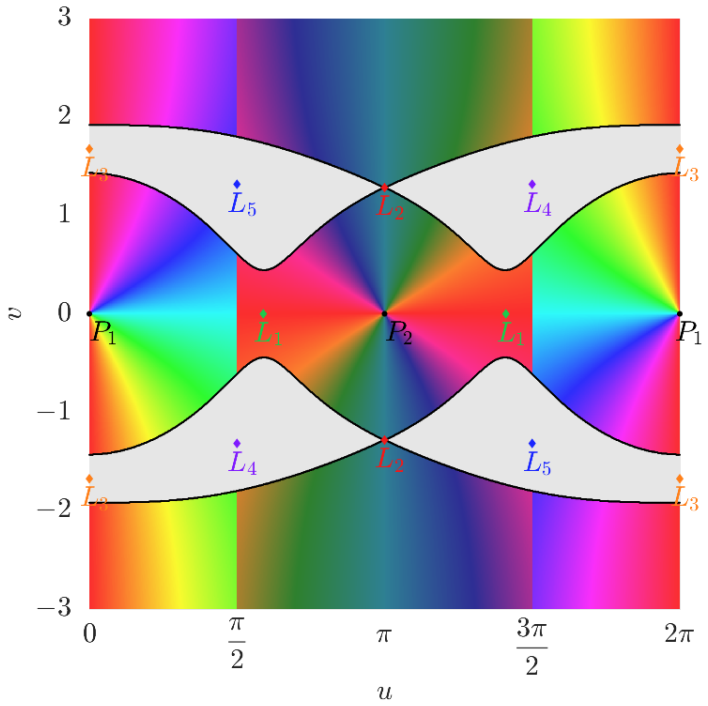

Figure 2.8: Thiele-Burrau transformation for $\mu = 0.2$ and C_{L_2}. The colors are correlated with Figure 2.7.

In order to obtain the equations of motion we need to compute

$$|f'(w)|^2 = \frac{1}{4}\left(\cosh^2 v - \cos^2 u\right) = \frac{\cosh(2v) - \cos(2u)}{8} = \frac{r_1 r_2}{2}.$$

In this way, the system is regular at all points and the equations of motion are given by

$$\begin{cases} u'' - r_1 r_2 v' = \left(\dfrac{r_1 r_2}{2}\mathcal{U}_{TB}\right)_u \\ \qquad\qquad = \dfrac{\sin u}{16}\left[2\cos^3 u + (1-2\mu)\left((\cosh^2 v - 3\cos^2 u)\cosh v - 8\right) - 4C\cos u\right], \\ v'' + r_1 r_2 u' = \left(\dfrac{r_1 r_2}{2}\mathcal{U}_{TB}\right)_v \\ \qquad\qquad = \dfrac{\sinh v}{16}\left[8 + 2\cosh^3 v - (1-2\mu)\left(3\cosh^2 v - \cos^2 u\right)\cos u - 4C\cosh v\right], \end{cases} \tag{2.40}$$

where

$$\mathcal{U}_{TB} = \frac{r_1^2}{2} + \frac{\mu\cos u\cosh v}{2} + \frac{(1-\mu)}{r_1} + \frac{\mu}{r_2} - \frac{C}{2}. \tag{2.41}$$

As we can see, despite the fact that hyperbolic functions appear when doing the Thiele-Burrau regularization, the system of equations that we obtain is very compact. This is very useful for manual computations (see for example [EL68]).

The Birkhoff transformation

The Birkhoff regularization [Bir15] is given by:

$$\begin{aligned} q = f(w) &= \frac{1}{4}\left(2w + \frac{1}{2w}\right) \\ &= \frac{1}{4}\left(2(u+iv) + \frac{1}{2(u+iv)}\right) = \frac{u}{2} + \frac{u}{8\left(u^2+v^2\right)} + i\left[\frac{v}{2} - \frac{v}{8\left(u^2+v^2\right)}\right]. \end{aligned} \tag{2.42}$$

This regularization (see Figure 2.9) duplicates the configuration space except the position of the two primaries that now are $P_1 = (1/2, 0)$ and $P_2 = (-1/2, 0)$ and introduce a new singularity in $w = 0$ that corresponds to $|q| \to \infty$ in $w = 0$.

With this transformation the distances of the third particle from P_1 and P_2 become

$$r_1 = \frac{|w-1/2|^2}{2|w|} = \frac{(u-1/2)^2+v^2}{2\sqrt{u^2+v^2}}, \qquad r_2 = \frac{|w+1/2|^2}{2|w|} = \frac{(u+1/2)^2+v^2}{2\sqrt{u^2+v^2}}.$$

In order to obtain the equations of motion we need to compute

$$|f'(w)|^2 = \frac{\left|4w^2-1\right|^2}{64\left|w\right|^4} = \frac{r_1 r_2}{u^2+v^2}.$$

In this way, the equations of motion are given by

$$\begin{cases} u'' - \dfrac{2r_1 r_2}{u^2+v^2}v' = \left(\dfrac{r_1 r_2}{u^2+v^2}\mathcal{U}_B\right)_u, \\ v'' + \dfrac{2r_1 r_2}{u^2+v^2}u' = \left(\dfrac{r_1 r_2}{u^2+v^2}\mathcal{U}_B\right)_v, \end{cases} \tag{2.43}$$

where

$$\frac{r_1 r_2}{u^2+v^2}\mathcal{U}_B = \frac{(1-\mu)\left(r_1^3+2\right)r_2 + \mu\left(r_2^3+2\right)r_1 - Cr_1 r_2}{2(u^2+v^2)}. \tag{2.44}$$

The expression of these equations are quite similar to Levi-Civita's, but the degree of the polynomials that appear are of higher degree and therefore require more effort to deal with.

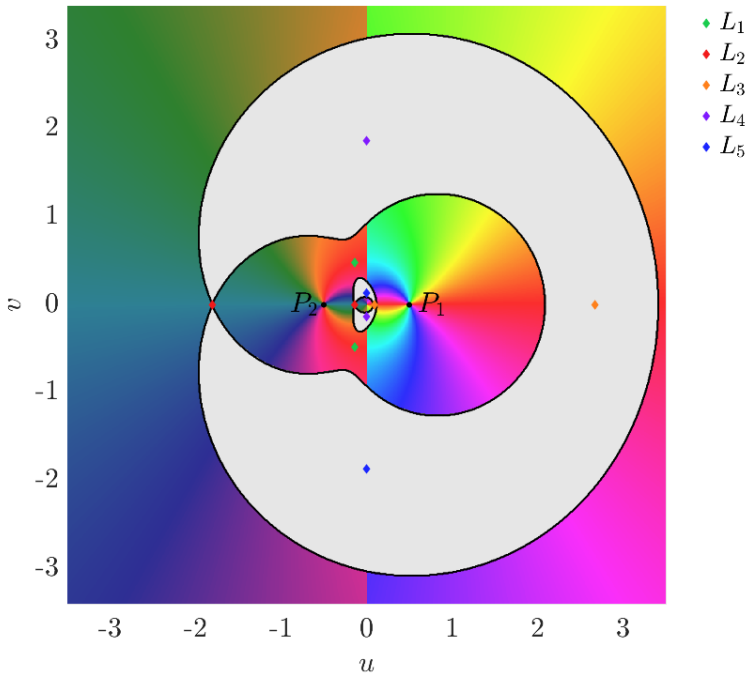

Figure 2.9: Birkhoff transformation for $\mu = 0.2$ and C_{L_2}. The colors are correlated with Figure 2.7.

Lemaître transformation

The last global regularization that we will consider is the Lemaître regularization [Lem55] which is given by

$$\begin{aligned} q = f(w) &= \frac{1}{4}\left(w^2 + \frac{1}{w^2}\right) \\ &= \frac{1}{4}\left((u+iv)^2 + \frac{1}{(u+iv)^2}\right) = \frac{(u^2-v^2)(1+(u^2+v^2)^2)}{4(u^2+v^2)^2} + i\frac{uv\left((u^2+v^2)^2-1\right)}{2(u^2+v^2)^2}. \end{aligned} \tag{2.45}$$

This regularization (see Figure 2.10) quadruplicates the configuration space except the position of the two primaries that now are $P_1 = (\pm 1, 0)$ and $P_2 = (0, \pm 1)$ and, like Birkhoff regularization, introduces a new singularity in $w = 0$ that corresponds to $|q| \to \infty$ in $w = 0$.

In order to obtain the equations of motion we need to compute

$$|f'(w)|^2 = \frac{\left|w^4 - 1\right|^2}{4\left|w\right|^6} = \frac{4r_1 r_2}{u^2+v^2},$$

where the distances to the primaries are now given by

$$r_1 = \frac{|w^2-1|^2}{4|w|^2} = \frac{(u^2+v^2)^2 - 2(u^2-v^2) + 1}{4\left(u^2+v^2\right)}, \qquad r_2 = \frac{|w^2+1|^2}{4|w|^2} = \frac{(u^2+v^2)^2 + 2(u^2-v^2) + 1}{4\left(u^2+v^2\right)}.$$

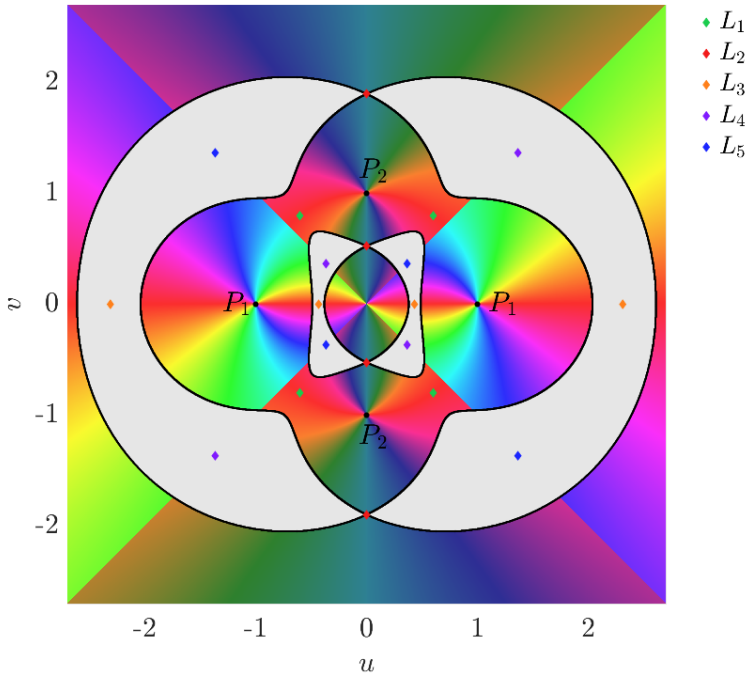

Figure 2.10: Lemaître transformation for $\mu = 0.2$ and C_{L_2}. The colors are correlated with Figure 2.7.

In this way, the equations of motion are given by

$$\begin{cases} u'' - \dfrac{8r_1r_2}{u^2+v^2}v' = \left(\dfrac{4r_1r_2}{u^2+v^2}\mathcal{U}_L\right)_u, \\ v'' + \dfrac{8r_1r_2}{u^2+v^2}u' = \left(\dfrac{4r_1r_2}{u^2+v^2}\mathcal{U}_L\right)_v, \end{cases} \tag{2.46}$$

where

$$\frac{4r_1r_2}{u^2+v^2}\mathcal{U}_L = 2\frac{(1-\mu)\left(r_1^3+2\right)r_2 + \mu\left(r_2^3+2\right)r_1 - Cr_1r_2}{u^2+v^2}. \tag{2.47}$$

In a similar way, these equations are similar to Levi-Civita's and Birkhoff's, but the degree of the polynomials that appear are of higher degree and therefore they are not very useful because of their computational cost.

Generalization of global regularization methods

The previous regularizations admit different generalizations. In particular Wintner [Win30] generalized the Birkhoff regularization to

$$q = f(w) = \frac{1}{2}\frac{(w+1/2)^{2n} + (w-1/2)^{2n}}{(w+1/2)^{2n} - (w-1/2)^{2n}}, \tag{2.48}$$

for $n \in \mathbb{N}$, where the case $n = 1$ corresponds to the Birkhoff regularization. Similarly, Broucke [Bro65] generalizes the Thiele–Burrau transformation to

$$q = f(w) = \frac{1}{2}\cos(\alpha w), \tag{2.49}$$

and the Birkhoff regularization to

$$q = f(w) = \frac{1}{4}\left(w^{\alpha} + \frac{1}{w^{\alpha}}\right), \tag{2.50}$$

where $\alpha \in \mathbb{R} \setminus \{0\}$.

However, all these global regularizations can be written in the same general form:

$$q = f(w) = A\left(h(w) + \frac{1}{h(w)}\right), \tag{2.51}$$

where A is a constant. In particular, all the general regularizations explained we select $A = 1/4$ and the value of $h(w)$ is given by:

- $h(w) = e^{iw}$ for the Thiele-Burrau transformation.
- $h(w) = 2w$ for the Birkhoff transformation.
- $h(w) = w^2$ for the Lemaître transformation.
- $h(w) = \dfrac{(w+1/2)^n + (w-1/2)^n}{(w+1/2)^n - (w-1/2)^n}$ for the Wintner transformation.
- $h(w) = e^{i\alpha w}$ for the Broucke generalization of the Thiele-Burrau transformation.
- $h(w) = w^{\alpha}$ for the Broucke generalization of the Birkhoff transformation.

Furthermore, as we are interested in ejection / collision orbits, it is important to note that with these regularizations the velocities at the singular points of system (1.3) are given by:

- $|w'|^2 = 2(1-\mu)\,|h'(w_1)|^2$ for $r_1 = 0$,
- $|w'|^2 = 2\mu\,|h'(w_2)|^2$ for $r_2 = 0$,

where w_i corresponds to the position of P_i, $i = 1, 2$.

Finally, it is important to remark that in this dissertation we will deal with the case of $C < C_{L_1}$ only in a numerical way and therefore a good alternative to do it will be to consider the Birkhoff and Lemaitre regularizations. However, the expressions obtained with these regularizations are very similar to those obtained with Levi-Civita but, as we have said previously, the maximum degree of the polynomials that appear in these two global regularizations is higher than in the case of Levi-Civita and therefore it requires a higher computational cost to deal with them. For this reason we have decided to consider local Levi-Civita regularizations around each primary (see Figure 2.5) for values of $C < C_{L_1}$.

Chapter 3

Numerical Computation of n-EC orbits of the RTBP

In this chapter we will detail the numerical results obtained for a particular case of ejection-collision orbit which we have called n-ejection-collision orbits and denoted by n-EC orbits. We will restrict ourselves mainly to the values of the Jacobi constant $C \geq C_{L_1}$ allowing μ to vary from 0 to 1, so that we will only study the ejection and collision with the first primary. This will allow us to consider only a local regularization to study these orbits since the collision with the second primary is not possible for these values of C if we are considering the motion in the neighborhood of the first primary . However, we will see how when considering slightly broader Hill regions (associated with $C \in [C_{L_{2,3}}, C_{L_1})$) new ejection-collision orbits appear, but we will study this phenomenon in more depth in Chapter 6.

Thus, the first step is to introduce the ejection-collision orbits that we will study.

Definition 3.1. *We call n-ejection-collision orbit of a primary, simply noted by n-EC orbit, to the orbit that the particle describes when ejects from a primary and reaches n times a relative maximum in the distance with respect to this primary before colliding with it.*

As we will consider values of $\mu \in (0, 1)$ we will study only the n-EC orbits associated to the first primary. Furthermore, as we will see, this definition is useful only if we consider a sufficiently restricted Hill region.

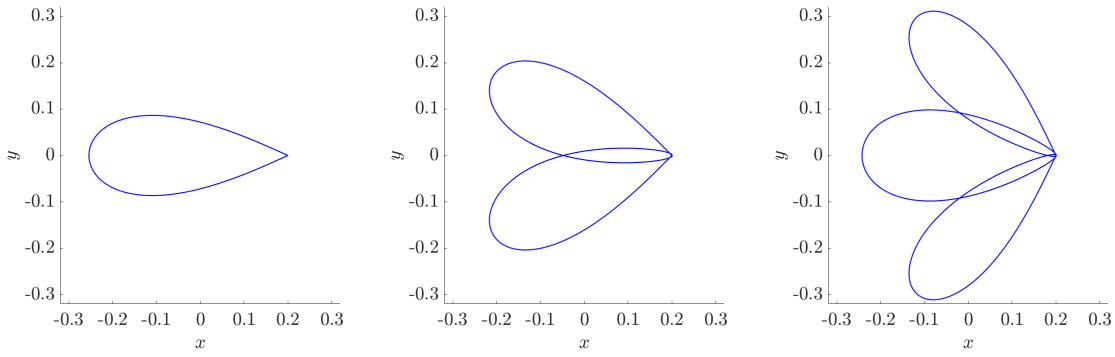

Figure 3.1: Examples of n-EC orbits for $n = 1, 2, 3$ (*from left to right*), $\mu = 0.2$ and $C = 4.25$. For $n = 2$ ($n = 3$), there are 1 (2) close passages to collision between ejection and collision.

It is important to note that the work related to ejection-collision orbits that can be found in [ARV13],

[CL88], [DF89], [LL88], [LMA85], [ML98], [Piñ95], corresponds to the particular case of 1-EC orbits. So we will make a special emphasis in this case but we will deal with the general case $n \geq 1$ (see Figure 3.1 for examples of n-EC orbits).

In particular, for the 1-EC orbits of the RTBP the strongest result was the one that can be found in [CL88], where it is shown that given a $\mu \in (0,1)$ there are four 1-EC orbits for a values of C large enough. In this chapter we will extend numerically this result for smaller values of C and for the case $n \geq 1$, and we will see how a $\hat{C}(\mu, n)$ exists such that for all $C \geq \hat{C}(\mu, n)$ there are exactly four n-EC orbits.

In order to study the n-EC orbits we will consider basically two systems, the one given by the McGehee regularization (2.5) and the one given by the Levi-Civita transformation (2.26) and we will present three different methods in order to find and study the ejection-collision orbits. Therefore, the first step is to compute the initial conditions necessary to obtain these orbits.

3.1 Preliminaries for the ejection/collision orbits

The ejection/collision orbits have a very different character according to which system we consider them. The ejection (collision) occurs in infinite time if we work with the McGehee regularization so from a numerical point of view we cannot exactly start from the ejection (collision). This difficulty does not appear in Levi-Civita, since the ejection (collision) occurs in finite time.

In this way, if we want to study the ejection-collision orbits we have to see what initial conditions we have to take to start from the ejection or collision in both regularized systems.

3.1.1 Ejection/collision in the McGehee regularized system

As we said in Section 2.1 the set of ejection-collision orbits is the set of orbits obtained from the intersection $W^u(S^1_+) \cap W^s(S^1_-)$, that is the set of heteroclinic connections between the points of S^1_+ and S^1_- and the first step is the computation of the ejection (collision) orbits, that is, we need to compute the unstable (stable) manifold of any equilibrium point belonging to S^1_+ (S^1_-).

To do so, fixed a value of $H = \mathfrak{h}$, in order to consider initial conditions for an ejection orbit, we make two comments: on the one hand, for each equilibrium point $P \in S^1_+$, the 2D $W^u(P)$ is tangent to the plane passing through P generated by the eigenvectors $\boldsymbol{v}_1$ and $\boldsymbol{v}_2$ (see Section 2.1), i.e. vectors like $\boldsymbol{v} = (\alpha, 0, \beta, 0)$, with $\alpha, \beta \in \mathbb{R}$. On the other hand, we recall that the energy level set $H = \mathfrak{h}$ is defined implicitly by (2.6), and the normal vector to this energy level set at point $P = (0, \vartheta_0, v_0, 0)$ is $\boldsymbol{n} = (-\mathfrak{h} - \frac{3}{2}\mu, 0, v_0, 0)$. So the vectors $\boldsymbol{v}$ (generating the tangent plane $W^u(P)$) must be perpendicular to $\boldsymbol{n}$, i.e. they must satisfy

$$\alpha(-\mathfrak{h} - \frac{3}{2}\mu) + \beta v_0 = 0.$$

In this way, the normalized vector tangent to $W^u(P)$ for $H = \mathfrak{h}$ is given by

$$\boldsymbol{w}_1 = \frac{1}{\sqrt{(\mathfrak{h} + 3\mu/2)^2 + v_0^2}} \left(v_0, 0, \mathfrak{h} + \frac{3\mu}{2}, 0 \right). \tag{3.1}$$

If we want to consider the linear approximation to this manifold we will take the initial condition of an ejection orbit associated with the point $P = (0, \vartheta_0, v_0, 0)$ as

$$(0, \vartheta_0, v_0, 0) + s\boldsymbol{w}_1, \tag{3.2}$$

with $s > 0$ a small quantity (typically 10^{-6} to 10^{-8}). This has the main advantage of being very simple but it has a clear disadvantage: for obtaining a small error we must use a sufficiently small s

and therefore we will need more integration time, which will cause numerical error to accumulate. In order to avoid this problem we will use approximations of high order that can be computed via the parameterization method (see [CFdlL03a, CFdlL03b, CFdlL05]).

The parameterization method

The parameterization method allows us to obtain a high-order approximation of invariant manifolds associated with a dynamical system $\boldsymbol{z}' = \boldsymbol{F}(\boldsymbol{z})$. In our case we want to obtain the invariant manifold associated with the equilibrium point P_+, tangent to the vector $\boldsymbol{w}_1$.

To simplify the notation, we will define $\boldsymbol{z} = (r, \vartheta, v, u)$ and we rewrite the system (2.5) as $\boldsymbol{z}' = \boldsymbol{F}(\boldsymbol{z})$. To find a parameterization $\boldsymbol{z} = \boldsymbol{W}(s)$ of the invariant manifold $W^u(P_+)$ associated with the energy level $H = \mathfrak{h}$ (this is tangent to $\boldsymbol{w}_1$ in P_+) such that $\boldsymbol{W}(0) = P_+$ we have to solve the invariance equation

$$\boldsymbol{F}(\boldsymbol{W}(s)) = D\boldsymbol{W}(s) f(s). \tag{3.3}$$

where the internal dynamics of the manifold is given by the equation $s' = f(s)$ with $f(0) = 0$.

In order to solve the equation (3.3) the typical strategy is to find power series in terms of s of W and f (see [HCF$^+$16]). However, in our case, due to the expression of the system (2.5), it does not admit a series expansion in s and to deal with it we must consider an expansion in powers of $s^{1/2}$.

To simplify the problem to be solved, we consider the system

$$\boldsymbol{Z}' = \boldsymbol{G}(\boldsymbol{Z}) = S^{-1}\boldsymbol{F}(P_+ + S\boldsymbol{Z}), \tag{3.4}$$

where S is the matrix that has column vectors the eigenvectors of $DF(P_+)$ given by $\boldsymbol{w}_1$ and

$$\boldsymbol{w}_2 = \frac{1}{\sqrt{(\mathfrak{h} + 3\mu/2)^2 + v_0^2}} \left(\mathfrak{h} + \frac{3\mu}{2}, 0, -v_0, 0\right), \qquad \boldsymbol{w}_3 = \boldsymbol{v}_3, \qquad \boldsymbol{w}_4 = \frac{\boldsymbol{v}_4}{||\boldsymbol{v}_4||},$$

where the expression of the vectors $\boldsymbol{v}_i$ is given in (2.9). In this way the equilibrium point of (3.4) is $\mathbf{0}$ and

$$D\boldsymbol{G}(\mathbf{0}) = \begin{pmatrix} v_0 & 0 & 0 & 0 \\ 0 & v_0 & 0 & 0 \\ 0 & 0 & 0 & 0 \\ 0 & 0 & 0 & -v_0/2 \end{pmatrix}, \tag{3.5}$$

and the equation that we have to solve becomes

$$\boldsymbol{G}(\boldsymbol{\mathcal{W}}(s)) = D\boldsymbol{\mathcal{W}}(s) f(s). \tag{3.6}$$

with $\boldsymbol{W}(s) = P_+ + S\boldsymbol{\mathcal{W}}(s)$ that implies $\boldsymbol{\mathcal{W}}(0) = \mathbf{0}$. Thus we have to find $\boldsymbol{\mathcal{W}}(s)$ and $f(s)$ as an expansion in terms of $s^{1/2}$

$$\begin{cases} \boldsymbol{\mathcal{W}}(s) = \displaystyle\sum_{i\geq 2} \boldsymbol{\mathcal{W}}_{i/2}(s) = \sum_{i\geq 2} \boldsymbol{\omega}_{i/2} s^{i/2} & \text{with } \boldsymbol{\omega}_1 = (1,0,0,0), \\ f(s) = \displaystyle\sum_{i\geq 2} f_{i/2}(s) = \sum_{i\geq 2} \mathrm{f}_{i/2} s^{i/2} & \text{with } \mathrm{f}_1 = \lambda_1 = v_0, \end{cases}$$

and we will introduce subscript $_{<k/2}$ or $_{\leq k/2}$ in order to denote the truncation of the expansion until the order $(k-1)/2$ and $k/2$ respectively. For example

$$\boldsymbol{\mathcal{W}}_{<k}(s) = \sum_{i=2}^{k-1} \boldsymbol{\mathcal{W}}_{i/2}(s) \quad \text{and} \quad \boldsymbol{\mathcal{W}}_{\leq k}(s) = \sum_{i=2}^{k} \boldsymbol{\mathcal{W}}_{i/2}(s).$$

At this point the goal is to compute the terms $\boldsymbol{\omega}_{k/2}$ and $f_{k/2}$ for $k>1$ once we know $\boldsymbol{\mathcal{W}}_{<k/2}(s)$ and $f_{<k/2}(s)$ (i.e. knowing $\boldsymbol{\mathcal{W}}_1$, ... , $\boldsymbol{\mathcal{W}}_{(k-1)/2}$ and f_1, ... , $f_{(k-1)/2}$).

We know the expression on the left of the invariance equation (3.6) up to order $(k-1)/2$, i.e.

$$\left[\boldsymbol{G}(\boldsymbol{\mathcal{W}}_{<k/2}(s))\right]_{<k/2}=\left[\boldsymbol{G}\left(\sum_{i=2}^{k-1}\boldsymbol{\mathcal{W}}_{i/2}(s)\right)\right]_{<k/2}.$$

Thus, we will first compute the homogeneous terms of degree k of the composition $\boldsymbol{G}(\boldsymbol{\mathcal{W}}_{<k/2}(s))$ and of the matrix product $D\boldsymbol{\mathcal{W}}_{<k/2}(s)f_{<k/2}(s)$ which we will denote by:

$$\left[\boldsymbol{G}(\boldsymbol{\mathcal{W}}_{<k/2}(s))\right]_{k/2}=\left[\boldsymbol{G}\left(\sum_{i=2}^{k-1}\boldsymbol{\mathcal{W}}_{i/2}(s)\right)\right]_{k/2},$$
$$\left[D\boldsymbol{\mathcal{W}}_{<k/2}(s)f_{<k/2}(s)\right]_{k/2}=\sum_{i=3}^{k-1}D\boldsymbol{\mathcal{W}}_{i/2}(s)f_{(k+2-i)/2}(s).$$

In this way, the terms of order $k/2$ of the invariance equation (3.6)

$$\left[\boldsymbol{G}(\boldsymbol{\mathcal{W}}_{\leq k/2}(s))\right]_{k/2}=\left[D\boldsymbol{\mathcal{W}}_{\leq k/2}(s)f_{\leq k/2}(s)\right]_{k/2},$$
$$\left[\boldsymbol{G}(\boldsymbol{\mathcal{W}}_{<k/2}(s))\right]_{k/2}+D\boldsymbol{G}(\mathbf{0})\boldsymbol{\mathcal{W}}_{k/2}(s)=\left[D\boldsymbol{\mathcal{W}}_{<k/2}(s)f_{<k/2}(s)\right]_{k/2}+D\boldsymbol{\mathcal{W}}_{k/2}(s)f_1(s)+D\boldsymbol{\mathcal{W}}_1(s)f_{k/2}(s),$$

lead us to the cohomological equation of order $k/2$ for $\boldsymbol{\mathcal{W}}_{k/2}$ and $f_{k/2}$

$$D\boldsymbol{G}(\mathbf{0})\boldsymbol{\mathcal{W}}_{k/2}(s)-D\boldsymbol{\mathcal{W}}_{k/2}(s)f_1(s)-D\boldsymbol{\mathcal{W}}_1(s)f_{k/2}(s)=-\boldsymbol{E}_{k/2}(s),\tag{3.7}$$

where $\boldsymbol{E}_{k/2}(s)=\left[\boldsymbol{G}(\boldsymbol{\mathcal{W}}_{<k/2}(s))\right]_{k/2}-\left[D\boldsymbol{\mathcal{W}}_{<k/2}(s)f_{<k/2}(s)\right]_{k/2}$ is the error of order $k/2$.

Therefore, considering a normal form parameterization style we have

$$\begin{cases}\boldsymbol{\omega}^j_{k/2}=\dfrac{\eta^j_{k/2}}{\lambda_j-\frac{k}{2}\lambda_1} & \text{for } k>2,\\ \mathrm{f}_{k/2}=0\end{cases}\tag{3.8}$$

where $\eta^j_{k/2}$ denotes the $j=1,...,4$ component of $\boldsymbol{\eta}_{k/2}=-\boldsymbol{E}_{k/2}(s)/s^{k/2}$.

The first terms of the manifold $\boldsymbol{W}(s)$ are given by

$$\begin{aligned}\boldsymbol{W}_{\leq 4}(s)=&\begin{pmatrix}0\\ \vartheta_0\\ v_0\\ 0\end{pmatrix}+\begin{pmatrix}v_0\\ 0\\ \hbar\\ 0\end{pmatrix}\frac{s}{B}-\frac{v_0^{1/2}}{3B^{3/2}}\begin{pmatrix}0\\ 2\\ 0\\ 3v_0\end{pmatrix}s^{3/2}+\frac{\hbar}{2v_0B^2}\begin{pmatrix}2v_0\\ 0\\ \hbar\\ 0\end{pmatrix}s^2-\frac{3\hbar}{10v_0^{1/2}B^{5/2}}\begin{pmatrix}0\\ 2\\ 0\\ 5v_0\end{pmatrix}s^{5/2}\\ &+\frac{1}{28v_0^2B^3}\begin{pmatrix}21v_0\hbar^2\\ -4\mu v_0^3\sin(2\vartheta_0)\\ 7\hbar^3+7\mu v_0^4[1+3\cos(2\vartheta_0)]\\ -12\mu v_0^4\sin(2\vartheta_0)\end{pmatrix}s^3-\frac{3\hbar^2}{14v_0^{3/2}B^{7/2}}\begin{pmatrix}0\\ 2\\ 0\\ 7v_0\end{pmatrix}s^{7/2}\\ &+\frac{1}{336v_0^3B^4}\begin{pmatrix}28v_0\left(6\hbar^3+\mu v_0^4\left[1+3\cos(2\vartheta_0)\right]\right)\\ -\mu v_0^3\left(80\hbar\sin(2\vartheta_0)+7v_0^2\left[\sin\vartheta_0+5\sin(3\vartheta_0)\right]\right)\\ 42\hbar^4+28\mu v_0^4\left(7\hbar\left[1+3\cos(2\vartheta_0)\right]+3v_0^2\left[1-5\cos(2\vartheta_0)\right]\cos\vartheta_0\right)\\ -4\mu v_0^4\left(80\hbar\sin(2\vartheta_0)-7v_0^2\left[\sin\vartheta_0+5\sin(3\vartheta_0)\right]\right)\end{pmatrix}s^4,\end{aligned}$$

where $\hbar=\mathfrak{h}+3\mu/2$ and $B=\sqrt{\hbar^2+v_0^2}$.

It is important to note that $s \geq 0$, since $r \geq 0$ and that we have the 2D parameterization of the manifold $\boldsymbol{W}$ in terms of $(\mathfrak{h}, s)$.

We have implemented this procedure to calculate the approximation of the manifold up to the desired order, but in practice we have usually worked with the approximation of order 5-10 in s.

3.1.2 Ejection/collision in the Levi-Civita regularized system

The Levi-Civita regularization offers a much simpler treatment of the ejection/collision, since we can start directly from the point of ejection/collision. Furthermore, this ejection/collision, unlike the McGehee transformation, occurs in finite time. In particular, once the level of the Jacobi constant has been set in the system (2.26), we only have to set the direction in which such ejection/collision will take place, since the velocity module is fixed by (2.29).

In this way, given a value of the mass parameter μ, we define the ejection (collision) orbits manifold of energy level C as the set of orbits that have initial conditions

$$(0, 0, 2\sqrt{2(1-\mu)}\cos\theta_0, 2\sqrt{2(1-\mu)}\sin\theta_0), \qquad \theta_0 \in [0, 2\pi) \tag{3.9}$$

integrated forward (backward) in time. Observe that in this case it is enough to consider a value of $\theta_0 \in [0, \pi)$ due to the duplication of the configuration plane.

It is important to note that the relation between the angles in the McGehee regularization and Levi-Civita regularization in given by $\vartheta_0 = 2\theta_0$.

3.2 Numerical methods

In this section we will present 3 different methods in order to study the n-EC orbits: The first method is based on the intersection of the ejection orbits manifold and the collision orbits manifold, the second method will consist of the study of the angular momentum when the distance to the first primary is minimal; and the third method, which will consist of looking at other indicators that we can obtain thanks to the fact that the n-EC orbits are heteroclinic connections with the McGehee regularization.

3.2.1 Method I: Intersection of Manifolds

The method of the intersection of manifolds is a classical method to study heteroclinic connections and for this reason we will explain it for the McGehee system but, as we will see, has an analogous application for the Levi-Civita system.

The idea consists in fixing a Poincaré section and integrating the unstable manifold $W^u(S^1_+)$ (forward in time) and the stable manifold $W^s(S^1_-)$ (backward in time) up to this section and then look for intersections of both manifolds in the Poincaré section.

For our purpose we will consider two Poincaré sections

$$\Sigma_M : \{g(r, \vartheta, v, u) = v = 0,\ v' < 0\},$$
$$\Sigma_m : \{g(r, \vartheta, v, u) = v = 0,\ v' > 0\}.$$

that respectively correspond to a local maximum and local minimum in the distance with respect to the first primary.

For our purpose let us introduce the following definition

Definition 3.2. *We define D_k^+ as the k-th intersection of the ejection orbits manifold with Σ_M and D_k^- as the k-th intersection of the collision orbits manifold with Σ_M. In a similar way we define d_k^+ as the k-th intersection of the ejection orbits manifold with Σ_m and d_k^- as the k-th intersection of the collision orbits manifold with Σ_m.*

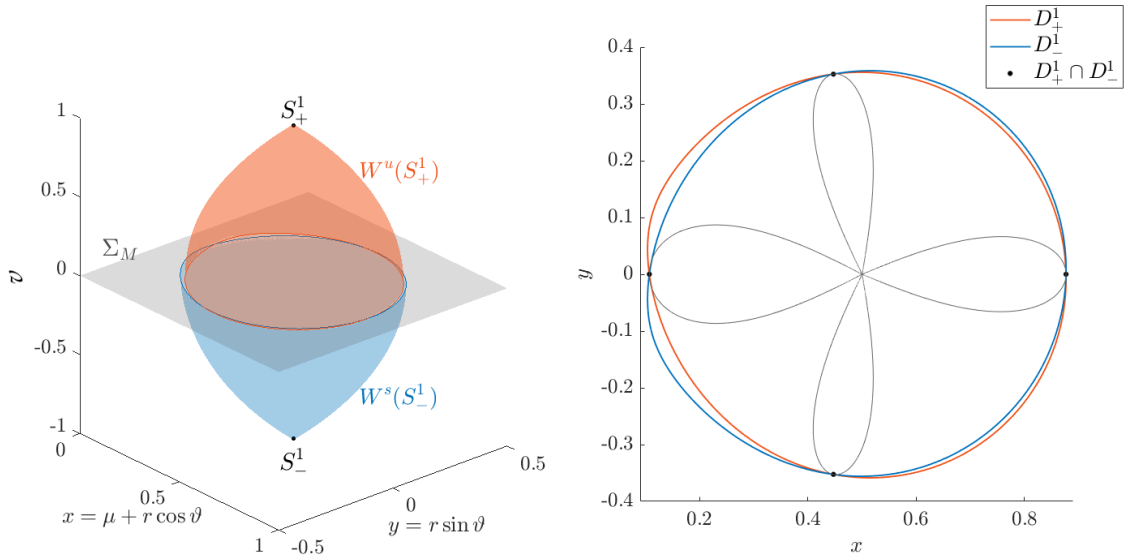

Figure 3.2: Left. $W^u(S_+^1)$ (ejection orbits in red) and $W^s(S_-^1)$ (collision orbits in blue) up to Σ_M for $\mu = 0.5$ and $C_{L_1}(\mu)$. Right. The associated curves D_1^+ (red) and D_1^- (blue) with the corresponding intersections (black dots). In grey the trajectories of the four 1-EC orbits.

The strategy at this point is to compute the intersection between the curves D_i^+ and D_j^- (or similarly the intersection of d_k^+ and d_l^-) in order to compute the ejection-collision orbits, but this has a problem for the McGehee system, the curves $d_i^\pm$ are not well defined and the curves $D_j^\pm$ are only well defined for $j = 1$. This is because there are 1-EC orbits so there are points of d_1^- that will go directly to collision, therefore, we will not be able to obtain them numerically (due to the heteroclinic connection). But with this strategy we can compute easily the 1-EC (see Figure 3.2).

This problem does not happen with the Levi-Civita regularization. In particular if we define the curves $D_j^\pm$ and $d_i^\pm$ in the Levi-Civita system, i.e. the intersection of the ejection/collision orbits manifolds with Σ_M and Σ_m, that are now defined by

$$\begin{aligned} \Sigma_M &: \{h(u, v, u', v') = uu' + vv' = 0,\ h' < 0\}, \\ \Sigma_m &: \{h(u, v, u', v') = uu' + vv' = 0,\ h' > 0\}, \end{aligned} \tag{3.10}$$

we have that due to the duplication of the space

Lemma 1. *The number of intersections in the Levi-Civita system between D_i^+ and D_j^- corresponds to twice the number of $(i + j - 1)$-EC orbits.*

Proof. If an orbit belongs to the ejection orbits manifold and the collision orbits manifold, it is an ejection-collision orbit. In addition, the number of relative maxima in the distance to the first primary of such EC orbit is equal to the number of times that the orbit will cross Σ_M and that is i (following the ejection orbits manifold) plus $j - 1$ (following the collision orbits manifold). Finally, since the Levi-Civita regularization doubles the configuration space, we have that the cardinal $|D_i^+ \cap D_j^-|$ is twice the number of $(i + j - 1)$-EC orbits. □

and in a similar way

Lemma 2. *The number of intersections in the Levi-Civita system between d_i^+ and d_j^- corresponds to twice the number of $(i + j)$-EC orbits.*

Proof. Analogous to Lemma 1. □

At this point it is important to note that in practice it is only necessary to compute the points of the curves D^+_{i+1} and D^+_j (or d^+_i and d^+_j) with $i+j=n$ to obtain the n-EC orbits, since, due to the symmetry of the problem (1.6), we know the expressions of D^-_{i+1} and D^-_j (or d^-_i and d^-_j).

3.2.2 Method II: The angular momentum

The second method we will consider is based on the angular momentum, or quantities related to it. It is well known that collision orbits have angular momentum 0 at the collision (since the distance to the first primary is 0) and that with the sign of the angular momentum we can know in which direction we are going around the primary. In this way, if we consider the value of the angular momentum at the minimum distance to the first primary (that is, the angular momentum at $d^\pm_i$) we can detect collisions with the changes of sign. Thus, in order to detect n-EC orbits we will study the zeros of the angular momentum at the n-th intersection with Σ_m (see Figure 3.3).

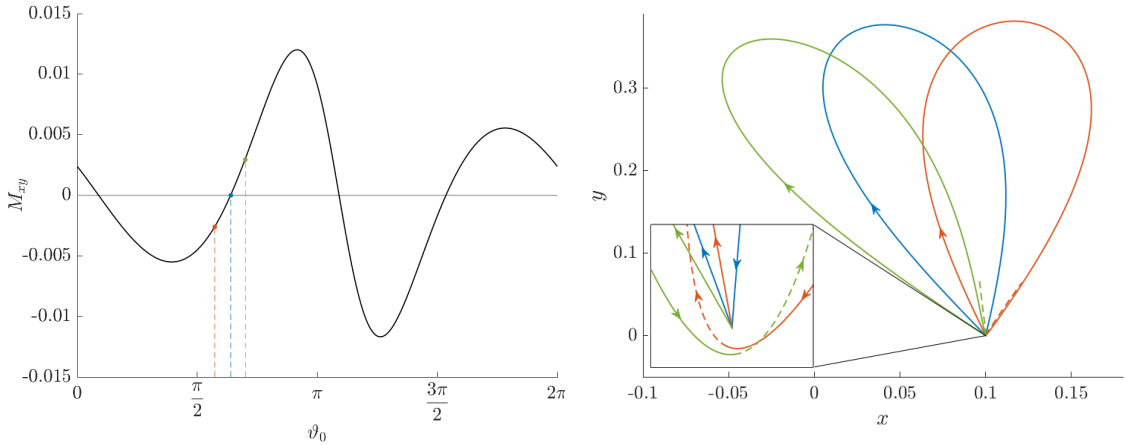

Figure 3.3: Left. Angular momentum of the ejection orbits at the first intersection with Σ_m for $\mu = 0.1$ and $C = -2H = 5$. Right. Trajectories of the orbits marked in the left figure. In red an ejection orbit with negative angular momentum at the first intersection with Σ_m, in blue a 1-EC orbit and in green a ejection orbit with positive angular momentum at the first intersection with Σ_m.

In the synodical coordinates the angular momentum with respect to the first primary is given by

$$M_{xy} = (x-\mu, y) \times (\dot{x}, \dot{y}) = (x-\mu)\dot{y} - y\dot{x}.$$

In order to study it in the McGehee regularized system we can translate this quantity into polar coordinates easily and then to the McGehee variables

$$M_{xy} = r^2\dot{\vartheta} = r^{1/2}\vartheta' = r^{1/2}u. \tag{3.11}$$

Therefore, to study the n-EC orbits, we need to compute this quantity at the n-th crossing with Σ_m.

In a similar way we can compute the angular momentum in terms of the Levi-Civita variables, or define directly the angular momentum in Levi-Civita coordinates, that is

$$M_{LC} = uv' - vu'. \tag{3.12}$$

This quantity is not the same (see Figure 3.4), but has the same effect in order to detect collision orbits and the advantage of the easy computation.

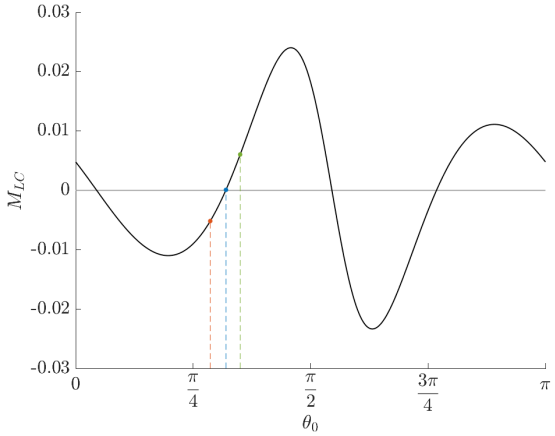

Figure 3.4: M_{LC} of the ejection orbits at the first intersection with Σ_m for $\mu = 0.1$ and $C = -2H = 5$. The values marked correspond to the orbits of the Figure 3.3.

3.2.3 Method III: Consequences of the heteroclinic connections

As we have seen, in McGehee's regularized system (2.5) the n-EC orbits can be seen as heteroclinic connections between points of S^1_+ and points of S^1_-. Thus, to detect the n-EC orbits for a given μ and C, we will consider the n-th intersection of the manifold of ejection orbits with the section Σ_m, i.e. d_n^+ and we will look at the time required for the intersection with Σ_m as a function of the initial angle (see Figure 3.5 left).

As they are heteroclinic connections they need infinite time to reach the collision, and we will detect these as asymptotes in time.

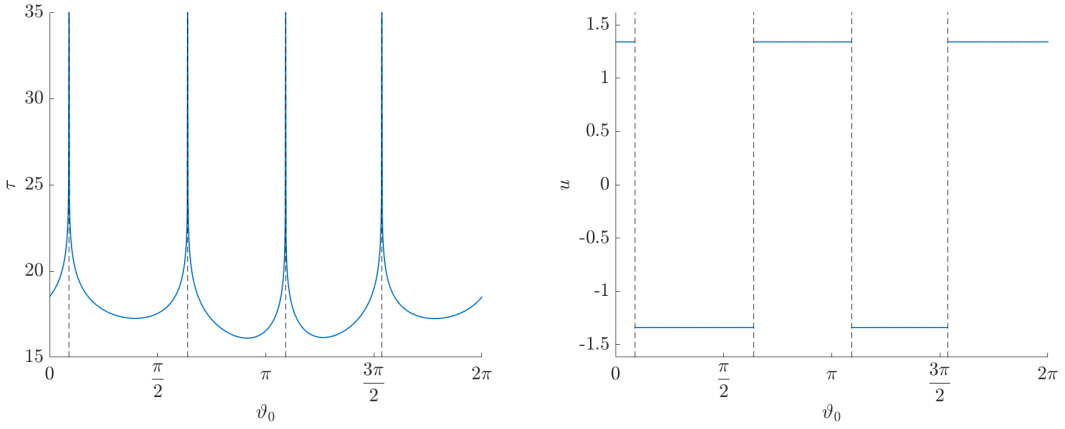

Figure 3.5: Values of τ (left) and u (right) of the ejection orbits at the first intersection with Σ_m for $\mu = 0.1$ and $C = -2H = 5$. The asymptotes of τ and the discontinuities of u correspond to 1-EC orbits.

Another way to detect these collisions is simply by looking at the value of u (see Figure 3.5 right), since as we saw earlier, the angular momentum in McGehee coordinates is given by (3.11) and we have $r \geq 0$, so it is sufficient to find the points where the sign change of u occurs.

3.3 Comparison between methods and regularizations

The natural question at this point is what method or regularizations to work with. In this section we will discuss the advantages and disadvantages of each of the previous methods and see which regularization is more convenient.

3.3.1 Comparison between methods

The traditional method to study the n-EC orbits would be method I. The study and computation of heteroclinic connections by means of the intersection of the stable and unstable manifolds is a technique that has been widely used (see for example [BMO13] and references therein).

In this case, computing the intersections of the manifold of ejection orbits and the manifold of collision orbits presents a clear advantage over the other methods thanks to the symmetry of the problem (1.6). If we select a suitable Poincaré section we can reduce integration time in half. This optimal selection for computing the n-EC orbits is as follows:

- if $n = 2k - 1$ with $k \in \mathbb{N}$ we compute D_k^+ (and we obtain by the symmetry D_k^-),
- if $n = 2k$ with $k \in \mathbb{N}$ we compute d_k^+ (and we obtain by the symmetry d_k^-).

By cons, this method requires an extra step, since we have to obtain the intersection points between D_k^+ and D_k^- (or d_k^+ and d_k^-).

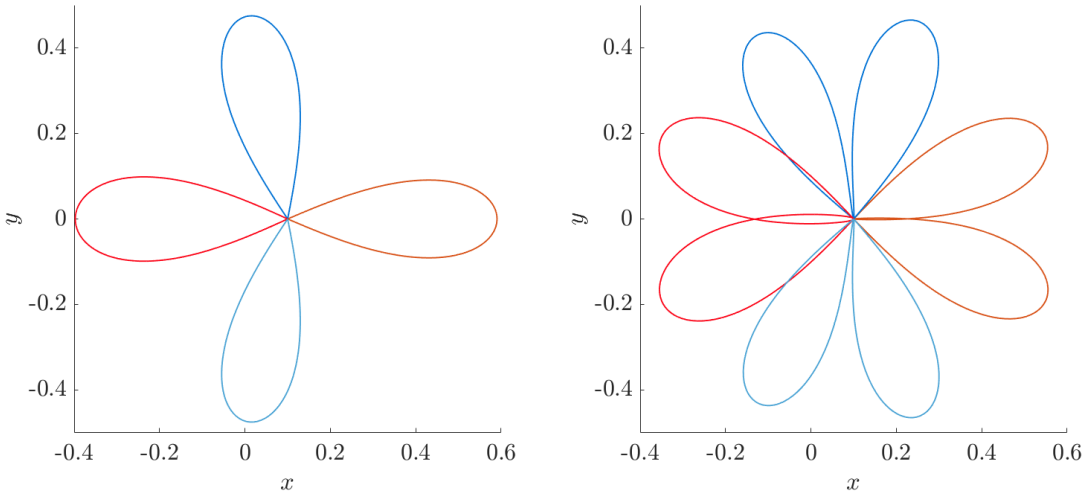

Figure 3.6: The four n-EC orbits for $n = 1, 2$ (*from left to right*) that exist for $\mu = 0.1$ and $C = 4$. In red the symmetric n-EC orbits with respect to the x axis and in blue the non symmetric n-EC orbits but symmetric one of the other with respect to the x axis.

However, the symmetry of the problem allows us to get more out of this method, since we can distinguish between (a priori) two possible types of n-EC orbits: a symmetric or non symmetric n-EC orbit.

- In the case of symmetric n-EC orbits, it is enough to find that the ejection orbits have coordinates $(x, y = 0, \dot{x} = 0, \dot{y})$ at the k-th intersection with Σ_M when $n = 2k - 1$ or with Σ_m when $n = 2k$, since if this condition is satisfied the orbit will collide due to the symmetry (1.6) (see red orbits of Figure 3.6).

- In the case of non-symmetric n-EC orbits, the symmetry plays another important role, since if there is an n-EC orbit that is not itself symmetric, there must be another n-EC symmetric to it (see blue orbits of Figure 3.6). This implies that we only need to compute the intersection of the curves D_k^+ and D_k^- (or d_k^+ and d_k^-) for $y > 0$.

On the other hand, methods II and III require the integration of the ejection orbits up to the n-th intersection with Σ_m in order to obtain the n-EC orbits, that is, we have to integrate approximately double with respect to method I. Nevertheless, they present a clear advantage over the method I: we can obtain the n-EC orbits directly studying simply the quantities M_{xy}, M_{LC}, τ or u in this n-th intersection with Σ_m for determining the collision.

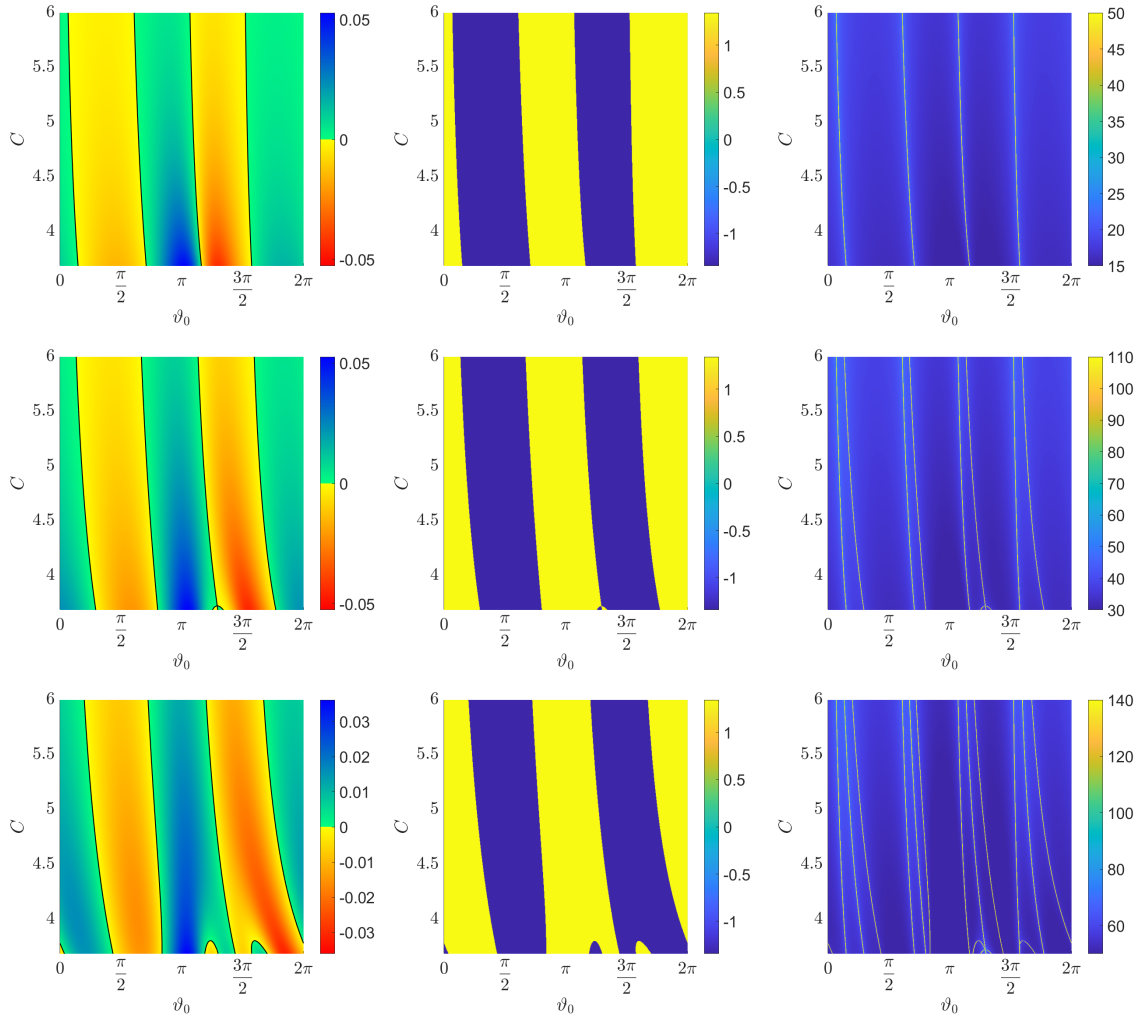

Figure 3.7: Values of M_{xy}, u and τ (*from left to right*) of the ejection orbits at the $n = 1, 2, 3$ (*from top to bottom*) intersection with Σ_m for $\mu = 0.1$ and $C \in [C_{L_1}, 6]$.

As we saw in the previous section, the quantities M_{xy} and M_{LC} of the ejections orbits are practically analogous at the intersections with Σ_m, so we will only illustrate the first case.

If we compare M_{xy}, u and τ of the ejection orbits at the n-th intersection with Σ_m (se Figure 3.7) we observe that the solutions are the same for the three methods if $n = 1$ but, if we consider $n > 1$ we observe some discrepancies in the output obtained between the method of the singularity in time and the other methods. These discrepancies are due to the fact that singularities in time accumulate, i.e. the singularities in time in the second intersection with Σ_m correspond to 1-EC or 2-EC orbits, the singularities in time in the third intersection with Σ_m correspond to 1-EC, 2-EC or 3-EC orbits, and

so on. Thus, one way to detect only the n-EC orbits is to see only the new singularities that appear when we compare the $(n-1)$th and the n-th intersection with Σ_m. However, this can be very difficult if we consider large values of n (see Figure 3.8) so this method will only be useful for small values of n (for example $n \leq 10$).

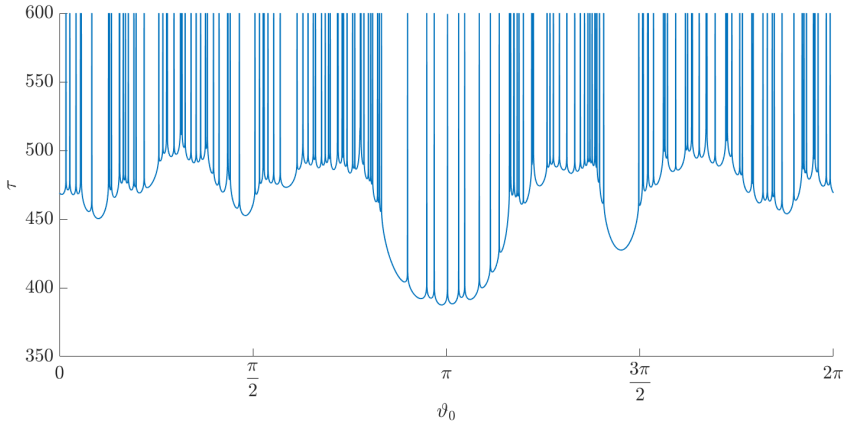

Figure 3.8: Values of τ of the ejection orbits at the 25th intersection with Σ_m for $\mu = 0.1$ and $C = 5$.

Although the study of τ of the ejection orbits at the intersection with Σ_m has the handicap of having to consider small values of n, it allows us to detect some phenomena of these orbits, as we will see in the next section.

Regarding the other two methods (M_{xy}/M_{LC} and u), it is clear that by definition (3.11) the results are the same and they have the advantage of indicating only the n-EC orbits.

3.3.2 Comparison between McGehee and Levi-Civita regularizations

The next natural step is to see which of the two local regulations that we have presented is more convenient for us to work with. It is important to note that we have used both regularizations and we have seen that both regularizations have advantages and disadvantages.

On the one hand, McGehee's regularization has a clear advantage over Levi-Civita's transformation, it is a much more intuitive regularization and allows us to directly know the expression of the trajectories in polar coordinates.

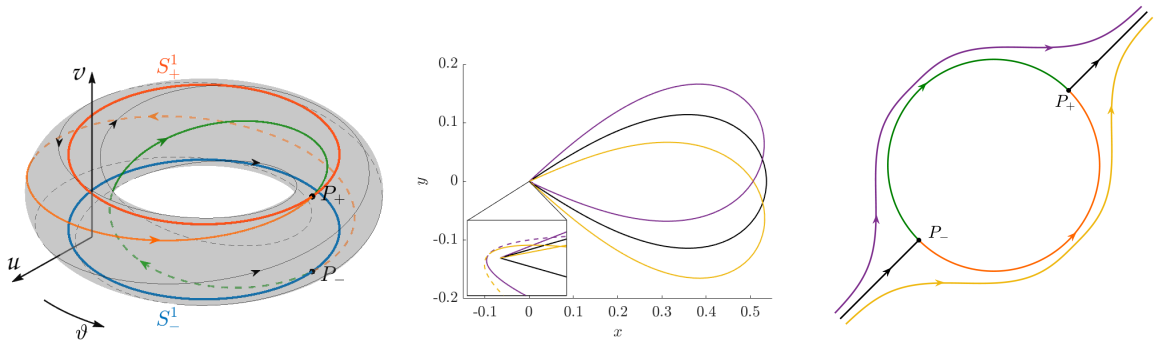

Figure 3.9: Left. Collision manifold Λ. Middle. Three ejection orbits, the purple, the black and the yellow ones have angular momentum $M_{xy} > 0, 0, < 0$ respectively at the first crossing with Σ_m. The black one is an 1-EC orbit. Right. Schematic behaviour of two orbits that go close to collision.

This technique, as we have said before, consists in a blowup of the collision, which allows us to have a complete information about the behavior of the orbits near and in the collision (see Figure 3.9).

Furthermore, despite the fact that it cannot happen in the RTBP, in other classical problems the McGehee regularization has an additional advantage over the Levi-Civita transformation, which is that it allows to study the multiple collision and not just the binary collision of two bodies. This is essential for some other problems (see for example [ARMO19] where the authors made a complete study of the EC orbits in the symmetric collinear four-body problem).

By cons, the price of working in polar coordinates and having the collision manifold as an invariant manifold of the system is that, as we have seen previously, the ejection-collision orbits are heteroclinic connections. This is not a problem if we only want to study the orbits of 1-EC collision, since if we want to obtain them numerically we can use the parameterization method to start the integration far enough away from the collision and then compute the intersection of the curves D_1^+ and D_1^-. Nevertheless, if we want to study the n-EC orbits for $n > 1$ this is not a good system to work with, since we will necessarily have to deal with close approach to collisions and previous collisions.

This is precisely the strong point of the Levi-Civita regularization, since despite not being such an intuitive regularization nor does it show the information that the collision manifold gives us, it allows us to study the n-EC orbits in finite time and starting directly from the collision. So, although the equations of motion have a more complicated expression in Levi-Civita, working with them has a much lower computational cost.

For this reason, massive numerical simulations have been done using the regularized Levi-Civita system.

3.4 Numerical results for the n-EC orbits

Two of the main goals of this dissertation are, on the one hand, to verify and numerically extend the results of the existence of four 1-EC orbits and, on the other, to generalize them for the case $n \geq 1$. For this reason, we will divide this section into two cases, the particular case $n = 1$ and the general case $n \geq 1$.

3.4.1 The case of 1-EC orbits

As we have said previously, the result from which we started is the one that can be found in [CL88] where the authors prove the following theorem:

Theorem 1. *Given a value of the mass parameter $\mu \in (0, 1)$ there exists a $\hat{C}(\mu)$ big enough such that for all values of the Jacobi constant $C \geq \hat{C}(\mu)$ the are exactly four 1-EC orbits.*

Before proceeding it is important to make two remarks.

Remark 1. *In [CL88] the authors prove the existence of four ejection-collision orbits, but taking into account the Definition 3.1 we can see easily how these orbits correspond to 1-EC orbits.*

Remark 2. *Similarly, Theorem 1 does not say anything about how these orbits are, but observing its proof in [CL88] and through symmetry (1.6) we can characterize the orbits with the following corollary.*

Corollary 3.4.1. *The four 1-EC orbits of Theorem 1 can be characterized as:*

- *Two 1-EC orbits are symmetric with respect to the x axis.*
- *Two 1-EC orbits have symmetric trajectory one of the other with respect to the x axis.*

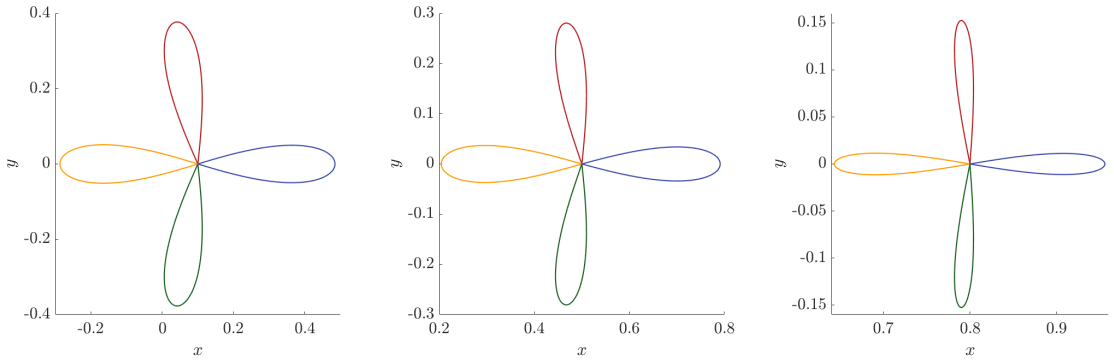

Figure 3.10: Trajectories of the four 1-EC orbits α_1 (yellow), β_1 (green), γ_1 (blue) and δ_1 (red) for $\mu = 0.1,\ 0.5,\ 0.8$ (from left to right) and $C = 5$.

In this way, we will note these 1-EC orbits as α_1 and γ_1 for the symmetric orbits with respect to the x axis and for β_1 and δ_1 to the symmetric orbits of each other (see Figure 3.10).

Our goal at this point is to extend the analytic results to less restrictive values of C. To do this, we have done a complete exploration for values of $\mu \in (0, 1)$ and $C \geq C_{L_1}(\mu)$. The results obtained are that we can extend numerically Theorem 1 and Corollary 3.4.1 for values of $C \geq \hat{C}(\mu) = C_{L_1}(\mu)$.

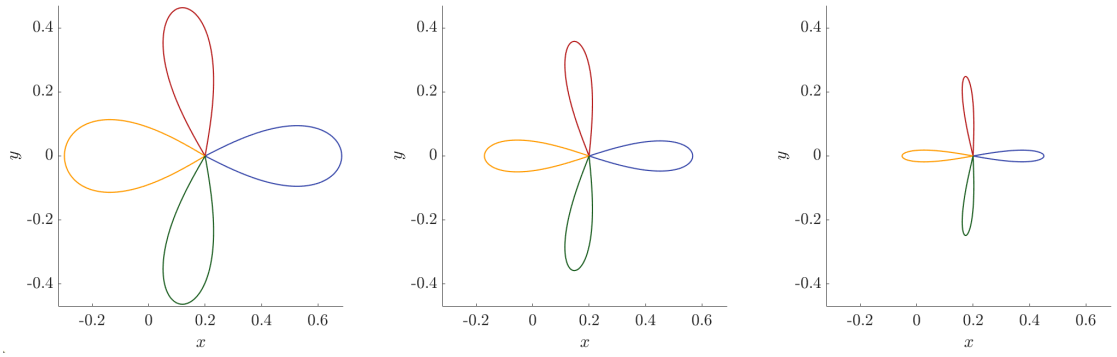

Figure 3.11: Trajectories of the four 1-EC orbits α_1 (yellow), β_1 (green), γ_1 (blue) and δ_1 (red) for $\mu = 0.2$ and $C = C_{L_1},\ 5,\ 7$ (from left to right).

To illustrate this result and some more specific characteristics obtained, let us previously consider a specific value of μ and various values of C, such as those illustrated in Figure 3.11 for $\mu = 0.2$ and $C = C_{L_1},\ 5,\ 7$. In this Figure we can see an expected result: the size of the 1-EC orbits increases as the energy increases (that is, the value of the Jacobi constant C decreases). But not only that, we also see how the trajectories of the 1-EC orbits tend to condense on the axes as C increases.

This last consideration implies that the initial angle θ_0 of the 1-EC orbits tends to 0, $\pi/4$, $\pi/2$ and $3\pi/4$ for γ_1, δ_1, α_1 and β_1 respectively as C increases. This result can be better seen in Figure 3.12 where we plot the evolution of the initial angle θ_0 as a function of C for different values of μ.

Furthermore, in Figure 3.12 we can observe how the initial angles of the four 1-EC orbits tend much faster to the limit values as μ increases.

Finally, in Figure 3.13 we can see the evolution of the 4 families of 1-EC orbits that exist for values of $\mu \in (0, 1)$ and $C \in [C_{L_1}(\mu), 8]$.

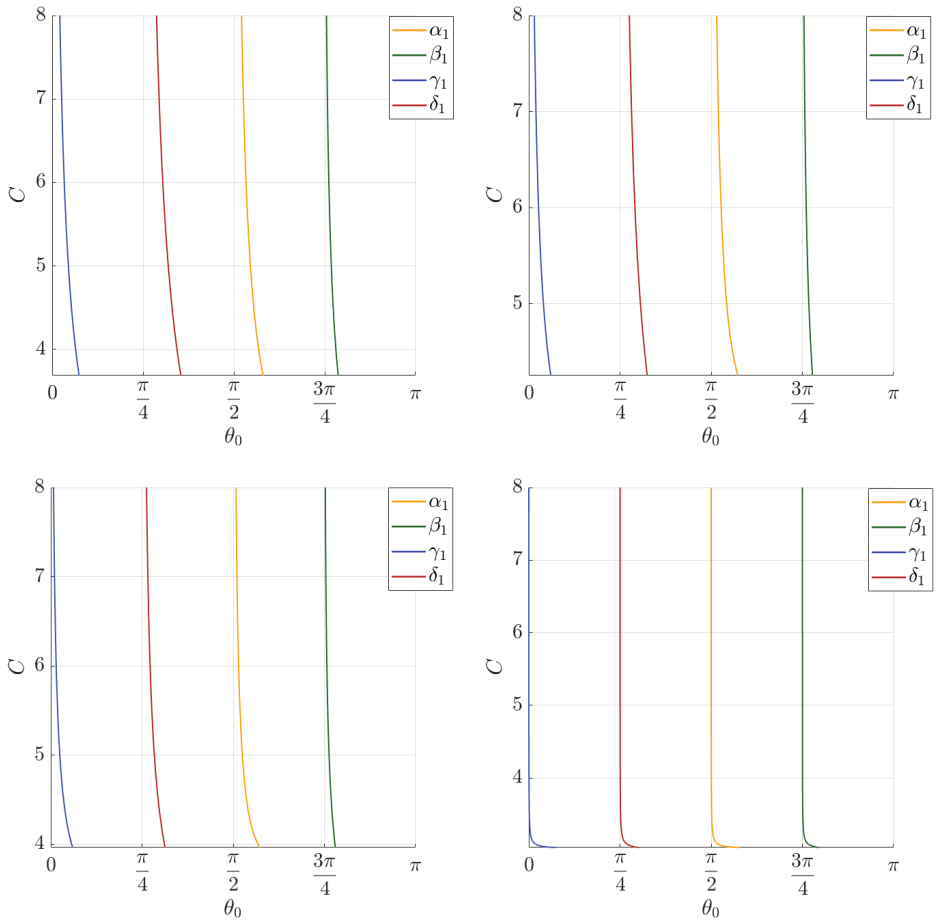

Figure 3.12: Initial condition for the 1-EC orbits as a function of $C \in [C_{L_1}(\mu), 8]$ for $\mu = 0.1$, 0.5, 0.8, 0.999 (from left to right and top to bottom).

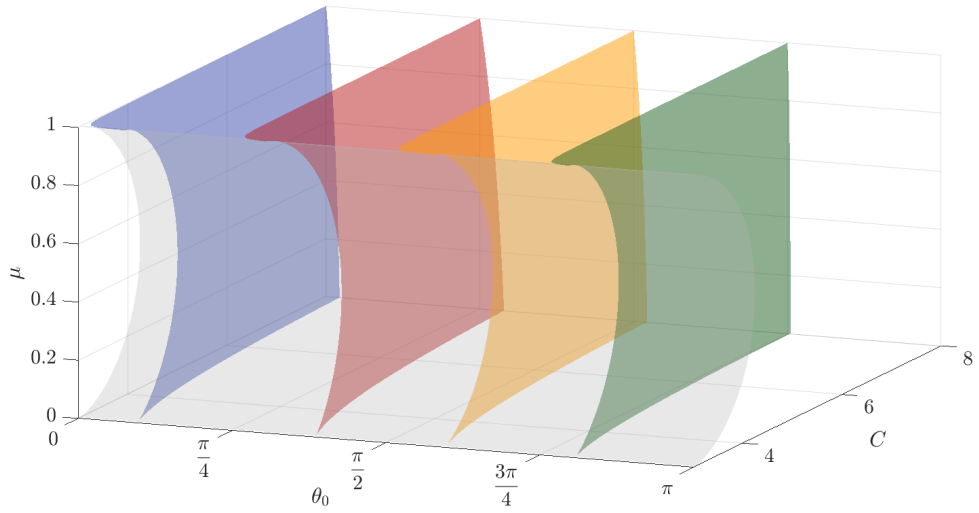

Figure 3.13: Initial condition for the 1-EC orbits as a function of $\mu \in (0, 1)$ and $C \in [C_{L_1}(\mu), 8]$. For every value of (μ, C) we have four 1-EC orbits corresponding to α_1 (yellow), β_1 (green), γ_1 (blue) and δ_1 (red). In grey the value of $C_{L_1}(\mu)$.

At this point the natural question is whether these results for 1-EC orbits are still valid for values of $C < C_{L_1}(\mu)$. It is clear that for these values of C the richness of the dynamics that can take place is much bigger, due to not only the possible collision with both primaries, but also the chaotic involved dynamics because of the existence of unstable periodic orbits and their invariant manifolds (just take into account the Lyapunov periodic orbits for instance, see [BMO13] and references therein). In particular, new bifurcating families of 1-EC orbits appear.

In order to illustrate this result, we apply the method of the singularity in time (previously introduced in Subsection 3.2.3) varying $C \geq C_{L_2}(\mu)$ for $\mu = 0.5$. As we said previously, for a fixed C, the angles ϑ_0 (where $\vartheta_0 = 2\theta_0$) for which the time τ needed to intersect with Σ_m tend to infinity, correspond to the particular values of ϑ_0 for which there exist 1-EC orbits.

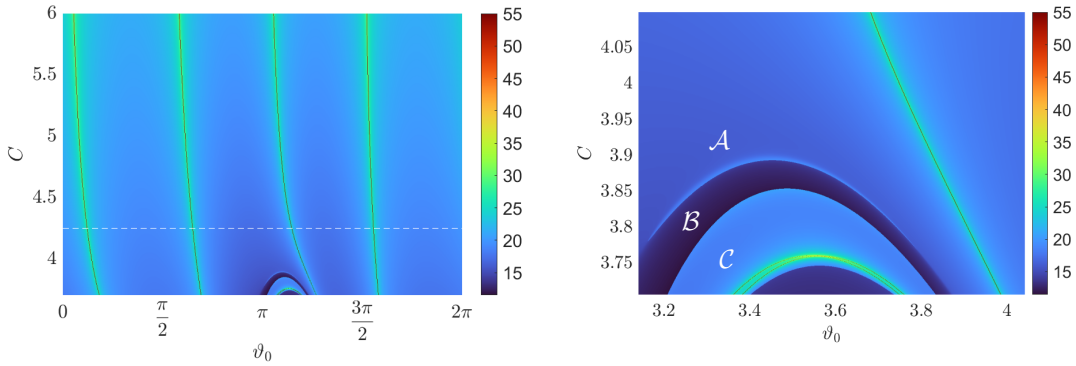

Figure 3.14: Left. Value of τ of the ejection orbits at the first intersection with Σ_m for $\mu = 0.5$ as a function of $\vartheta_0 \in [0, 2\pi)$ and $C \in [C_{L_2}, 6]$. The discontinuous white line corresponds to $C = C_{L_1}$. Right. Zoom of the left plot.

We remark from Figure 3.14, that for $C < C_{L_1}(\mu)$ there appear new bifurcated families (although difficult to be seen in the left subplot).

In Figure 3.14 right we plot a zoom in a neighborhood of the α_1 family. We observe two new families which we call η_1 and ξ_1. But before describing this bifurcation, we remark three different regions, labelled by $\mathcal{A}$, $\mathcal{B}$ and $\mathcal{C}$. First of all, we see that the ejection orbits that live in $\mathcal{A}$ and $\mathcal{C}$ have a similar value of time τ needed to intersect with Σ_m, but a smaller one for the region $\mathcal{B}$ in between.

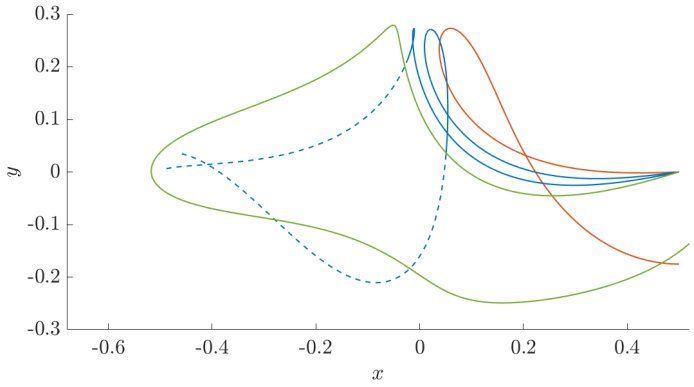

Figure 3.15: $\mu = 0.5$. Different ejection orbits belonging to region $\mathcal{A}$ (red), $\mathcal{B}$ (blue) and $\mathcal{C}$ (green) for $C = 3.835$. All of them have a continuous path up to the first intersection with Σ_m and a discontinuous path only for those orbits in region $\mathcal{B}$ for a long range of time.

The behavior of the orbits in these regions is the following (see Figure 3.15): orbits in region $\mathcal{A}$ do not

have enough energy to go to the small primary ejecting in this direction and they behave in a usual way, starting at ejection with the big primary, having a loop and returning close to it (see orbit red in Figure 3.15). Those orbits in region $\mathcal{B}$ (in blue) do have enough energy to go close to the small primary ejecting in this direction, but not enough energy to go in a direct path, they describe a small loop before getting there. Just short after the loop they reach Σ_m and that is the reason why the integration time needed is smaller in the region $\mathcal{B}$ (see the continuous small loop of the two orbits in blue in Figure 3.15). Finally those orbits in region $\mathcal{C}$ have enough energy to visit the small primary and return back (close) to the big one (see the long green orbit in Figure 3.15). This behavior is due to the influence of LPO_1 (Lyapunov periodic orbit around L_1), a phenomenon that we will study in more detail in Chapter 6.

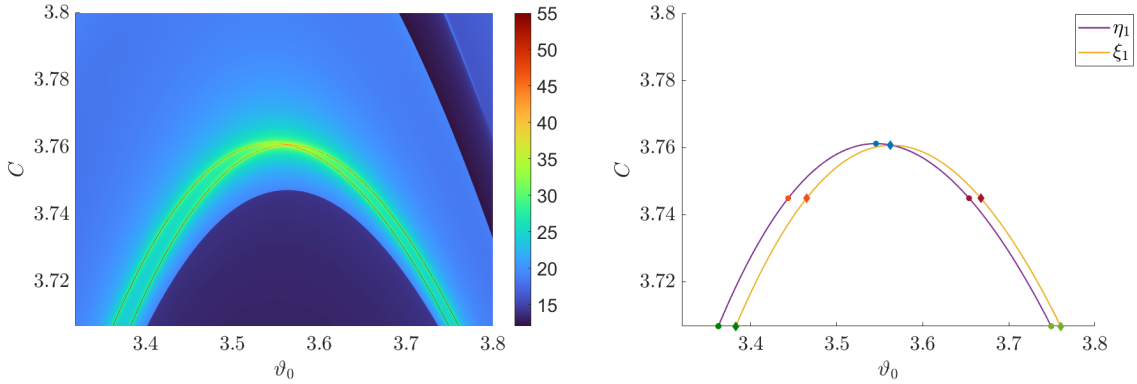

Figure 3.16: $\mu = 0.5$. Left. Zoom (of Figure 3.14) of the new bifurcated families. Right. The two new bifurcation families of 1-EC orbits η_1 and ξ_1.

Let us focus now on the bifurcated families η_1 and ξ_1 (see Figure 3.14). These new 1-EC orbits detected correspond to orbits that visit the region close to the small primary at his first intersection with Σ_M. If we zoom this region (see Figure 3.16) we observe in a clever way the two different bifurcated families η_1 and ξ_1. When decreasing C, the first family that appears is η_1 (see purple curve in Figure 3.16 right). As far as C decreases, a new branching point appears, and we obtain a new family labelled ξ_1 (yellow curve in Figure 3.16 right). The 1-EC orbits belonging to η_1 are symmetric with respect to the x axis. In Figure 3.17 left, we plot the 1-EC orbit (in blue) where η_1 is born, and in red and in green the two 1-EC orbits of family η_1 for two decreasing fixed values of C denoted with a point of the same color in Figure 3.16. The 1-EC orbits belonging to ξ_1 are non symmetric, but they have symmetric trajectories one of the other with respect to the x axis. In Figure 3.17 right, we plot the EC orbit (in blue) where ξ_1 is born (that belongs to η_1), and in red and in green the two corresponding 1-EC orbits of family ξ_1 for two decreasing fixed values of C denoted with a point of the same color in Figure 3.16.

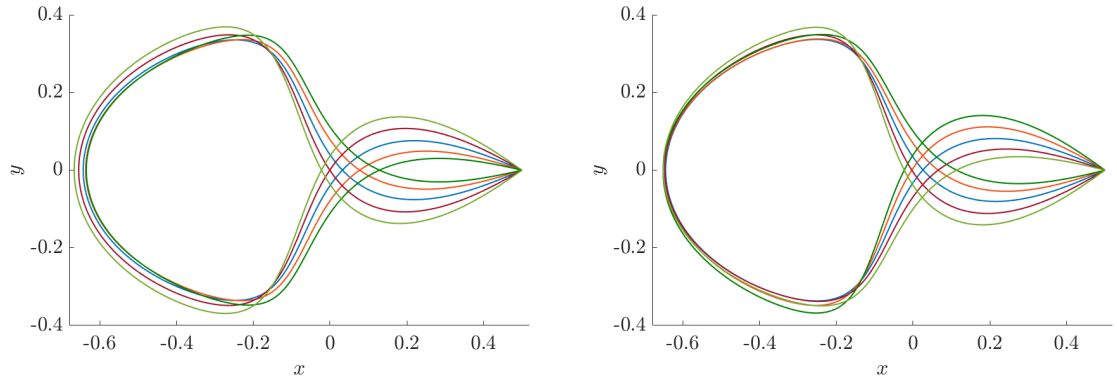

Figure 3.17: $\mu = 0.5$. 1-EC bifurcated orbits belonging to η_1 (left) and ξ_1 (right) for the values of (ϑ_0, C) denoted with the same color in Figure 3.16.

Therefore we can conclude that the existence of only four 1-EC orbits is no longer true for lower values of the Jacobi constant C, since there appear new ones. We plot in Figure 3.18 eight 1-EC orbits for $\mu = 0.5$ and $C_{L_2}(0.5)$, together with the Hill's region.

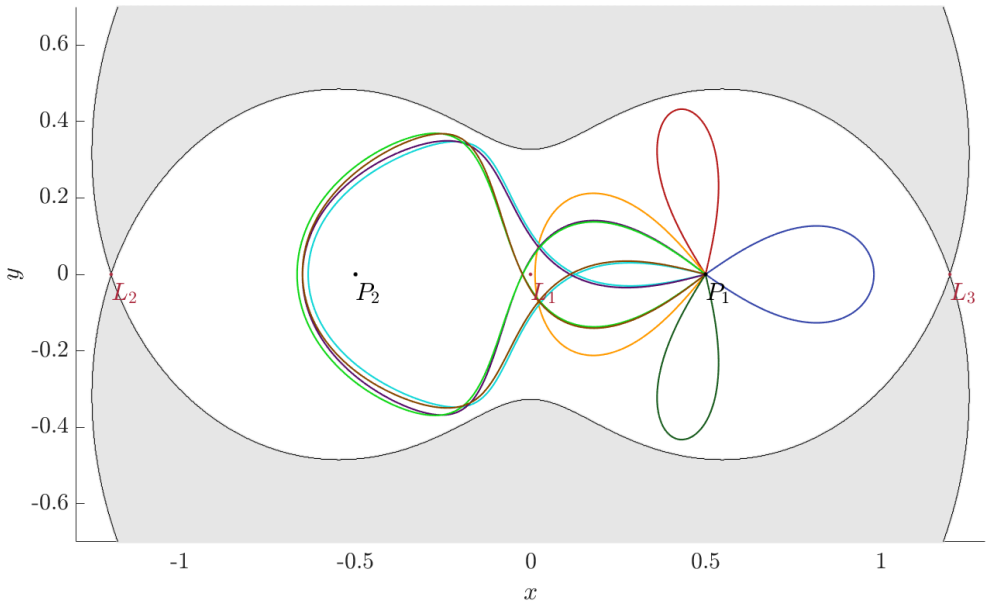

Figure 3.18: (x, y) projection of the eight 1-EC orbits that exist for $\mu = 0.5$ and $C_{L_2}(\mu)$.

A final remark is that the bifurcation described for $\mu = 0.5$ also takes place for other values of μ and less restrictive Hill's regions (lower values of C). Of course, as far as the Hill's regions allow non-bounded motions, a very rich dynamics starting at ejection with the big primary takes place.

3.4.2 The general case

The first goal of this subsection is to try to generalize the results obtained for the 1-EC orbits for the general case of the n-EC orbits. Recall that an n-EC orbit is an orbit which ejects from the first primary, reaches n times a relative maximum in the distance with respect to the first primary before colliding with it.

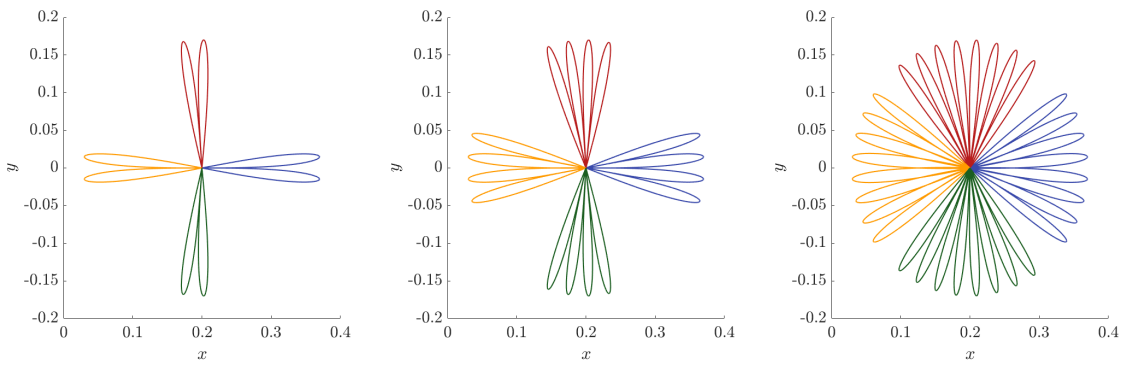

Figure 3.19: Trajectories of the four n-EC orbits α_n (yellow), β_n (green), γ_n (blue) and δ_n (red) for $n = 2$, 4, 8 (from left to right), $\mu = 0.2$ and $C = 10$.

The numerical results obtained show that for all $\mu \in (0,1)$ and n from 1 to 100 there exists a $\hat{C}(\mu, n)$ such that for $C \geq \hat{C}(\mu, n)$ there exist exactly four n-EC orbits, which can be characterized in a way similar to the characterization of the 1-EC orbits:

- Two n-EC orbits both symmetric with respect to the x axis.
- Two n-EC orbits symmetric to each other with respect to the x axis.

Similarly, we will note these n-EC orbits as α_n and γ_n for the symmetric orbits with respect to the x axis and for β_n and δ_n to the symmetric orbits of each other (see Figure 3.19).

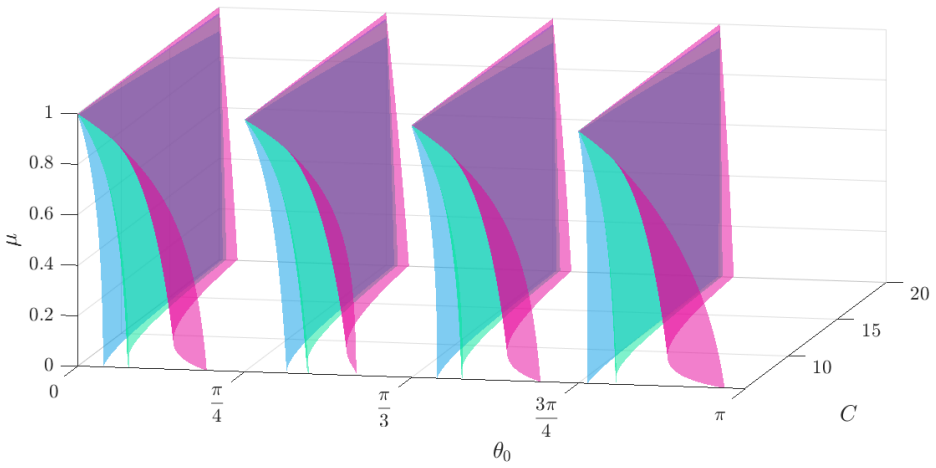

Figure 3.20: Continuation of families γ_n, δ_n, α_n and β_n of n-EC orbits for $n = 1, 2, 5$ (blue, green and purple colors respectively) in θ_0 and $C \in [5.5, 20]$ when varying $\mu \in (0,1)$ (on the vertical axis).

The n-EC orbits also meet some specific characteristics of the 1-EC orbits. On the one hand, we have that the size of the n-EC orbits increases when the value of the Jacobi constant C decreases and, on the other hand, we observe how the trajectories of the n-EC orbits tend to condense on the axes as C increases. This last consideration, as in the case $n = 1$, implies that the initial angle θ_0 of these four n-EC orbits tends to 0, $\pi/4$, $\pi/2$ and $3\pi/4$ for γ_n, δ_n, α_n and β_n respectively as C increases. In a similar way we can observe how the initial angles of the four 1-EC orbits tends much faster to the limit values as μ increases and, of course, as n grows this limit takes longer to become apparent, see for example Figure 3.20 where we plot the initial condition θ_0 of the 4 families of n-EC orbits that exist, for $n = 1, 2, 5$ for values of $\mu \in (0,1)$ and $C \in [5.5, 20]$.

However, the evolution of the n-EC is not so simple if we consider smaller values of the Jacobi constant C or higher values of n than those drawn in Figure 3.20: the existence of exactly four n-EC orbits is not always true for these values.

Therefore, at this point the goals are mainly two:

- To study the evolution of the n-EC orbits when we decrease the value of C and/or increase the value of n.
- To compute and examine the evolution of $\hat{C}(\mu, n)$, i.e. the value of the Jacobi Constant such that such that for $C \geq \hat{C}(\mu, n)$ there exist four n-EC orbits as a function of n and μ.

Studying the first point is an arduous task and almost impossible because since even if we restrict this study for values of $C \geq C_{L_1}$, we can consider values of n higher as we want. Notwithstanding that, our goal will be to illustrate and understand the two phenomena that we will observe, the bifurcation and confluence of families of n-EC orbits

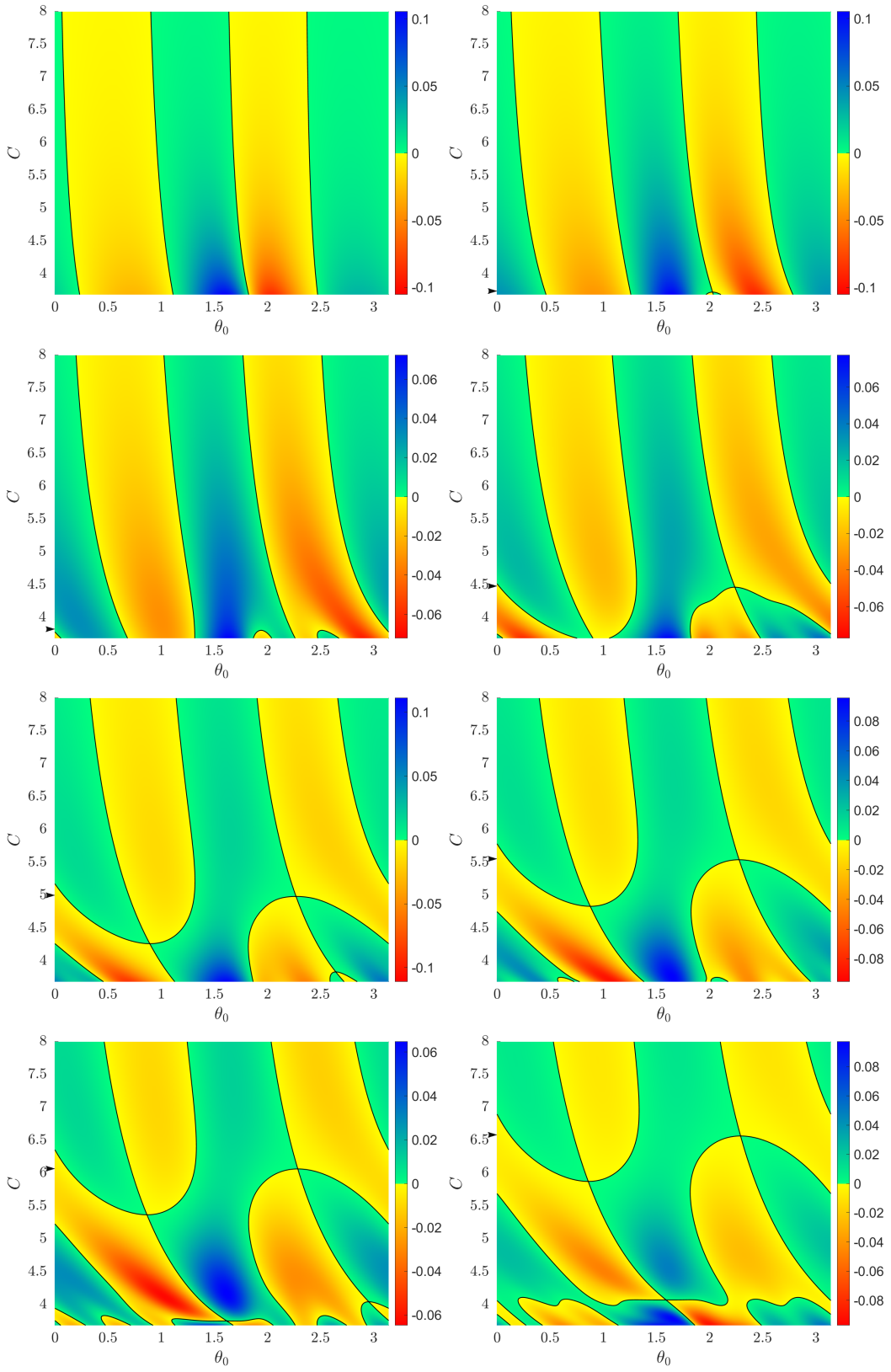

Figure 3.21: Bifurcation diagrams (value of $M_n(\theta_0)$) for $\mu = 0.1$, $n = 1, ..., 8$ and C in $[C_{L_1}, 8]$. The value of $\hat{C}(\mu, n)$, for $\mu = 0.1$ is also indicated in each plot with an arrow in the vertical axis.

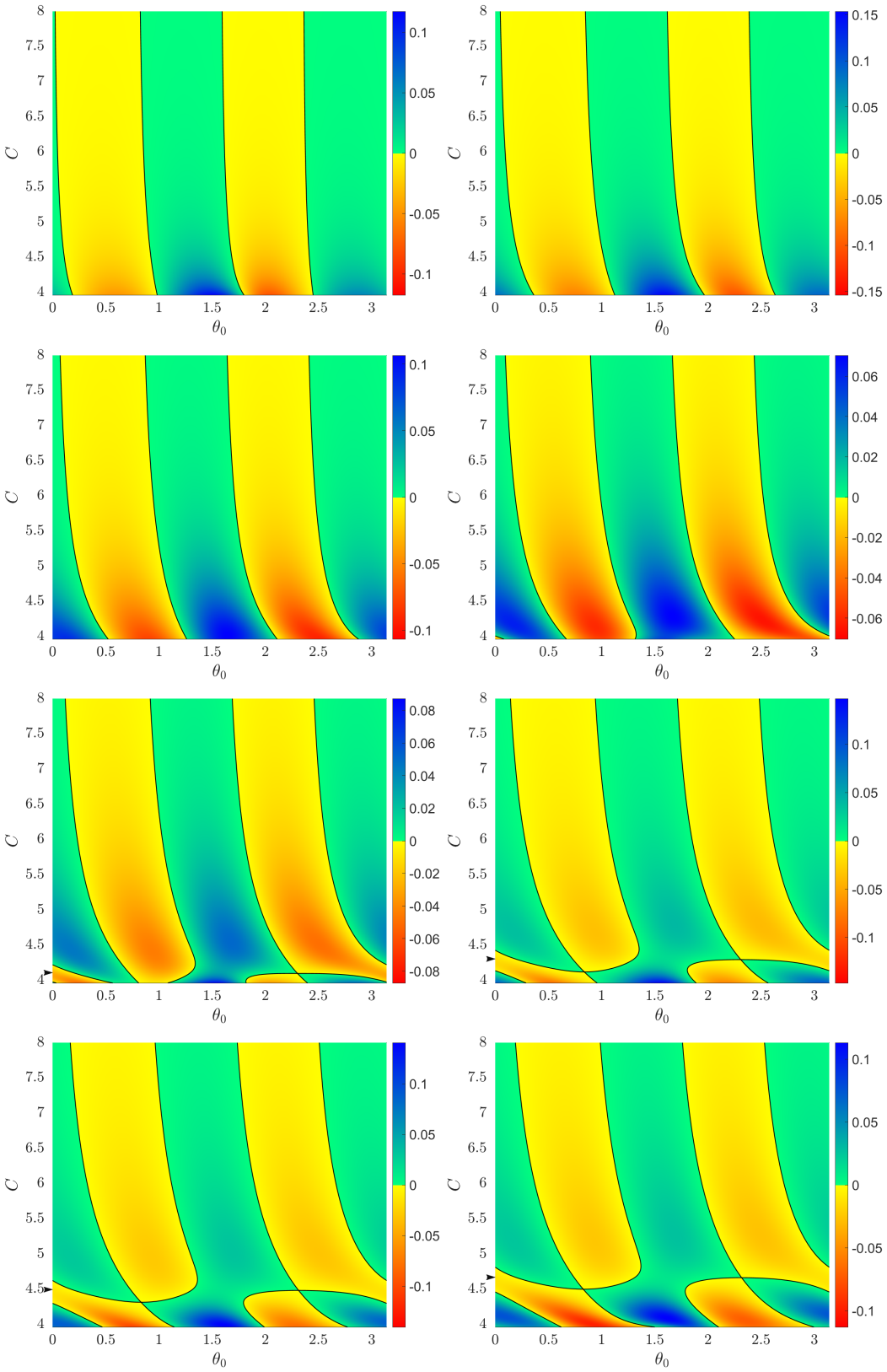

Figure 3.22: Bifurcation diagrams (value of $M_n(\theta_0)$) for $\mu = 0.8$, $n = 1, ..., 8$ and C in $[C_{L_1}, 8]$. The value of $\hat{C}(\mu, n)$, for $\mu = 0.8$ is also indicated in each plot with an arrow in the vertical axis.

To have a global and exhaustive insight, we have done massive numerical simulations in the following sense: we have fixed μ (for example $\mu = 0.1$), and for a range of values of $C \geq C_{L_1}$ (for example $C \in [C_{L_1}, 8]$) we have computed the value of the angular momenta at the n-th intersection with Σ_m for $n \geq 1$ as a function of the initial angle $\theta_0 \in [0, \pi)$. In order to simplify the notation, we will denote this value of the angular momentum as $M_n(\theta_0)$, although of course it also depends on μ and C. In Figures 3.21 and 3.22 we plot the obtained results for $\mu = 0.1$ and $\mu = 0.8$, and $n = 1, ..., 8$ what we call *bifurcation diagrams*. For n fixed, we plot the diagram (θ_0, C) and the color standing for the value of $M_n(\theta_0)$. The drastic change of color (from yellow to green, denoted by black) describes the change of sign of $M_n(\theta_0)$ and therefore the existence of an n-EC orbit. So for any C fixed, we clearly see the number of n-EC orbits.

Let us focus on the case of $\mu = 0.1$. In Figure 3.21 we can easily observe some of the previously commented results, and in particular we clearly see how as we increase the value n new families of n-EC orbits appear. If we look attentively Figure 3.21 we can see how the value of $\hat{C}(\mu = 0.1, n)$ increases as the n increases (see black arrow in the vertical axis). But not only that, we also see how the richness of new orbits is increasing as n increases. For example if we consider the case $n = 7$ and $n = 8$ (see Figure 3.21) we can observe a great richness of new families of n-EC orbits in the neighborhood of the C_{L_1} values.

When we take a bigger value of μ, for example, $\mu = 0.8$, we obtain Figure 3.22. Comparing the plots obtained with those of Figure 3.21, we observe two effects: the value of $\hat{C}(\mu, n)$ is smaller, for the same value of n, and moreover, for $n = 2, 3, 4$, a value of $\hat{C}(\mu, n)$ smaller than C_{L_1} is required (compare the four first plots in Figures 3.21 and 3.22). For bigger values of μ and for the same value of $C \geq C_{L_1}$, the Hill region gets really smaller, when increasing μ, so quite naturally, the probability of bifurcations decreases. On the other hand, taking $C < C_{L_1}$ represents an enlarging of the Hill's region and therefore a more powerful influence of the second primary, that in this case is the bigger one, so an easier scenario to have bifurcations.

At this point it is important to note the following remark:

Remark 3. *The strategy to compute the n-th intersection with Σ_m and compute the value of the angular momentum may not be the best strategy if we consider smaller C values, since, for example for values of $C < C_{L_1}$ the particle could be perfectly in a neighborhood of the second primary. To avoid possible problems, we have numerically verified the condition $u = v = 0$.*

Among all these new bifurcations in which new families of n -EC orbits appear, we will focus only on those associated with the limit value $\hat{C}(\mu, n)$.

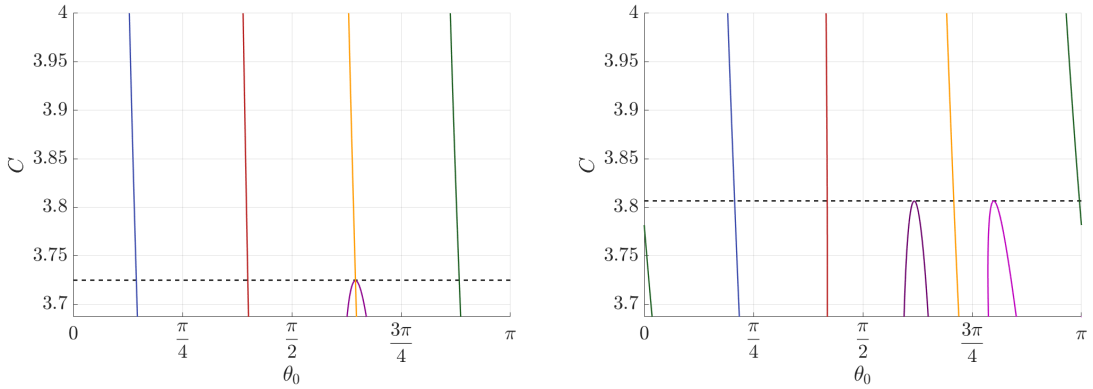

Figure 3.23: Initial condition for the n-EC orbits for $n = 2$ (left) and $n = 3$ (right) as a function of $C \in [C_{L_1}(\mu), 4]$ for $\mu = 0.1$. We have the original four n-EC orbits corresponding to α_n (yellow), β_n (green), γ_n (blue) and δ_n (red), and the new families (purple). The discontinuous black line denotes the value of $\hat{C}(\mu, n)$.

If we look at Figures 3.21 and 3.22 we can see the two types of bifurcations that are associated with this value. In general ($n \neq 3$), the situation is the one that can be observed in Figure 3.23 left where we go from four to six n-EC orbits. The other case is associated with $n = 3$ where we go from four to eight 3-EC orbits (see Figure 3.23 right).

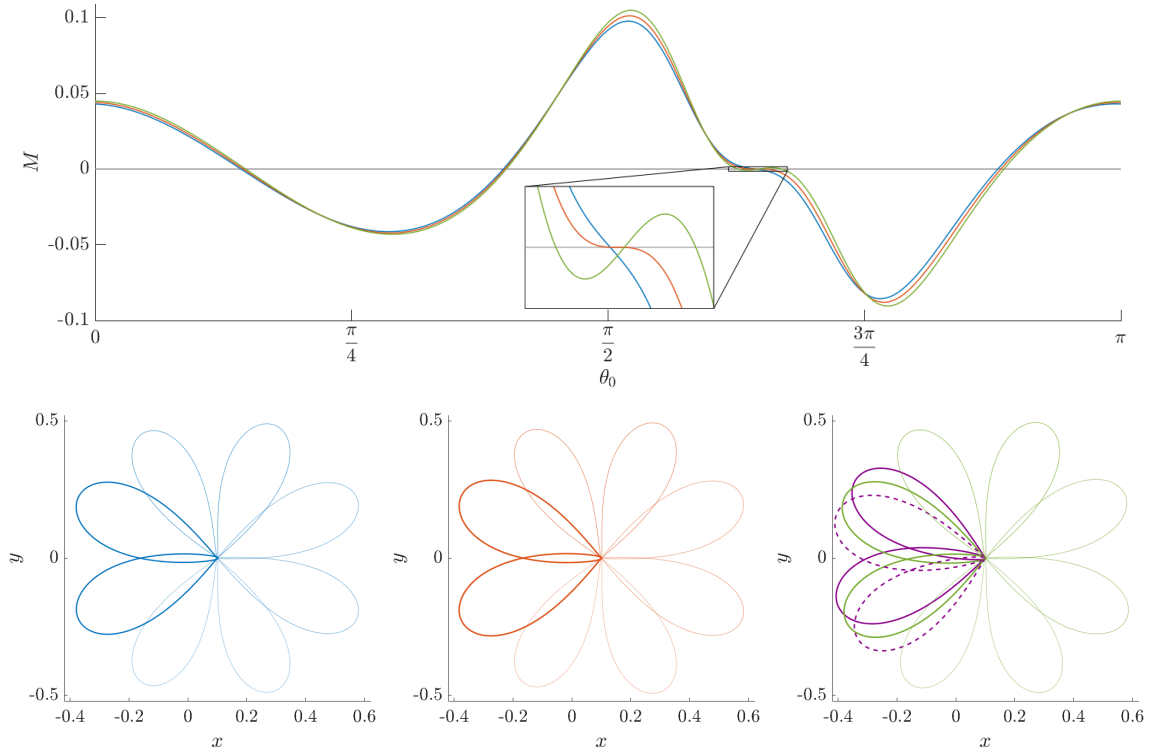

Figure 3.24: $\mu = 0.1$, $n = 2$. Top. We plot the angular momentum $M_2(\theta_0)$. Notice the zoom area where the appearance of two new bifurcating orbits (in green), besides the family α_2 is observed when decreasing C. Bottom. Left, middle and right. The four original 2-EC orbits (the colour code corresponds to the top figure) for $C = 3.76$ (in blue), $\hat{C}(0.1, 2) \approx 3.72442505$ (the bifurcating value, in red), $C = 3.69$ (in green). In darker blue, red and green respectively those 2-EC orbits belonging to family α_2 and in purple the two new bifurcated 2-EC orbits are plotted.

The first type of bifurcation (the one that occurs in the cases $n \neq 3$) corresponds to a bifurcation that originates from the α_n family and that gives rise to -setting a specific value of C- two new n-EC orbits.

Let us describe, in more detail, this type of bifurcation for the case $n = 2$. To do this, let us carefully observe the zoom area in Figure 3.24 top. Locally, at a neighborhood of the value of θ_0 of such EC orbit, for some value of C the angular momentum has a unique transversal intersection with the x-axis (that is $M_2(\theta_0) = 0$, $M_2'(\theta_0) = 0$) . For $C = 3.76$ this intersection corresponds to the 2-EC orbit belonging to the family α_2 (see the blue curve). For the bifurcating value $\hat{C}(0.1, 2) \approx 3.72442505$, $M_2(\theta_0)$ crosses tangently the x axis (see the red curve). For smaller values of C, $M(\theta_0)$ crosses the x axis three times, giving rise to two new bifurcating families of 2-EC orbits (see the green curve) besides family α_2 which persists. The new 2-EC orbits are (obviously due to symmetry (1.6)) one symmetric with respect to the other. From a global point of view, for a range $C < \hat{C}(0.1, 2)$, varying $\theta_0 \in [0, \pi)$, $M_2(\theta_0)$ crosses six times, that is, we obtain six 2-EC orbits. We show these 2-EC orbits in Figure 3.24 bottom. More precisely, on the three plots, the four 2-EC orbits are shown (in the plane (x, y)) and those 2-EC orbits of family α_2 are plotted in a darker color. Since the family α_2 persists after the bifurcation, the 2-EC orbits are plotted in the left, middle and right plots. The two new bifurcating 2-EC orbits after the bifurcation are also shown on the right plot.

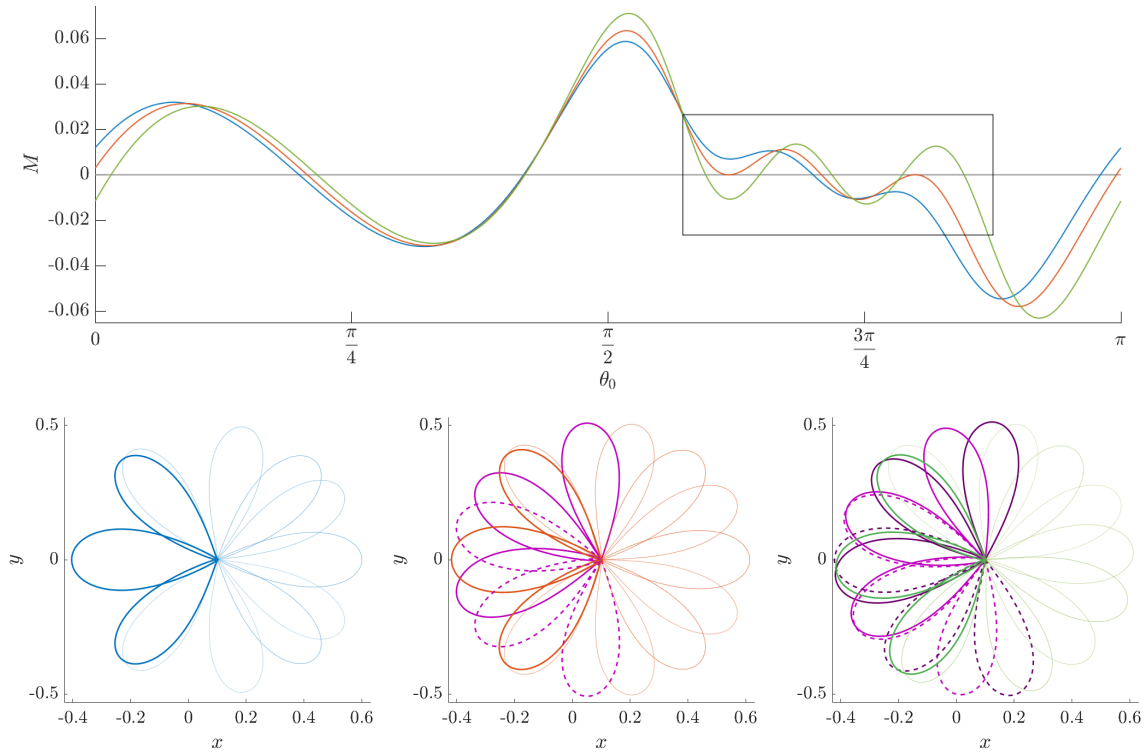

Figure 3.25: $\mu = 0.1$, $n = 3$. Top. We plot the angular momentum $M_3(\theta_0)$. Notice the zoom area where the appearance of four new bifurcating orbits (in green), besides the family α_3 is observed when decreasing C. Bottom. Left, middle and right. The four original 3-EC orbits (the colour code corresponds to the top figure) for $C = 3.9$ (in blue), $\hat{C}(0.1, 3) \approx 3.80644009$ (the bifurcating value, in red), $C = 3.7$ (in green). In darker blue, red and green respectively those 3-EC orbits belonging to family α_2. and in purple the two new bifurcated 2-EC orbits are plotted. In the middle plot, also the two tangent new bifurcated 3-EC orbits are plotted in purple. In the right plot, also the four new bifurcated 3-EC orbits are plotted in purple.

The second kind of bifurcation associated with $\hat{C}(\mu, n)$ is what occurs in the case $n = 3$. If we observe Figure 3.25 we can clearly see how decreasing C, the angular momentum $M_3(\theta_0)$ typically crosses four times the x-axis (for $\theta_0 \in [0, \pi)$), as expected (see the blue curve in the top figure). However at some bifurcating value $\hat{C}(0.1, 3)$ there appear two tangencies (say from nowhere, see the red curve inside the box in Figure 3.25 top); each tangency gives rise to two families when doing the continuation of families decreasing C. See the green curve inside the box in Figure 3.25 top. So from a global point of view, for a range of $C < \hat{C}(0.1, 3)$ and $\theta_0 \in [0, \pi)$, the angular momentum $M_3(\theta_0) = 0$ crosses eight times the x-axis. We show these 3-EC orbits in Figure 3.25 bottom. More specifically, on the three plots, the four 3-EC orbits are shown (in the plane (x, y)) and those 3-EC orbits of family α_3 are plotted in a darker color. The two 3-EC orbits that appear due to the tangency of $M_3(\theta_0)$ with the x-axis are also plotted on the middle plot. Moreover, the four new bifurcating 3-EC orbits after the bifurcation are also shown on the right plot. A continuous and discontinuous line with the same color correspond to EC orbits that are symmetric one with respect to the other one. In fact, due to the symmetry of the problem, we might only consider the two intersection points (those on the left hand side or on the right one of the value of θ_0 in α_3), and the other two intersection points would be obtained by symmetry.

The natural question at this point is to study the evolution of $\hat{C}(\mu, n)$. The strategy to compute numerically $\hat{C}$, for a fixed $\mu \in (0, 1)$ and given n, is the following: fixed a value C_b large enough we take the interval $I = [C_{L_1}, C_b]$ of values of C, and for each $C \in I$, (starting at C_b) we vary $\theta_0 \in [0, \pi)$

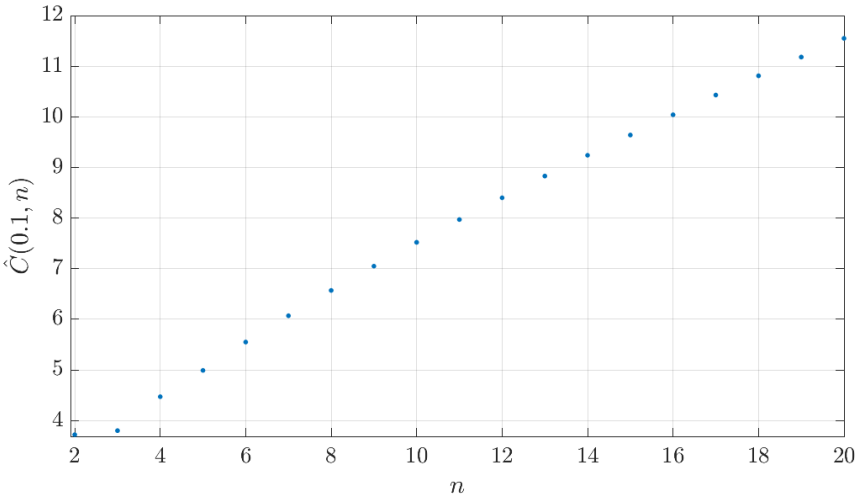

Figure 3.26: Value of $\hat{C}(0.1, n)$ for $n = 2, ..., 20$.

(that defines the initial conditions of an ejection orbit in synodical Levi-Civita variables) and find the four specific values of θ_0 (such that $M(\theta_0) = 0$) corresponding to the expected four n-EC orbits. So we have four n-EC orbits for that value of C and decreasing C we obtain four families of n-EC orbits. However as we decrease C, we find a value of $C \in I$ such that more than four n-EC orbits are found. This means that new families have bifurcated. Next we refine the value of C such that it is the frontier before appearing new families of n-EC orbits. That is precisely the specific value of $\hat{C}$.

In Figure 3.26 we can see the evolution of $\hat{C}(0.1, n)$ (on the vertical axis) increasing n from 2 to 20 (on the horizontal one). We observe that the $\hat{C}(0.1, 1)$ is not on the plot because bifurcations appear when $C < C_{L_1}$ in this case. As expected, (and as could guess from Figure 3.21) when n increases, a bigger value of $\hat{C}$ is obtained, that is, bifurcations of EC orbits appear earlier, in the sense that $\hat{C}$ is bigger. On the contrary, for smaller values of n, $\hat{C}$ is smaller; so we obtain larger ranges for C, meaning that for $C \in (\hat{C}, \infty)$ there exist four and only four families of n-EC orbits.

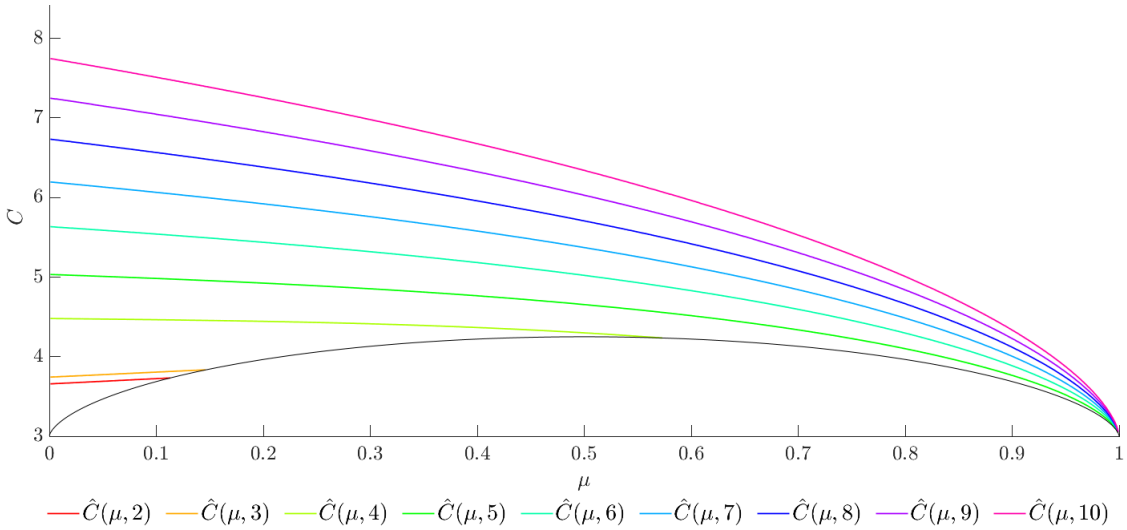

Figure 3.27: Value of $\hat{C}(\mu, n)$ for $\mu \in (0, 1)$ and $n = 2, ..., 10$.

In Figure 3.27 we show the results obtained for $\mu \in (0, 1)$ and $n = 2, ..., 10$. Also the curve (μ, C_{L_1}) has been plotted (in black). Recall that, as mentioned previously, we are focussed on values of $C \geq C_{L_1}$.

We remark that for $n = 1$, the value $\hat{C}(\mu, 1)$ is less than C_{L_1} and therefore is not considered. Moreover for the specific value of $\mu = 0.1$ we recover the indicated values in Figure 3.21. From Figure 3.27 two comments must be noticed:

1. the value of $\hat{C}(\mu, n)$ increases when n increases (generalization of the case $\mu = 0.1$). This means that for higher values of n, that is longer time spans integrations, the effect of the other primary is more visible.

2. Fixed $n > 3$, the dependence of $\hat{C}(\mu, n)$ with respect to μ follows a similar pattern for different $n > 3$. We also see how $\hat{C}(\mu, n) \to 3$ when $\mu \to 1$.

These same results will be evidenced in Chapters 4 and 5. In particular, in Chapter 5 we will see how this pattern of $\hat{C}(\mu, n)$ (Figure 3.27, $n > 3$) coincides with the expression of the analytical threshold of $\hat{C}(\mu, n)$ obtained.

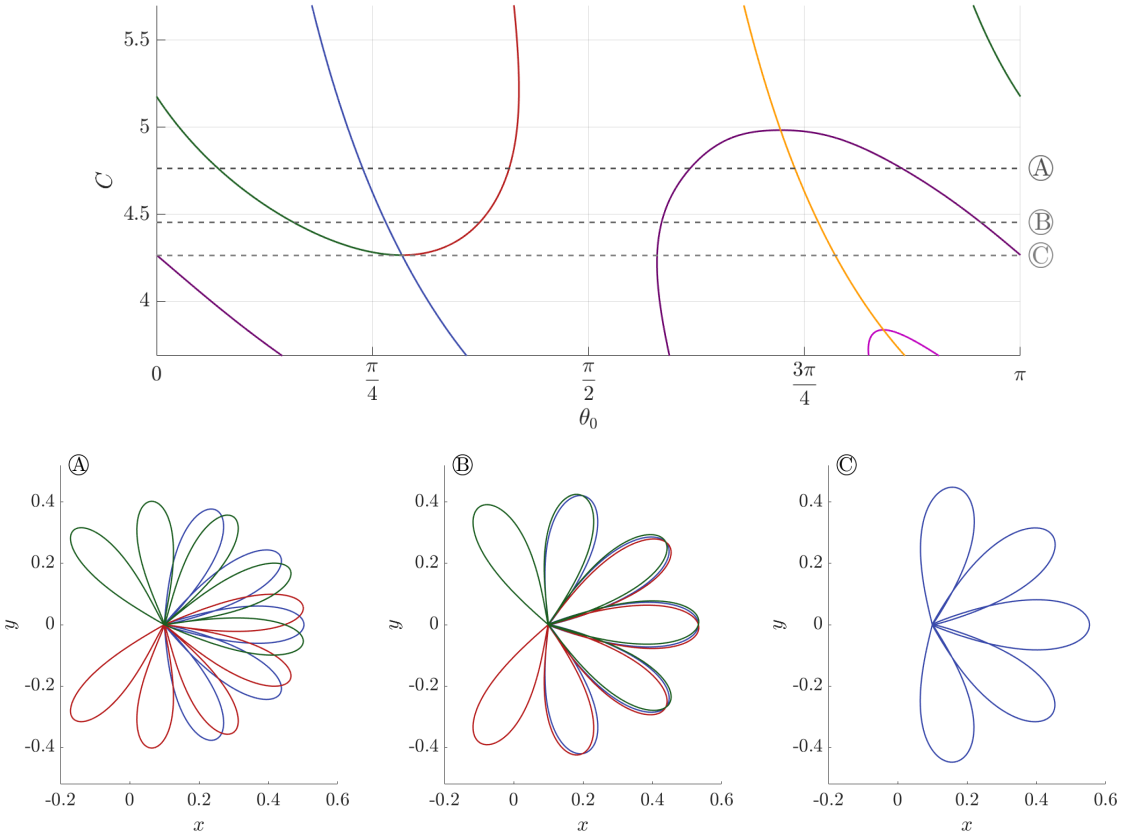

Figure 3.28: $\mu = 0.1$, $n = 5$. Top. Initial condition for the n-EC orbits corresponding to α_5 (yellow), β_5 (green), γ_5 (blue) and δ_5 (red), and the new families (purple) as a function of C . Bottom the trajectories of the 5-EC orbits β_5, γ_5 and δ_5 for the values of C denoted in the top figure.

To finish this subsection, it is important to note another phenomenon that we observe, the phenomenon of confluence of families of n-EC orbits. In Figure 3.28 we can see this phenomenon for the case of 5-EC orbits. In it we see how the orbits associated with the families β_5 and δ_5 (symmetric one of the other) end up coming together in the family of γ_5 (symmetric orbit).

We have observed that the families of orbits associated with β_n and δ_n always end up converging in the family of γ_n for values of n that are large enough, since if n is small, the value of C_{L_1} is reached

before being able to observe this phenomenon. However, as we will see in the next subsection, this continues to be true for small n, but with some minor nuances.

3.4.3 Evolution of the four n-EC orbits

The goal of this subsection is to see what is the evolution of the original four families of n-EC orbits for less restrictive values of C (allowing even unbounded motion for ejection orbits). In this way, we want to see, on the one hand, how the β_n and δ_n families continue to converge in γ_n (with some considerations) and, on the other, illustrate the immense richness that exists in the evolution of the dynamics of these four n-EC orbits. To do so, we will study the evolution of these orbits as a function of the mass parameter. We will start by describing the dynamics for small μ values and we will increase this value to see the phenomena that appear.

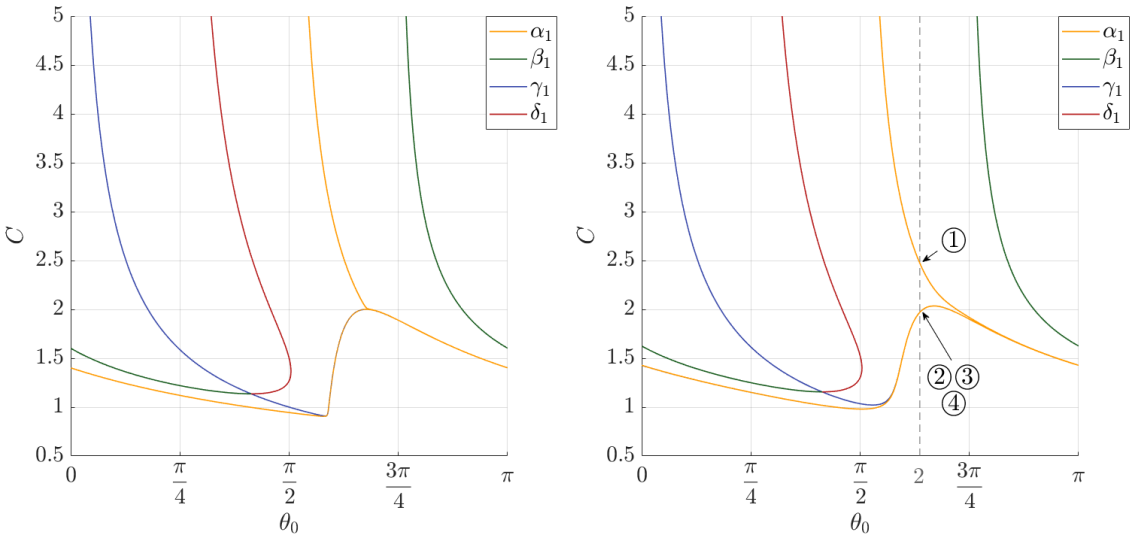

Figure 3.29: Evolution of the initial condition of the four original 1-EC orbits for $\mu = 0.0001$ (left) and $\mu = 0.01$ (right).

In this way, we will start by observing this evolution for small values of μ and $n = 1$. In Figure 3.29 we can see the evolution of the original four 1-EC orbits, for $\mu = 0.0001$ and $\mu = 0.01$. In this Figure we can observe how the qualitative behavior is the same for the two values of μ shown and we see two remarkable phenomena. On the one hand, the families β_1 and δ_1 converge on family γ_1 as it happened for higher values of n. On the other hand, we see how by doing the numerical continuation of families α_1 and γ_1, they tend to get very close, but without merging. Furthermore, we see how, at least initially, α_1 and γ_1 approach towards a periodic orbit (see Figure 3.30).

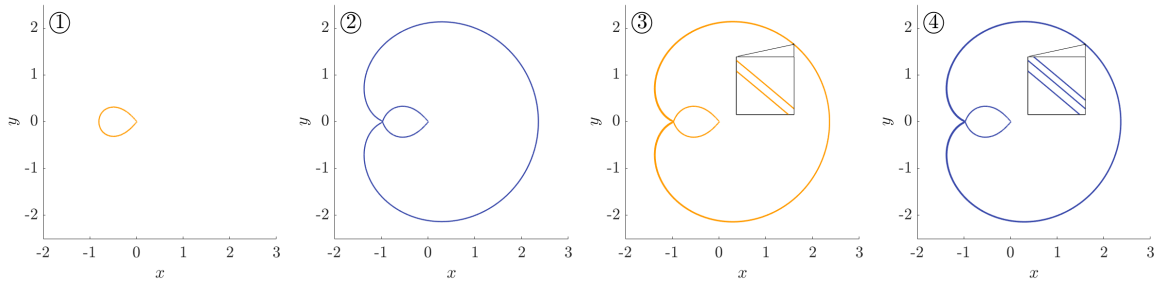

Figure 3.30: First four EC orbits obtained with $\theta_0 = 2$ belonging to α_1 (yellow) or γ_1 (blue) for $\mu = 0.01$ when we decrease the value of C. The values of the Jacobi constant are $C \approx 2.472170770645$, $C \approx 1.970463731686$, $C \approx 1.970412419219$ and $C \approx 1.970412407739$ respectively (from left to right).

This last phenomenon is very important since it reveals the local character of the definition of n-EC orbit. The two plots on the right of Figure 3.30 show two orbits that we obtain by continuing the families α_1 and γ_1 that have respectively two and three local maxima in the distance with respect to the first primary before colliding with it, and recall that the definition of n-EC orbit that we have given at the beginning of the chapter: an n-EC orbit is the orbit that ejects from the first primary and reaches n times a relative maximum in the distance with respect to the first primary before colliding with it. Therefore we see that this definition is no longer consistent for all the orbits of the family α_1 and γ_1, since they have more than one local maximum in the distance with respect to the first primary before colliding with it.

At this point one can try to find alternative definitions for the n-EC orbits. The first and most natural idea about it would be one using the qualitative concept of *close approach*. Let us first observe that the definition given for n-EC orbit is equivalent to the orbit that ejects from the first primary and collides with it in the n relative minimum in the distance with respect to the first primary. Therefore, we can replace the n relative minimum in the distance with respect to part by n close approaches.

This generalization of the definition fits well for this particular case, but apart from losing its rigor and quantitative simplicity, it does not always work well as we will see.

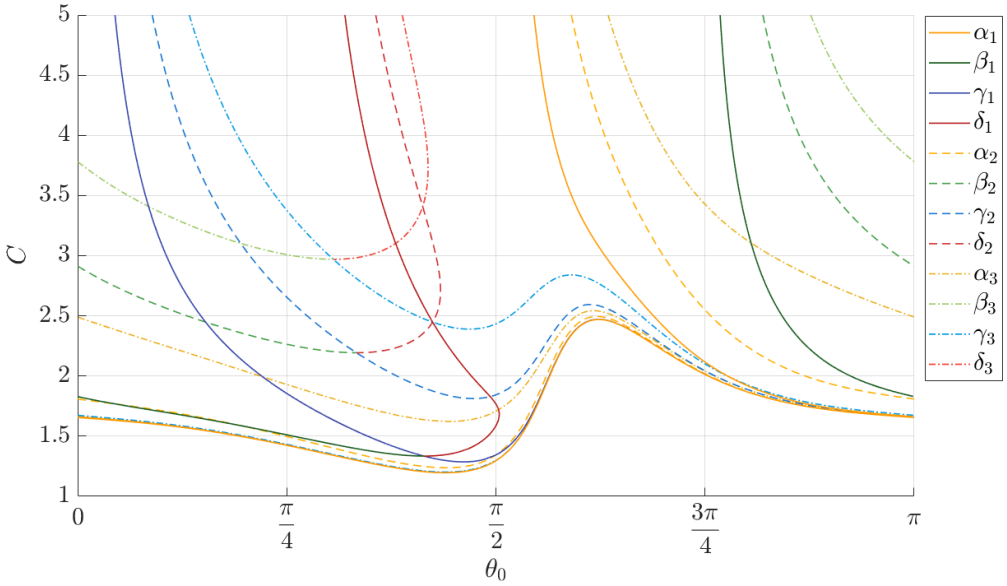

Figure 3.31: Evolution of the initial condition of the four original n-EC orbits for $\mu = 0.1$ and $n = 1, 2, 3$.

If we consider values of n larger and we gradually increase the value of μ (see Figure 3.31) we observe that the behavior of the four original families of n-EC orbits is very similar and qualitatively the same as previously described. On the one hand, the families β_n and δ_n converge on family γ_n and in the other hand, we see how the families α_n and γ_n tend to get very close but without merging.

However, the situation becomes more complex if we increase the value of μ. Take for example the case $\mu = 0.2$ described in Figure 3.32. The first comment to make is that the numerical continuation has been made until the collision of the different families with the second primary. But this collision phenomenon that we now easily observe is not the only one that appears.

Let us consider first the evolution of the δ_1 family. If we compare the evolution of the δ_1 family for $\mu = 0.2$ (Figure 3.32) with the evolution for $\mu = 0.1$ (Figure 3.31) we can see how it is cleared deformed around $C = 2$. This deformation is even more evident if we compare it with smaller values

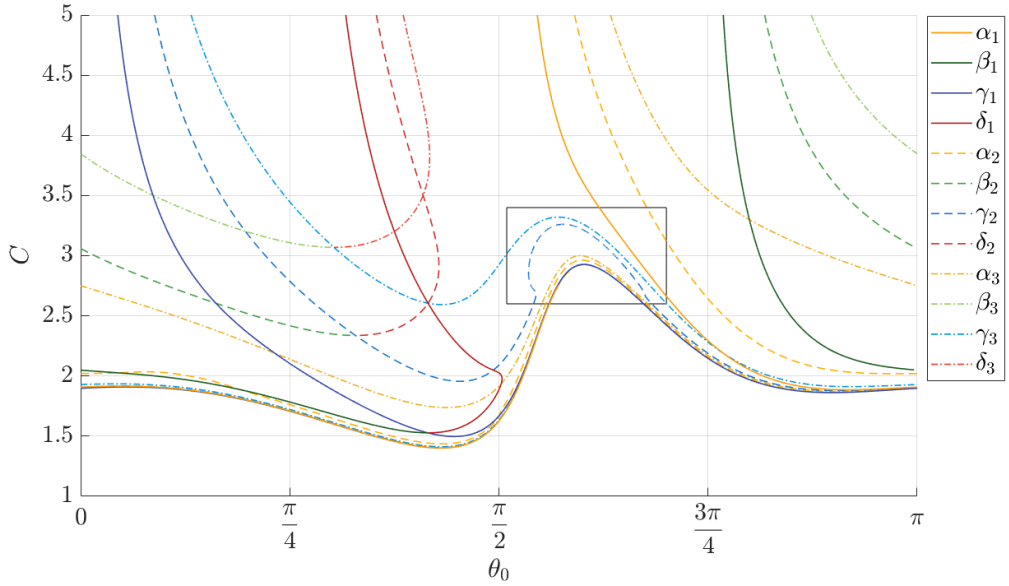

Figure 3.32: Evolution of the initial condition of the four original n-EC orbits for $\mu = 0.2$ and $n = 1, 2, 3$.

of μ (see Figure 3.29). This phenomenon is due to the influence of the triangular equilibrium points, L_4 for the case of δ_1 and L_5 for the case of β_1 (since the orbits of these families are symmetric one of the other). As we will see, for greater values of μ these equilibrium points will play a fundamental role in the evolution of these families. Recall that $L_{4,5}$ are complex saddles for $\mu \in (\mu_R, 1 - \mu_R)$.

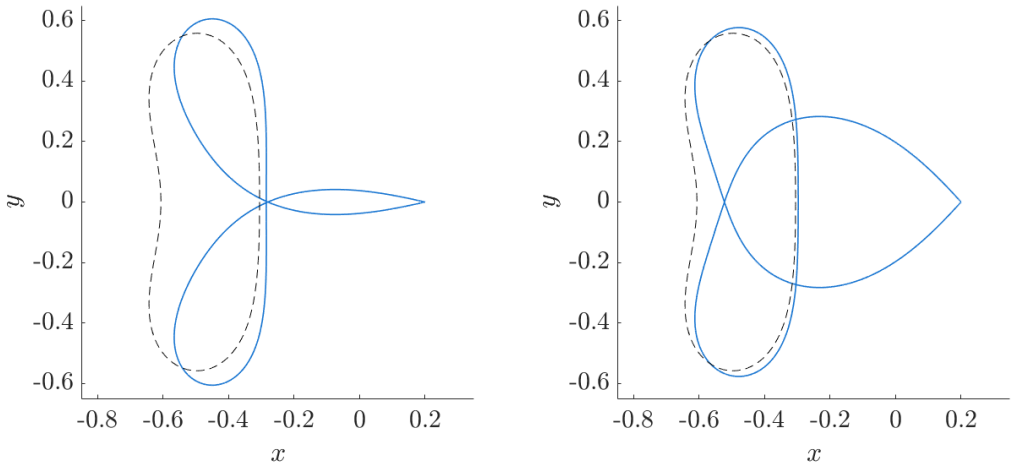

Figure 3.33: EC orbits of γ_2 belonging to the region inside the box in Figure 3.32 with $C = 3$ (and $\mu = 0.2$). The discontinuous black line is the LPO_1 for these values of μ and C.

The other phenomenon that we observe is relative to the deformation that appears in γ_2 (compare the γ_2 inside the region in the box in Figure 3.32 with the Figure 3.31). This deformation (see Figure 3.33) is produced by the influence of the Lyapunov periodic orbit associated with the point L_1 (LPO_1). As we can see, the attempt to generalize the definition of n-EC orbits using the close approaches is not valid for this case. We will study with more detail the role of LPO_1 in Chapter 6.

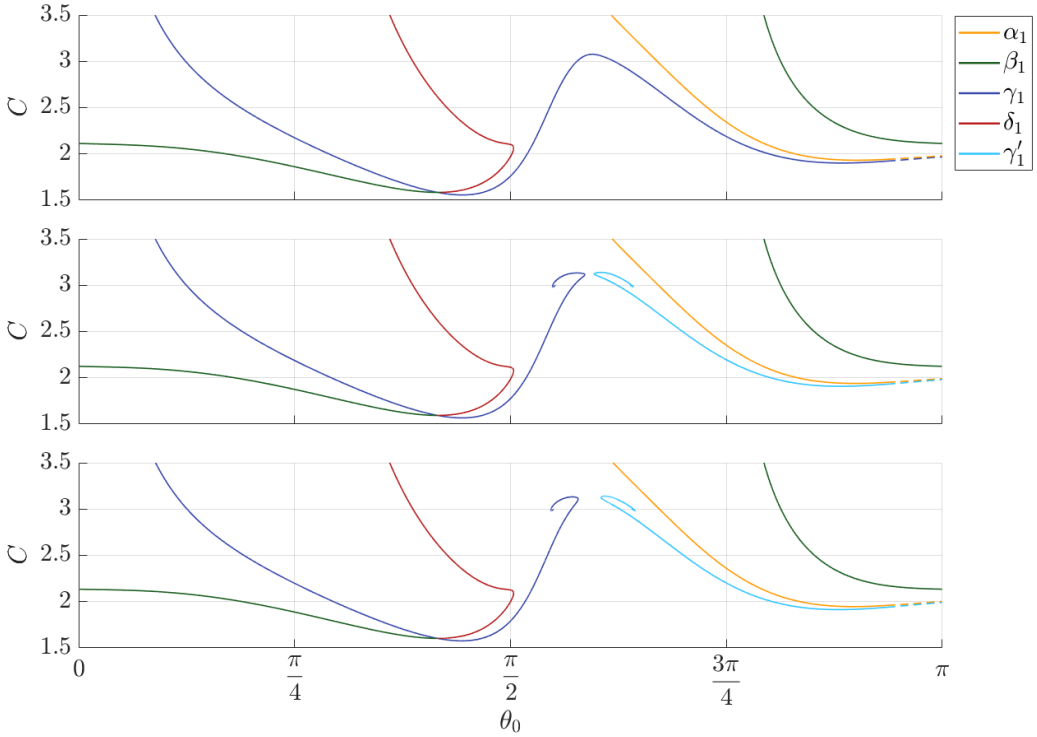

Figure 3.34: Evolution of the initial condition of the four original 1-EC orbits for $\mu = 0.23$, 0.235, 0.24 (from top to bottom).

If we increase the value of μ a little more we see that the equilibrium points L_4 and L_5 make the family of 1 -EC orbits associated with γ_1 divide into two families (see Figure 3.34). This is due to the fact that heteroclinic connections involving the ejection, the collision and the equilibrium points L_4 and L_5 appear.

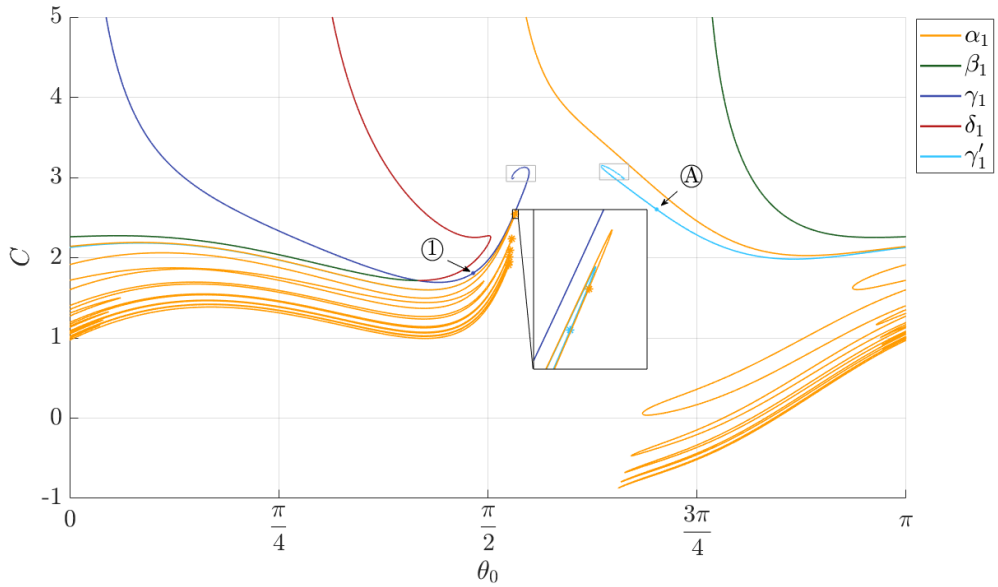

Figure 3.35: Evolution of the initial condition of the four original 1-EC orbits for $\mu = 0.3$. The "$*$" denotes a collision with the second primary.

A detailed study of the heteroclinic connections between L_4 and L_5 can be found in [GLM89] but in our case the connections of these points with ejection and collision also play a fundamental role. To see this phenomenon in more detail we will consider the evolution of the four initial families of 1-EC orbits for $\mu = 0.3$ (see Figure 3.35).

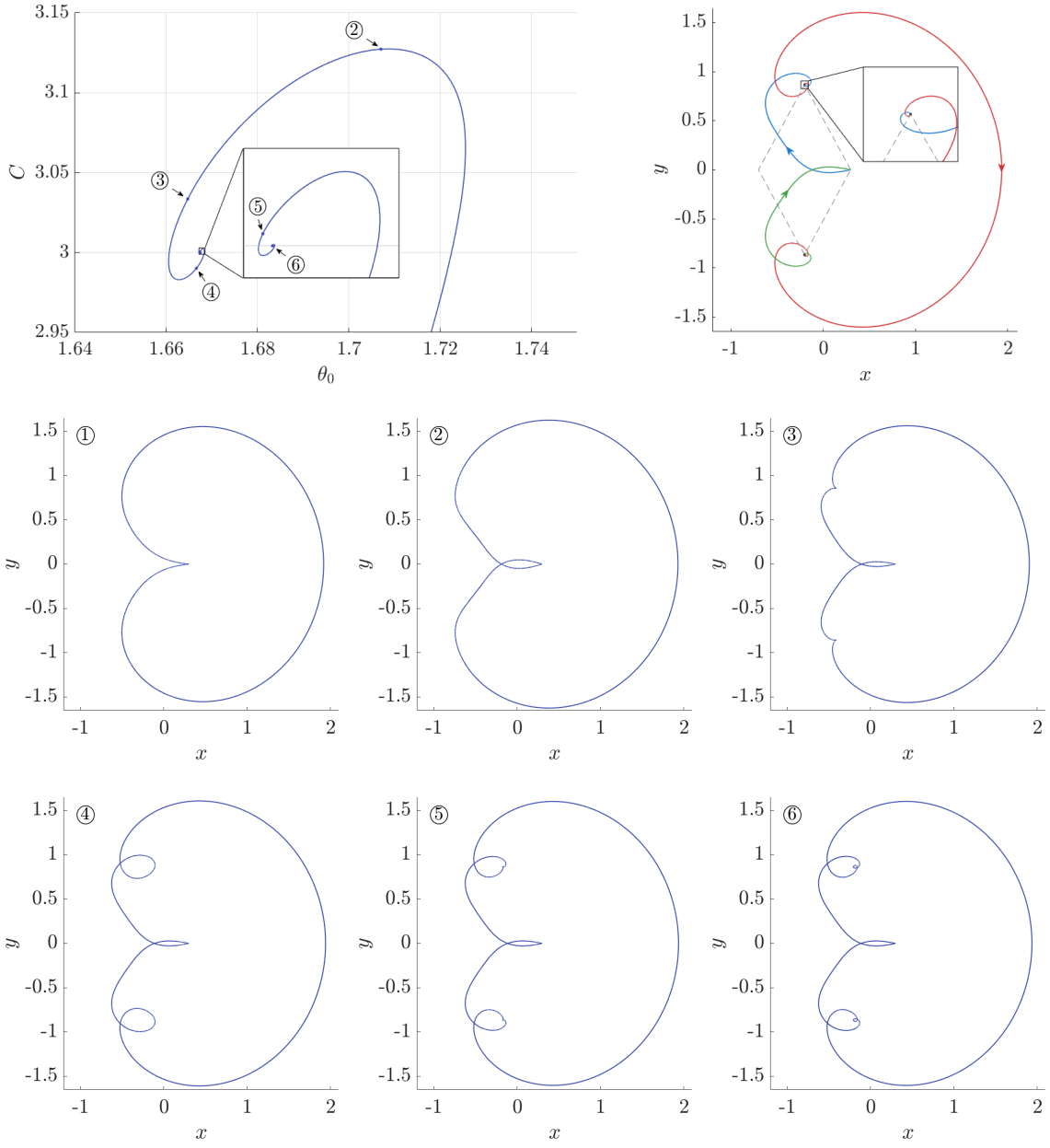

Figure 3.36: $\mu = 0.3$. Zoom of the boxed region of Figure 3.35 around γ_1 (top left). The three connections from ejection to L_4 (blue), L_4 to L_5 (red) and L_5 to collision (green) that are the limit of the family γ_1 (top right). The other plots corresponds to the EC orbits that have the initial condition marked in the top left figure and in the Figure 3.35.

In Figure 3.36 we can clearly see the influence of the manifolds of the points L_4 and L_5 in the family γ_1. In particular, in the top left plot of Figure 3.36 we observe the zoom of the boxed region around γ_1 of Figure 3.35, and we see how the initial conditions of the EC orbits of this family spiral around and tend to the connection ejection-L_4 (see the blue line in top right plot of Figure 3.36). As γ_1 is a

family of symmetric EC orbits, to collide again we need to reach L_5 through an heteroclinic connection L_4-L_5 (red curve) and finally go from L_5 to collision through the symmetric connection to ejection-L_4 that we us previously (green curve). In the other plots in Figure 3.36 we see how the EC orbits of the γ_1 family tend to the limit value of the connections previously discussed.

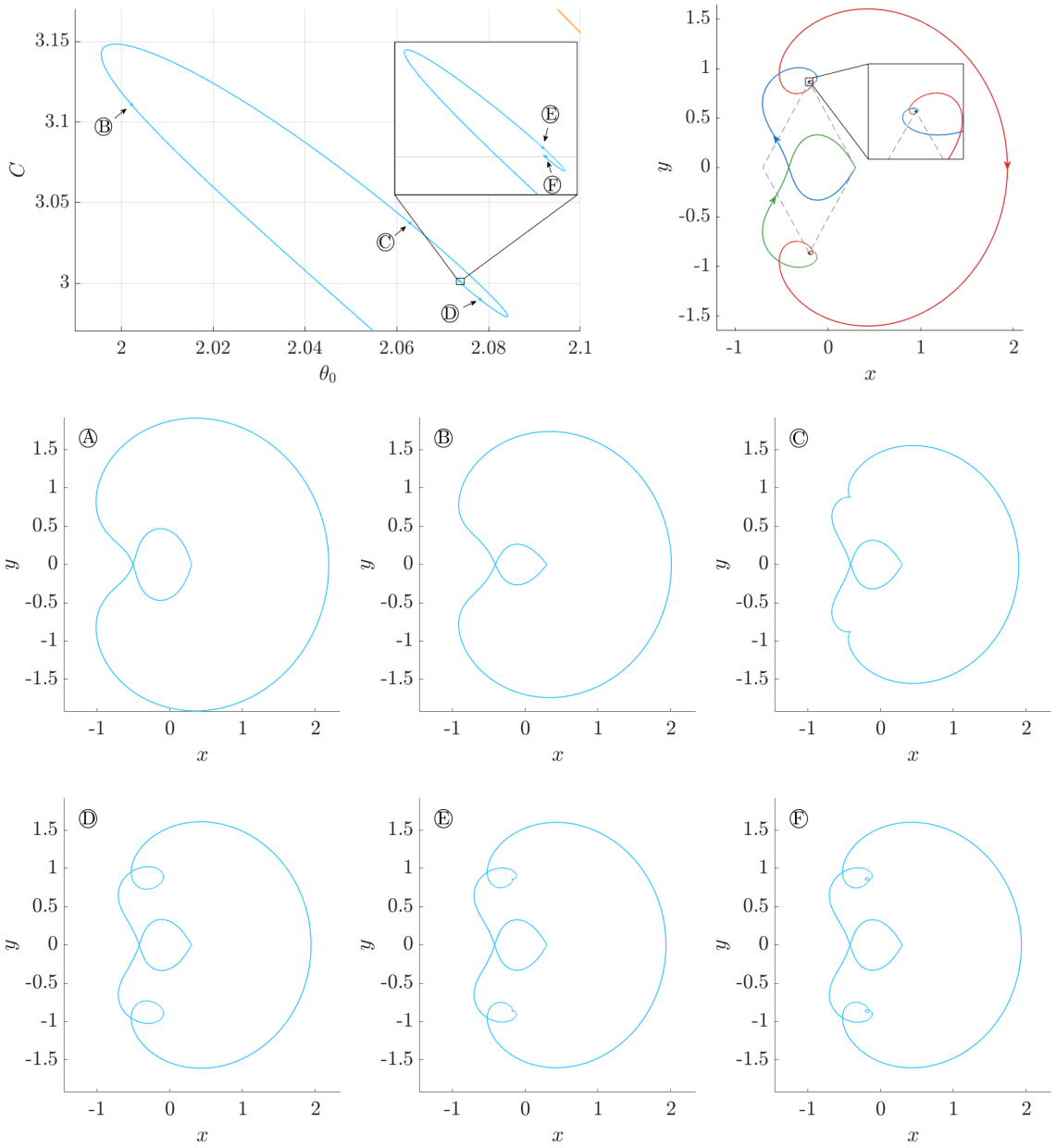

Figure 3.37: $\mu = 0.3$. Zoom of the boxed region of Figure 3.35 around γ_1' (top left). The three connections from ejection to L_4 (blue), L_4 to L_5 (red) and L_5 to collision (green) that are the limit of the family γ_1' (top right). The other plots corresponds to the EC orbits that have the initial condition marked in the top left figure and in the Figure 3.35.

In a similar way Figure 3.37 we can clearly see the influence of the manifolds of the points L_4 and L_5 in the family γ_1'. In the top left plot of Figure 3.37 we observe the zoom of the boxed region around γ_1' of Figure 3.35, and we see how the initial conditions of the EC orbits of this family spiral around and tend to a different connection ejection-L_4 than the family γ_1 (see the blue line in top right plot of

Figure 3.37 and compare with Figure 3.36). To return to collision, the same heteroclinical connection from L_4 to L_5 as in the γ_1 case is used (red line) and then the symmetric connection to go from L_5 to collision (green curve). In the other plots in Figure 3.37 we see how the EC orbits of the γ_1' family tend to the limit value of the connections described in the top right plot.

In this way we see how the dynamics associated with the triangular equilibrium points is responsible for capturing the γ_1 family and causing it to divide in two. The family γ_1' continues to have the same behavior that γ_1 had for smaller values of μ and we observe that the families α_1 and γ_1' tend to get very close but without merging.

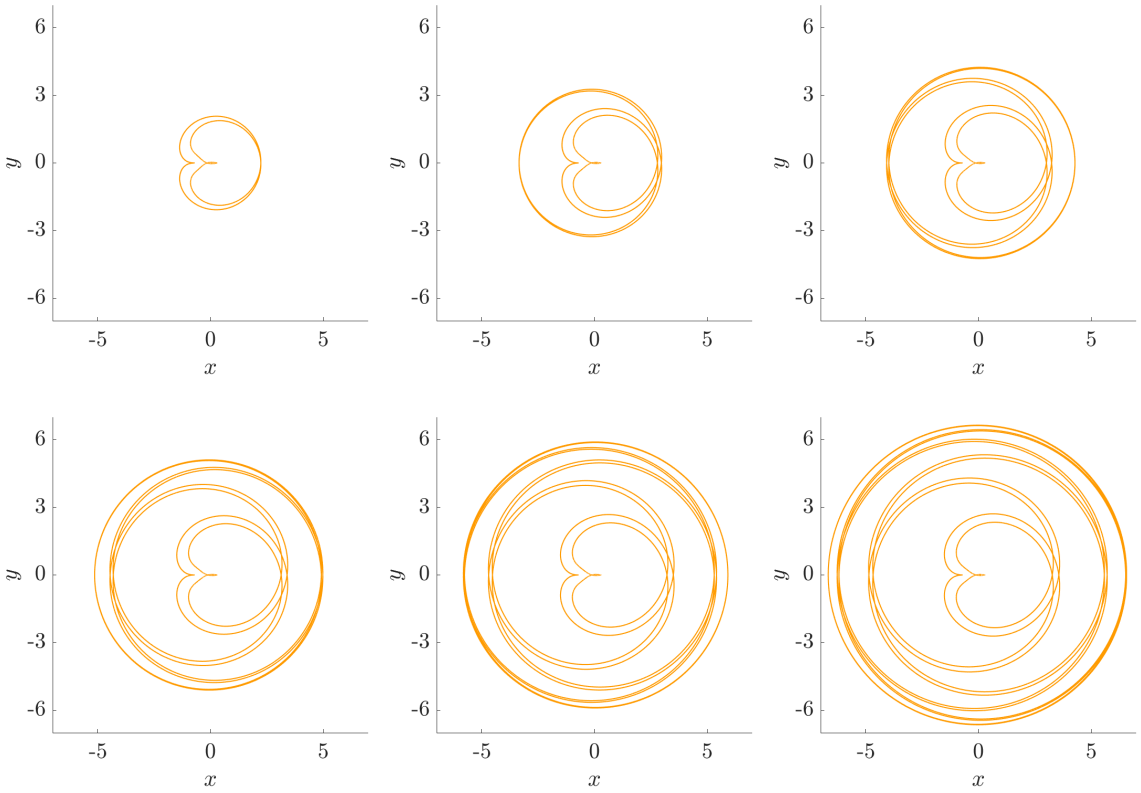

Figure 3.38: First 6 collisions with the second primary of α_1 for $\mu = 0.3$.

In Figure 3.35 we can also observe another different phenomenon, that of collisions that appear with the second primary. In particular, in Figure 3.35 we have made the continuation of the families α_1 and γ_1' until the sixth collision with the second primary. The initial conditions of these orbits that collide with the second primary before colliding with the first primary are marked with an asterisk. On the one hand, we see how the initial conditions of the orbits that collide with the second primary of α_1 and γ_1' families are very close (see the region with zoom). On the other hand, we see how the evolution of the family α_1 (and also γ_1') between each orbit colliding with the second primary is very similar (piece of curve between asterisks of Figure 3.35).

Furthermore, the behavior of these orbits that present an intermediate collision with the second primary before colliding with the first primary is very interesting, since on the one hand, we can see how the initial angle of these orbits is very similar, and on the other, see Figure 3.38, the k-th orbit of the family α_1 that collides with the second primary appears to be the same the $k-1$-th orbit of the family α_1 that collides with the second primary with an extra exterior revolution. (Compare for example the top left plot of Figure 3.38, that is the first orbit belonging to α_1 with an intermediate collision with the second primary, with the top middle plot, that corresponds to the second orbit of

α_1 with an intermediate collision with the second primary).

Similarly in Figure 3.35 we observe how the families β_1 and δ_1 collapse in γ_1 but we see how the deformation in δ_1 is increasing.

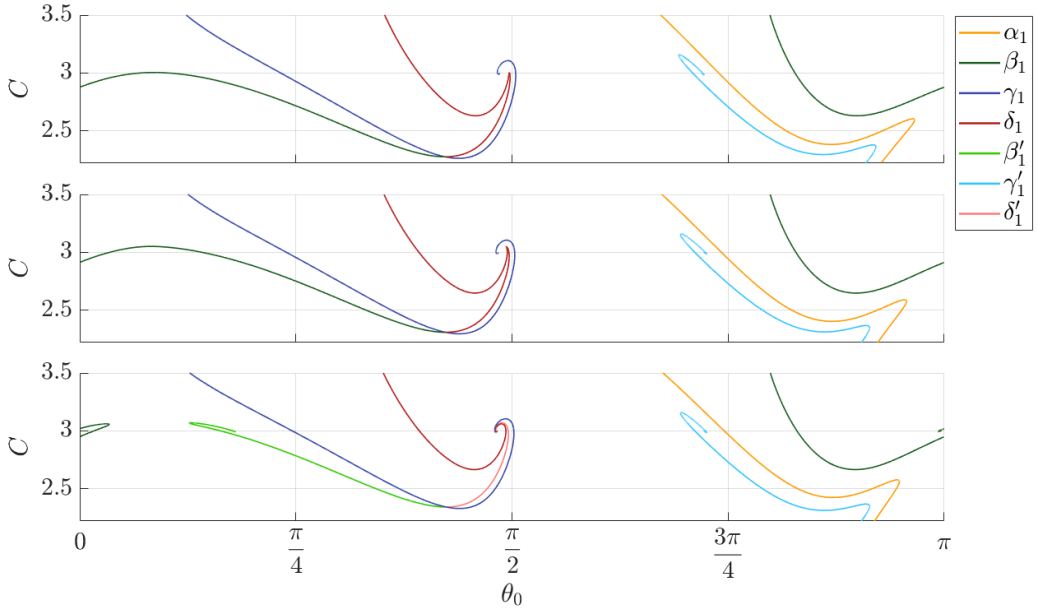

Figure 3.39: Evolution of the initial condition of the four original 1-EC orbits for $\mu = 0.62$, 0.64, 0.66 (from top to bottom).

In Figure 3.39 we can see how the points L_4 and L_5 end up playing a fundamental role in the evolution of the β_1 and δ_1 families, since when considering values of μ big enough, they end up catching the β_1 and δ_1 families and causing them to split into two families.

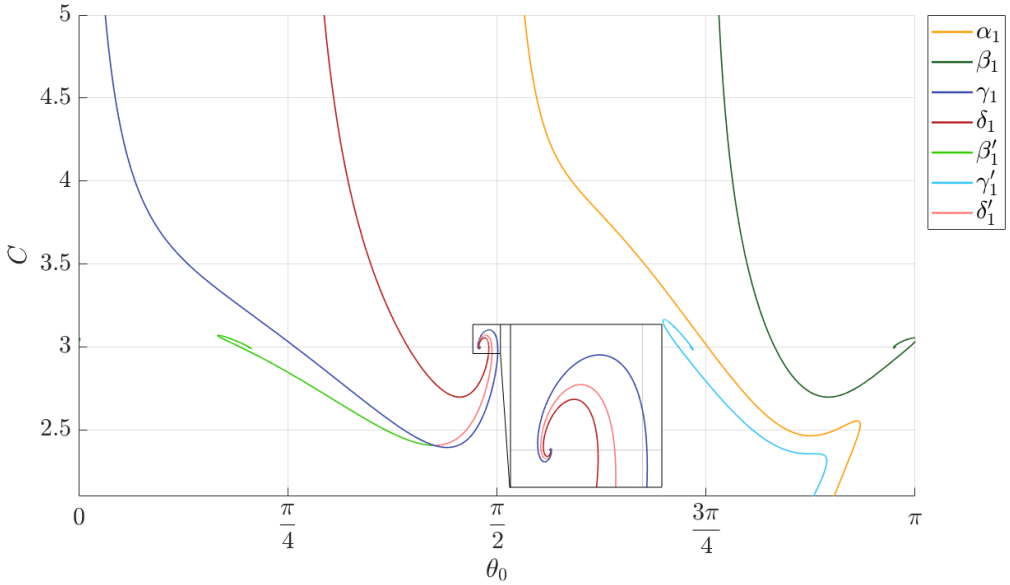

Figure 3.40: Evolution of the initial condition of the four original 1-EC orbits for $\mu = 0.7$.

The phenomenon is quite similar to the one previously described with γ_1 and γ_1', but this time it occurs thanks to two new connections from L_4 to collision in the case of the families δ_1 and δ_1' or by the symmetry the appearance of two new connections from ejection to L_5 for the case of the families β_1 and β_1'.

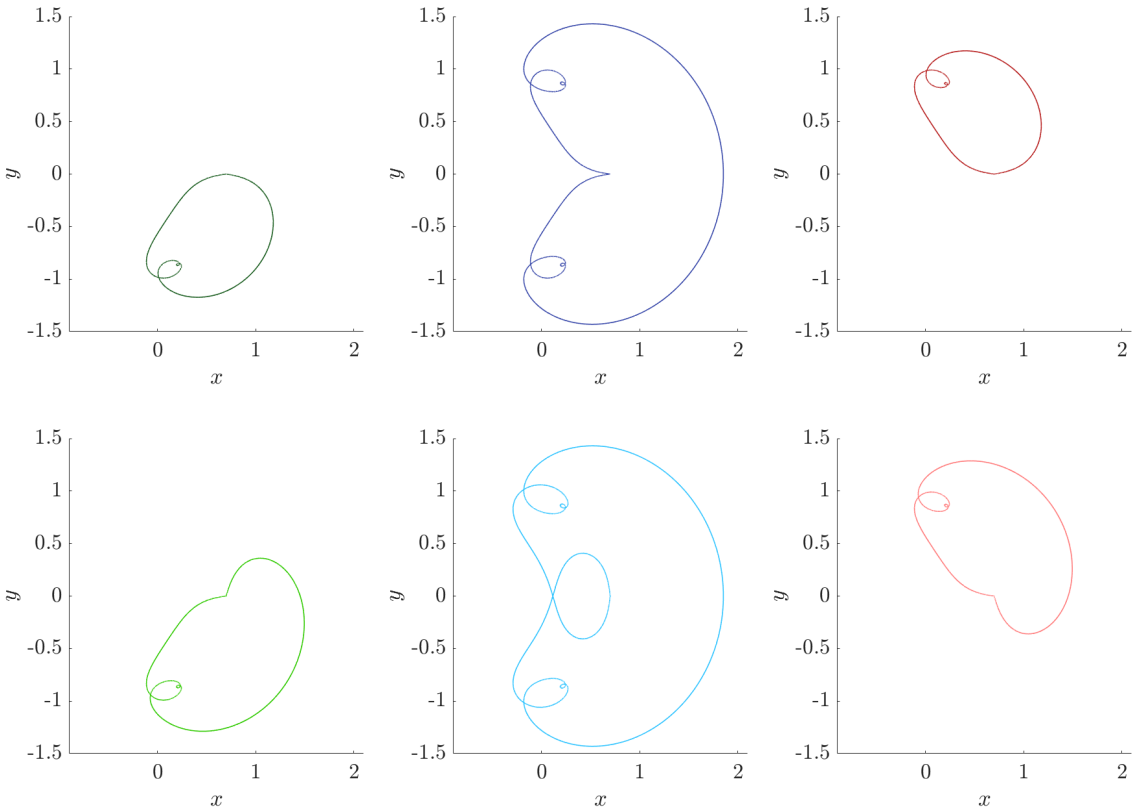

Figure 3.41: Limit orbits for the families β_1, γ_1, δ_1, β_1', γ_1' and δ_1' (from left to right and top to bottom) for $\mu = 0.7$.

For this same reason, we can observe (see Figure 3.39 or more clearly Figure 3.40) how the initial condition of the EC orbits over which the families δ_1 and δ_1' spiral is the same, since these orbits follow the same connection from ejection to L_4 that γ_1 and they return from L_4 to collision using two different connections, and instead (due to symmetry) β_1 and β_1' reach L_5 using two different connections but they return following the same connection which uses the γ_1 family to go from L_5 to collision (see Figure 3.41).

This can be seen more clearly by comparing Figure 3.41 with Figure 3.42 where we plot in color all the connections involving ejection/collision, L_4 and/or L_5 which appear in the evolution of the four original families of 1-EC orbits. In particular, the limit orbits of δ_1 and δ_1' eject from the first primary and reach L_4 using the darker blue connection of Figure 3.42 but return from L_4 to collision following the pink and the red connections respectively. By the symmetry the limit orbits of β_1 and β_1' eject from the first primary to L_5 following the orange and yellow connections respectively and return following the darker green connection from L_5 to collision.

In this way, we can continue to claim that the β_1' and δ_1' families, which are the natural continuations of the β_1 and δ_1 families, collapse into γ_1.

To conclude, as we explained at the beginning, the objective of this subsection was not to analyze

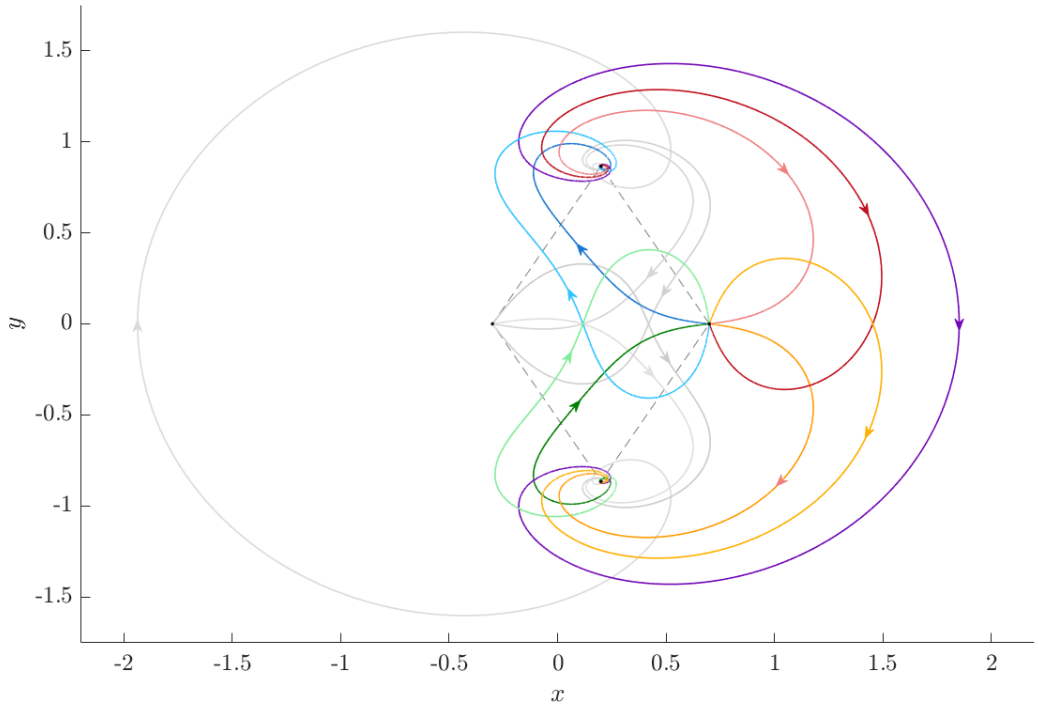

Figure 3.42: In color the connections between ejection/collision, L_4 and/or L_5 that play a role in the evolution of the original four families of 1-EC orbits for $C = 3$ and $\mu = 0.7$. In grey the connections that play a role for the original four families of 1-EC orbits of the second primary (case $\mu = 0.3$).

in detail the evolution of the n-EC orbits, but to show, on the one hand, the limitation of the above definition when considering values of C small and on the other to illustrate the great richness that appears in the dynamics. It is important to note that we have only focused on the four original families of n-EC orbits to do so, but the amount of new EC orbits and interactions with different invariant objects that appear if we consider small C values is practically impossible to study globally.

In particular, we will dedicate Chapter 6 to study the interaction of the EC orbits with a very specific invariant object, the Lyapunov periodic orbits associated with the point L_1. As we will see, despite limiting this study to values of $C \geq C_{L_{2,3}}$, the dynamics that appears is extremely rich.

Chapter 4

Analytical existence of 4 n-EC orbits I

The objective of this chapter will be to obtain a first analytical result on the existence of four n-EC orbits. The first idea would be to try to generalize for all $n \geq 1$ the previously known results (in particular the results of Theorem 1) about the existence of four 1-EC orbits, but the problem is that the techniques to obtain all of them end up using the McGehee regularization and a similar strategy: calculate the intersection between the manifold of the ejection orbits and the manifold of the collision orbits (which would correspond to the strategy of calculating $D_1^+ \cap D_1^-$ previously introduced in 3.2). This presents a clear problem when $n > 1$, since the curves D_k^+ (or similarly D_k^-) are not continuous for $k > 1$ if we work with the McGehee regularized system because there are previous collisions (that is, the collisions corresponding to the j-EC orbits, with $j = 1, ..., k-1$).

For this reason we should avoid using McGehee regularization but it is interesting to review the ideas used previously.

On the one hand, the first analytical result regarding the existence of 1-EC orbits is the one that can be found in [LL88] where the authors, based on McGehee's regularized system, show that there are at least two 1-EC orbits for sufficiently small values of μ and for all values of $C > C_{L_1}$. Naturally, to show this result the authors use an expansion in terms of μ.

On the other hand, as we said before, in [CL88], the authors prove that given any $\mu \in (0, 1)$ there are four 1-EC orbits for values of C large enough. The proof of this theorem is simple and elegant since it is based on performing a Levi-Civita regularization following Conley's ideas [Con63]. Once this change is made, the authors use a blow-up of the collision following McGehee's ideas and observe the existence of these four 1-EC orbits for values of C large enough.

In this chapter, as in [LL88], we will work with the solution expressed as a power series of μ but in our case we will use Levi-Civita regularization. It is true that the regularized system of Levi-Civita (2.26) has a less compact expression than that of McGehee (2.5), but it has the clear advantage that the ejection/collision occur in finite time and we avoid the problem of the previous collisions.

In this way, by setting any value of n, and C large enough, we will be able to find a value of μ sufficiently small for which there are exactly four n-EC orbits.

We note that the contents of this chapter have been published in [ORS20a].

4.1 Main Theorem

In order to find the number of n-EC orbits we can follow basically two strategies that correspond to the two first methods introduced in Chapter 3. The first option (Method I) is to compute the closed curves D_i^+ and D_j^-, with $n = i + j - 1$. By Lemma 1 (in Chapter 3) the number of intersections in the Levi-Civita system between D_i^+ and D_j^- corresponds to twice the number of n-EC orbits. The second option is to compute the angular momentum M_{LC} (3.12) at the n-th intersection with Σ_m, defined as $\Sigma_m = \{h(u, v, u', v') = uu' + vv' = 0,\ h' > 0\}$, i.e. we need to compute the angular momentum at the n-th minimum distance with the primary.

In this chapter we will use this second method in order to prove the theorem but the alternative proof, following the other method, can be found in [ORS20a].

The existence, the number and the characteristics of the n-ejection-collision orbits for small enough values of the mass parameter and for sufficiently restricted Hill regions can be summarized in the following theorem.

Theorem 2. *For C big enough and for all $n \in \mathbb{N}$ there exists a $\hat{\mu}(C, n)$ such that for $\mu \leq \hat{\mu}(C, n)$ there exist exactly four n-EC orbits, which can be characterized by:*

- *Two n-EC orbits both symmetric with respect to the x axis.*
- *Two n-EC orbits symmetric to each other with respect to the x axis.*

The respective families (when varying C) are labelled by α_n, γ_n, β_n and δ_n.

The proof of Theorem 2 is based on a perturbative approach. First of all, we note that we can rewrite the equations of motion (2.26) as

$$\begin{aligned}\begin{pmatrix} u \\ v \\ u' \\ v' \end{pmatrix}' &= \begin{pmatrix} u' \\ v' \\ 8(u^2+v^2)v' + 12(u^2+v^2)^2 u - 4Cu \\ -8(u^2+v^2)u' + 12(u^2+v^2)^2 v - 4Cv \end{pmatrix} + \mu \begin{pmatrix} 0 \\ 0 \\ 4u + 16u^3 + \dfrac{8u}{r_2} - \dfrac{8u(u^2+v^2)(u^2+v^2+1)}{r_2^3} \\ 4v - 16v^3 + \dfrac{8v}{r_2} - \dfrac{8v(u^2+v^2)(u^2+v^2-1)}{r_2^3} \end{pmatrix} \\ &= \boldsymbol{F}_0(u, v, u', v') + \mu \boldsymbol{F}_1(u, v).\end{aligned} \tag{4.1}$$

We look for n-EC orbits expressed as a series expansion in μ:

$$\boldsymbol{u} = \boldsymbol{u}_0 + \mu \boldsymbol{u}_1 + \mathcal{O}(\mu^2),$$

where $\boldsymbol{u} = \boldsymbol{u}(s)$, $\boldsymbol{u}_0 = \boldsymbol{u}_0(s)$ and $\boldsymbol{u}_1 = \boldsymbol{u}_1(s)$. Developing with respect to μ we have:

$$\begin{aligned}\boldsymbol{u}' = \left(\boldsymbol{u}_0 + \mu \boldsymbol{u}_1 + \mathcal{O}(\mu^2)\right)' &= \boldsymbol{F}_0\left(\boldsymbol{u}_0 + \mu \boldsymbol{u}_1 + \mathcal{O}(\mu^2)\right) + \mu \boldsymbol{F}_1\left(\boldsymbol{u}_0 + \mathcal{O}(\mu)\right) \\ &= \boldsymbol{F}_0(\boldsymbol{u}_0) + \mu D\boldsymbol{F}_0(\boldsymbol{u}_0)\boldsymbol{u}_1 + \mu \boldsymbol{F}_1(\boldsymbol{u}_0) + \mathcal{O}(\mu^2).\end{aligned} \tag{4.2}$$

Therefore, $\boldsymbol{u}_0$ and $\boldsymbol{u}_1$ must satisfy

$$\boldsymbol{u}_0' = \boldsymbol{F}_0(\boldsymbol{u}_0), \tag{4.3}$$

$$\boldsymbol{u}_1' = D\boldsymbol{F}_0(\boldsymbol{u}_0)\boldsymbol{u}_1 + \boldsymbol{F}_1(\boldsymbol{u}_0), \tag{4.4}$$

that is, $\boldsymbol{u}_0$ is a solution of the 2-body problem in Levi-Civita rotating coordinates with $\mu = 0$ and $\boldsymbol{u}_1(s)$ is obtained as

$$\boldsymbol{u}_1(s) = X(s)\boldsymbol{u}_{1,0} + X(s)\int_0^s X^{-1}(s)\boldsymbol{F}_1(\boldsymbol{u}_0(s))\, ds, \tag{4.5}$$

where $X(s) := \dfrac{\partial \boldsymbol{u}_0}{\partial \boldsymbol{u}_{0,0}}(s)$ is a matrix and $\dfrac{\partial}{\partial \boldsymbol{u}_{0,0}} = \left(\dfrac{\partial}{\partial u_{0,0}}, \dfrac{\partial}{\partial v_{0,0}}, \dfrac{\partial}{\partial u'_{0,0}}, \dfrac{\partial}{\partial v'_{0,0}}\right)$, being $\boldsymbol{u}_{0,0} = \boldsymbol{u}_0(0)$ and $\boldsymbol{u}_{1,0} = \boldsymbol{u}_1(0)$ the initial conditions.

Regarding the initial conditions, an ejection orbit will satisfy $(u(0), v(0)) = (0, 0)$, and due to (2.29) the velocity is a vector with norm $2\sqrt{2(1-\mu)}$ and an initial angle $\theta_0 \in [0, 2\pi)$ such that

$$\begin{aligned} \boldsymbol{u}(0) &= (0, 0, 2\sqrt{2(1-\mu)}\cos\theta_0, 2\sqrt{2(1-\mu)}\sin\theta_0) \\ &= \boldsymbol{u}_0(0) + \mu\boldsymbol{u}_1(0) + \mathcal{O}(\mu^2) = \boldsymbol{u}_{0,0} + \mu\boldsymbol{u}_{1,0} + \mathcal{O}(\mu^2), \end{aligned} \tag{4.6}$$

with

$$\boldsymbol{u}_{0,0} = (0, 0, 2\sqrt{2}\cos\theta_0, 2\sqrt{2}\sin\theta_0), \qquad \boldsymbol{u}_{1,0} = (0, 0, -\sqrt{2}\cos\theta_0, -\sqrt{2}\sin\theta_0). \tag{4.7}$$

The next step consists on computing the n-th minimum in the distance to the primary (located at the origin) the particle ejected from. This requires to compute the precise time denoted by s^*, needed to reach the n-th intersection with Σ_m. We will compute this time as an expansion series in μ, as a function of the initial angle θ_0 i.e.:

$$s^*(\theta_0) = s_0^*(\theta_0) + \mu s_1^*(\theta_0) + \mathcal{O}(\mu^2). \tag{4.8}$$

The last step will be to express the angular momentum at the n-th intersection with Σ_m as

$$\begin{aligned} M_n(\theta_0) &= \big(uv' - vu'\big)(s^*) \\ &= \Big(u_0(s_0^* + \mu s_1^*) + \mu u_1(s_0^*)\Big)\Big(v_0'(s_0^* + \mu s_1^*) + \mu v_1'(s_0^*)\Big) \\ &\quad - \Big(v_0(s_0^* + \mu s_1^*) + \mu v_1(s_0^*)\Big)\Big(u_0'(s_0^* + \mu s_1^*) + \mu u_1'(s_0^*)\Big) + \mathcal{O}(\mu^2) \\ &= \big(u_0v_0' - v_0u_0'\big)(s_0^*) + \mu\Big[s_1^*\big(u_0v_0'' - v_0u_0''\big)(s_0^*) + \big(u_0v_1' + u_1v_0' - v_0u_1' - v_1u_0'\big)(s_0^*)\Big] \\ &\quad + \mathcal{O}(\mu^2). \end{aligned} \tag{4.9}$$

For our purpose, let us introduce the following Lemma:

Lemma 3. *Assume C large enough and μ sufficiently small. An ejection orbit is an EC orbit if and only if the ejection orbit satisfies that at a minimum in the distance (with the primary) the angular momentum $M = uv' - vu' = 0$.*

Proof. The minimum distance condition (i.e. the intersection with Σ_m) is given by:

$$\begin{aligned} &uu' + vv' = 0, \\ &uu'' + u'^2 + vv'' + v'^2 > 0, \end{aligned} \tag{4.10}$$

and the angular momentum condition $M = uv' - vu' = 0$:

$$uv' = vu'. \tag{4.11}$$

We will distinguish between two cases:

1. $v' \neq 0$. Then, from (4.11):

$$u = \frac{vu'}{v'} \text{ and by (4.10) } \Longrightarrow \frac{vu'}{v'}u' + vv' = 0 \Longrightarrow vu'^2 + vv'^2 = v(u'^2 + v'^2) = 0 \Longrightarrow v = 0,$$

and, by (4.11) also $u = 0$.

2. $v' = 0$, we will have two subcases:
   (a) if $u' \neq 0$, then by (4.10) and (4.11) we get $u = v = 0$.
   (b) $u' = 0$ then, using equations (4.1):

$$uu'' + vv'' = -4C(u^2 + v^2) + 12(u^2 + v^2)^3 + \mathcal{O}(\mu).$$

Therefore, if μ is small enough we only need to compute $-4C(u^2 + v^2) + 12(u^2 + v^2)^3$. If C is large enough, we can bound easily $u^2 + v^2 < 1$, therefore

$$C > 3(u^2 + v^2)^2,$$

which contradicts the second item of (4.10). We conclude that $u = v = 0$.

On the other hand, it is clear that if a collision takes place, i. e. $u = v = 0$ and $u'^2 + v'^2 = 8(1 - \mu)$, then conditions (4.10) and (4.11) are trivially satisfied. □

Remark 4. *Note that the condition μ small enough is not necessary as we will see in Lemma 7 in Chapter 5.*

Recall that the goal is to compute the angular momentum at the n-th crossing with Σ_m, i.e. obtain (4.9), in order to find the zeros of this quantity. In this way, the first step is to solve the problem for the case $\mu = 0$ and then add the perturbation.

4.2 The non-perturbed case

In order to find an explicit expression for the solution $\boldsymbol{u}_0(s)$ of the non perturbed system ($\mu = 0$) (that is the 2-body problem) in rotating Levi-Civita (LC) coordinates, we will consider previously the problem in sidereal (non-rotating) coordinates, since it is simpler to solve and will be useful to obtain the first order of the perturbed solution $\boldsymbol{u}_1(s)$.

4.2.1 2-body problem in Levi-Civita sideral coordinates

It is well known that the problem of two bodies (P_1 and P), where (X, Y) is the position of P in sidereal coordinates is described by the system of ODE

$$\begin{cases} \dfrac{d^2X}{dt^2} = -\dfrac{X}{R^3}, \\ \dfrac{d^2Y}{dt^2} = -\dfrac{Y}{R^3}, \end{cases} \tag{4.12}$$

where $R = \sqrt{X^2 + Y^2}$ and with a singularity at the origin (collision) $(X, Y) = (0, 0)$. The Levi-Civita transformation to new coordinates $(\hat{u}_0, \hat{v}_0)$ and new time s defined by

$$\begin{cases} X = \hat{u}_0^2 - \hat{v}_0^2, \\ Y = 2\hat{u}_0\hat{v}_0, \\ \dfrac{dt}{ds} = 4\left(\hat{u}_0^2 + \hat{v}_0^2\right), \end{cases} \tag{4.13}$$

regularizes the ODE giving rise to the new system (see [Sze67] for details)

$$\begin{cases} \hat{u}_0'' = -4K\hat{u}_0, \\ \hat{v}_0'' = -4K\hat{v}_0, \end{cases} \tag{4.14}$$

where $' = d/ds$, $K = -2E$ and E is the energy integral. Taking into account the relationship between E and the Jacobi constant C and the angular momentum M, $E = -C/2 + M$ and the fact that $M = X\dot{Y} - Y\dot{X}$ becomes $M = (\hat{u}_0\hat{v}_0' - \hat{v}_0\hat{u}_0')/2$, the previous system becomes

$$\begin{cases} \hat{u}_0'' = -4(C - \hat{u}_0\hat{v}_0' + \hat{v}_0\hat{u}_0')\hat{u}_0, \\ \hat{v}_0'' = -4(C - \hat{u}_0\hat{v}_0' + \hat{v}_0\hat{u}_0')\hat{v}_0. \end{cases} \tag{4.15}$$

As it is well known the system (4.15) preserves the angular momentum, so we have:

Lemma 4. *The quantity $-\hat{u}_0\hat{v}_0' + \hat{v}_0\hat{u}_0'$ is constant along the trajectories*

Proof. Simply by deriving and replacing the values of $\hat{u}_0''$ and $\hat{v}_0''$ we have:

$$\frac{d}{ds}\big(-\hat{u}_0\hat{v}_0' + \hat{v}_0\hat{u}_0'\big) = -\hat{u}_0\hat{v}_0'' + \hat{v}_0\hat{u}_0'' = 4(C - \hat{u}_0\hat{v}_0' + \hat{v}_0\hat{u}_0')\hat{u}_0\hat{v}_0 - 4(C - \hat{u}_0\hat{v}_0' + \hat{v}_0\hat{u}_0')\hat{u}_0\hat{v}_0 = 0.$$

□

Keeping that in mind, the solution of (4.15) with initial conditions $\hat{\boldsymbol{u}}_0(0) = \hat{\boldsymbol{u}}_{0,0}$ is given by:

$$\begin{cases} \hat{u}_0(s) = \hat{u}_{0,0}\cos(2\sqrt{K}s) + \dfrac{\hat{u}_{0,0}'}{2\sqrt{K}}\sin(2\sqrt{K}s), \\ \hat{v}_0(s) = \hat{v}_{0,0}\cos(2\sqrt{K}s) + \dfrac{\hat{v}_{0,0}'}{2\sqrt{K}}\sin(2\sqrt{K}s), \end{cases} \tag{4.16}$$

where $K = C - \hat{u}_{0,0}\hat{v}_{0,0}' + \hat{v}_{0,0}\hat{u}_{0,0}'$ and has derivatives:

$$\begin{cases} \hat{u}_0'(s) = -2\sqrt{K}\hat{u}_{0,0}\sin(2\sqrt{K}s) + \hat{u}_{0,0}'\cos(2\sqrt{K}s), \\ \hat{v}_0'(s) = -2\sqrt{K}\hat{v}_{0,0}\sin(2\sqrt{K}s) + \hat{v}_{0,0}'\cos(2\sqrt{K}s). \end{cases} \tag{4.17}$$

We are interested in ejection orbits, which have initial conditions $(0, 0, 2\sqrt{2}\cos\theta_0, 2\sqrt{2}\sin\theta_0)$, with $\theta_0 \in [0, 2\pi)$, i.e.

$$\begin{cases} \hat{u}_0(s) = \dfrac{\sqrt{2}\cos\theta_0}{\sqrt{C}}\sin(2\sqrt{C}s), \\ \hat{v}_0(s) = \dfrac{\sqrt{2}\sin\theta_0}{\sqrt{C}}\sin(2\sqrt{C}s). \end{cases} \tag{4.18}$$

With this equation it is immediate to see the value of s_0^* because the minimum distance does not vary with or without rotation:

$$s_0^* = \frac{n\pi}{2\sqrt{C}}. \tag{4.19}$$

Remark 5. *Note that the value of s_0^* is independent of θ_0.*

In this way, it is easy to see that for the ejection orbits we have

$$\hat{\boldsymbol{u}}_0(s_0^*) = 2\sqrt{2}(-1)^n(0, 0, \cos\theta_0, \sin\theta_0). \tag{4.20}$$

For our purpose, it is necessary to study the system in synodical coordinates with the aim of analyzing the consequences of the rotation and because we will also need the 2-body solution in the synodical coordinates to calculate the first order solution $\boldsymbol{u}_1$.

4.2.2 2-body problem in Levi-Civita synodical coordinates

In order to have the solution $\boldsymbol{u}_0(s)$ in Levi-Civita rotating frame, we simply apply the rotation transformation to the solution (4.16) in Levi-Civita sidereal coordinates. This is shown in the following lemma.

Lemma 5. *The solution of* (4.3) *is given by*

$$\begin{aligned}
u_0(s) &= \hat{u}_0\cos(-t/2) - \hat{v}_0\sin(-t/2),\\
v_0(s) &= \hat{u}_0\sin(-t/2) + \hat{v}_0\cos(-t/2),\\
u_0'(s) &= \Big(\hat{u}_0' + 2(\hat{u}_0^2+\hat{v}_0^2)\hat{v}_0\Big)\cos(-t/2) - \Big(\hat{v}_0' - 2(\hat{u}_0^2+\hat{v}_0^2)\hat{u}_0\Big)\sin(-t/2),\\
v_0'(s) &= \Big(\hat{u}_0' + 2(\hat{u}_0^2+\hat{v}_0^2)\hat{v}_0\Big)\sin(-t/2) + \Big(\hat{v}_0' - 2(\hat{u}_0^2+\hat{v}_0^2)\hat{u}_0\Big)\cos(-t/2),
\end{aligned} \tag{4.21}$$

where $\hat{u}_0$, $\hat{v}_0$, $\hat{u}_0'$, $\hat{v}_0'$ *and* t *stand for* $\hat{u}_0(s)$, $\hat{v}_0(s)$, $\hat{u}_0'(s)$, $\hat{v}_0'(s)$ *and* $t(s)$, *and* t *satisfies* (4.13).

Proof. We simply make use of the change of variables (using complex notation)

- $W = \hat{u} + i\hat{v} \longmapsto Z = X + iY$ by $Z = W^2$, where (X, Y) are the cartesian sidereal variables.
- $Z \longmapsto z = x+iy$ by $z = e^{-it}Z$, i.e. the rotation to transform from sidereal to synodic coordinates (x, y).
- $z \longmapsto w = u + iv$ by $z = w^2$, being (u, v) the synodical Levi-Civita variables.

So the relation $w = e^{-\frac{t}{2}i}W$ for the 2-body problem can be written as

$$\begin{aligned}
u_0(s) &= \hat{u}_0\cos(-t/2) - \hat{v}_0\sin(-t/2),\\
v_0(s) &= \hat{u}_0\sin(-t/2) + \hat{v}_0\cos(-t/2).
\end{aligned} \tag{4.22}$$

On the other hand, $u_0'(s)$ and $v_0'(s)$ are obtained using $\dfrac{dt}{ds} = 4(\hat{u}_0^2 + \hat{v}_0^2)$. □

The relation between the sidereal initial conditions and the synodical ones can be obtained from the previous lemma

$$\begin{cases}
u_{0,0} = \hat{u}_{0,0},\\
v_{0,0} = \hat{v}_{0,0},\\
u_{0,0}' = \hat{u}_{0,0}' + 2(\hat{u}_{0,0}^2 + \hat{v}_{0,0}^2)\hat{v}_{0,0},\\
v_{0,0}' = \hat{v}_{0,0}' - 2(\hat{u}_{0,0}^2 + \hat{v}_{0,0}^2)\hat{u}_{0,0},
\end{cases}
\qquad
\begin{cases}
\hat{u}_{0,0} = u_{0,0},\\
\hat{v}_{0,0} = v_{0,0},\\
\hat{u}_{0,0}' = u_{0,0}' - 2(u_{0,0}^2 + v_{0,0}^2)v_{0,0},\\
\hat{v}_{0,0}' = v_{0,0}' + 2(u_{0,0}^2 + v_{0,0}^2)u_{0,0}.
\end{cases} \tag{4.23}$$

Remark 6. *In the particular case of ejection orbits, the initial conditions both in sidereal and synodical coordinates are* $\boldsymbol{u}_{0,0} = (0, 0, 2\sqrt{2}\cos\theta_0, 2\sqrt{2}\sin\theta_0)$, $\theta_0 \in [0, 2\pi)$.

Remark 7. *We also note that if we express the position of the particle with Levi-Civita sidereal variables, using polar complex notation, that is,* $W = Re^{i\theta_{sid}}$, *where* θ_{sid} *refers to the polar angle, then we have the corresponding two points in Levi-Civita synodical variables; using polar complex notation we obtain*

$$w_+ = Re^{i\left(\theta_{sid} - \frac{t}{2}\right)}, \tag{4.24a}$$

$$w_- = Re^{i\left(\theta_{sid} + \pi - \frac{t}{2}\right)}, \tag{4.24b}$$

but we can omit expression (4.24b) *due to the symmetry* (2.27a).

Now let us obtain an explicit expression for $t(s)$.

Lemma 6.

$$(a)\quad \left(u_0^2+v_0^2\right)(s)=\left(\hat{u}_{0,0}^2+\hat{v}_{0,0}^2\right)\cos^2(2\sqrt{K}s)+\frac{\hat{u}_{0,0}\hat{u}'_{0,0}+\hat{v}_{0,0}\hat{v}'_{0,0}}{\sqrt{K}}\cos(2\sqrt{K}s)\sin(2\sqrt{K}s) \tag{4.25}$$
$$+\frac{\hat{u}'^2_{0,0}+\hat{v}'^2_{0,0}}{4K}\sin^2(2\sqrt{K}s).$$

$$(b)\quad t(s)=\left(2(\hat{u}_{0,0}^2+\hat{v}_{0,0}^2)+\frac{\hat{u}'^2_{0,0}+\hat{v}'^2_{0,0}}{2K}\right)s+\left(4(\hat{u}_{0,0}^2+\hat{v}_{0,0}^2)-\frac{\hat{u}'^2_{0,0}+\hat{v}'^2_{0,0}}{K}\right)\frac{\sin(4\sqrt{K}s)}{8\sqrt{K}} \tag{4.26}$$
$$+\frac{\hat{u}_{0,0}\hat{u}'_{0,0}+\hat{v}_{0,0}\hat{v}'_{0,0}}{K}\sin^2(2\sqrt{K}s).$$

Proof. (a) It follows directly from (4.16).

(b) It follows directly from the integration

$$t(s)=\int 4(\hat{u}_0^2+\hat{u}_0^2)\,ds. \tag{4.27}$$

□

In particular, for the ejection orbits we have

$$t(s)=\frac{4}{C}s-\frac{\sin(4\sqrt{C}s)}{C^{3/2}}. \tag{4.28}$$

In this way

$$t(s_0^*)=\frac{2\pi n}{C^{3/2}}, \tag{4.29}$$

and $\boldsymbol{u}_0(s_0^*)$ is given by

$$\begin{cases} u_0(s_0^*)=0,\\ v_0(s_0^*)=0,\\ u'_0(s_0^*)=2\sqrt{2}(-1)^n\left[\cos\theta_0\cos\left(-\frac{\pi n}{C^{3/2}}\right)-\sin\theta_0\sin\left(-\frac{\pi n}{C^{3/2}}\right)\right],\\ v'_0(s_0^*)=2\sqrt{2}(-1)^n\left[\cos\theta_0\sin\left(-\frac{\pi n}{C^{3/2}}\right)+\sin\theta_0\cos\left(-\frac{\pi n}{C^{3/2}}\right)\right]. \end{cases}$$

Remark 8. *As* $u_0(s_0^*)=v_0(s_0^*)=0$ *we can express* (4.9) *simply as*

$$M_n(\theta_0)=\mu\big(u_1v'_0-v_1u'_0\big)(s_0^*)+\mathcal{O}(\mu^2). \tag{4.30}$$

4.3 The perturbed problem

By Remark 8, we need to solve equation (4.30), so we only need to compute $u_1(s_0^*)$ and $v_1(s_0^*)$.

As previously mentioned, the solution of (4.4) is given by (4.5), therefore, the first step is to compute X in a cunning way. To do so we will use the relationship between sidereal and synodic coordinates, so from (4.21) we have:

$$\begin{aligned}
\frac{\partial u_0}{\partial \boldsymbol{u}_{0,0}}(s) &= \boldsymbol{V}_1 \cos(-t/2) - \boldsymbol{V}_2 \sin(-t/2),\\
\frac{\partial v_0}{\partial \boldsymbol{u}_{0,0}}(s) &= \boldsymbol{V}_1 \sin(-t/2) + \boldsymbol{V}_2 \cos(-t/2),\\
\frac{\partial u_0'}{\partial \boldsymbol{u}_{0,0}}(s) &= \boldsymbol{V}_3 \cos(-t/2) - \boldsymbol{V}_4 \sin(-t/2),\\
\frac{\partial v_0'}{\partial \boldsymbol{u}_{0,0}}(s) &= \boldsymbol{V}_3 \sin(-t/2) + \boldsymbol{V}_4 \cos(-t/2),
\end{aligned} \tag{4.31}$$

where:

$$\begin{aligned}
\boldsymbol{V}_1 \equiv \boldsymbol{V}_1(s) &= \left[\frac{\partial \hat{u}_0}{\partial \boldsymbol{u}_{0,0}} + \frac{\hat{v}_0}{2}\frac{\partial t}{\partial \boldsymbol{u}_{0,0}}\right](s),\\
\boldsymbol{V}_2 \equiv \boldsymbol{V}_2(s) &= \left[\frac{\partial \hat{v}_0}{\partial \boldsymbol{u}_{0,0}} - \frac{\hat{u}_0}{2}\frac{dt}{\partial \boldsymbol{u}_{0,0}}\right](s),\\
\boldsymbol{V}_3 \equiv \boldsymbol{V}_3(s) &= \left[\frac{\partial \hat{u}_0'}{\partial \boldsymbol{u}_{0,0}} + 2\left(\hat{u}_0^2 + 3\hat{v}_0^2\right)\frac{\partial \hat{v}_0}{\partial \boldsymbol{u}_{0,0}} + 4\hat{u}_0\hat{v}_0\frac{\partial \hat{u}_0}{\partial \boldsymbol{u}_{0,0}} + \frac{\hat{v}_0' - 2(\hat{u}_0^2+\hat{v}_0^2)\hat{u}_0}{2}\frac{\partial t}{\partial \boldsymbol{u}_{0,0}}\right](s),\\
\boldsymbol{V}_4 \equiv \boldsymbol{V}_4(s) &= \left[\frac{\partial \hat{v}_0'}{\partial \boldsymbol{u}_{0,0}} - 2\left(3\hat{u}_0^2 + \hat{v}_0^2\right)\frac{\partial \hat{u}_0}{\partial \boldsymbol{u}_{0,0}} - 4\hat{u}_0\hat{v}_0\frac{\partial \hat{v}_0}{\partial \boldsymbol{u}_{0,0}} - \frac{\hat{u}_0' + 2(\hat{u}_0^2+\hat{v}_0^2)\hat{v}_0}{2}\frac{\partial t}{\partial \boldsymbol{u}_{0,0}}\right](s),
\end{aligned} \tag{4.32}$$

i.e.:

$$X = RV = \begin{pmatrix} \cos(-t/2) & -\sin(-t/2) & 0 & 0\\ \sin(-t/2) & \cos(-t/2) & 0 & 0\\ 0 & 0 & \cos(-t/2) & -\sin(-t/2)\\ 0 & 0 & \sin(-t/2) & \cos(-t/2) \end{pmatrix} \begin{pmatrix} \boldsymbol{V}_1\\ \boldsymbol{V}_2\\ \boldsymbol{V}_3\\ \boldsymbol{V}_4 \end{pmatrix}, \tag{4.33}$$

where V is the matrix that has rows given by $\boldsymbol{V}_i$, $i = 1, ..., 4$.

Thus, we only need to compute previously:

$$\begin{aligned}
\frac{\partial \hat{\boldsymbol{u}}_0}{\partial \boldsymbol{u}_{0,0}}(s) &= \frac{\partial \hat{\boldsymbol{u}}_0}{\partial \hat{\boldsymbol{u}}_{0,0}}(s)\frac{\partial \hat{\boldsymbol{u}}_{0,0}}{\partial \boldsymbol{u}_{0,0}},\\
\frac{\partial t}{\partial \boldsymbol{u}_{0,0}}(s) &= \frac{\partial t}{\partial \hat{\boldsymbol{u}}_{0,0}}(s)\frac{\partial \hat{\boldsymbol{u}}_{0,0}}{\partial \boldsymbol{u}_{0,0}}.
\end{aligned} \tag{4.34}$$

The computation of $\dfrac{\partial \hat{\boldsymbol{u}}_{0,0}}{\partial \boldsymbol{u}_{0,0}}$ is immediate from (4.23) and in the case of ejection orbits it is simply the identity matrix Id since we just need to substitute in this matrix the values of the initial conditions $(0, 0, 2\sqrt{2}\cos\theta_0, 2\sqrt{2}\sin\theta_0)$ for an ejection orbit,

$$\frac{\partial \hat{\boldsymbol{u}}_{0,0}}{\partial \boldsymbol{u}_{0,0}}(0,0,2\sqrt{2}\cos\theta_0, 2\sqrt{2}\sin\theta_0) = \begin{pmatrix} 1 & 0 & 0 & 0 \\ 0 & 1 & 0 & 0 \\ -4u_{0,0}v_{0,0} & -2u_{0,0}^2 - 6v_{0,0}^2 & 1 & 0 \\ 6u_{0,0}^2 + 2v_{0,0}^2 & 4u_{0,0}v_{0,0} & 0 & 1 \end{pmatrix}\Bigg|_{(0,0,2\sqrt{2}\cos\theta_0, 2\sqrt{2}\sin\theta_0)} = Id. \tag{4.35}$$

To facilitate the reading of this section, the values of $\dfrac{\partial \hat{\boldsymbol{u}}_0}{\partial \hat{\boldsymbol{u}}_{0,0}}$, $\dfrac{\partial t}{\partial \hat{\boldsymbol{u}}_{0,0}}$ and other values necessary for the computation of V can be found in the Appendix 4.A.1. Similarly, the complete expression of the matrix V and V^{-1} can be found in it.

Once the matrix V^{-1} has been calculated, we can compute the product $X^{-1}\boldsymbol{F}_1 = V^{-1}R^{-1}\boldsymbol{F}_1$ but the resulting expression to be integrated is quite unwieldy. The first step to simplify the expression is to introduce the variable $\tau = 2\sqrt{C}s$ (see Appendix 4.A.2). In this way we eliminate the terms related with C from most trigonometric expressions, except those that have a direct relationship with the rotation (i.e. with $t(s)$)

$$\begin{aligned} &\sin(2\sqrt{C}s) = \sin(\tau), \\ &\sin(-t/2) = \sin\left(-\frac{2}{C}s + \frac{\sin(4\sqrt{C}s)}{2C^{3/2}}\right) = \sin\left(\frac{1}{C^{3/2}}\frac{-2\tau + \sin(2\tau)}{2}\right), \end{aligned}$$

and similarly with the cosine terms.

Despite this change, the resulting expression cannot be integrated in finite form with elementary functions. To deal with this last expression we consider a series expansion in $1/\sqrt{C}$. This expansion can be done since

- $\dfrac{1}{2\sqrt{C}}V^{-1}$ has a closed expression: constant terms and terms of higher order in $1/\sqrt{C}$.
- R^{-1} is simply a rotation.
- $\boldsymbol{F}_1$ depends only on u and v, and the denominator r_2 is of the form $\sqrt{1+\mathcal{O}(C^{-1})}$, therefore it can be expanded.

The computation details are given in Appendix 4.A.2.

Thus, the integral in (4.5) becomes

$$\int_0^s X^{-1}(s)\boldsymbol{F}_1(\boldsymbol{u}_0(s))ds = \int_0^\tau \frac{1}{2\sqrt{C}}X^{-1}\left(\frac{\tau}{2\sqrt{C}}\right)\boldsymbol{F}_1\left(\boldsymbol{u}_0\left(\frac{\tau}{2\sqrt{C}}\right)\right)d\tau. \tag{4.36}$$

The expressions obtained after these considerations (simplifying the notation) are as follows, where $\left(X^{-1}\boldsymbol{F}_1\right)_i$ is the i-th component of $X^{-1}\boldsymbol{F}_1$

$$
\begin{aligned}
\frac{1}{2\sqrt{C}}\left(X^{-1}\boldsymbol{F}_1\right)_1 =& -\frac{3\sqrt{2}\cos\theta_0\sin^2\tau}{C^{3/2}} - \frac{24\sqrt{2}\cos\theta_0\left(2\cos^4\theta_0-1\right)\sin^6\tau}{C^{7/2}} + \mathcal{O}(C^{-9/2}),\\
\frac{1}{2\sqrt{C}}\left(X^{-1}\boldsymbol{F}_1\right)_2 =& -\frac{3\sqrt{2}\sin\theta_0\sin^2\tau}{C^{3/2}} - \frac{24\sqrt{2}\sin\theta_0\left(2\sin^4\theta_0-1\right)\sin^6\tau}{C^{7/2}} + \mathcal{O}(C^{-9/2}),\\
\frac{1}{2\sqrt{C}}\left(X^{-1}\boldsymbol{F}_1\right)_3 =& \frac{6\sqrt{2}\cos\theta_0\cos\tau\sin\tau}{C} + \frac{12\sqrt{2}\sin\theta_0\sin\tau\left(\sin\tau-\tau\cos\tau\right)}{C^{5/2}}\\
&+ \frac{48\sqrt{2}\cos\theta_0\left(2\cos^4\theta_0-1\right)\cos\tau\sin^5\tau}{C^3}\\
&- \frac{128\sqrt{2}\sin^7\tau\cos\tau\cos\theta_0(5\cos^6\theta_0-6\cos^2\theta_0+2)}{C^4} + \mathcal{O}(C^{-9/2}),\\
\frac{1}{2\sqrt{C}}\left(X^{-1}\boldsymbol{F}_1\right)_4 =& \frac{6\sqrt{2}\sin\theta_0\cos\tau\sin\tau}{C} - \frac{12\sqrt{2}\cos\theta_0\sin\tau\left(\sin\tau-\tau\cos\tau\right)}{C^{5/2}}\\
&+ \frac{48\sqrt{2}\sin\theta_0\left(2\sin^4\theta_0-1\right)\cos\tau\sin^5\tau}{C^3}\\
&- \frac{128\sqrt{2}\sin^7\tau\cos\tau\sin\theta_0(5\sin^6\theta_0-6\sin^2\theta_0+2)}{C^4} + \mathcal{O}(C^{-9/2})
\end{aligned}
\tag{4.37}
$$

Integrating these results with respect to s on the interval $[0, s_0^*]$ or $[0, \pi n]$ with respect to τ (see Appendix 4.A.2) and using (4.43) we obtain the following expressions for $u_1(s_0^*)$ and $v_1(s_0^*)$

$$
\begin{aligned}
u^1(s_0^*) =& -\frac{(-1)^n 3\sqrt{2}\pi n\cos\theta_0}{2C^{3/2}} - \frac{(-1)^n 3\sqrt{2}\pi^2 n^2\sin\theta_0}{2C^3}\\
&+ \frac{(-1)^n 15\sqrt{2}\pi n(1-2\cos^4\theta_0)\cos\theta_0}{2C^{7/2}} + \mathcal{O}(C^{-9/2}),\\
v^1(s_0^*) =& -\frac{(-1)^n 3\sqrt{2}\pi n\sin\theta_0}{2C^{3/2}} + \frac{(-1)^n 3\sqrt{2}\pi^2 n^2\cos\theta_0}{2C^3}\\
&+ \frac{(-1)^n 15\sqrt{2}\pi n(1-2\sin^4\theta_0)\sin\theta_0}{2C^{7/2}} + \mathcal{O}(C^{-9/2}).
\end{aligned}
\tag{4.38}
$$

Finally, from (4.30) we have

$$
M_n(\theta_0) = \frac{-15\mu n\pi\sin(4\theta_0)}{C^{7/2}} + \mu\mathcal{O}(C^{-9/2}) + \mathcal{O}(\mu^2). \tag{4.39}
$$

Since we look for the zeros of $M_n(\theta_0)$, we write dividing the previous equation by $\mu C^{-7/2}$,

$$
\bar{M}_n(\theta_0) = -15n\pi\sin(4\theta_0) + \mathcal{O}(C^{-1}) + \mathcal{O}(C^{7/2}\mu). \tag{4.40}
$$

Now we apply the Implicit Function Theorem and for C large enough and exists a μ small enough such that the equation (4.40) has four and only four roots in $[0, \pi)$ given by

$$
\theta_0 = \frac{\pi m}{4} + \mathcal{O}(C^{-1}, \mu C^{7/2}). \tag{4.41}
$$

It is clear from (4.40) that the roots θ_0 are simple, therefore we have proved that there exist exactly four n-EC orbits.

Finally, applying the symmetries (2.27) of the problem we can conclude that those n-EC orbits with an intersection angle with $m = 0, 2$ correspond to symmetric n-EC orbits (in the sense that the (x, y)

projection is symmetric with respect to the x axis). Those n-EC orbits with an intersection angle with $m = 1, 3$ correspond to orbits that are symmetric one from the other n-EC orbits (in the sense that the (x, y) projection of one orbit is symmetric with respect to the other one with respect to the x axis).

This finishes the proof of Theorem 2.

Remark 9. *As we have mentioned at the beginning of this chapter, instead of considering the method of the angular momentum, we can consider the strategy of the intersection of the curves D_j^+ and D_i^- with $i + j = n + 1$ in order to prove that there exist exactly four n-EC orbits. The proof is again based on a perturbative approach in μ and the detailed explanation can be found in [ORS20a].*

Recall that for C given, D_i^+ and D_j^- are curves in $\mathbb{R}^4$. However, since by definition they are obtained as curves in Σ_M, we can consider only their projection in the (u, v) configuration space. Note that we do not need to compute D_k^-, it can be obtained directly from D_k^+ via the symmetry (2.27).

The idea at this point is to express these curves in polar coordinates, so we will write, abusing notation, $D_i^+ = (R_i^+, \theta_i)$. In particular, we can express the polar coordinates as a function of the ejection angle θ_0, i.e. $(R_i^+(\theta_0), \theta_i(\theta_0))$. Nevertheless, in order to compute the intersection of $(R_i^+(\theta_0), \theta_i(\theta_0))$ and $(R_j^-(\theta_0), \theta_j(\theta_0))$ we need to express R_i^+ and R_j^- as a function of the same angle. This implies that we need to reach a higher order in the expansion in terms of $C^{-1/2}$ than if we use the angular momentum technique, since the rotational velocity of the system is of order $C^{-3/2}$. Besides, the expressions needed to compute R_k^+ (i.e. the value of u and v at the k-th intersection with Σ_M) are much more complicated than the necessary expressions for the angular momentum.

For these reasons, the strategy of the angular momentum is more convenient.

4.A Appendix

4.A.1 Computation of V and V^{-1}

This subsection shows the computations needed to obtain V and V^{-1}. According to (4.32) we need to compute $\dfrac{\partial \hat{\boldsymbol{u}}_0}{\partial \boldsymbol{u}_{0,0}}$ and $\dfrac{\partial t}{\partial \boldsymbol{u}_{0,0}}$, which are expressions that depend on s and the initial values $\boldsymbol{u}_{0,0}$. Due to (4.34) and (4.35) it suffices to compute $\dfrac{\partial \hat{\boldsymbol{u}}_0}{\partial \hat{\boldsymbol{u}}_{0,0}}$ and $\dfrac{\partial t}{\partial \hat{\boldsymbol{u}}_{0,0}}$. All these derivatives are evaluated on ejection orbits, i.e. with initial conditions $\hat{\boldsymbol{u}}_{0,0} = \boldsymbol{u}_{0,0} = (0, 0, 2\sqrt{2}\cos\theta_0, 2\sqrt{2}\sin\theta_0)$, and they will be denoted with the subscript e after a vertical bar or a square bracket. These expressions are functions of s, θ_0 and C.

Computation of $\left.\dfrac{\partial \hat{\boldsymbol{u}}_0}{\partial \hat{\boldsymbol{u}}_{0,0}}\right|_e$ and $\left.\dfrac{\partial t}{\partial \hat{\boldsymbol{u}}_{0,0}}\right|_e$

- $\left.\dfrac{\partial \hat{u}_0}{\partial \hat{u}_{0,0}}\right|_e = \left[1 - \dfrac{4\cos\theta_0 \sin\theta_0}{C} s\right] \cos\left(2\sqrt{C}s\right) + \dfrac{2\cos\theta_0 \sin\theta_0}{C^{3/2}} \sin\left(2\sqrt{C}s\right)$

- $\left.\dfrac{\partial \hat{u}_0}{\partial \hat{v}_{0,0}}\right|_e = \dfrac{4\cos^2\theta_0}{C} s \cos\left(2\sqrt{C}s\right) - \dfrac{2\cos^2\theta_0}{C^{3/2}} \sin\left(2\sqrt{C}s\right)$

- $\left.\frac{\partial \hat{u}_0}{\partial \hat{u}'_{0,0}}\right|_e = \frac{1}{2\sqrt{C}}\sin\left(2\sqrt{C}s\right)$
- $\left.\frac{\partial \hat{u}_0}{\partial \hat{v}'_{0,0}}\right|_e = 0$
- $\left.\frac{\partial \hat{v}_0}{\partial \hat{u}_{0,0}}\right|_e = -\frac{4\sin^2\theta_0}{C}s\cos\left(2\sqrt{C}s\right) + \frac{2\sin^2\theta_0}{C^{3/2}}\sin\left(2\sqrt{C}s\right)$
- $\left.\frac{\partial \hat{v}_0}{\partial \hat{v}_{0,0}}\right|_e = \left[1 + \frac{4\cos\theta_0\sin\theta_0}{C}s\right]\cos\left(2\sqrt{C}s\right) - \frac{2\cos\theta_0\sin\theta_0}{C^{3/2}}\sin\left(2\sqrt{C}s\right)$
- $\left.\frac{\partial \hat{v}_0}{\partial \hat{u}'_{0,0}}\right|_e = 0$
- $\left.\frac{\partial \hat{v}_0}{\partial \hat{v}'_{0,0}}\right|_e = \frac{1}{2\sqrt{C}}\sin\left(2\sqrt{C}s\right)$
- $\left.\frac{\partial \hat{u}'_0}{\partial \hat{u}_{0,0}}\right|_e = \left[-2\sqrt{C} + \frac{8\cos\theta_0\sin\theta_0}{\sqrt{C}}s\right]\sin\left(2\sqrt{C}s\right)$
- $\left.\frac{\partial \hat{u}'_0}{\partial \hat{v}_{0,0}}\right|_e = -\frac{8\cos^2\theta_0}{\sqrt{C}}s\sin\left(2\sqrt{C}s\right)$
- $\left.\frac{\partial \hat{u}'_0}{\partial \hat{u}'_{0,0}}\right|_e = \cos\left(2\sqrt{C}s\right)$
- $\left.\frac{\partial \hat{u}'_0}{\partial \hat{v}'_{0,0}}\right|_e = 0$
- $\left.\frac{\partial \hat{v}'_0}{\partial \hat{u}_{0,0}}\right|_e = \frac{8\sin^2\theta_0}{\sqrt{C}}s\sin\left(2\sqrt{C}s\right)$
- $\left.\frac{\partial \hat{v}'_0}{d\hat{v}_{0,0}}\right|_e = -\left[2\sqrt{C} + \frac{8\cos\theta_0\sin\theta_0}{\sqrt{C}}s\right]\sin\left(2\sqrt{C}s\right)$
- $\left.\frac{\partial \hat{v}'_0}{\partial \hat{u}'_{0,0}}\right|_e = 0$
- $\left.\frac{\partial \hat{v}'_0}{\partial \hat{v}'_{0,0}}\right|_e = \cos\left(2\sqrt{C}s\right)$
- $\left.\frac{\partial t}{\partial \hat{u}_{0,0}}\right|_e = \frac{4\sqrt{2}\sin\theta_0}{C^2}\left[2 + \cos\left(4\sqrt{C}s\right)\right]s - \frac{3\sqrt{2}\sin\theta_0}{C^{5/2}}\sin\left(4\sqrt{C}s\right) + \frac{2\sqrt{2}\cos\theta_0}{C}\sin^2\left(2\sqrt{C}s\right)$
- $\left.\frac{\partial t}{\partial \hat{v}_{0,0}}\right|_e = -\frac{4\sqrt{2}\cos\theta_0}{C^2}\left[2 + \cos\left(4\sqrt{C}s\right)\right]s + \frac{3\sqrt{2}\cos\theta_0}{C^{5/2}}\sin\left(4\sqrt{C}s\right) + \frac{2\sqrt{2}\sin\theta_0}{C}\sin^2\left(2\sqrt{C}s\right)$
- $\left.\frac{\partial t}{\partial \hat{u}'_{0,0}}\right|_e = \frac{2\sqrt{2}\cos\theta_0}{C}s - \frac{\sqrt{2}\cos\theta_0}{2C^{3/2}}\sin\left(4\sqrt{C}s\right)$

- $\left.\dfrac{\partial t}{\partial \hat{v}'_{0,0}}\right|_e = \dfrac{2\sqrt{2}\sin\theta_0}{C}s - \dfrac{\sqrt{2}\sin\theta_0}{2C^{3/2}}\sin\left(4\sqrt{C}s\right)$

Computation of V

- $V_{11} = \left[\dfrac{\partial \hat{u}_0}{\partial u_{0,0}} + \dfrac{\hat{v}_0}{2}\dfrac{\partial t}{\partial u_{0,0}}\right]_e$
  $= \cos\left(2\sqrt{C}s\right) - \dfrac{4}{C}\sin\theta_0\cos\theta_0\cos\left(2\sqrt{C}s\right)s + \dfrac{2}{C^{3/2}}\sin\theta_0\cos\theta_0\sin^3\left(2\sqrt{C}s\right)$
  $+ \dfrac{4}{C^{5/2}}\sin^2\theta_0\left[2\cos^2\left(2\sqrt{C}s\right)+1\right]\sin\left(2\sqrt{C}s\right)s - \dfrac{6}{C^3}\sin^2\theta_0\sin^2\left(2\sqrt{C}s\right)\cos\left(2\sqrt{C}s\right)$

- $V_{12} = \left[\dfrac{\partial \hat{u}_0}{\partial v_{0,0}} + \dfrac{\hat{v}_0}{2}\dfrac{\partial t}{\partial v_0}\right]_e$
  $= \dfrac{4}{C}\cos^2\theta_0\cos\left(2\sqrt{C}s\right)s - \dfrac{2}{C^{3/2}}\left[1-\sin^2\theta_0\sin^2\left(2\sqrt{C}s\right)\right]\sin\left(2\sqrt{C}s\right)$
  $- \dfrac{4}{C^{5/2}}\cos\theta_0\sin\theta_0\left[1+2\cos^2\left(2\sqrt{C}s\right)\right]\sin\left(2\sqrt{C}s\right)s$
  $+ \dfrac{6}{C^3}\cos\theta_0\sin\theta_0\sin^2\left(2\sqrt{C}s\right)\cos\left(2\sqrt{C}s\right)$

- $V_{13} = \left[\dfrac{\partial \hat{u}_0}{\partial u'_{0,0}} + \dfrac{\hat{v}_0}{2}\dfrac{\partial t}{\partial u'_{0,0}}\right]_e$
  $= \dfrac{1}{2\sqrt{C}}\sin\left(2\sqrt{C}s\right)$
  $+ \dfrac{2}{C^{3/2}}\cos\theta_0\sin\theta_0\sin\left(2\sqrt{C}s\right)s - \dfrac{1}{C^2}\cos\theta_0\sin\theta_0\cos\left(2\sqrt{C}s\right)\sin^2\left(2\sqrt{C}s\right)$

- $V_{14} = \left[\dfrac{\partial \hat{u}_0}{\partial v'_{0,0}} + \dfrac{\hat{v}_0}{2}\dfrac{\partial t}{\partial v'_{0,0}}\right]_e$
  $= \dfrac{2}{C^{3/2}}\sin^2\theta_0\sin\left(2\sqrt{C}s\right)s - \dfrac{1}{C^2}\sin^2\theta_0\cos\left(2\sqrt{C}s\right)\sin^2\left(2\sqrt{C}s\right)$

- $V_{21} = \left[\dfrac{\partial \hat{v}_0}{\partial u_{0,0}} - \dfrac{\hat{u}_0}{2}\dfrac{\partial t}{\partial u_{0,0}}\right]_e$
  $= -\dfrac{4}{C}\sin^2\theta_0\cos\left(2\sqrt{C}s\right)s + \dfrac{2}{C^{3/2}}\left[1-\cos^2\theta_0\sin^2\left(2\sqrt{C}s\right)\right]\sin\left(2\sqrt{C}s\right)$
  $- \dfrac{4}{C^{5/2}}\cos\theta_0\sin\theta_0\left[1+2\cos^2\left(2\sqrt{C}s\right)\right]\sin\left(2\sqrt{C}s\right)s$
  $+ \dfrac{6}{C^3}\cos\theta_0\sin\theta_0\sin^2\left(2\sqrt{C}s\right)\cos\left(2\sqrt{C}s\right)$

- $V_{22} = \left[\dfrac{\partial \hat{v}_0}{\partial v_{0,0}} - \dfrac{\hat{u}_0}{2}\dfrac{\partial t}{\partial v_{0,0}}\right]_e$
  $= \cos\left(2\sqrt{C}s\right) + \dfrac{4}{C}\sin\theta_0\cos\theta_0\cos\left(2\sqrt{C}s\right)s - \dfrac{2}{C^{3/2}}\sin\theta_0\cos\theta_0\sin^3\left(2\sqrt{C}s\right)$
  $+ \dfrac{4}{C^{5/2}}\cos^2\theta_0\left[2\cos^2\left(2\sqrt{C}s\right)+1\right]\sin\left(2\sqrt{C}s\right)s$
  $- \dfrac{6}{C^3}\cos^2\theta_0\sin^2\left(2\sqrt{C}s\right)\cos\left(2\sqrt{C}s\right)$

- $V_{23} = \left[\frac{\partial \hat{v}_0}{\partial u'_{0,0}} - \frac{\hat{u}_0}{2}\frac{\partial t}{\partial u'_{0,0}}\right]_e$
$= -\frac{2}{C^{3/2}}\cos^2\theta_0 \sin\left(2\sqrt{C}s\right)s + \frac{1}{C^2}\cos^2\theta_0\cos\left(2\sqrt{C}s\right)\sin^2\left(2\sqrt{C}s\right)$

- $V_{24} = \left[\frac{\partial \hat{v}_0}{\partial v'_{0,0}} - \frac{\hat{u}_0}{2}\frac{\partial t}{\partial v'_{0,0}}\right]_e$
$= \frac{1}{2\sqrt{C}}\sin\left(2\sqrt{C}s\right) - \frac{2}{C^{3/2}}\cos\theta_0\sin\theta_0\sin\left(2\sqrt{C}s\right)s$
$+ \frac{1}{C^2}\cos\theta_0\sin\theta_0\cos\left(2\sqrt{C}s\right)\sin^2\left(2\sqrt{C}s\right)$

- $V_{31} = \left[\frac{\partial \hat{u}'_0}{\partial u_{0,0}} + 2\left(\hat{u}_0^2 + 3\hat{v}_0^2\right)\frac{\partial \hat{v}_0}{\partial u_{0,0}} + 4\hat{u}_0\hat{v}_0\frac{\partial \hat{u}_0}{\partial u_{0,0}} + \frac{\hat{v}'_0 - 2(\hat{u}_0^2+\hat{v}_0^2)\hat{u}_0}{2}\frac{\partial t}{\partial u_{0,0}}\right]_e$
$= -2\sqrt{C}\sin\left(2\sqrt{C}s\right) + \frac{8}{\sqrt{C}}\cos\theta_0\sin\theta_0\sin\left(2\sqrt{C}s\right)s$
$+ \frac{4}{C}\cos\theta_0\sin\theta_0\left[2 - 3\cos^2\left(2\sqrt{C}s\right)\right]\cos\left(2\sqrt{C}s\right)$
$- \frac{8}{C^2}\sin^2\theta_0\left[5 - 8\cos^2\left(2\sqrt{C}s\right)\right]\cos\left(2\sqrt{C}s\right)s$
$+ \frac{4}{C^{5/2}}\left[6\sin^2\theta_0 - \left(9 - 11\cos^2\theta_0\right)\cos^2\left(2\sqrt{C}s\right) - 2\cos^2\theta_0\cos^4\left(2\sqrt{C}s\right)\right]\sin\left(2\sqrt{C}s\right)$
$- \frac{16}{C^{7/2}}\cos\theta_0\sin\theta_0\left[1 + 2\cos^2\left(2\sqrt{C}s\right)\right]\sin^3\left(2\sqrt{C}s\right)s$
$+ \frac{24}{C^4}\cos\theta_0\sin\theta_0\cos\left(2\sqrt{C}s\right)\sin^4\left(2\sqrt{C}s\right)$

- $V_{32} = \left[\frac{\partial \hat{u}'_0}{\partial v_{0,0}} + 2\left(\hat{u}_0^2 + 3\hat{v}_0^2\right)\frac{\partial \hat{v}_0}{\partial v_{0,0}} + 4\hat{u}_0\hat{v}_0\frac{\partial \hat{u}_0}{\partial v_{0,0}} + \frac{\hat{v}'_0 - 2(\hat{u}_0^2+\hat{v}_0^2)\hat{u}_0}{2}\frac{\partial t}{\partial v_{0,0}}\right]_e$
$= -\frac{8}{\sqrt{C}}\cos^2\theta_0\sin\left(2\sqrt{C}s\right)s$
$+ \frac{4}{C}\left[3 - 2\cos^2\theta_0 - \left(4 - 3\cos^2\theta_0\right)\cos^2\left(2\sqrt{C}s\right)\right]\cos\left(2\sqrt{C}s\right)$
$+ \frac{8}{C^2}\cos\theta_0\sin\theta_0\left[5 - 8\cos^2\left(2\sqrt{C}s\right)\right]\cos\left(2\sqrt{C}s\right)s$
$- \frac{4}{C^{5/2}}\cos\theta_0\sin\theta_0\left[6 - 11\cos^2\left(2\sqrt{C}s\right) + 2\cos^4\left(2\sqrt{C}s\right)\right]\sin\left(2\sqrt{C}s\right)$
$+ \frac{16}{C^{7/2}}\cos^2\theta_0\left[1 + 2\cos^2\left(2\sqrt{C}s\right)\right]\sin^3\left(2\sqrt{C}s\right)s$
$- \frac{24}{C^4}\cos^2\theta_0\cos\left(2\sqrt{C}s\right)\sin^4\left(2\sqrt{C}s\right)$

- $V_{33} = \left[\frac{\partial \hat{u}'_0}{\partial u'_{0,0}} + 2\left(\hat{u}_0^2 + 3\hat{v}_0^2\right)\frac{\partial \hat{v}_0}{\partial u'_{0,0}} + 4\hat{u}_0\hat{v}_0\frac{\partial \hat{u}_0}{\partial u'_{0,0}} + \frac{\hat{v}'_0 - 2(\hat{u}_0^2+\hat{v}_0^2)\hat{u}_0}{2}\frac{\partial t}{\partial u'_{0,0}}\right]_e$
$= \cos\left(2\sqrt{C}s\right) + \frac{4}{C}\cos\theta_0\sin\theta_0\cos\left(2\sqrt{C}s\right)s$
$+ \frac{2}{C^{3/2}}\cos\theta_0\sin\theta_0\left[2 - 3\cos^2\left(2\sqrt{C}s\right)\right]\sin\left(2\sqrt{C}s\right)$
$- \frac{8}{C^{5/2}}\cos^2\theta_0\sin^3\left(2\sqrt{C}s\right)s$
$+ \frac{4}{C^3}\cos^2\theta_0\cos\left(2\sqrt{C}s\right)\sin^4\left(2\sqrt{C}s\right)$

- $V_{34} = \left[\dfrac{\partial \hat{u}'_0}{\partial v'_{0,0}} + 2\left(\hat{u}_0^2 + 3\hat{v}_0^2\right) \dfrac{\partial \hat{v}_0}{\partial v'_{0,0}} + 4\hat{u}_0\hat{v}_0 \dfrac{\partial \hat{u}_0}{\partial v'_{0,0}} + \dfrac{\hat{v}'_0 - 2(\hat{u}_0^2 + \hat{v}_0^2)\hat{u}_0}{2} \dfrac{\partial t}{\partial v'_{0,0}} \right]_e$
$= \dfrac{4}{C} \sin^2\theta_0 \cos\left(2\sqrt{C}s\right) s$
$- \dfrac{2}{C^{3/2}} \left[3 - 2\sin^2\theta_0 - (4 - 3\sin^2\theta_0)\cos^2\left(2\sqrt{C}s\right)\right] \sin\left(2\sqrt{C}s\right)$
$- \dfrac{8}{C^{5/2}} \cos\theta_0 \sin\theta_0 \sin^3\left(2\sqrt{C}s\right) s$
$+ \dfrac{4}{C^3} \cos\theta_0 \sin\theta_0 \cos\left(2\sqrt{C}s\right) \sin^4\left(2\sqrt{C}s\right)$

- $V_{41} = \left[\dfrac{\partial \hat{v}'_0}{\partial u_{0,0}} - 2\left(3\hat{u}_0^2 + \hat{v}_0^2\right) \dfrac{\partial \hat{u}_0}{\partial u_{0,0}} - 4\hat{u}_0\hat{v}_0 \dfrac{\partial \hat{v}_0}{\partial u_{0,0}} - \dfrac{\hat{u}'_0 + 2(\hat{u}_0^2 + \hat{v}_0^2)\hat{v}_0}{2} \dfrac{\partial t}{\partial u_{0,0}} \right]_e$
$= \dfrac{8}{\sqrt{C}} \sin^2\theta_0 \sin\left(2\sqrt{C}s\right) s$
$- \dfrac{4}{C} \left[3 - 2\sin^2\theta_0 - (4 - 3\sin^2\theta_0)\cos^2\left(2\sqrt{C}s\right)\right] \cos\left(2\sqrt{C}s\right)$
$+ \dfrac{8}{C^2} \cos\theta_0 \sin\theta_0 \left[5 - 8\cos^2\left(2\sqrt{C}s\right)\right] \cos\left(2\sqrt{C}s\right) s$
$- \dfrac{4}{C^{5/2}} \cos\theta_0 \sin\theta_0 \left[6 - 11\cos^2\left(2\sqrt{C}s\right) + 2\cos^4\left(2\sqrt{C}s\right)\right] \sin\left(2\sqrt{C}s\right)$
$- \dfrac{16}{C^{7/2}} \sin^2\theta_0 \left[1 + 2\cos^2\left(2\sqrt{C}s\right)\right] \sin^3\left(2\sqrt{C}s\right) s$
$+ \dfrac{24}{C^4} \sin^2\theta_0 \cos\left(2\sqrt{C}s\right) \sin^4\left(2\sqrt{C}s\right)$

- $V_{42} = \left[\dfrac{\partial \hat{v}'_0}{\partial v_{0,0}} - 2\left(3\hat{u}_0^2 + \hat{v}_0^2\right) \dfrac{\partial \hat{u}_0}{\partial v_{0,0}} - 4\hat{u}_0\hat{v}_0 \dfrac{\partial \hat{v}_0}{\partial v_{0,0}} - \dfrac{\hat{u}'_0 + 2(\hat{u}_0^2 + \hat{v}_0^2)\hat{v}_0}{2} \dfrac{\partial t}{\partial v_{0,0}} \right]_e$
$= -2\sqrt{C} \sin\left(2\sqrt{C}s\right) - \dfrac{8}{\sqrt{C}} \cos\theta_0 \sin\theta_0 \sin\left(2\sqrt{C}s\right) s$
$- \dfrac{4}{C} \cos\theta_0 \sin\theta_0 \left[2 - 3\cos^2\left(2\sqrt{C}s\right)\right] \cos\left(2\sqrt{C}s\right)$
$- \dfrac{8}{C^2} \cos^2\theta_0 \left[5 - 8\cos^2\left(2\sqrt{C}s\right)\right] \cos\left(2\sqrt{C}s\right) s$
$+ \dfrac{4}{C^{5/2}} \left[6\cos^2\theta_0 - (9 - 11\sin^2\theta_0)\cos^2\left(2\sqrt{C}s\right) - 2\sin^2\theta_0 \cos^4\left(2\sqrt{C}s\right)\right] \sin\left(2\sqrt{C}s\right)$
$+ \dfrac{16}{C^{7/2}} \cos\theta_0 \sin\theta_0 \left[1 + 2\cos^2\left(2\sqrt{C}s\right)\right] \sin^3\left(2\sqrt{C}s\right) s$
$- \dfrac{24}{C^4} \cos\theta_0 \sin\theta_0 \cos\left(2\sqrt{C}s\right) \sin^4\left(2\sqrt{C}s\right)$

- $V_{43} = \left[\dfrac{\partial \hat{v}'_0}{\partial u'_{0,0}} - 2\left(3\hat{u}_0^2 + \hat{v}_0^2\right) \dfrac{\partial \hat{u}_0}{\partial u'_{0,0}} - 4\hat{u}_0\hat{v}_0 \dfrac{\partial \hat{v}_0}{\partial u'_{0,0}} - \dfrac{\hat{u}'_0 + 2(\hat{u}_0^2 + \hat{v}_0^2)\hat{v}_0}{2} \dfrac{\partial t}{\partial u'_{0,0}} \right]_e$
$= -\dfrac{4}{C} \cos^2\theta_0 \cos\left(2\sqrt{C}s\right) s$
$- \dfrac{2}{C^{3/2}} \left[3 - 2\cos^2\theta_0 - (4 - 3\cos^2\theta_0)\cos^2\left(2\sqrt{C}s\right)\right] \sin\left(2\sqrt{C}s\right)$
$- \dfrac{8}{C^{5/2}} \cos\theta_0 \sin\theta_0 \sin^3\left(2\sqrt{C}s\right) s$
$+ \dfrac{4}{C^3} \cos\theta_0 \sin\theta_0 \cos\left(2\sqrt{C}s\right) \sin^4\left(2\sqrt{C}s\right)$

- $V_{44} = \left[\dfrac{\partial \hat{v}_0'}{\partial v_{0,0}'} - 2\left(3\hat{u}_0^2 + \hat{v}_0^2\right) \dfrac{\partial \hat{u}_0}{\partial v_{0,0}'} - 4\hat{u}_0\hat{v}_0 \dfrac{\partial \hat{v}_0}{\partial v_{0,0}'} - \dfrac{\hat{u}_0' + 2(\hat{u}_0^2 + \hat{v}_0^2)\hat{v}_0}{2} \dfrac{\partial t}{\partial v_{0,0}'} \right]_e$
$= \cos\left(2\sqrt{C}s\right) - \dfrac{4}{C}\cos\theta_0 \sin\theta_0 \cos\left(2\sqrt{C}s\right) s$
$- \dfrac{2}{C^{3/2}}\cos\theta_0 \sin\theta_0 \left[2 - 3\cos^2\left(2\sqrt{C}s\right)\right] \sin\left(2\sqrt{C}s\right)$
$- \dfrac{8}{C^{5/2}}\sin^2\theta_0 \sin^3\left(2\sqrt{C}s\right) s$
$+ \dfrac{4}{C^3}\sin^2\theta_0 \cos\left(2\sqrt{C}s\right) \sin^4\left(2\sqrt{C}s\right)$

Computation of V^{-1}

According to the theorem of Liouville, the determinant of the matrix $V(s)$ is identically 1 because the trace of $D\boldsymbol{F}_0(\boldsymbol{u}^0)$ in (4.4) is zero.

- $V_{1,1}^{-1} = \cos\left(2\sqrt{C}s\right) + \dfrac{4}{C}\cos\theta_0 \sin\theta_0 \cos\left(2\sqrt{C}s\right) s$
$+ \dfrac{2}{C^{3/2}}\left[2 - 3\cos^2\left(2\sqrt{C}s\right)\right] \cos\theta_0 \sin\theta_0 \sin\left(2\sqrt{C}s\right)$
$+ \dfrac{24}{C^{5/2}}\cos^2\theta_0 \sin^3\left(2\sqrt{C}s\right) s - \dfrac{12}{C^3}\cos^2\theta_0 \cos\left(2\sqrt{C}s\right) \sin^4\left(2\sqrt{C}s\right)$
- $V_{1,2}^{-1} = -\dfrac{4}{C}\cos^2\theta_0 \cos\left(2\sqrt{C}s\right) s + \dfrac{2}{C^{3/2}}\left[1 + 2\sin^2\theta_0 - 3\sin^2\theta_0 \cos^2\left(2\sqrt{C}s\right)\right] \sin\left(2\sqrt{C}s\right)$
$+ \dfrac{24}{C^{5/2}}\cos\theta_0 \sin\theta_0 \sin^3\left(2\sqrt{C}s\right) s - \dfrac{12}{C^3}\cos\theta_0 \sin\theta_0 \cos\left(2\sqrt{C}s\right) \sin^4\left(2\sqrt{C}s\right)$
- $V_{1,3}^{-1} = -\dfrac{1}{2\sqrt{C}}\sin\left(2\sqrt{C}s\right) - \dfrac{2}{C^{3/2}}\cos\theta_0 \sin\theta_0 \sin\left(2\sqrt{C}s\right) s$
$+ \dfrac{1}{C^2}\cos\theta_0 \sin\theta_0 \cos\left(2\sqrt{C}s\right) \sin^2\left(2\sqrt{C}s\right)$
- $V_{1,4}^{-1} = \dfrac{2}{C^{3/2}}\cos^2\theta_0 \sin\left(2\sqrt{C}s\right) s - \dfrac{1}{C^2}\cos^2\theta_0 \cos\left(2\sqrt{C}s\right) \sin^2\left(2\sqrt{C}s\right)$
- $V_{2,1}^{-1} = \dfrac{4}{C}\sin^2\theta_0 \cos\left(2\sqrt{C}s\right) s - \dfrac{2}{C^{3/2}}\left[1 + 2\cos^2\theta_0 - 3\cos^2\theta_0 \cos^2\left(2\sqrt{C}s\right)\right] \sin\left(2\sqrt{C}s\right)$
$+ \dfrac{24}{C^{5/2}}\cos\theta_0 \sin\theta_0 \sin^3\left(2\sqrt{C}s\right) s$
$- \dfrac{12}{C^3}\cos\theta_0 \sin\theta_0 \cos\left(2\sqrt{C}s\right) \sin^4\left(2\sqrt{C}s\right)$
- $V_{2,2}^{-1} = \cos\left(2\sqrt{C}s\right) - \dfrac{4}{C}\cos\theta_0 \sin\theta_0 \cos\left(2\sqrt{C}s\right) s$
$- \dfrac{2}{C^{3/2}}\left[2 - 3\cos^2\left(2\sqrt{C}s\right)\right] \cos\theta_0 \sin\theta_0 \sin\left(2\sqrt{C}s\right)$
$+ \dfrac{24}{C^{5/2}}\sin^2\theta_0 \sin^3\left(2\sqrt{C}s\right) s$
$- \dfrac{12}{C^3}\sin^2\theta_0 \cos\left(2\sqrt{C}s\right) \sin^4\left(2\sqrt{C}s\right)$
- $V_{2,3}^{-1} = -\dfrac{2}{C^{3/2}}\sin^2\theta_0 \sin\left(2\sqrt{C}s\right) s + \dfrac{1}{C^2}\sin^2\theta_0 \cos\left(2\sqrt{C}s\right) \sin^2\left(2\sqrt{C}s\right)$

- $V_{2,4}^{-1} = -\frac{1}{2\sqrt{C}}\sin\left(2\sqrt{C}s\right) + \frac{2}{C^{3/2}}\cos\theta_0\sin\theta_0\sin\left(2\sqrt{C}s\right)s$
$-\frac{1}{C^2}\cos\theta_0\sin\theta_0\cos\left(2\sqrt{C}s\right)\sin^2\left(2\sqrt{C}s\right)$

- $V_{3,1}^{-1} = 2\sqrt{C}\sin\left(2\sqrt{C}s\right) - \frac{8}{\sqrt{C}}\cos\theta_0\sin\theta_0\sin\left(2\sqrt{C}s\right)s$
$-\frac{4}{C}\left[2-3\cos^2\left(2\sqrt{C}s\right)\right]\cos\theta_0\sin\theta_0\cos\left(2\sqrt{C}s\right)$
$-\frac{8}{C^2}\sin^2\theta_0\cos\left(2\sqrt{C}s\right)s$
$-\frac{4}{C^{5/2}}\left[6\cos^2\theta_0-(1+11\cos^2\theta_0)\cos^2\left(2\sqrt{C}s\right)+6\cos^2\theta_0\cos^4\left(2\sqrt{C}s\right)\right]\sin\left(2\sqrt{C}s\right)$
$+\frac{48}{C^{7/2}}\left[1-2\cos^2\left(2\sqrt{C}s\right)\right]\cos\theta_0\sin\theta_0\sin^3\left(2\sqrt{C}s\right)s$
$+\frac{24}{C^4}\cos\theta_0\sin\theta_0\cos\left(2\sqrt{C}s\right)\sin^4\left(2\sqrt{C}s\right)$

- $V_{3,2}^{-1} = -\frac{8}{\sqrt{C}}\sin^2\theta_0\sin\left(2\sqrt{C}s\right)s - \frac{4}{C}\left[2-3\cos^2\left(2\sqrt{C}s\right)\right]\sin^2\theta_0\cos\left(2\sqrt{C}s\right)$
$+\frac{8}{C^2}\cos\theta_0\sin\theta_0\cos\left(2\sqrt{C}s\right)s$
$-\frac{4}{C^{5/2}}\left[6-11\cos^2\left(2\sqrt{C}s\right)+6\cos^4\left(2\sqrt{C}s\right)\right]\cos\theta_0\sin\theta_0\sin\left(2\sqrt{C}s\right)$
$+\frac{48}{C^{7/2}}\left[1-2\cos^2\left(2\sqrt{C}s\right)\right]\sin^2\theta_0\sin^3\left(2\sqrt{C}s\right)s$
$+\frac{24}{C^4}\sin^2\theta_0\cos\left(2\sqrt{C}s\right)\sin^4\left(2\sqrt{C}s\right)$

- $V_{3,3}^{-1} = \cos\left(2\sqrt{C}s\right) - \frac{4}{C}\cos\theta_0\sin\theta_0\cos\left(2\sqrt{C}s\right)s$
$+\frac{2}{C^{3/2}}\cos\theta_0\sin\theta_0\sin^3\left(2\sqrt{C}s\right)$
$-\frac{4}{C^{5/2}}\left[1-2\cos^2\left(2\sqrt{C}s\right)\right]\sin^2\theta_0\sin\left(2\sqrt{C}s\right)s$
$-\frac{2}{C^3}\sin^2\theta_0\cos\left(2\sqrt{C}s\right)\sin^2\left(2\sqrt{C}s\right)$

- $V_{3,4}^{-1} = -\frac{4}{C}\sin^2\theta_0\cos\left(2\sqrt{C}s\right)s - \frac{2}{C^{3/2}}\cos^2\theta_0 * \sin^3\left(2\sqrt{C}s\right)$
$+\frac{4}{C^{5/2}}\left[1-2\cos^2\left(2\sqrt{C}s\right)\right]\cos\theta_0\sin\theta_0\sin\left(2\sqrt{C}s\right)s$
$+\frac{2}{C^3}\cos\theta_0\sin\theta_0\cos\left(2\sqrt{C}s\right)\sin^2\left(2\sqrt{C}s\right)$

- $V_{4,1}^{-1} = \frac{8}{\sqrt{C}}\cos^2\theta_0\sin\left(2\sqrt{C}s\right)s + \frac{4}{C}\left[2-3\cos^2\left(2\sqrt{C}s\right)\right]\cos^2\theta_0\cos\left(2\sqrt{C}s\right)$
$+\frac{8}{C^2}\cos\theta_0\sin\theta_0\cos\left(2\sqrt{C}s\right)s$
$-\frac{4}{C^{5/2}}\left[6-11\cos^2\left(2\sqrt{C}s\right)+6\cos^4\left(2\sqrt{C}s\right)\right]\cos\theta_0\sin\theta_0\sin\left(2\sqrt{C}s\right)$
$-\frac{48}{C^{7/2}}\left[1-2\cos^2\left(2\sqrt{C}s\right)\right]\cos^2\theta_0\sin^3\left(2\sqrt{C}s\right)s$
$-\frac{24}{C^4}\cos^2\theta_0\cos\left(2\sqrt{C}s\right)\sin^4\left(2\sqrt{C}s\right)$

- $V_{4,2}^{-1} = 2\sqrt{C}\sin\left(2\sqrt{C}s\right) + \frac{8}{\sqrt{C}}\cos\theta_0\sin\theta_0\sin\left(2\sqrt{C}s\right)s$
  $+ \frac{4}{C}\left[2 - 3\cos^2\left(2\sqrt{C}s\right)\right]\cos\theta_0\sin\theta_0\cos\left(2\sqrt{C}s\right)$
  $- \frac{8}{C^2}\cos^2\theta_0\cos\left(2\sqrt{C}s\right)s$
  $- \frac{4}{C^{5/2}}\left[6\sin^2\theta_0 - \left(1 + 11\sin^2\theta_0\right)\cos^2\left(2\sqrt{C}s\right) + 6\sin^2\theta_0\cos^4\left(2\sqrt{C}s\right)\right]\sin\left(2\sqrt{C}s\right)$
  $- \frac{48}{C^{7/2}}\left[1 - 2\cos^2\left(2\sqrt{C}s\right)\right]\cos\theta_0\sin\theta_0\sin^3\left(2\sqrt{C}s\right)s$
  $- \frac{24}{C^4}\cos\theta_0\sin\theta_0\cos\left(2\sqrt{C}s\right)\sin^4\left(2\sqrt{C}s\right)$
- $V_{4,3}^{-1} = \frac{4}{C}\cos^2\theta_0\cos\left(2\sqrt{C}s\right)s + \frac{2}{C^{3/2}}\sin^2\theta_0\sin^3\left(2\sqrt{C}s\right)$
  $+ \frac{4}{C^{5/2}}\left[1 - 2\cos^2\left(2\sqrt{C}s\right)\right]\cos\theta_0\sin\theta_0\sin\left(2\sqrt{C}s\right)s$
  $+ \frac{2}{C^3}\cos\theta_0\sin\theta_0\cos\left(2\sqrt{C}s\right)\sin^2\left(2\sqrt{C}s\right)$
- $V_{4,4}^{-1} = \cos\left(2\sqrt{C}s\right) + \frac{4}{C}\cos\theta_0\sin\theta_0\cos\left(2\sqrt{C}s\right)s$
  $- \frac{2}{C^{3/2}}\cos\theta_0\sin\theta_0\sin^3\left(2\sqrt{C}s\right)$
  $- \frac{4}{C^{5/2}}\left[1 - 2\cos^2\left(2\sqrt{C}s\right)\right]\cos^2\theta_0\sin\left(2\sqrt{C}s\right)s$
  $- \frac{2}{C^3}\cos^2\theta_0\cos\left(2\sqrt{C}s\right)\sin^2\left(2\sqrt{C}s\right)$

4.A.2 Computation of the solution of first order

In this appendix we use the variable $\tau = 2\sqrt{C}s$ introduced in Section 4.3 in order to simplify the expressions. With this new variable we have from (4.28)

$$t(\tau) = \frac{2\tau - \sin(2\tau)}{C^{3/2}}. \tag{4.42}$$

The function $\boldsymbol{F}_1 = (0, 0, F_{13}, F_{14})$ in (4.1) is given by

- $F_{13} = \frac{4\sqrt{2}}{\sqrt{C}}\sin\tau U_1(\theta_0,\tau) + \frac{32\sqrt{2}}{C^{3/2}}\sin^3\tau U_1^3(\theta_0,\tau) + \frac{8\sqrt{2}\sin\tau U_1(\theta_0,\tau)}{\sqrt{C}r_2}$
  $- \frac{16\sqrt{2}\sin^3\tau}{C^{3/2}r_2^3}\left(\frac{2}{C}\sin^2\tau + 1\right)U_1(\theta_0,\tau),$
- $F_{14} = \frac{4\sqrt{2}}{\sqrt{C}}\sin\tau U_2(\theta_0,\tau) - \frac{32\sqrt{2}}{C^{3/2}}\sin^3\tau U_2^3(\theta_0,\tau) + \frac{8\sqrt{2}\sin\tau U_2(\theta_0,\tau)}{\sqrt{C}r_2}$
  $- \frac{16\sqrt{2}\sin^3\tau}{C^{3/2}r_2^3}\left(\frac{2}{C}\sin^2\tau - 1\right)U_2(\theta_0,\tau),$

where

- $U_1(\theta_0,\tau) = \cos\theta_0 \cos\left(\dfrac{1}{C^{3/2}}\dfrac{-2\tau+\sin(2\tau)}{2}\right) - \sin\theta_0 \sin\left(\dfrac{1}{C^{3/2}}\dfrac{-2\tau+\sin(2\tau)}{2}\right),$
- $U_2(\theta_0,\tau) = \cos\theta_0 \sin\left(\dfrac{1}{C^{3/2}}\dfrac{-2\tau+\sin(2\tau)}{2}\right) + \sin\theta_0 \cos\left(\dfrac{1}{C^{3/2}}\dfrac{-2\tau+\sin(2\tau)}{2}\right),$
- $r_2 = \sqrt{1+\dfrac{2}{C}\cos\left(2\theta_0+\dfrac{-2\tau+\sin(2\tau)}{C^{3/2}}\right)\sin^2\tau+\dfrac{4}{C^2}\sin^4\tau}.$

The second step is to compute $X^{-1}\boldsymbol{F}_1$ and its integral over $[0,n\pi]$. The full function $\boldsymbol{F}_1$ gives rise to expressions which are not easy to be integrated. Expanding $\boldsymbol{F}_1$ in powers of $C^{-1/2}$ up to order $C^{-7/2}$ we are able to give an analytic result for C large enough. Considering the expansions

- $\cos(t(\tau)/2) = \sum_{i=0}(-1)^i \dfrac{(2\tau-\sin(2\tau))^{2i}}{4^i C^{3i}(2i)!},$
- $\sin(\pm t(\tau)/2) = \mp\sum_{i=0}(-1)^i \dfrac{(2\tau-\sin(2\tau))^{2i+1}}{2^{2i+1}C^{3(2i+1)/2}(2i+1)!},$

we obtain the following expressions for $\displaystyle\int \frac{1}{2\sqrt{C}} X^{-1}\boldsymbol{F}_1$

$$\begin{aligned}
\int_0^{n\pi} \frac{1}{2\sqrt{C}}\left(X^{-1}\boldsymbol{F}_1\right)_1 d\tau &= -\frac{3\sqrt{2}\pi n\cos\theta_0}{2C^{3/2}} + \frac{15\sqrt{2}\pi n(1-2\cos^4\theta_0)\cos\theta_0}{2C^{7/2}} + \mathcal{O}(C^{-9/2}),\\
\int_0^{n\pi} \frac{1}{2\sqrt{C}}\left(X^{-1}\boldsymbol{F}_1\right)_2 d\tau &= -\frac{3\sqrt{2}\pi n\sin\theta_0}{2C^{3/2}} + \frac{15\sqrt{2}\pi n(1-2\sin^4\theta_0)\sin\theta_0}{2C^{7/2}} + \mathcal{O}(C^{-9/2}),\\
\int_0^{n\pi} \frac{1}{2\sqrt{C}}\left(X^{-1}\boldsymbol{F}_1\right)_3 d\tau &= \frac{9\sqrt{2}\pi n\sin\theta_0}{C^{5/2}} + \mathcal{O}(C^{-9/2}),\\
\int_0^{n\pi} \frac{1}{2\sqrt{C}}\left(X^{-1}\boldsymbol{F}_1\right)_4 d\tau &= -\frac{9\sqrt{2}\pi n\cos\theta_0}{C^{5/2}} + \mathcal{O}(C^{-9/2}).
\end{aligned} \tag{4.43}$$

The final step is to compute $\boldsymbol{u}_1(s)$ from (4.5). The following formulas are obtained for $\boldsymbol{u}_1(s_0^*)$ (actually only the components u_1 and v_1 are required)

$$\begin{aligned}
u_1(s_0^*) &= -\frac{(-1)^n 3\sqrt{2}\pi n\cos\theta_0}{2C^{3/2}} - \frac{(-1)^n 3\sqrt{2}\pi^2 n^2\sin\theta_0}{2C^3}\\
&\quad + \frac{(-1)^n 15\sqrt{2}\pi n(1-2\cos^4\theta_0)\cos\theta_0}{2C^{7/2}} + \mathcal{O}(C^{-9/2}),\\
v^1(s_0^*) &= -\frac{(-1)^n 3\sqrt{2}\pi n\sin\theta_0}{2C^{3/2}} + \frac{(-1)^n 3\sqrt{2}\pi^2 n^2\cos\theta_0}{2C^3}\\
&\quad + \frac{(-1)^n 15\sqrt{2}\pi n(1-2\sin^4\theta_0)\sin\theta_0}{2C^{7/2}} + \mathcal{O}(C^{-9/2}).
\end{aligned} \tag{4.44}$$

Chapter 5

Analytical existence of 4 n-EC orbits II

In Chapter 4 an analytical proof of the existence of four n-EC orbits ejecting from (and colliding with) the big primary for any $n \geq 1$ given, C big enough and $\mu > 0$ small enough was carried out. The proof was based on a perturbative approach in μ.

The key point of this chapter is to generalize this previous result and prove the existence of four n-EC orbits ejecting from (and colliding with) the big or small primary, for any $n \geq 1$ and C big enough, so *any value of the mass parameter* $\mu \in (0, 1)$ is possible in this context.

For analytical and numerical purposes, though, we will use a characterization for an EC orbit, based upon the zero value of its angular momentum (similarly to the strategy introduced in Subsection 3.2.3), defined from now on as $M := U\dot{V} - V\dot{U}$ (for some suitable variables (U, V) to be defined later), at a minimum distance with the primary the particle ejected from (see Lemma 7 below). So in order to obtain an n-EC orbit, for $n \geq 1$, $\mu \in (0, 1)$ and C given, first we will compute the corresponding ejection solution for each initial condition. Second we will determine the precise time τ^* when the particle reaches the n-th minimum in the distance to P_1, i.e. the n-th intersection with Σ_m (3.10). At time τ^* we will compute the value of the angular momentum that is, $(U\dot{V} - V\dot{U})(\tau^*)$. Varying $\theta_0 \in [0, \pi)$ (recall the double covering of the configuration plane using Levi-Civita coordinates) we will obtain the corresponding angular momentum where τ^* will depend on θ_0, so we will have a function depending on the initial θ_0, and we will denote it simply by $M_n(\theta_0) = (U\dot{V} - V\dot{U})(\tau^*)$ (overlooking the additional dependence on C and μ). The zeros of $M_n(\theta_0) = 0$ will provide us with the precise values of θ_0 such that the corresponding ejection orbit is precisely an n-EC orbit.

Now, we proceed to state the theorem about the existence, the number and the characteristics of the n-ejection-collision orbits for any value of the mass parameter and for sufficiently restricted Hill regions.

Theorem A. *There exists an $\hat{L}$ such that for $L \geq \hat{L}$ and for any value of $\mu \in (0, 1)$, $n \in \mathbb{N}$ and $C = 3\mu + Ln^{2/3}(1 - \mu)^{2/3}$, there exist exactly four n-EC orbits, which can be characterized by:*

- *Two n-EC orbits both symmetric with respect to the x axis.*
- *Two n-EC orbits symmetric to each other with respect to the x axis.*

We will note these four families of n-EC orbits as α_n and γ_n for the symmetric orbits with respect to the x axis and for β_n and δ_n to the symmetric orbits of each other

In order to prove Theorem A we will first state a weaker version of this theorem, Theorem B, but the proof of this second version will provide light on the approach (mainly a suitable scaling in the configuration variables, time and the Jacobi constant C) used to prove the more general version of Theorem B.

Theorem B. *For all $n \in \mathbb{N}$, there exists a $\hat{K}(n)$ such that for $K \geq \hat{K}(n)$ and for any value of $\mu \in (0,1)$ and $C = 3\mu + K(1-\mu)^{2/3}$, there exist exactly four n-EC orbits, which can be characterized in the same way as in Theorem A.*

We remark that in Theorem B, we have a uniform constant $\hat{K}(n)$ for any value of $\mu \in (0,1)$. This implies that when $\mu \to 1$ the value of the Jacobi constant (for which Theorem B holds) tends to 3, as C_{L_1} does as well with the same kind of asymptotic expansion. Precisely, and as shown in the proof of Theorem B, the expansion of C_{L_1} was the inspiration to choose a suitable scaling in the variables, time and C. In Theorem A we express $\hat{K}(n)$ as $\hat{L}n^{2/3}$.

Before starting with the proof of the Theorems it is important to note that we have based the proof on the calculation of the angular momentum at the n-th intersection of the ejection orbits with Σ_m and, from the shape of the system (4.1) we can see that this function will be of the form $M_n(\theta_0) = \mu\mathcal{F}(n, \theta_0, \mu, C)$, where $\mathcal{F}$ is an analytic function in μ. But instead of using the angular momentum computation strategy, one can choose to use the strategy of computing the intersection of manifolds, i.e. obtain the intersection of the curves D_i^+ and D_j^- (see Definition 3.2). To use this method, the strategy is identical, except for the change in time and in the calculation of the objective function (radial distance at the k-th intersection with Σ_M instead of angular moment in the n-th intersection with Σ_m).

Furthermore, we will see how the results of these two theorems can be applied to the case of the Hill problem, and we will see how the form of the analytical expression of the threshold corresponds to the numerical value of the threshold computed.

Finally, it is important to note that the contents of this chapter have been extracted from [MSORS21].

5.1 Proof of Theorem B

In order to prove Theorem B, let us fix $C \geq C_{L_1}$ (recall that C_{L_1} is always bigger than 3) and consider the following change of variables and time in system (2.26)

$$\begin{cases} u = \sqrt{\dfrac{2(1-\mu)}{C-3\mu}}U, \\ v = \sqrt{\dfrac{2(1-\mu)}{C-3\mu}}V, \\ \tau = 2\sqrt{C-3\mu}s, \end{cases} \tag{5.1}$$

that corresponds to the change that normalizes the linear term of the Levi-Civita system (2.26) and the initial condition of the ejection orbits (3.9). Denoting by $\dot{} = \frac{d}{d\tau}$ the new time derivative the system (2.26) transforms to the following

$$\begin{cases} \ddot{U} = -\dfrac{(C-\mu)U}{C-3\mu} + \dfrac{8(1-\mu)\left(U^2+V^2\right)\dot{V}}{(C-3\mu)^{3/2}} + \dfrac{12(1-\mu)^2\left(U^2+V^2\right)^2 U}{(C-3\mu)^3} + \dfrac{8\mu(1-\mu)U^3}{(C-3\mu)^2} \\ \qquad + \dfrac{2\mu U}{(C-3\mu)R_2} - \dfrac{4\mu(1-\mu)U(U^2+V^2)[2(1-\mu)(U^2+V^2)+(C-3\mu)]}{(C-3\mu)^3 R_2^3}, \\ \ddot{V} = -\dfrac{(C-\mu)V}{C-3\mu} - \dfrac{8(1-\mu)\left(U^2+V^2\right)\dot{U}}{(C-3\mu)^{3/2}} + \dfrac{12(1-\mu)^2\left(U^2+V^2\right)^2 V}{(C-3\mu)^3} - \dfrac{8\mu(1-\mu)V^3}{(C-3\mu)^2} \\ \qquad + \dfrac{2\mu V}{(C-3\mu)R_2} - \dfrac{4\mu(1-\mu)V(U^2+V^2)[2(1-\mu)(U^2+V^2)-(C-3\mu)]}{(C-3\mu)^3 R_2^3}, \end{cases} \tag{5.2}$$

where $R_2 = \sqrt{1+\frac{4(1-\mu)(U^2-V^2)}{C-3\mu}+\frac{4(1-\mu)^2(U^2+V^2)^2}{(C-3\mu)^2}}$. It is important to remark that the properties (2.28), (2.29), (2.30) are preserved (translated to the new variables), and so are the symmetries obtained in the Levi-Civita regularization, i. e.:

$$(\tau, U, V, \dot{U}, \dot{V}) \to (\tau, -U, -V, -\dot{U}, -\dot{V}), \tag{5.3a}$$

$$(\tau, U, V, \dot{U}, \dot{V}) \to (-\tau, -U, V, \dot{U}, -\dot{V}). \tag{5.3b}$$

The proof of the theorem is based on two main ideas: (i) a perturbative approach taking $\delta = 1/\sqrt{C-3\mu}$ as a small parameter, and (ii) the requirement of the angular momentum to be zero at a minimum distance with the primary the particle ejected from.

First of all we can observe the expansions of $1/R_2$ and $1/R_2^3$ are of the form:

$$\begin{aligned} \frac{1}{R_2} &= 1 - 2(1-\mu)(U^2-V^2)\delta^2 + 4(1-\mu)^2[U^4+V^4-4U^2V^2]\delta^4 + \sum_{k\geq 3}(1-\mu)^k P_{2k}(U,V)\delta^{2k}, \\ \frac{1}{R_2^3} &= 1 - 6(1-\mu)(U^2-V^2)\delta^2 + \sum_{k\geq 2}(1-\mu)^k Q_{2k}(U,V)\delta^{2k}, \end{aligned} \tag{5.4}$$

where $P_{2k}(U,V)$ and $Q_{2k}(U,V)$ are polynomials sum of monomials of degree $2k$.

So if we expand the system (5.2) with respect to δ we obtain:

$$\begin{cases} \ddot{U} = -U + 8(1-\mu)(U^2+V^2)\dot{V}\delta^3 + 12(1-\mu)^2\left[2\mu\left(U^4-2U^2V^2-V^4\right)+(U^2+V^2)^2\right]U\delta^6 \\ \qquad + \mu\displaystyle\sum_{k\geq 4}(1-\mu)^{k-1}\bar{P}_{2k-1}(U,V)\delta^{2k}, \\ \ddot{V} = -V - 8(1-\mu)(U^2+V^2)\dot{U}\delta^3 + 12(1-\mu)^2\left[2\mu\left(V^4-2U^2V^2-U^4\right)+(U^2+V^2)^2\right]V\delta^6 \\ \qquad + \mu\displaystyle\sum_{k\geq 4}(1-\mu)^{k-1}\bar{Q}_{2k-1}(U,V)\delta^{2k}, \end{cases} \tag{5.5}$$

which is an analytical system of ODE in δ and $\bar{P}_{2k-1}(U,V)$ and $\bar{Q}_{2k-1}(U,V)$ are polynomials sum of monomials of degree $2k-1$.

Before proceeding it is important to make two observations:

1. We can introduce the parameter $\varepsilon = (1-\mu)^{1/3}\delta$. So we have:

$$\varepsilon^2 = (1-\mu)^{2/3}\delta^2 = \frac{(1-\mu)^{2/3}}{C-3\mu}. \tag{5.6}$$

2. We also know that $C \geq C_{L_1}(\mu)$ since otherwise the Hill region of motion allows transits between both primaries and the system (5.2) is not regular at the position of the second primary. As it is well known the expansion of $C_{L_1}(\mu)$ is (see [Sze67], substituting μ by $1-\mu$)

$$C_{L_1}(\mu) = 3 + 9\left(\frac{1-\mu}{3}\right)^{2/3} - 7\frac{1-\mu}{3} + \mathcal{O}((1-\mu)^{4/3}), \tag{5.7}$$

therefore, if it is possible we will like to have a uniform parameter K with the same order in $(1-\mu)$. So, introducing the variable K as $C = 3\mu + K(1-\mu)^{2/3}$ we have that the previous expression (5.6) becomes:

$$\varepsilon^2 = \frac{(1-\mu)^{2/3}}{3\mu + K(1-\mu)^{2/3} - 3\mu} = \frac{(1-\mu)^{2/3}}{K(1-\mu)^{2/3}} = \frac{1}{K}.$$

With the previous two observations we can improve the change (5.1), consequently we will consider the following change in (2.26)

$$\begin{cases} u = \dfrac{\sqrt{2}(1-\mu)^{1/6}}{\sqrt{K}}U, \\ v = \dfrac{\sqrt{2}(1-\mu)^{1/6}}{\sqrt{K}}V, \\ \tau = 2\sqrt{K}(1-\mu)^{1/3}s, \\ C = 3\mu + K(1-\mu)^{2/3}. \end{cases} \tag{5.8}$$

So, in terms of $\varepsilon = 1/\sqrt{K}$ the system (5.5) has the following expression:

$$\begin{cases} \ddot{U} = -U + 8(U^2+V^2)\dot{V}\varepsilon^3 + 12\left[2\mu\left(U^4 - 2U^2V^2 - V^4\right) + (U^2+V^2)^2\right]U\varepsilon^6 \\ \qquad + \mu\displaystyle\sum_{k\geq 4}(1-\mu)^{\frac{k-3}{3}}\bar{P}_{2k-1}(U,V)\varepsilon^{2k}, \\ \ddot{V} = -V - 8(U^2+V^2)\dot{U}\varepsilon^3 + 12\left[2\mu\left(V^4 - 2U^2V^2 - U^4\right) + (U^2+V^2)^2\right]V\varepsilon^6 \\ \qquad + \mu\displaystyle\sum_{k\geq 4}(1-\mu)^{\frac{k-3}{3}}\bar{Q}_{2k-1}(U,V)\varepsilon^{2k}. \end{cases} \tag{5.9}$$

Second let us prove the following characterization for an EC orbit, based upon the zero value of the angular momentum at a minimum distance with the primary.

Lemma 7. *Assume C large enough. An ejection orbit is an EC orbit if and only if the ejection orbit satisfies that at a minimum in the distance (with the primary) the angular momentum $M = U\dot{V} - V\dot{U} = 0$.*

Proof. The minimum distance condition is given by:

$$\begin{aligned} &U\dot{U} + V\dot{V} = 0, \\ &U\ddot{U} + \dot{U}^2 + V\ddot{V} + \dot{V}^2 > 0, \end{aligned} \tag{5.10}$$

and the angular momentum condition $M = U\dot{V} - V\dot{U} = 0$:

$$U\dot{V} = V\dot{U}. \tag{5.11}$$

We will distinguish between two cases:

1. $\dot{V} \neq 0$. Then, from (5.11):

   $$U = \frac{V\dot{U}}{\dot{V}} \text{ and by (5.10) } \Longrightarrow \frac{V\dot{U}}{\dot{V}}\dot{U} + V\dot{V} = 0 \Longrightarrow V\dot{U}^2 + V\dot{V}^2 = V(\dot{U}^2 + \dot{V}^2) = 0 \Longrightarrow V = 0,$$

   and, by (5.11) also $U = 0$.

2. $\dot{V} = 0$, we will have two subcases:

   (a) if $\dot{U} \neq 0$, then by (5.10) and (5.11) we get $U = V = 0$.

   (b) $\dot{U} = 0$ then, using equations (5.9):

   $$U\ddot{U} + V\ddot{V} = -(U^2 + V^2) + \mathcal{O}(\varepsilon^6(|U|^4 + |V|^4)),$$

   but this quantity is negative for ε small enough, if $U^2 + V^2 > 0$, which contradicts the second item of (5.10). We conclude that $U = V = 0$.

On the other hand, it is clear that if a collision takes place, i. e. $U = V = 0$ and $\dot{U}^2 + \dot{V}^2 = 1$, then conditions (5.10) and (5.11) are trivially satisfied. □

Now let us proceed. Using the vectorial notation $\boldsymbol{U} = (U, V, \dot{U}, \dot{V})^T$, the system (5.9) can be written as

$$\dot{\boldsymbol{U}} = \boldsymbol{G}(\boldsymbol{U}) \quad = \boldsymbol{G}_0(\boldsymbol{U}) + \varepsilon^3\boldsymbol{G}_3(\boldsymbol{U}) + \varepsilon^6\boldsymbol{G}_6(U, V) + \sum_{k\geq 4} \varepsilon^{2k} G_{2k}(U, V), \tag{5.12}$$

where

$$\boldsymbol{G}_0(\boldsymbol{U}) = \begin{pmatrix} \dot{U} \\ \dot{V} \\ -U \\ -V \end{pmatrix}, \qquad \boldsymbol{G}_3(\boldsymbol{U}) = 8 \begin{pmatrix} 0 \\ 0 \\ (U^2 + V^2)\dot{V} \\ -(U^2 + V^2)\dot{U} \end{pmatrix},$$

$$\boldsymbol{G}_6(U, V) = 12 \begin{pmatrix} 0 \\ 0 \\ \left[2\mu\left(U^4 - 2U^2V^2 - V^4\right) + (U^2 + V^2)^2\right] U \\ \left[2\mu\left(V^4 - 2U^2V^2 - U^4\right) + (U^2 + V^2)^2\right] V \end{pmatrix}, \tag{5.13}$$

$$\boldsymbol{G}_{2k}(U, V) = \mu(1 - \mu)^{\frac{k-3}{3}} \begin{pmatrix} 0 \\ 0 \\ \bar{P}_{2k-1}(U, V), \\ \bar{Q}_{2k-1}(U, V) \end{pmatrix} \text{ for } k \geq 4.$$

We remark that $\boldsymbol{G}_0$ and $\boldsymbol{G}_3$ are the only functions that depend on $\dot{U}$ and $\dot{V}$, the remaining ones depending only on U and V. Moreover we observe that the expressions appearing in the expansions are polynomials. Both properties allow to significantly simplify the computations.

The next natural step consists of obtaining a solution $\boldsymbol{U} = \boldsymbol{U}(\tau)$ as a series expansion in ε:

$$\boldsymbol{U} = \sum_{j\geq 0} \boldsymbol{U}_j \varepsilon^j. \tag{5.14}$$

As a usual procedure to obtain the functions $\boldsymbol{U}_j$, we plug $\boldsymbol{U}$ in system (5.12), and comparing the powers in ε, we obtain a system of ODE for $\boldsymbol{U}_j$.

Computation of the functions $\boldsymbol{U}_j$

Now we proceed to compute the explicit expressions for $\boldsymbol{U}_j(\tau) = (U_j(\tau), V_j(\tau), \dot{U}_j(\tau), \dot{V}_j(\tau))$, for any j. Actually we will show that, in order to prove Theorem B, we only need to find explicitly the functions $\boldsymbol{U}_j$ up to order $j = 6$. A priori, we know that it is sufficient to compute the angular momentum up to order 6 in ε since we have seen in Chapter 4 that for proving Theorem 2 it is necessary to expand the angular momentum up to order $C^{-7/2}$. Besides, thanks to the normalization of the variables through the change (5.8), we reduce the order in a factor $1/\sqrt{C}$.

Any ejection orbit, in the variable $\boldsymbol{U}$, has the initial condition

$$\boldsymbol{U}(0, \theta_0) = (0, 0, \cos\theta_0, \sin\theta_0), \quad \theta_0 \in [0, 2\pi), \tag{5.15}$$

so we have

$$\boldsymbol{U}_0(0, \theta_0) = (0, 0, \cos\theta_0, \sin\theta_0), \qquad \boldsymbol{U}_j(0, \theta_0) = \boldsymbol{0}, \qquad j \geq 1. \tag{5.16}$$

Solution for $\varepsilon = 0$:

We must solve the system:

$$\begin{cases} \ddot{U}_0 = -U_0, \\ \ddot{V}_0 = -V_0, \end{cases} \tag{5.17}$$

which is a harmonic oscillator. For an ejection orbit with initial conditions as (5.15), we obtain $\boldsymbol{U}_0(0, \theta_0)$ given by (5.16). Then the function $\boldsymbol{U}_0$ is given by

$$\begin{aligned} U_0(\tau, \theta_0) &= \cos\theta_0 \sin\tau, \\ V_0(\tau, \theta_0) &= \sin\theta_0 \sin\tau, \\ \dot{U}_0(\tau, \theta_0) &= \cos\theta_0 \cos\tau, \\ \dot{V}_0(\tau, \theta_0) &= \sin\theta_0 \cos\tau. \end{aligned} \tag{5.18}$$

Solution for $\varepsilon \neq 0$:

In order to find the functions $\boldsymbol{U}_j$, we must solve the successive resulting ODE when substituting $\boldsymbol{U}$ by the series expansion in (5.9) up to the desired order.

We observe that, for $j \geq 1$, the linear non homogeneous system of ODE to be solved is

$$\frac{d\boldsymbol{U}_j}{d\tau} = D\boldsymbol{G}_0(\boldsymbol{U}_0)\boldsymbol{U}_j + \boldsymbol{F}_j(\boldsymbol{U}_0, \boldsymbol{U}_1, ..., \boldsymbol{U}_{j-3}),$$

where the homogeneous system is always the same but the independent term changes and increases in complexity with j.

Since a fundamental matrix for the homogeneous system (the first order variational equations) is given by

$$X(\tau) = \begin{pmatrix} \cos\tau & 0 & \sin\tau & 0 \\ 0 & \cos\tau & 0 & \sin\tau \\ -\sin\tau & 0 & \cos\tau & 0 \\ 0 & -\sin\tau & 0 & \cos\tau \end{pmatrix}, \tag{5.19}$$

and the initial conditions are $\boldsymbol{U}_j(0, \theta_0) = \boldsymbol{0}$ for $j \geq 1$, we obtain the following well known formula

$$\boldsymbol{U}_j(\tau, \theta_0) = X(\tau) \int_0^\tau X^{-1}(s)\boldsymbol{F}_j(\boldsymbol{U}_0(s), ..., \boldsymbol{U}_{j-3}(s))ds. \tag{5.20}$$

The corresponding explicit expressions are the following:

$$U_3(\tau,\theta_0) = (\tau - \cos\tau\sin\tau)\sin\tau\sin\theta_0,$$

$$V_3(\tau,\theta_0) = -(\tau - \cos\tau\sin\tau)\sin\tau\cos\theta_0,$$

$$U_6(\tau,\theta_0) = -\frac{(\tau-\cos\tau\sin\tau)^2\sin\tau - \mu(15\tau\cos\tau - (8+9\cos^2\tau - 2\cos^4\tau)\sin\tau)(1-2\cos^4\theta_0)}{2}\cos\theta_0,$$

$$V_6(\tau,\theta_0) = -\frac{(\tau-\cos\tau\sin\tau)^2\sin\tau - \mu(15\tau\cos\tau - (8+9\cos^2\tau - 2\cos^4\tau)\sin\tau)(1-2\sin^4\theta_0)}{2}\sin\theta_0,$$

(5.21)

with $U_i(\tau,\theta_0) = V_i(\tau,\theta_0) = 0$ for $i = 1,2,4,5,7$. Once we have the ejection solution up to order $j = 6$, the next step consists of computing the n-th minimum in the distance to the primary (located at the origin) the particle ejected from as a function of the initial θ_0. Equivalently we want to compute the n-th minimum of the function $\left(U^2+V^2\right)(\tau)$. This requires to compute the precise time denoted by τ^*, needed to reach the n-th minimum in distance. We apply the Implicit Function Theorem to the function $(U\dot{U}+V\dot{V})(\tau^*) = 0$ in order to obtain an expansion series in ε. Note, that we can apply the IFT thanks to the fact that $(U\ddot{U}+V\ddot{V}+\dot{U}^2+\dot{V}^2)(\tau_0^*) = 1$. In this way, we can express τ^* as

$$\tau^* = \sum_{i=0}^{6}\tau_i^*\varepsilon^i + \mathcal{O}(\varepsilon^7).$$

We can easily compute τ_0^*, since we have a harmonic oscillator:

$$\tau_0^* = n\pi.$$

Writing the function $U\dot{U}+V\dot{V}$ as an expansion series in ε (including the time) and collecting terms of the same order, we can successively find the terms τ_i^* (up to order 6, higher order terms in the following section):

$$\tau_6^*(n,\theta_0) = \frac{15\mu n\pi(1+3\cos(4\theta_0))}{8}, \tag{5.22}$$

with $\tau_i(n,\theta_0) = 0$ for $i = 1,2,3,4,5,7$.

Now we are ready to compute the angular momentum $M_n(\theta_0) = (U\dot{V}-V\dot{U})(\tau^*)$ whose expansion is:

$$M_n(\theta_0) = -\frac{15\mu n\pi\sin(4\theta_0)}{4}\varepsilon^6 + \mu\mathcal{O}\left(\varepsilon^8\right), \tag{5.23}$$

or in short, since we look for the zeros of $M(\theta_0) = 0$, we write, dividing the previous equation by ε^6,

$$\hat{M}_n(\theta_0) = -\frac{15n\pi\sin(4\theta_0)}{4} + \mathcal{O}\left(\varepsilon^2\right). \tag{5.24}$$

Now we apply the Implicit Function Theorem and for $\varepsilon > 0$ small enough we obtain that the equation (5.24) has four and only four roots in $[0,\pi)$ given by

$$\theta_0 = \frac{\pi m}{4} + \mathcal{O}(\varepsilon^2), \quad m = 0,1,2,3, \tag{5.25}$$

regardless the value of the parameter μ. It is clear from (5.24) that the roots θ_0 are simple.

So we have proved that there exist exactly four n-EC orbits. Moreover, applying the symmetries of the system we can conclude that those EC orbits with an intersection angle with $m = 0,2$ correspond to symmetric n-EC orbits (in the sense that the (x,y) projection is symmetric with respect to the x

axis). Such EC orbits belong to families γ_n and α_n when varying ε (or C). Those EC orbits with an intersection angle with $m = 1, 3$ correspond to symmetric n-EC orbits (in the sense that the (x, y) projection is symmetric one with respect to the other one). Such EC orbits belong to families δ_n and β_n.

Finally, it is important to note that with a change in time $\hat{\tau} = \tau/n$ we can reach the collision in a time $\pi + \mathcal{O}(\varepsilon^6)$.

This finishes the proof of Theorem B.

5.2 A brief comment on bifurcations

So far we have applied the Implicit Function Theorem to infer the existence of four and only four n-EC orbits, for K big enough (that is $\varepsilon = 1/\sqrt{K}$ small enough) and any value of μ. In this procedure the minimum order required was order 6 for both the functions $\boldsymbol{U}_j$ and τ_j^*. Of course, when ε becomes bigger, the Implicit Function Theorem may not be applied anymore and bifurcations appear. This section is focussed on illustrating qualitatively such bifurcations.

The first task is to compute the angular momentum $M(\theta_0)$ to higher order. To do so we need higher order terms for both the functions first $\boldsymbol{U}_j$ and then τ_j^*. Applying the same procedure as in the proof of the Theorem B we obtain

$$U_7(\tau, \theta_0) = 0,$$

$$V_7(\tau, \theta_0) = 0,$$

$$\begin{aligned} U_8(\tau, \theta_0) = {} & \frac{\mu(1-\mu)^{1/3}}{6} \left[105\tau\cos\tau - (48 + 87\cos^2\tau - 38\cos^4\tau + 8\cos^6\tau)\sin\tau\right] \\ & * (5\cos^6\theta_0 - 6\cos^2\theta_0 + 2)\cos\theta_0, \end{aligned}$$

$$\begin{aligned} V_8(\tau, \theta_0) = {} & -\frac{\mu(1-\mu)^{1/3}}{6} \left[105\tau\cos\tau - (48 + 87\cos^2\tau - 38\cos^4\tau + 8\cos^6\tau)\sin\tau\right] \\ & * (5\sin^6\theta_0 - 6\sin^2\theta_0 + 2)\sin\theta_0, \end{aligned}$$

$$\begin{aligned} U_9(\tau, \theta_0) = {} & -\frac{1}{24}\Big[4(\tau - \cos\tau\sin\tau)^3\sin\tau - \mu\Big(3\tau(23 + 144\cos^2\tau + 8\cos^4\tau)\sin\tau \\ & - (379 - 217\cos^2\tau - 178\cos^4\tau + 16\cos^6\tau)\cos\tau - 480\tau(1 + 6\cos^2\tau)\sin\tau\cos^2\theta_0 \\ & + 32(81 - 53\cos^2\tau - 32\cos^4\tau + 4\cos^6\tau)\cos\tau\cos^2\theta_0 - 360\tau^2\cos\tau\cos^4\theta_0 \\ & + 240\tau(3 + 15\cos^2\tau - \cos^4\tau)\sin\tau\cos^4\theta_0 \\ & - 8(374 - 257\cos^2\tau - 143\cos^4\tau + 26\cos^6\tau)\cos\tau\cos^4\theta_0\Big)\Big]\sin\theta_0, \end{aligned}$$

$$\begin{aligned} V_9(\tau, \theta_0) = {} & \frac{1}{24}\Big[4(\tau - \cos\tau\sin\tau)^3\sin\tau - \mu\Big(3\tau(23 + 144\cos^2\tau + 8\cos^4\tau)\sin\tau \\ & - (379 - 217\cos^2\tau - 178\cos^4\tau + 16\cos^6\tau)\cos\tau - 480\tau(1 + 6\cos^2\tau)\sin\tau\sin^2\theta_0 \\ & + 32(81 - 53\cos^2\tau - 32\cos^4\tau + 4\cos^6\tau)\cos\tau\sin^2\theta_0 - 360\tau^2\cos\tau\sin^4\theta_0 \\ & + 240\tau(3 + 15\cos^2\tau - \cos^4\tau)\sin\tau\sin^4\theta_0 \\ & - 8(374 - 257\cos^2\tau - 143\cos^4\tau + 26\cos^6\tau)\cos\tau\sin^4\theta_0\Big)\Big]\cos\theta_0, \end{aligned}$$

$$U_{10}(\tau,\theta_0)=\frac{\mu(1-\mu)^{2/3}}{8}\Big[315\tau\cos\tau-\big(128+325\cos^2\tau-210\cos^4\tau+88\cos^6\tau \\ -16\cos^8\tau\big)\sin\tau\Big](3-20\cos^2\theta_0+30\cos^4\theta_0-14\cos^8\theta_0)\cos\theta_0,$$

$$V_{10}(\tau,\theta_0)=\frac{\mu(1-\mu)^{2/3}}{8}\Big[315\tau\cos\tau-\big(128+325\cos^2\tau-210\cos^4\tau+88\cos^6\tau \\ -16\cos^8\tau\big)\sin\tau\Big](3-20\sin^2\theta_0+30\sin^4\theta_0-14\sin^8\theta_0)\sin\theta_0.$$

Then, writing the function $U\dot{U}+V\dot{V}$ as an expansion series in ε and collecting terms of the same order, we can successively find the terms τ_i^* of order $i=7,...,10$:

$$\tau_7^*(n,\theta_0)=0,$$

$$\tau_8^*(n,\theta_0)=-\frac{35\mu(1-\mu)^{1/3}n\pi\cos(2\theta_0)(5\cos^2(2\theta_0)-3)}{4},$$

$$\tau_9^*(n,\theta_0)=\frac{15\mu n^2\pi^2\sin(4\theta_0)}{2},$$

$$\tau_{10}^*(n,\theta_0)=\frac{315\mu(1-\mu)^{2/3}n\pi(13-10\cos(4\theta_0)-35\cos^2(4\theta_0))}{256}.$$

Now we are ready to compute the explicit expression for the angular momentum $M_n(\theta_0)=(U\dot{V}-V\dot{U})(\tau^*)$ up to order 10 which is the following:

$$M_n(\theta_0)=-\frac{15\mu n\pi\sin(4\theta_0)}{4}\varepsilon^6+\frac{105\mu(1-\mu)^{1/3}n\pi\left(\sin(2\theta_0)+5\sin(6\theta_0)\right)}{64}\varepsilon^8+\frac{15\mu n^2\pi^2\cos(4\theta_0)}{2}\varepsilon^9 \\ -\frac{315\mu(1-\mu)^{2/3}n\pi(2\sin(4\theta_0)+7\sin(8\theta_0))}{128}\varepsilon^{10}+\mathcal{O}(\varepsilon^{11}). \tag{5.26}$$

It is clear that if ε is small enough, the dominant term is ε^6, and the zeros of $M_n(\theta_0)$ are related to the term $\sin(4\theta_0)$, therefore we obtain four n-EC orbits.

However let us discuss what happens for bigger values of ε, or equivalently for smaller values of C. In subsection 3.4.2 we have illustrated two different kinds of bifurcations that take place when doing the continuation of families of n-EC orbits and that can be explained precisely from the analytical expression of $M_n(\theta_0)$ to higher order just obtained.

The first kind of bifurcation can be inferred just taking into account the terms of $M_n(\theta_0)$ up to order 8 in (5.26). If we truncate the expression in this order, for sufficiently large value of ε the role of the $\sin(6\theta_0)$ produce a bifurcation responsible of two new families of n-EC orbits. See Figure 3.24 top for $\mu=0.1$ and $n=2$.

The second kind of bifurcation can be inferred from the expression of $M_n(\theta_0)$ up to order 10 given in (5.26). If we truncate the expression in this order, for sufficiently large value of ε the role of the $\sin(8\theta_0)$ produce a bifurcation responsible of four new families of n-EC orbits. See Figure 3.25 top for $\mu=0.1$ and $n=3$.

This does not mean that these bifurcations come from these terms, but it gives us a qualitative idea of how complex the dynamics becomes.

5.3 Proof of Theorem A

In order to prove Theorem A let us introduce a new parameter L defined as $K = Ln^{2/3}$. In this way, the change (5.8) can be written as:

$$\begin{cases} u = \dfrac{\sqrt{2}(1-\mu)^{1/6}}{\sqrt{L}n^{1/3}}\mathcal{U}, \\ v = \dfrac{\sqrt{2}(1-\mu)^{1/6}}{\sqrt{L}n^{1/3}}\mathcal{V}, \\ \mathcal{T} = 2\sqrt{L}n^{1/3}(1-\mu)^{1/3}s, \\ C = 3\mu + Ln^{2/3}(1-\mu)^{2/3}. \end{cases} \tag{5.27}$$

If we make this change in (2.26) and consider the expansion with respect to the parameter $\xi = 1/\sqrt{L}$ we obtain

$$\begin{cases} \ddot{\mathcal{U}} = -\mathcal{U} + \dfrac{8(\mathcal{U}^2+\mathcal{V}^2)\dot{\mathcal{V}}}{n}\xi^3 + \dfrac{12\left[2\mu\left(\mathcal{U}^4 - 2\mathcal{U}^2\mathcal{V}^2 - \mathcal{V}^4\right) + (\mathcal{U}^2+\mathcal{V}^2)^2\right]\mathcal{U}}{n^2}\xi^6 \\ \qquad + \mu\displaystyle\sum_{k\geq 4}\frac{(1-\mu)^{\frac{k-3}{3}}\bar{P}_{2k-1}(\mathcal{U},\mathcal{V})}{n^{2k/3}}\xi^{2k}, \\ \ddot{\mathcal{V}} = -\mathcal{V} - \dfrac{8(\mathcal{U}^2+\mathcal{V}^2)\dot{\mathcal{U}}}{n}\xi^3 + \dfrac{12\left[2\mu\left(\mathcal{V}^4 - 2\mathcal{U}^2\mathcal{V}^2 - \mathcal{U}^4\right) + (\mathcal{U}^2+\mathcal{V}^2)^2\right]\mathcal{V}}{n^2}\xi^6 \\ \qquad + \mu\displaystyle\sum_{k\geq 4}\frac{(1-\mu)^{\frac{k-3}{3}}\bar{Q}_{2k-1}(\mathcal{U},\mathcal{V})}{n^{2k/3}}\xi^{2k}, \end{cases} \tag{5.28}$$

which is the same system as (5.9) rewriting $\varepsilon = \xi/n^{1/3}$. In this way we can write $\boldsymbol{\mathcal{U}}$ as a power series of ξ

$$\boldsymbol{\mathcal{U}} = \sum_{k\geq 0}\boldsymbol{\mathcal{U}}_k\xi^k \quad \text{with} \quad \boldsymbol{\mathcal{U}}_k(\mathcal{T},\theta_0) = \frac{1}{n^{k/3}}\boldsymbol{U}_k(\mathcal{T},\theta_0). \tag{5.29}$$

In the same way, the time needed to reach the n-th minimum in the distance with respect to the first primary is given by

$$\mathcal{T}^*(n,\theta_0) = \sum_{k\geq 0}\mathcal{T}_k^*\xi^k \quad \text{with} \quad \mathcal{T}_k^* = \frac{1}{n^{k/3}}\tau_k^*. \tag{5.30}$$

Finally, defining the angular momentum in the n-th minimum as $\mathcal{M}_n(\theta_0) = (\mathcal{U}\dot{\mathcal{V}} - \mathcal{V}\dot{\mathcal{U}})(\mathcal{T}^*(n,\theta_0))$ we obtain a analogous quantity to (5.23):

$$\mathcal{M}_n(\theta_0) = -\frac{15\mu\pi\sin(4\theta_0)}{4n}\xi^6 + \mu\mathcal{O}\left(\xi^8\right). \tag{5.31}$$

In order to obtain the result of the statement of the theorem we need to verify that all the terms included in $\mathcal{O}(\xi^8)$ have at least one term n dividing that is, it is of the form $\mathcal{O}(\xi^8, 1/n)$.

If this was true we could write $\mathcal{M}_n(\theta_0)$ as

$$\mathcal{M}_n(\theta_0) = -\frac{15\mu\pi\sin(4\theta_0)}{4n}\xi^6 + \frac{\mu}{n}\mathcal{O}\left(\xi^8\right), \tag{5.32}$$

and then extract the common factor $1/n$ and apply the IFT obtaining the statement of Theorem A.

To prove this is true is not entirely immediate and requires a few calculations, since we know that the solution is uniform in $1/n^{1/3}$ but we have $\mathcal{T}_0^* = \pi n$ and due to the resonance of the system the order of $\mathcal{T}$ in the solution increases as we consider larger terms of $\boldsymbol{\mathcal{U}}_k$.

Precisely what we will do first is to look at the highest order of $\mathcal{T}$ for each $\mathcal{U}_k$ and $\mathcal{V}_k$. Recall that the functions $\mathcal{U}_k$ and $\mathcal{V}_k$ are polynomials in $\mathcal{T}$, $\sin\mathcal{T}$ and $\cos\mathcal{T}$.

In this way, for example, the largest order that appears in $\mathcal{J}(\mathcal{T})$ defined as

$$\mathcal{J}(\mathcal{T}) = \mathcal{T}^3 \sin\mathcal{T} - \mathcal{T}\cos^5\mathcal{T}, \tag{5.33}$$

is 3 (due to the term $\mathcal{T}^3$), and we will denote by $\mathrm{ord}_{\mathcal{T}}(\mathcal{J}) = 3$.

Furthermore, we note that

$$\mathrm{ord}_{\mathcal{T}}(\mathcal{J}_1\mathcal{J}_2) \leq \mathrm{ord}_{\mathcal{T}}(\mathcal{J}_1) + \mathrm{ord}_{\mathcal{T}}(\mathcal{J}_2),$$

or more generally

$$\mathrm{ord}_{\mathcal{T}}\left(\prod_{i=1}^{m}\mathcal{J}_m\right) \leq \sum_{i=1}^{m}\mathrm{ord}_{\mathcal{T}}(\mathcal{J}_i).$$

At this point we will state the following lemma

Lemma 8. $\mathrm{ord}_{\mathcal{T}}(\boldsymbol{\mathcal{U}}_{3k+i}) \leq k$ *where* $i = 0, 1, 2$.

Proof. Before proceeding, note that we can rewrite the statement of the lemma by

$$\mathrm{ord}_{\mathcal{T}}(\boldsymbol{\mathcal{U}}_{3k+i}) \leq \left\lfloor \frac{3k+i}{3} \right\rfloor,$$

where $i = 0, 1, 2$ and $\lfloor x \rfloor$ denotes the greatest integer less than or equal to x and therefore

$$\left\lfloor \frac{3k+i}{3} \right\rfloor = k.$$

We will prove this lemma using induction. From the previous sections we know that

$$\begin{array}{lll} \mathrm{ord}_{\mathcal{T}}(\boldsymbol{\mathcal{U}}_0) = 0, & \mathrm{ord}_{\mathcal{T}}(\boldsymbol{\mathcal{U}}_1) = 0, & \mathrm{ord}_{\mathcal{T}}(\boldsymbol{\mathcal{U}}_2) = 0, \\ \mathrm{ord}_{\mathcal{T}}(\boldsymbol{\mathcal{U}}_3) = 1, & \mathrm{ord}_{\mathcal{T}}(\boldsymbol{\mathcal{U}}_4) = 0, & \mathrm{ord}_{\mathcal{T}}(\boldsymbol{\mathcal{U}}_5) = 0, \\ \mathrm{ord}_{\mathcal{T}}(\boldsymbol{\mathcal{U}}_6) = 2, & \mathrm{ord}_{\mathcal{T}}(\boldsymbol{\mathcal{U}}_7) = 0, & \mathrm{ord}_{\mathcal{T}}(\boldsymbol{\mathcal{U}}_8) = 1, \\ \mathrm{ord}_{\mathcal{T}}(\boldsymbol{\mathcal{U}}_9) = 3, & \mathrm{ord}_{\mathcal{T}}(\boldsymbol{\mathcal{U}}_{10}) = 1. & \end{array}$$

In this way we see that the base case is true. The next steep is to prove that if the statement is true for k then it is true for $k+1$.

If it is true for the k-th case then we have

$$\begin{aligned} \max_j\left(\mathrm{ord}_{\mathcal{T}}(\boldsymbol{\mathcal{U}}_{3k+i-j}\boldsymbol{\mathcal{U}}_j)\right) &\leq \max_j\left(\mathrm{ord}_{\mathcal{T}}(\boldsymbol{\mathcal{U}}_{3k+i-j}) + \mathrm{ord}_{\mathcal{T}}(\boldsymbol{\mathcal{U}}_j)\right) \\ &\leq \max_j\left(\lfloor(3k+i-j)/3\rfloor + \lfloor j/3\rfloor\right) = k, \end{aligned}$$

where $i = 0, 1, 2$. This expression can be generalized as

$$\max_{\sum_{j=1}^{m} l_j = 3k+i}\left(\mathrm{ord}_{\mathcal{T}}\left(\prod_{j=1}^{m}\boldsymbol{\mathcal{U}}_{l_j}\right)\right) \leq k. \tag{5.34}$$

This will play a key role, as it tells us that if we have a sum of monomials of a certain degree such that the sum of their indices must be p we know that their order in $\mathcal{T}$ will be $\leq \lfloor p/3 \rfloor$.

Recall that we can obtain the solutions by

$$\boldsymbol{\mathcal{U}}_l(\mathcal{T}, \theta_0) = X(\mathcal{T}) \int_0^{\mathcal{T}} X^{-1}(s) \boldsymbol{\mathcal{F}}_l \left(\boldsymbol{\mathcal{U}}_{\leq l-3}(s, \theta_0) \right) ds, \tag{5.35}$$

where

$$\boldsymbol{\mathcal{U}}_{\leq m} = \sum_{l=0}^{m} \boldsymbol{\mathcal{U}}_l \xi^l, \tag{5.36}$$

and

$$\boldsymbol{\mathcal{F}}_l(\boldsymbol{\mathcal{U}}_{\leq l-3}) = [\boldsymbol{\mathcal{G}}_3(\boldsymbol{\mathcal{U}}_{\leq l-3})]_{(l-3)} + \sum_{j=3}^{\lfloor l/2 \rfloor} [\boldsymbol{\mathcal{G}}_{2j}(\mathcal{U}_{\leq l-2j}, \mathcal{V}_{\leq l-2j})]_{(l-2j)}, \tag{5.37}$$

with

$$\boldsymbol{\mathcal{G}}_3(\boldsymbol{\mathcal{U}}) = \frac{1}{n} \boldsymbol{G}_3(\boldsymbol{\mathcal{U}}), \qquad \boldsymbol{\mathcal{G}}_{2j}(\mathcal{U}, \mathcal{V}) = \frac{1}{n^{2j/3}} \boldsymbol{G}_{2j}(\mathcal{U}, \mathcal{V}), \quad j \geq 3,$$

and the subscript $_{(m)}$ denotes that the sum of the subscripts of each monomial has to be m, for example, $[\boldsymbol{\mathcal{G}}_3(\boldsymbol{\mathcal{U}}_{\leq l-3})]_{(l-3)}$ is given by

$$[\boldsymbol{\mathcal{G}}_3(\boldsymbol{\mathcal{U}}_{\leq l-3})]_{(l-3)} = \frac{8}{n} \sum_{i=0}^{l-3} \begin{pmatrix} 0 \\ 0 \\ \dot{\mathcal{V}}_i \sum_{j=0}^{l-3-i} (\mathcal{U}_j \mathcal{U}_{l-3-i-j} + \mathcal{V}_j \mathcal{V}_{l-3-i-j}) \\ -\dot{\mathcal{U}}_i \sum_{j=0}^{l-3-i} (\mathcal{U}_j \mathcal{U}_{l-3-i-j} + \mathcal{V}_j \mathcal{V}_{l-3-i-j}) \end{pmatrix}, \tag{5.38}$$

and the $[\boldsymbol{\mathcal{G}}_{2j}]_{(l-2j)}$ are sum of monomials of degree $2j-1$ in $\mathcal{U}$ and $\mathcal{V}$ such that the sum of the indices of the $\mathcal{U}_i$ and $\mathcal{V}_i$ of each monomial is exactly $l-2j$.

In this way, using (5.34) we can easily bound the order in $\mathcal{T}$ of the summands of $\boldsymbol{\mathcal{F}}_l(\boldsymbol{\mathcal{U}}_{\leq l-3})$

$$\begin{aligned} &\mathrm{ord}_{\mathcal{T}} \left([\boldsymbol{\mathcal{G}}_3(\boldsymbol{\mathcal{U}}_{\leq l-3})]_{(l-3)} \right) \leq \lfloor (l-3)/3 \rfloor, \\ &\mathrm{ord}_{\mathcal{T}} \left([\boldsymbol{\mathcal{G}}_{2j}(\boldsymbol{\mathcal{U}}_{\leq l-2j})]_{(l-2j)} \right) \leq \lfloor (l-2j)/3, \rfloor \quad \text{for } j \geq 3, \end{aligned}$$

and note that $\lfloor (l-3)/3 \rfloor > \lfloor (l-2j)/3 \rfloor$ for $j \geq 3$.

So we have that the highest order in $\mathcal{T}$ that can appear in $\boldsymbol{\mathcal{F}}_{3(k+1)+i}$ with $i = 0, 1, 2$ is k. Thus, by multiplying X^{-1} by $\boldsymbol{\mathcal{F}}_{3(k+1)+i}$ and integrating, the maximum order that we can achieve in $\mathcal{T}$ is $k+1$, so we obtain

$$\mathrm{ord}_{\mathcal{T}}(\boldsymbol{\mathcal{U}}_{3(k+1)+i}) \leq k+1.$$

□

If we look more carefully at the order in $\mathcal{T}$ of the first terms of $\boldsymbol{\mathcal{U}}_k$ we see that we can improve Lemma 8 by imposing that $\mathrm{ord}_{\mathcal{T}}(\boldsymbol{\mathcal{U}}_4) = \mathrm{ord}_{\mathcal{T}}(\boldsymbol{\mathcal{U}}_5) = 0$. Using this information and repeating the proof of Lemma 8 (distinguishing the cases $3k$ from $3k+1$ and $3k+2$) we obtain

$$\begin{cases} \mathrm{ord}_{\mathcal{T}}(\boldsymbol{\mathcal{U}}_{3k}) \leq k, \\ \mathrm{ord}_{\mathcal{T}}(\boldsymbol{\mathcal{U}}_{3k+i}) \leq k-1 \quad \text{for } i = 1, 2, \end{cases} \tag{5.39}$$

which is the expression that we will use.

However, this is not enough to guarantee that we will have as a common factor $1/n$ in the terms $\boldsymbol{\mathcal{U}}_{3k}(\mathcal{T}^*, \theta_0)$, since these terms have a summand of the form $\mathcal{T}^k/n^k$ that when evaluating it in $\mathcal{T}_0^*$ will

make the n^k dividing disappear completely. Therefore, we need to know more exactly the expressions of the terms $\boldsymbol{\mathcal{U}}_{3k}$.

Before proceeding, let us see the following lemma:

Lemma 9. *Given $f_k(\theta_0)$ by*

$$f_k(\theta_0) = \begin{cases} \cos\theta_0 & \text{if } k = 4p, \\ \sin\theta_0 & \text{if } k = 4p+1, \\ -\cos\theta_0 & \text{if } k = 4p+2, \\ -\sin\theta_0 & \text{if } k = 4p+3. \end{cases}$$

then

$$\sum_{k=0}^{m} \frac{f_k f_{m-k} + f_{k+1} f_{m-k+1}}{k!(m-k)!} = \begin{cases} 1 \text{ if } m = 0, \\ 0 \text{ otherwise.} \end{cases}$$

Proof. We will distinguish the two cases:

- Case $m = 0$:
$$f_0 f_0 + f_1 f_1 = \cos^2\theta_0 + \sin^2\theta_0 = 1.$$
- Case $m > 0$:

  Note that
$$\sum_{k=0}^{m} \frac{f_k f_{m-k} + f_{k+1} f_{m-k+1}}{k!(m-k)!} = \frac{1}{m!} \sum_{k=0}^{m} \binom{m}{k} \left[f_k f_{m-k} + f_{k+1} f_{m-k+1} \right],$$
  therefore
  - If m is odd we have that all the summands are 0, since the terms that we have are of the form $\cos\theta_0 \sin\theta_0 - \cos\theta_0 \sin\theta_0$.
  - If m is even we have:
$$\sum_{k=0}^{m} \binom{m}{k} \left[f_k f_{m-k} + f_{k+1} f_{m-k+1} \right] = \sum_{k=0}^{m} \binom{m}{k} (-1)^k = 0.$$

□

At this point we can characterize $\boldsymbol{\mathcal{U}}_{3k}$ by the following lemma:

Lemma 10. *The terms $\boldsymbol{\mathcal{U}}_{3k}$, are given by:*

$$\mathcal{U}_{3k} = \frac{f_k(\theta_0)}{k! n^k} \mathcal{T}^k \sin\mathcal{T} + O(\mathcal{T}^{k-1}), \qquad \mathcal{V}_{3k} = \frac{f_{k+1}(\theta_0)}{k! n^k} \mathcal{T}^k \sin\mathcal{T} + O(\mathcal{T}^{k-1}),$$
$$\dot{\mathcal{U}}_{3k} = \frac{f_k(\theta_0)}{k! n^k} \mathcal{T}^k \cos\mathcal{T} + O(\mathcal{T}^{k-1}), \qquad \dot{\mathcal{V}}_{3k} = \frac{f_{k+1}(\theta_0)}{k! n^k} \mathcal{T}^k \cos\mathcal{T} + O(\mathcal{T}^{k-1}).$$

Proof. To prove this, we will again use an inductive process.

We have already calculated the base cases in the previous sections, so we will assume that it is true for the k-th case and we will see that it is then true for the $k+1$ case.

We also know that the highest order terms in $\mathcal{T}$ of $\boldsymbol{\mathcal{U}}_{3(k+1)}$ will come from $\boldsymbol{\mathcal{G}}_3$ and the combination of the terms of $\boldsymbol{\mathcal{U}}_{3j}$ of $\boldsymbol{\mathcal{U}}_{\leq 3k}$. In this way

$$
\begin{aligned}
[\boldsymbol{\mathcal{G}}_3(\boldsymbol{\mathcal{U}}_{\leq 3k})]_{(3k)} &= \frac{8}{n}\sum_{a+b+c=k}\begin{pmatrix}0\\0\\(\mathcal{U}_{3a}\mathcal{U}_{3b}+\mathcal{V}_{3a}\mathcal{V}_{3b})\,\dot{\mathcal{V}}_{3c}\\-(\mathcal{U}_{3a}\mathcal{U}_{3b}+\mathcal{V}_{3a}\mathcal{V}_{3b})\,\dot{\mathcal{U}}_{3c}\end{pmatrix}+O(\mathcal{T}^{k-1})\\
&= \frac{8}{n}\sum_{i=0}^{k}\left[\sum_{j=0}^{i}\left[\mathcal{U}_{3j}\mathcal{U}_{3(i-j)}+\mathcal{V}_{3j}\mathcal{V}_{3(i-j)}\right]\right]\begin{pmatrix}0\\0\\\dot{\mathcal{V}}_{3(k-i)}\\-\dot{\mathcal{U}}_{3(k-i)}\end{pmatrix}+O(\mathcal{T}^{k-1})\\
&= \frac{8}{n}\sum_{i=0}^{k}\left[\sum_{j=0}^{i}\left[\frac{f_j}{j!n^j}\mathcal{T}^j\sin\mathcal{T}\frac{f_{i-j}}{(i-j)!n^{i-j}}\mathcal{T}^{i-j}\sin\mathcal{T}\right.\right.\\
&\qquad\left.\left.+\frac{f_{j+1}}{j!n^j}\mathcal{T}^j\sin\mathcal{T}\frac{f_{i-j+1}}{(i-j)!n^{i-j}}\mathcal{T}^{i-j}\sin\mathcal{T}\right]\begin{pmatrix}0\\0\\\frac{f_{k-i+1}}{(k-i)!n^{k-i}}\mathcal{T}^{k-i}\cos\mathcal{T}\\-\frac{f_{k-i}}{(k-i)!n^{k-i}}\mathcal{T}^{k-i}\cos\mathcal{T}\end{pmatrix}\right]+O(\mathcal{T}^{k-1})\\
&= \frac{8\mathcal{T}^k\sin^2\mathcal{T}\cos\mathcal{T}}{n^{k+1}}\sum_{i=0}^{k}\left[\frac{1}{(k-i)!}\sum_{j=0}^{i}\left[\frac{f_jf_{i-j}+f_{j+1}f_{i-j+1}}{j!(i-j)!}\right]\begin{pmatrix}0\\0\\f_{k-i+1}\\-f_{k-i}\end{pmatrix}\right]+O(\mathcal{T}^{k-1})\\
&\overset{(*)}{=} \frac{8\mathcal{T}^k\sin^2\mathcal{T}\cos\mathcal{T}}{k!n^{k+1}}\begin{pmatrix}0\\0\\f_{k+1}\\-f_k\end{pmatrix}+O(\mathcal{T}^{k-1})\\
&= \frac{8\mathcal{T}^k\sin^2\mathcal{T}\cos\mathcal{T}}{k!n^{k+1}}\begin{pmatrix}0\\0\\f_{k+1}\\f_{k+2}\end{pmatrix}+O(\mathcal{T}^{k-1}),
\end{aligned}
$$

where in $(*)$ we used the Lemma 9. Therefore

$$
\begin{aligned}
\int_0^{\mathcal{T}} X^{-1}\boldsymbol{\mathcal{F}}_{3k+3}\,d\mathcal{T} &= \int_0^{\mathcal{T}}\left[X^{-1}[\boldsymbol{\mathcal{G}}_3(\boldsymbol{\mathcal{U}}_{\leq 3k})]_{(3k)}+O(\mathcal{T}^{k-1})\right]\,d\mathcal{T}\\
&= \int_0^{\mathcal{T}}\left[X^{-1}\frac{8}{k!n^{k+1}}\begin{pmatrix}0\\0\\f_{k+1}\mathcal{T}^k\sin^2\mathcal{T}\cos\mathcal{T}\\f_{k+2}\mathcal{T}^k\sin^2\mathcal{T}\cos\mathcal{T}\end{pmatrix}+O(\mathcal{T}^{k-1})\right]d\mathcal{T}\\
&= \frac{8}{k!n^{k+1}}\int_0^{\mathcal{T}}\left[\begin{pmatrix}-f_{k+1}\mathcal{T}^k\sin^3\mathcal{T}\cos\mathcal{T}\\-f_{k+2}\mathcal{T}^k\sin^3\mathcal{T}\cos\mathcal{T}\\f_{k+1}\mathcal{T}^k\sin^2\mathcal{T}\cos^2\mathcal{T}\\f_{k+2}\mathcal{T}^k\sin^2\mathcal{T}\cos^2\mathcal{T}\end{pmatrix}+O(\mathcal{T}^{k-1})\right]d\mathcal{T}\\
&= \frac{1}{(k+1)!n^{k+1}}\begin{pmatrix}0\\0\\f_{k+1}\mathcal{T}^{k+1}\\f_{k+2}\mathcal{T}^{k+1}\end{pmatrix}+O(\mathcal{T}^k).
\end{aligned}
$$

Finally, multiplying by X we obtain:

$$
\begin{aligned}
\mathcal{U}_{3(k+1)} &= \frac{f_{k+1}(\theta_0)}{(k+1)!n^{k+1}}\mathcal{T}^{k+1}\sin\mathcal{T}+O(\mathcal{T}^k), \qquad \mathcal{V}_{3(k+1)} = \frac{f_{k+2}(\theta_0)}{(k+1)!n^{k+1}}\mathcal{T}^{k+1}\sin\mathcal{T}+O(\mathcal{T}^k),\\
\dot{\mathcal{U}}_{3(k+1)} &= \frac{f_{k+1}(\theta_0)}{(k+1)!n^{k+1}}\mathcal{T}^{k+1}\cos\mathcal{T}+O(\mathcal{T}^k), \qquad \dot{\mathcal{V}}_{3(k+1)} = \frac{f_{k+2}(\theta_0)}{(k+1)!n^{k+1}}\mathcal{T}^{k+1}\cos\mathcal{T}+O(\mathcal{T}^k).
\end{aligned}
$$

□

At this point we can easily see that the terms $\mathcal{T}_p^*$ with $p = 3k + i$, for $k \geq 1$ and $i = 0, 1, 2$, will be at least of order $\mathcal{O}(1/n)$ (that is, they will be null or have a common factor of $1/n$ at least). The process is inductive again. We already have that it is verified for the base cases and to make the inductive step we have to write the equation from which the p-th term is obtained, i.e. imposing $\mathcal{U}\dot{\mathcal{U}} + \mathcal{V}\dot{\mathcal{V}} = 0$.

$$\begin{aligned}\left(\mathcal{U}\dot{\mathcal{U}} + \mathcal{V}\dot{\mathcal{V}}\right)(\mathcal{T}^*) &= \sum_{i\geq 0}\left[\xi^i \sum_{j=0}^{i}\left(\mathcal{U}_j\dot{\mathcal{U}}_{i-j} + \mathcal{V}_j\dot{\mathcal{V}}_{i-j}\right)(\mathcal{T}^*)\right] \\ &= \sum_{i=0}^{p}\left[\xi^i \sum_{j=0}^{i}\left(\mathcal{U}_j\dot{\mathcal{U}}_{i-j} + \mathcal{V}_j\dot{\mathcal{V}}_{i-j}\right)\left(\sum_{l=0}^{p-i}\mathcal{T}_l^*\xi^l\right)\right] + \mathcal{O}\left(\xi^{p+1}\right) \\ &= \left(\mathcal{U}_0\dot{\mathcal{U}}_0 + \mathcal{V}_0\dot{\mathcal{V}}_0\right)\left(\sum_{l=0}^{p}\mathcal{T}_l^*\xi^l\right) + \sum_{i=1}^{p}\left[\xi^i \sum_{j=0}^{i}\left(\mathcal{U}_j\dot{\mathcal{U}}_{i-j} + \mathcal{V}_j\dot{\mathcal{V}}_{i-j}\right)\left(\sum_{l=0}^{p-i}\mathcal{T}_l^*\xi^l\right)\right] \\ &\quad + \mathcal{O}\left(\xi^{p+1}\right).\end{aligned} \tag{5.40}$$

Before developing further the last expression of (5.40) we can observe that, on one hand, the only term that has the term $\mathcal{T}_p^*$ is the one that comes from the expression $\mathcal{U}_0\dot{\mathcal{U}}_0 + \mathcal{V}_0\dot{\mathcal{V}}_0$, which, as we know, has order 0 in $\mathcal{T}$ and does not have any n dividing. On the other hand, by the expression of $\boldsymbol{\mathcal{U}}_k$ given by Lemma 10 and using the Lemma 9 we have,

$$\sum_{j=0}^{l}\mathcal{U}_{3j}\dot{\mathcal{U}}_{3(l-j)} + \mathcal{V}_{3j}\dot{\mathcal{V}}_{3(l-j)} = \mathcal{O}(\mathcal{T}^{l-1})/n^l.$$

Therefore, we can extract a common factor of at least $1/n$ from the terms of the summatory from $i = 1$ to p when we evaluate them.

Hence, we see that the terms $\mathcal{T}_p^*$ with $p = 3k+i$, for $k \geq 1$ and $i = 0, 1, 2$, are at least of order $\mathcal{O}(1/n)$.

In a similar way the angular momentum $\mathcal{M}_n$ is given by

$$\begin{aligned}\mathcal{M}_n &= \left(\mathcal{U}\dot{\mathcal{V}} - \mathcal{V}\dot{\mathcal{U}}\right)(\mathcal{T}^*) \\ &= \sum_{i\geq 0}\left[\xi^i \sum_{j=0}^{i}\left(\mathcal{U}_j\dot{\mathcal{V}}_{i-j} - \mathcal{V}_j\dot{\mathcal{U}}_{j-i}\right)(\mathcal{T}^*)\right] \\ &= \sum_{i=0}^{p}\left[\xi^i \sum_{j=0}^{i}\left(\mathcal{U}_j\dot{\mathcal{V}}_{i-j} - \mathcal{V}_j\dot{\mathcal{U}}_{j-i}\right)\left(\sum_{l=0}^{p-i}\mathcal{T}_l^*\xi^l\right)\right] + \mathcal{O}\left(\xi^{p+1}\right),\end{aligned}$$

and, by Lemma 10 we have

$$\begin{aligned}(\mathcal{U}_{3a}\dot{\mathcal{V}}_{3b} - \mathcal{V}_{3a}\dot{\mathcal{U}}_{3b})(\mathcal{T}_0^*) &= \frac{f_a f_{b+1} - f_{a+1}f_b}{a!\,b!\,n^{a+b}}\mathcal{T}_0^{*a+b}\sin\mathcal{T}_0^*\cos\mathcal{T}_0^* + \frac{1}{n^{a+b}}\mathcal{O}\left(\mathcal{T}_0^{*a+b-1}\right) \\ &= \mathcal{O}\left(\frac{1}{n}\right), \quad \forall a, b.\end{aligned}$$

Therefore, all the terms in $\mathcal{M}_n(\theta_0)$ have (at least) the common factor $1/n$.

Finally, it is important to note that with a change in time $\hat{\mathcal{T}} = \mathcal{T}/n$ we can reach the collision in a time $\pi + \mathcal{O}(\xi^6)$.

This finishes the proof of Theorem A.

Remark 10. *It is important to note that the shape of the $\hat{C}(\mu, n)$ obtained in the Theorem A coincides with that obtained numerically. For this reason we reproduce again the Figure 3.27 in Figure 5.1.*

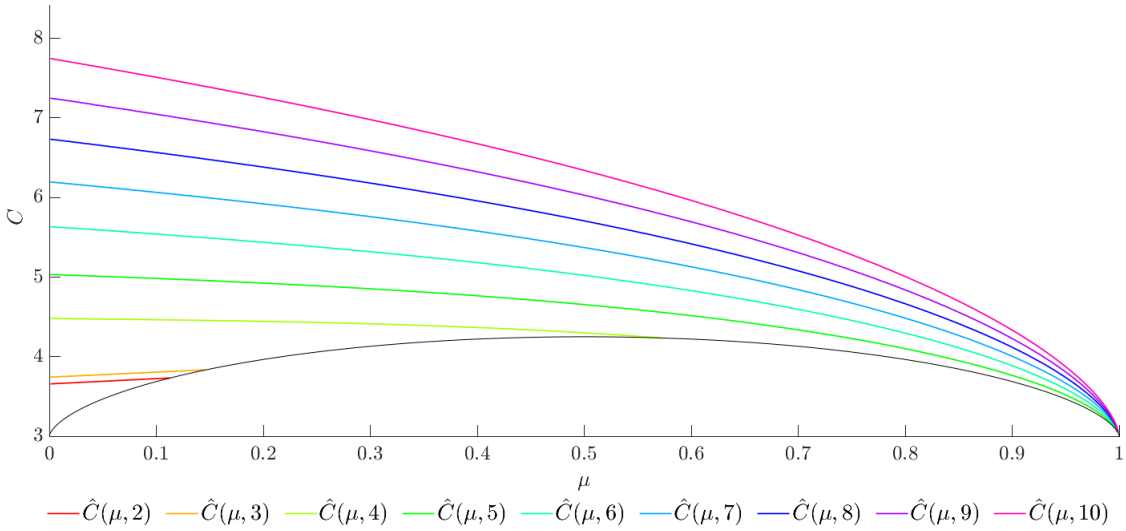

Figure 5.1: Value of $\hat{C}(\mu, n)$ for $\mu \in (0, 1)$ and $n = 2, ..., 10$.

5.4 Alternative proof of Theorem A

In this section we will make an alternative proof of Theorem A using the ideas presented in Chapter 4 and the idea of the change of coordinates used in this chapter. This alternative procedure makes the proof of Theorem A much easier than the version presented in the previous section. In this way, the first thing we will do is make the change of coordinates given by

$$\begin{cases} u = \dfrac{\sqrt{2}(1-\mu)^{1/6}}{\sqrt{L}n^{1/3}}\mathcal{U}, \\ v = \dfrac{\sqrt{2}(1-\mu)^{1/6}}{\sqrt{L}n^{1/3}}\mathcal{V}, \\ \hat{\mathcal{T}} = \dfrac{2\sqrt{L}(1-\mu)^{1/3}}{n^{2/3}}s, \\ C = 3\mu + Ln^{2/3}(1-\mu)^{2/3}. \end{cases} \tag{5.41}$$

Considering again an expansion with respect the variable $\xi = 1/\sqrt{L}$ we obtain the system

$$\begin{cases} \ddot{\mathcal{U}} = -n^2\mathcal{U} + 8(\mathcal{U}^2+\mathcal{V}^2)\dot{\mathcal{V}}\xi^3 + 12\left[2\mu\left(\mathcal{U}^4 - 2\mathcal{U}^2\mathcal{V}^2 - \mathcal{V}^4\right) + (\mathcal{U}^2+\mathcal{V}^2)^2\right]\mathcal{U}\xi^6 \\ \qquad\qquad + \mu\displaystyle\sum_{k\geq 4}\frac{(1-\mu)^{\frac{k-3}{3}}\bar{P}_{2k-1}(\mathcal{U},\mathcal{V})}{n^{2k/3-2}}\xi^{2k}, \\ \ddot{\mathcal{V}} = -n^2\mathcal{V} - 8(\mathcal{U}^2+\mathcal{V}^2)\dot{\mathcal{U}}\xi^3 + 12\left[2\mu\left(\mathcal{V}^4 - 2\mathcal{U}^2\mathcal{V}^2 - \mathcal{U}^4\right) + (\mathcal{U}^2+\mathcal{V}^2)^2\right]\mathcal{V}\xi^6 \\ \qquad\qquad + \mu\displaystyle\sum_{k\geq 4}\frac{(1-\mu)^{\frac{k-3}{3}}\bar{Q}_{2k-1}(\mathcal{U},\mathcal{V})}{n^{2k/3-2}}\xi^{2k}. \end{cases} \tag{5.42}$$

We can think that the previous system is a particular case of the system

$$\begin{cases} \ddot{\mathcal{U}} = -n^2\mathcal{U} + 8(\mathcal{U}^2+\mathcal{V}^2)\dot{\mathcal{V}}\xi_1^3 + 12(\mathcal{U}^2+\mathcal{V}^2)^2\mathcal{U}\xi_1^6 \\ \qquad + 24\mu\left(\mathcal{U}^4 - 2\mathcal{U}^2\mathcal{V}^2 - \mathcal{V}^4\right)\mathcal{U}\xi_2^6 + \mu\displaystyle\sum_{k\geq 4}\frac{(1-\mu)^{\frac{k-3}{3}}\bar{P}_{2k-1}(\mathcal{U},\mathcal{V})}{n^{2k/3-2}}\xi_2^{2k}, \\ \ddot{\mathcal{V}} = -n^2\mathcal{V} - 8(\mathcal{U}^2+\mathcal{V}^2)\dot{\mathcal{U}}\xi_1^3 + 12(\mathcal{U}^2+\mathcal{V}^2)^2\mathcal{V}\xi_1^6 \\ \qquad + 24\mu\left(\mathcal{V}^4 - 2\mathcal{U}^2\mathcal{V}^2 - \mathcal{U}^4\right)\mathcal{V}\xi_2^6 + \mu\displaystyle\sum_{k\geq 4}\frac{(1-\mu)^{\frac{k-3}{3}}\bar{Q}_{2k-1}(\mathcal{U},\mathcal{V})}{n^{2k/3-2}}\xi_2^{2k}, \end{cases} \tag{5.43}$$

when $\xi_1 = \xi_2$. In this way, we split the terms of ξ associated with the 2-body problem (ξ_1) and the ones associated with the perturbation of the second primary (ξ_2).

At this point, we will study system (5.43) as a perturbative problem in ξ_2, and therefore, our goal will be to find the solution to the problem as a power series of ξ_2, i.e.

$$\boldsymbol{\mathcal{U}} = \sum_{k\geq 0}\boldsymbol{\mathcal{U}}_k\xi_2^k.$$

In particular we want to obtain

$$\boldsymbol{\mathcal{U}} = \boldsymbol{\mathcal{U}}_0 + \boldsymbol{\mathcal{U}}_6\xi_2^6 + \mathcal{O}(\xi_2^8).$$

To simplify the notation, we express the system (5.43) as

$$\dot{\boldsymbol{\mathcal{U}}} = \boldsymbol{F}_0(\boldsymbol{\mathcal{U}}) + \mu\boldsymbol{F}_6(\mathcal{U},\mathcal{V})\xi_2^6 + \frac{\mu(1-\mu)^{1/3}}{n^{2/3}}\mathcal{O}(\xi_2^8), \tag{5.44}$$

where

$$\boldsymbol{F}_0(\boldsymbol{\mathcal{U}}) = \begin{pmatrix} \dot{\mathcal{U}} \\ \dot{\mathcal{V}} \\ -n^2\mathcal{U} + 8(\mathcal{U}^2+\mathcal{V}^2)\dot{\mathcal{V}}\xi_1^3 + 12(\mathcal{U}^2+\mathcal{V}^2)^2\mathcal{U}\xi_1^6 \\ -n^2\mathcal{V} - 8(\mathcal{U}^2+\mathcal{V}^2)\dot{\mathcal{U}}\xi_1^3 + 12(\mathcal{U}^2+\mathcal{V}^2)^2\mathcal{V}\xi_1^6 \end{pmatrix}, \quad \boldsymbol{F}_6(\mathcal{U},\mathcal{V}) = 24\begin{pmatrix} 0 \\ 0 \\ \left(\mathcal{U}^4 - 2\mathcal{U}^2\mathcal{V}^2 - \mathcal{V}^4\right)\mathcal{U} \\ \left(\mathcal{V}^4 - 2\mathcal{U}^2\mathcal{V}^2 - \mathcal{U}^4\right)\mathcal{V} \end{pmatrix}.$$

It is important to note that the expressions included in $\mathcal{O}(\xi_2^8)$ are polynomials that depend solely on $\mathcal{U}$ and $\mathcal{V}$ and are uniform in $(1-\mu)^{1/3}$ and $1/n^{2/3}$.

Developing with respect to ξ_2 we have:

$$\begin{aligned} \dot{\boldsymbol{\mathcal{U}}} &= \dot{\boldsymbol{\mathcal{U}}}_0 + \dot{\boldsymbol{\mathcal{U}}}_6\xi_2^6 + \mathcal{O}(\xi_2^8) \\ &= \boldsymbol{F}_0(\boldsymbol{\mathcal{U}}_0 + \boldsymbol{\mathcal{U}}_6\xi_2^6 + \mathcal{O}(\xi_2^8)) + \mu\boldsymbol{F}_6\left(\mathcal{U}_0 + \mathcal{O}(\xi_2^6), \mathcal{V}_0 + \mathcal{O}(\xi_2^6)\right)\xi_2^6 + \mathcal{O}(\xi_2^8) \\ &= \boldsymbol{F}_0(\boldsymbol{\mathcal{U}}_0) + \xi_2^6 D\boldsymbol{F}_0(\boldsymbol{\mathcal{U}}_0)\boldsymbol{\mathcal{U}}_6 + \mu\xi_2^6\boldsymbol{F}_6(\mathcal{U}_0,\mathcal{V}_0) + \mathcal{O}(\xi_2^8). \end{aligned}$$

Therefore, $\boldsymbol{\mathcal{U}}_0$ and $\boldsymbol{\mathcal{U}}_6$ must satisfy

$$\dot{\boldsymbol{\mathcal{U}}}_0 = \boldsymbol{F}_0(\boldsymbol{\mathcal{U}}_0), \tag{5.45}$$

$$\dot{\boldsymbol{\mathcal{U}}}_6 = D\boldsymbol{F}_0(\boldsymbol{\mathcal{U}}_0)\boldsymbol{\mathcal{U}}_6 + \mu\boldsymbol{F}_6(\mathcal{U}_0,\mathcal{V}_0), \tag{5.46}$$

that is, $\boldsymbol{\mathcal{U}}_0$ is a solution of the 2-body problem in the new coordinates and $\boldsymbol{\mathcal{U}}_6$ is obtained as

$$\boldsymbol{\mathcal{U}}_6(\hat{\mathcal{T}}) = X(\hat{\mathcal{T}})\boldsymbol{\mathcal{U}}_{6,0} + \mu X(\hat{\mathcal{T}})\int_0^{\hat{\mathcal{T}}} X^{-1}(\hat{\mathcal{T}})\boldsymbol{F}_6(\mathcal{U}_0(\hat{\mathcal{T}}),\mathcal{V}_0(\hat{\mathcal{T}}))\,d\hat{\mathcal{T}},$$

where $X(\hat{\mathcal{T}}) = \dfrac{\partial \boldsymbol{\mathcal{U}}_0}{\partial \boldsymbol{\mathcal{U}}_{0,0}}(\hat{\mathcal{T}})$ and $\dfrac{\partial}{\partial \boldsymbol{\mathcal{U}}_{0,0}} = \left(\dfrac{\partial}{\partial \mathcal{U}_{0,0}}, \dfrac{\partial}{\partial \mathcal{V}_{0,0}}, \dfrac{\partial}{\partial \dot{\mathcal{U}}_{0,0}}, \dfrac{\partial}{\partial \dot{\mathcal{V}}_{0,0}}\right)$ being $\boldsymbol{\mathcal{U}}_{k,0} = \boldsymbol{\mathcal{U}}_k(0)$ the initial conditions.

Note that we are interested only in the ejection orbits and the initial conditions of these orbits are given by

$$\boldsymbol{\mathcal{U}}_{0,0} = (0, 0, n\cos\theta_0, n\sin\theta_0) \quad \text{and} \quad \boldsymbol{\mathcal{U}}_{k,0} = \mathbf{0}\ \forall k \geq 6, \tag{5.47}$$

therefore all the $\boldsymbol{\mathcal{U}}_k$ with $k \geq 6$ have a common factor of μ and we only need to compute

$$\boldsymbol{\mathcal{U}}_6(\hat{\mathcal{T}}) = \mu X(\hat{\mathcal{T}}) \int_0^{\hat{\mathcal{T}}} X^{-1}(\hat{\mathcal{T}}) \boldsymbol{F}_6(\mathcal{U}_0(\hat{\mathcal{T}}), \mathcal{V}_0(\hat{\mathcal{T}}))\, d\hat{\mathcal{T}}. \tag{5.48}$$

To prove the theorem, we will use the strategy of computing the angular momentum $\mathcal{M}_n(\theta_0)$ at the n-th minimum and find the values of θ_0 such that $\mathcal{M}_n(\theta_0) = 0$. In this way, the first step will be to calculate the time needed to reach the n-th minimum solving $\left[\mathcal{U}\dot{\mathcal{U}} + \mathcal{V}\dot{\mathcal{V}}\right](\theta_0, \hat{\mathcal{T}}^*) = 0$. Similarly, we will express $\hat{\mathcal{T}}^*$ as an expansion on ξ_2, so we want to find $\hat{\mathcal{T}}^*$ as

$$\hat{\mathcal{T}}^* = \hat{\mathcal{T}}_0^* + \xi_2^6 \hat{\mathcal{T}}_6^* + \mathcal{O}(\xi_2^8), \tag{5.49}$$

and, in particular, for the case $\xi_1 = \xi_2$ we will see that the terms $\hat{\mathcal{T}}_k^*$ with $k \geq 6$ have a common factor of μ and $1/n^2$ (and are also uniform in these variables).

The last step will be to calculate $\mathcal{M}_n(\theta_0)$ for the particular case $\xi_1 = \xi_2$.

Thus, first of all we need to solve the Kepler problem in an analogous way as in Chapter 4.

5.4.1 The non perturbed case

First of all, note that we already know that the solution (see Section 4.2) of the system

$$\begin{cases} \ddot{\mathcal{U}}_0 = -n^2\mathcal{U}_0 + 8(\mathcal{U}_0^2 + \mathcal{V}_0^2)\dot{\mathcal{V}}_0\xi_1^3 + 12(\mathcal{U}_0^2 + \mathcal{V}_0^2)^2\mathcal{U}_0\xi_1^6, \\ \ddot{\mathcal{V}}_0 = -n^2\mathcal{V}_0 - 8(\mathcal{U}_0^2 + \mathcal{V}_0^2)\dot{\mathcal{U}}_0\xi_1^3 + 12(\mathcal{U}_0^2 + \mathcal{V}_0^2)^2\mathcal{V}_0\xi_1^6, \end{cases} \tag{5.50}$$

since it corresponds to the solution (see Lemma 5) given by

$$\begin{cases} \mathcal{U}_0(\hat{\mathcal{T}}) = \bar{\mathcal{U}}_0(\hat{\mathcal{T}})\cos(-t/2) - \bar{\mathcal{V}}_0(\hat{\mathcal{T}})\sin(-t/2), \\ \mathcal{V}_0(\hat{\mathcal{T}}) = \bar{\mathcal{U}}_0(\hat{\mathcal{T}})\sin(-t/2) + \bar{\mathcal{V}}_0(\hat{\mathcal{T}})\cos(-t/2), \\ \dot{\mathcal{U}}_0(\hat{\mathcal{T}}) = \left[\dot{\bar{\mathcal{U}}}_0 + 2(\bar{\mathcal{U}}_0^2 + \bar{\mathcal{V}}_0^2)\bar{\mathcal{V}}_0\xi_1^3\right]\cos(-t/2) - \left[\dot{\bar{\mathcal{V}}}_0 - 2(\bar{\mathcal{U}}_0^2 + \bar{\mathcal{V}}_0^2)\bar{\mathcal{U}}_0\xi_1^3\right]\sin(-t/2), \\ \dot{\mathcal{U}}_0(\hat{\mathcal{T}}) = \left[\dot{\bar{\mathcal{U}}}_0 + 2(\bar{\mathcal{U}}_0^2 + \bar{\mathcal{V}}_0^2)\bar{\mathcal{V}}_0\xi_1^3\right]\sin(-t/2) + \left[\dot{\bar{\mathcal{V}}}_0 - 2(\bar{\mathcal{U}}_0^2 + \bar{\mathcal{V}}_0^2)\bar{\mathcal{U}}_0\xi_1^3\right]\cos(-t/2), \end{cases} \tag{5.51}$$

where $\bar{\mathcal{U}}_0$ and $\bar{\mathcal{V}}_0$ are the solutions of the 2-body problem in sideral coordinates

$$\begin{cases} \ddot{\bar{\mathcal{U}}}_0 = -\left[n^2 - 4(\bar{\mathcal{U}}_0\dot{\bar{\mathcal{V}}}_0 - \bar{\mathcal{V}}_0\dot{\bar{\mathcal{U}}}_0)\xi_1^3\right]\bar{\mathcal{U}}_0, \\ \ddot{\bar{\mathcal{V}}}_0 = -\left[n^2 - 4(\bar{\mathcal{U}}_0\dot{\bar{\mathcal{V}}}_0 - \bar{\mathcal{V}}_0\dot{\bar{\mathcal{U}}}_0)\xi_1^3\right]\bar{\mathcal{V}}_0, \end{cases} \tag{5.52}$$

and

$$\frac{dt}{d\hat{\mathcal{T}}} = 4(\bar{\mathcal{U}}_0^2 + \bar{\mathcal{V}}_0^2)\xi_1^3. \tag{5.53}$$

Recall that (see Lemma 4) the angular momenta is constant, i.e.

$$\left[\bar{\mathcal{U}}_0\dot{\bar{\mathcal{V}}}_0 - \bar{\mathcal{V}}_0\dot{\bar{\mathcal{U}}}_0\right](\hat{\mathcal{T}}) = \bar{\mathcal{U}}_{0,0}\dot{\bar{\mathcal{V}}}_{0,0} - \bar{\mathcal{V}}_{0,0}\dot{\bar{\mathcal{U}}}_{0,0}, \tag{5.54}$$

and therefore the solution of (5.52) is given by

$$\begin{cases} \bar{\mathcal{U}}_0(\hat{\mathcal{T}}) = \bar{\mathcal{U}}_{0,0}\cos(\omega\hat{\mathcal{T}}) + \dfrac{\dot{\bar{\mathcal{U}}}_{0,0}}{\omega}\sin(\omega\hat{\mathcal{T}}), \\ \bar{\mathcal{V}}_0(\hat{\mathcal{T}}) = \bar{\mathcal{V}}_{0,0}\cos(\omega\hat{\mathcal{T}}) + \dfrac{\dot{\bar{\mathcal{V}}}_{0,0}}{\omega}\sin(\omega\hat{\mathcal{T}}), \end{cases} \tag{5.55}$$

where $\omega = \sqrt{n^2 - 4(\bar{\mathcal{U}}_{0,0}\dot{\bar{\mathcal{V}}}_{0,0} - \bar{\mathcal{V}}_{0,0}\dot{\bar{\mathcal{U}}}_{0,0})\xi_1^3}$.

In a similar way, by Lemma 6 the value $t(\hat{\mathcal{T}})$ is given by

$$\begin{aligned} t(\hat{\mathcal{T}}) = 2\Bigg[& \left(\bar{\mathcal{U}}_{0,0}^2 + \bar{\mathcal{V}}_{0,0}^2\right)\left(\hat{\mathcal{T}} + \frac{\cos(\omega\hat{\mathcal{T}})\sin(\omega\hat{\mathcal{T}})}{\omega}\right) + \frac{2\left(\bar{\mathcal{U}}_{0,0}\dot{\bar{\mathcal{U}}}_{0,0} + \bar{\mathcal{V}}_{0,0}\dot{\bar{\mathcal{V}}}_{0,0}\right)}{\omega^2}\sin^2(\omega\hat{\mathcal{T}}) \\ & + \frac{\dot{\bar{\mathcal{U}}}_{0,0}^2 + \dot{\bar{\mathcal{V}}}_{0,0}^2}{\omega^2}\left(\hat{\mathcal{T}} - \frac{\cos(\omega\hat{\mathcal{T}})\sin(\omega\hat{\mathcal{T}})}{\omega}\right)\Bigg]\xi_1^3, \end{aligned} \tag{5.56}$$

and the relation between the sideral initial conditions and the synodical ones is the same as in (4.23) and can be obtained from (5.51) putting $\hat{\mathcal{T}} = 0$

$$\begin{cases} \mathcal{U}_{0,0} = \bar{\mathcal{U}}_{0,0}, \\ \mathcal{V}_{0,0} = \bar{\mathcal{V}}_{0,0}, \\ \dot{\mathcal{U}}_{0,0} = \dot{\bar{\mathcal{U}}}_{0,0} + 2(\bar{\mathcal{U}}_{0,0}^2 + \bar{\mathcal{V}}_{0,0}^2)\bar{\mathcal{V}}_{0,0}\xi_1^3, \\ \dot{\mathcal{V}}_{0,0} = \dot{\bar{\mathcal{V}}}_{0,0} - 2(\bar{\mathcal{U}}_{0,0}^2 + \bar{\mathcal{V}}_{0,0}^2)\bar{\mathcal{U}}_{0,0}\xi_1^3, \end{cases} \qquad \begin{cases} \bar{\mathcal{U}}_{0,0} = \mathcal{U}_{0,0}, \\ \bar{\mathcal{V}}_{0,0} = \mathcal{V}_{0,0}, \\ \dot{\bar{\mathcal{U}}}_{0,0} = \dot{\mathcal{U}}_{0,0} - 2(\mathcal{U}_{0,0}^2 + \mathcal{V}_{0,0}^2)\mathcal{V}_{0,0}\xi_1^3, \\ \dot{\bar{\mathcal{V}}}_{0,0} = \dot{\mathcal{V}}_{0,0} + 2(\mathcal{U}_{0,0}^2 + \mathcal{V}_{0,0}^2)\mathcal{U}_{0,0}\xi_1^3. \end{cases} \tag{5.57}$$

Let us remember that we are interested in the particular case of ejection orbits, which have as their initial condition

$$\bar{\boldsymbol{\mathcal{U}}}_{0,0} = (0, 0, n\cos\theta_0, n\sin\theta_0), \tag{5.58}$$

and therefore its solution is given by:

$$\begin{cases} \mathcal{U}_0(\theta_0, \hat{\mathcal{T}}) = \left[\cos\theta_0\cos\left(-t/2\right) - \sin\theta_0\sin\left(-t/2\right)\right]\sin(n\hat{\mathcal{T}}), \\ \mathcal{V}_0(\theta_0, \hat{\mathcal{T}}) = \left[\cos\theta_0\sin\left(-t/2\right) + \sin\theta_0\cos\left(-t/2\right)\right]\sin(n\hat{\mathcal{T}}), \end{cases} \tag{5.59}$$

with

$$t = 2\left[\hat{\mathcal{T}} - \frac{\cos(n\hat{\mathcal{T}})\sin(n\hat{\mathcal{T}})}{n}\right]\xi_1^3. \tag{5.60}$$

In this way from (5.59) it is very easy to see that the n-th minimum distance will be reached when $\hat{\mathcal{T}} = \pi$ so

$$\hat{\mathcal{T}}_0^* = \pi. \tag{5.61}$$

5.4.2 The perturbed problem

The first step to compute $\boldsymbol{\mathcal{U}}_6$ (as in Section 4.3) is to obtain X in a clever way. And we will consider the same expressions that in the previous chapter, i.e.:

$$\begin{aligned}
\frac{\partial \mathcal{U}_0}{\partial \boldsymbol{\mathcal{U}}_{0,0}}(\hat{\mathcal{T}}) &= \boldsymbol{A}_1 \cos(-t/2) - \boldsymbol{A}_2 \sin(-t/2),\\
\frac{\partial \mathcal{V}_0}{\partial \boldsymbol{\mathcal{U}}_{0,0}}(\hat{\mathcal{T}}) &= \boldsymbol{A}_1 \sin(-t/2) + \boldsymbol{A}_2 \cos(-t/2),\\
\frac{\partial \dot{\mathcal{U}}_0}{\partial \boldsymbol{\mathcal{U}}_{0,0}}(\hat{\mathcal{T}}) &= \boldsymbol{A}_3 \cos(-t/2) - \boldsymbol{A}_4 \sin(-t/2),\\
\frac{\partial \dot{\mathcal{U}}_0}{\partial \boldsymbol{\mathcal{U}}_{0,0}}(\hat{\mathcal{T}}) &= \boldsymbol{A}_3 \sin(-t/2) + \boldsymbol{A}_4 \cos(-t/2),
\end{aligned} \tag{5.62}$$

where:

$$\begin{aligned}
\boldsymbol{A}_1(\hat{\mathcal{T}}) &= \left[\frac{\partial \bar{\mathcal{U}}_0}{\partial \boldsymbol{\mathcal{U}}_{0,0}} + \frac{\bar{\mathcal{V}}_0}{2}\frac{\partial t}{\partial \boldsymbol{\mathcal{U}}_{0,0}}\right](\hat{\mathcal{T}}),\\
\boldsymbol{A}_2(\hat{\mathcal{T}}) &= \left[\frac{\partial \bar{\mathcal{V}}_0}{\partial \boldsymbol{\mathcal{U}}_{0,0}} - \frac{\bar{\mathcal{U}}_0}{2}\frac{dt}{\partial \boldsymbol{\mathcal{U}}_{0,0}}\right](\hat{\mathcal{T}}),\\
\boldsymbol{A}_3(\hat{\mathcal{T}}) &= \left[\frac{\partial \dot{\bar{\mathcal{U}}}_0}{\partial \boldsymbol{\mathcal{U}}_{0,0}} + 2\left(\bar{\mathcal{U}}_0^2 + 3\bar{\mathcal{V}}_0^2\right)\xi_1^3\frac{\partial \bar{\mathcal{V}}_0}{\partial \boldsymbol{\mathcal{U}}_{0,0}} + 4\bar{\mathcal{U}}_0\bar{\mathcal{V}}_0\xi_1^3\frac{\partial \bar{\mathcal{U}}_0}{\partial \boldsymbol{\mathcal{U}}_{0,0}} + \frac{\dot{\bar{\mathcal{V}}}_0 - 2(\bar{\mathcal{U}}_0^2 + \bar{\mathcal{V}}_0^2)\bar{\mathcal{U}}_0\xi_1^3}{2}\frac{\partial t}{\partial \boldsymbol{\mathcal{U}}_{0,0}}\right](\hat{\mathcal{T}}),\\
\boldsymbol{A}_4(\hat{\mathcal{T}}) &= \left[\frac{\partial \dot{\bar{\mathcal{V}}}_0}{\partial \boldsymbol{\mathcal{U}}_{0,0}} - 2\left(3\bar{\mathcal{U}}_0^2 + \bar{\mathcal{V}}_0^2\right)\xi_1^3\frac{\partial \bar{\mathcal{U}}_0}{\partial \boldsymbol{\mathcal{U}}_{0,0}} - 4\bar{\mathcal{U}}_0\bar{\mathcal{V}}_0\xi_1^3\frac{\partial \bar{\mathcal{V}}_0}{\partial \boldsymbol{\mathcal{U}}_{0,0}} - \frac{\dot{\bar{\mathcal{U}}}_0 + 2(\bar{\mathcal{U}}_0^2 + \bar{\mathcal{V}}_0^2)\bar{\mathcal{V}}_0\xi_1^3}{2}\frac{\partial t}{\partial \boldsymbol{\mathcal{U}}_{0,0}}\right](\hat{\mathcal{T}}),
\end{aligned} \tag{5.63}$$

and therefore

$$X = RA = \begin{pmatrix} \cos(-t/2) & -\sin(-t/2) & 0 & 0\\ \sin(-t/2) & \cos(-t/2) & 0 & 0\\ 0 & 0 & \cos(-t/2) & -\sin(-t/2)\\ 0 & 0 & \sin(-t/2) & \cos(-t/2)\end{pmatrix}\begin{pmatrix}\boldsymbol{A}_1\\ \boldsymbol{A}_2\\ \boldsymbol{A}_3\\ \boldsymbol{A}_4\end{pmatrix}, \tag{5.64}$$

where A is the matrix that has rows given by $\boldsymbol{A}_i$, $i = 1, ..., 4$.

Thus, we only need to compute previously:

$$\begin{aligned}
\frac{\partial \bar{\boldsymbol{\mathcal{U}}}_0}{\partial \boldsymbol{\mathcal{U}}_{0,0}}(\hat{\mathcal{T}}) &= \frac{\partial \bar{\boldsymbol{\mathcal{U}}}_0}{\partial \bar{\boldsymbol{\mathcal{U}}}_{0,0}}(\hat{\mathcal{T}})\frac{\partial \bar{\boldsymbol{\mathcal{U}}}_{0,0}}{\partial \boldsymbol{\mathcal{U}}_{0,0}},\\
\frac{\partial t}{\partial \boldsymbol{\mathcal{U}}_{0,0}}(\hat{\mathcal{T}}) &= \frac{\partial t}{\partial \bar{\boldsymbol{\mathcal{U}}}_{0,0}}(\hat{\mathcal{T}})\frac{\partial \bar{\boldsymbol{\mathcal{U}}}_{0,0}}{\partial \boldsymbol{\mathcal{U}}_{0,0}}.
\end{aligned} \tag{5.65}$$

As in the Chapter 4, the computation of $\dfrac{\partial \bar{\boldsymbol{\mathcal{U}}}_{0,0}}{\partial \boldsymbol{\mathcal{U}}_{0,0}}$ is immediate from (5.57) and in the case of ejection orbits it is simply the identity matrix Id since we just need to substitute in this matrix the values of the initial conditions $(0, 0, n\cos\theta_0, n\sin\theta_0)$ for an ejection orbit,

$$\frac{\partial \bar{\boldsymbol{\mathcal{U}}}_{0,0}}{\partial \boldsymbol{\mathcal{U}}_{0,0}}(0,0,n\cos\theta_0,n\sin\theta_0)=\left.\begin{pmatrix}1&0&0&0\\0&1&0&0\\-4\mathcal{U}_{0,0}\mathcal{V}_{0,0}&-2\mathcal{U}_{0,0}^2-6\mathcal{V}_{0,0}^2&1&0\\6\mathcal{U}_{0,0}^2+2\mathcal{V}_{0,0}^2&4\mathcal{U}_{0,0}\mathcal{V}_{0,0}&0&1\end{pmatrix}\right|_{(0,0,n\cos\theta_0,n\sin\theta_0)}=Id. \tag{5.66}$$

For our purpose it is enough to express A and R as

$$A_e=\begin{pmatrix}\cos(n\hat{\mathcal{T}})+\mathcal{O}(\xi_1^3)&\mathcal{O}(\xi_1^3)&\frac{\sin(n\hat{\mathcal{T}})+\mathcal{O}(\xi_1^3)}{n}&\frac{1}{n}\mathcal{O}(\xi_1^3)\\ \mathcal{O}(\xi_1^3)&\cos(n\hat{\mathcal{T}})+\mathcal{O}(\xi_1^3)&\frac{1}{n}\mathcal{O}(\xi_1^3)&\frac{\sin(n\hat{\mathcal{T}})+\mathcal{O}(\xi_1^3)}{n}\\ -n\sin(n\hat{\mathcal{T}})+n\mathcal{O}(\xi_1^3)&n\mathcal{O}(\xi_1^3)&\cos(n\hat{\mathcal{T}})+\mathcal{O}(\xi_1^3)&\mathcal{O}(\xi_1^3)\\ n\mathcal{O}(\xi_1^3)&-n\sin(n\hat{\mathcal{T}})+n\mathcal{O}(\xi_1^3)&\mathcal{O}(\xi_1^3)&\cos(n\hat{\mathcal{T}})+\mathcal{O}(\xi_1^3)\end{pmatrix}, \tag{5.67}$$

$$R_e=Id+\begin{pmatrix}\mathcal{O}(\xi_1^6)&\mathcal{O}(\xi_1^3)&0&0\\ \mathcal{O}(\xi_1^3)&\mathcal{O}(\xi_1^6)&0&0\\0&0&\mathcal{O}(\xi_1^6)&\mathcal{O}(\xi_1^3)\\0&0&\mathcal{O}(\xi_1^3)&\mathcal{O}(\xi_1^6)\end{pmatrix}, \tag{5.68}$$

where the subscript $_e$ denotes the evaluation in the initial condition of the ejection orbit.

Therefore,

$$X_e^{-1}\boldsymbol{F}_6(\mathcal{U}_{0,e},\mathcal{V}_{0,e})=24\sin^5(n\hat{\mathcal{T}})\begin{pmatrix}-\frac{\sin(n\hat{\mathcal{T}})\cos\theta_0(2\sin^4\theta_0-4\sin^2\theta_0+1)}{n}+\frac{1}{n}\mathcal{O}(\xi_1^3)\\ -\frac{\sin(n\hat{\mathcal{T}})\sin\theta_0(2\sin^4\theta_0-1)}{n}+\frac{1}{n}\mathcal{O}(\xi_1^3)\\ \cos(n\hat{\mathcal{T}})\cos\theta_0(2\sin^4\theta_0-4\sin^2\theta_0+1)+\mathcal{O}(\xi_1^3)\\ \cos(n\hat{\mathcal{T}})\cos\theta_0(2\sin^4\theta_0-1)+\mathcal{O}(\xi_1^3)\end{pmatrix}.$$

Integrating until the time $\hat{\mathcal{T}}_0^*=\pi$ and multiplying by X_e we obtain

$$\begin{aligned}\mathcal{U}_{6,e}(\hat{\mathcal{T}}_0^*)&=-\frac{15(-1)^n\mu\pi\cos\theta_0(2\cos^4\theta_0-1)}{2n}+\frac{\mu}{n}\mathcal{O}(\xi_1^3),\\ \mathcal{V}_{6,e}(\hat{\mathcal{T}}_0^*)&=-\frac{15(-1)^n\mu\pi\sin\theta_0(2\sin^4\theta_0-1)}{2n}+\frac{\mu}{n}\mathcal{O}(\xi_1^3),\\ \dot{\mathcal{U}}_{6,e}(\hat{\mathcal{T}}_0^*)&=-\frac{4(-1)^n\mu\cos\theta_0(2\cos^4\theta_0-1)}{n}+\mu\mathcal{O}(\xi_1^3),\\ \dot{\mathcal{V}}_{6,e}(\hat{\mathcal{T}}_0^*)&=-\frac{4(-1)^n\mu\sin\theta_0(2\sin^4\theta_0-1)}{n}+\mu\mathcal{O}(\xi_1^3).\end{aligned} \tag{5.69}$$

The next step is to compute $\hat{\mathcal{T}}_6^*(\theta_0)$ via the IFT:

$$\hat{\mathcal{T}}_6^*(\theta_0)=-\left[\frac{\mathcal{U}_{0,e}\dot{\mathcal{U}}_{6,e}+\dot{\mathcal{U}}_{0,e}\mathcal{U}_{6,e}+\mathcal{V}_{0,e}\dot{\mathcal{V}}_{6,e}+\dot{\mathcal{V}}_{0,e}\mathcal{V}_{6,e}}{\dot{\mathcal{U}}_{0,e}^2+\dot{\mathcal{V}}_{0,e}^2+\mathcal{U}_{0,e}\ddot{\mathcal{U}}_{0,e}+\mathcal{V}_{0,e}\ddot{\mathcal{V}}_{0,e}}\right](\hat{\mathcal{T}}_0^*)=\frac{15\mu\pi(3\cos(4\theta_0)+1))}{8n^2}+\frac{\mu}{n^2}\mathcal{O}(\xi_1^3). \tag{5.70}$$

It is important to remark at this point, that thanks to the recursivity

$$\boldsymbol{\mathcal{U}}_{k,e}(\hat{\mathcal{T}}) = X_e(\hat{\mathcal{T}}) \int_0^{\hat{\mathcal{T}}} X_e^{-1}(\hat{\mathcal{T}}) \left[\mu \boldsymbol{\mathcal{F}}_k(\mathcal{U}_{<k,e}, \mathcal{V}_{<k,e}) + \boldsymbol{\mathcal{G}}_k(\boldsymbol{\mathcal{U}}_{<k,e})\right] d\hat{\mathcal{T}},$$

where

$$\boldsymbol{\mathcal{F}}_k(\mathcal{U}_{<k,e}, \mathcal{V}_{<k,e}) = \left[\sum_{i=6}^{k} \boldsymbol{F}_i(\mathcal{U}_{<k,e}, \mathcal{V}_{<k,e})\xi_2^i\right]_{(k)}$$

$$\begin{aligned}\boldsymbol{\mathcal{G}}_k(\boldsymbol{\mathcal{U}}_{<\boldsymbol{k},\boldsymbol{e}}) = \Bigg[& \frac{1}{2!} D^2 \boldsymbol{F}_0(\boldsymbol{\mathcal{U}}_0) \left\{ \sum_{i=6}^{k-6} \boldsymbol{\mathcal{U}}_{i,e}\xi_2^i, \sum_{i=6}^{k-6} \boldsymbol{\mathcal{U}}_{i,e}\xi_2^i \right\} \\ & + \frac{1}{3!} D^3 \boldsymbol{F}_0(\boldsymbol{\mathcal{U}}_0) \left\{ \sum_{i=6}^{k-12} \boldsymbol{\mathcal{U}}_{i,e}\xi_2^i, \sum_{i=6}^{k-12} \boldsymbol{\mathcal{U}}_{i,e}\xi_2^i, \sum_{i=6}^{k-12} \boldsymbol{\mathcal{U}}_{i,e}\xi_2^i \right\} \\ & + \frac{1}{4!} D^4 \boldsymbol{F}_0(\boldsymbol{\mathcal{U}}_0) \left\{ \sum_{i=6}^{k-18} \boldsymbol{\mathcal{U}}_{i,e}\xi_2^i, \sum_{i=6}^{k-18} \boldsymbol{\mathcal{U}}_{i,e}\xi_2^i, \sum_{i=6}^{k-18} \boldsymbol{\mathcal{U}}_{i,e}\xi_2^i, \sum_{i=6}^{k-18} \boldsymbol{\mathcal{U}}_{i,e}\xi_2^i \right\} \\ & + \frac{1}{5!} D^5 \boldsymbol{F}_0(\boldsymbol{\mathcal{U}}_0) \left\{ \sum_{i=6}^{k-24} \boldsymbol{\mathcal{U}}_{i,e}\xi_2^i, \sum_{i=6}^{k-24} \boldsymbol{\mathcal{U}}_{i,e}\xi_2^i, \sum_{i=6}^{k-24} \boldsymbol{\mathcal{U}}_{i,e}\xi_2^i, \sum_{i=6}^{k-24} \boldsymbol{\mathcal{U}}_{i,e}\xi_2^i, \sum_{i=6}^{k-24} \boldsymbol{\mathcal{U}}_{i,e}\xi_2^i \right\} \Bigg]_{(k)},\end{aligned}$$

we have that all the successive orders are of the form

$$\mathcal{U}_k = \frac{\mu}{n}\mathcal{O}(1), \quad \mathcal{V}_k = \frac{\mu}{n}\mathcal{O}(1), \quad \dot{\mathcal{U}}_k = \mu\mathcal{O}(1), \quad \dot{\mathcal{V}}_k = \mu\mathcal{O}(1), \quad \forall k \geq 6,$$

where $\mathcal{O}(1)$ denotes that the function are uniform in μ, ξ_1^3 and $1/n^{1/3}$ and, similarly

$$\hat{\mathcal{T}}_k^* = \frac{\mu}{n^2}\mathcal{O}(1) \quad \forall k \geq 6.$$

In this way, we prove

$$\mathcal{M}_n(\theta_0) = -\frac{15\mu\pi\sin(4\theta_0)}{4}\xi_2^6 + \mu\mathcal{O}(\xi_1^3\xi_2^6) + \mu\mathcal{O}(\xi_2^8). \tag{5.71}$$

Therefore, choosing $\xi_1 = \xi_2 = \xi$ with $\xi = \min(\xi_1, \xi_2)$ we obtain

$$\mathcal{M}_n(\theta_0) = -\frac{15\mu\pi\sin(4\theta_0)}{4}\xi^6 + \mu\mathcal{O}(\xi^8). \tag{5.72}$$

5.5 Results for the Hill problem

As we have seen in Chapter 1, Hill's problem is a limit case of RTBP. In this way, the results obtained in the previous sections can easily be extrapolated to the case of Hill's problem. In particular, if in (2.31) we introduce the new variables

$$\begin{cases} u_h = \sqrt{\dfrac{2}{K}} U_h, \\ v_h = \sqrt{\dfrac{2}{K}} V_h, \\ \tau = 2\sqrt{K}s, \end{cases} \tag{5.73}$$

we obtain the system

$$\begin{cases} \ddot{U} = -U + \dfrac{8(U^2+V^2)\dot{V}}{K^{3/2}} + \dfrac{12\left[2\left(U^4-2U^2V^2-V^4\right)+(U^2+V^2)^2\right]U}{K^3}, \\ \ddot{V} = -V - \dfrac{8(U^2+V^2)\dot{U}}{K^{3/2}} + \dfrac{12\left[2\left(V^4-2U^2V^2-U^4\right)+(U^2+V^2)^2\right]V}{K^3}, \end{cases} \tag{5.74}$$

which is the same system of equations that we have obtained in (5.9) imposing $\mu = 1$ and recalling that $\varepsilon = 1/\sqrt{K}$.

In this way, using the extra symmetry (1.16b) of the Hill problem we obtain the following Corollary of Theorem B:

Corollary 5.5.1. *In the Hill problem, for all $n \in \mathbb{N}$, there exists a $\hat{K}(n)$ such that for $K \geq \hat{K}(n)$ there exist exactly four n-EC orbits, which can be characterized by:*

- *Two n-EC orbits themselves symmetric with respect to the x axis and one symmetric to the other over the y axis.*
- *Two n-EC orbits themselves symmetric with respect to the y axis and one symmetric to the other over the x axis.*

The respective families (when varying K) are labelled by α_n, γ_n, β_n and δ_n.

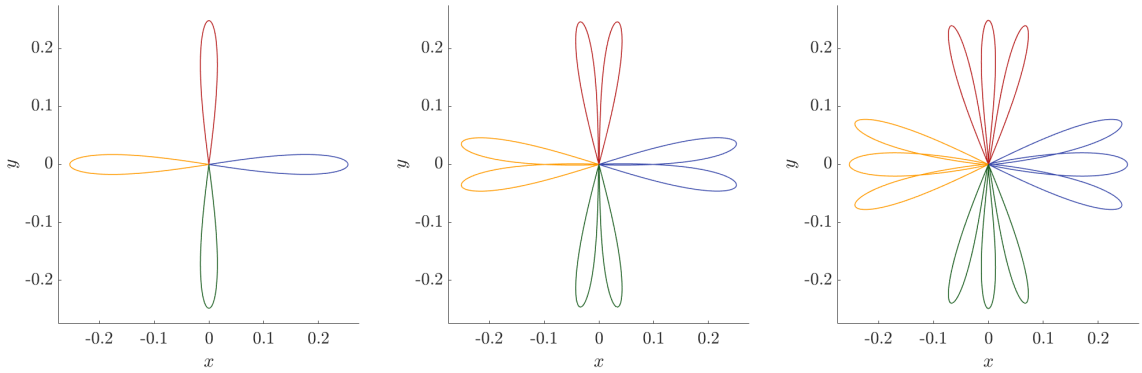

Figure 5.2: Trajectories of the four n-EC orbits α_n (yellow), β_n (green), γ_n (blue) and δ_n (red) for $n = 1, 2, 3$ (from left to right) and $K = 8$.

It is important to note that the proof is exactly the same with the observation, as we have said before, that the families of orbits that were symmetric with respect to the x axis in the RTBP (α_n and γ_n) are now also symmetric one of the other with respect to the y axis, and the families were symmetric one of the other in the restricted problem (β_n and δ_n) are now also symmetric themselves with respect to the y axis (see Figure 5.2).

Furthermore, thanks to the fact that the polynomials $\hat{P}_k$ and $\hat{Q}_k$ disappear, it is not necessary to consider an expansion in terms of $\varepsilon = 1/\sqrt{K}$ and it can be considered directly an expansion on $\epsilon = 1/K^{3/2}$.

As in the previous case, thanks to the fact that the polynomials $\hat{P}_k$ and $\hat{Q}_k$ disappear, it is not necessary to consider an expansion in terms of $\xi = 1/\sqrt{L}$ and it can be considered directly an expansion on $\eta = 1/L^{3/2}$.

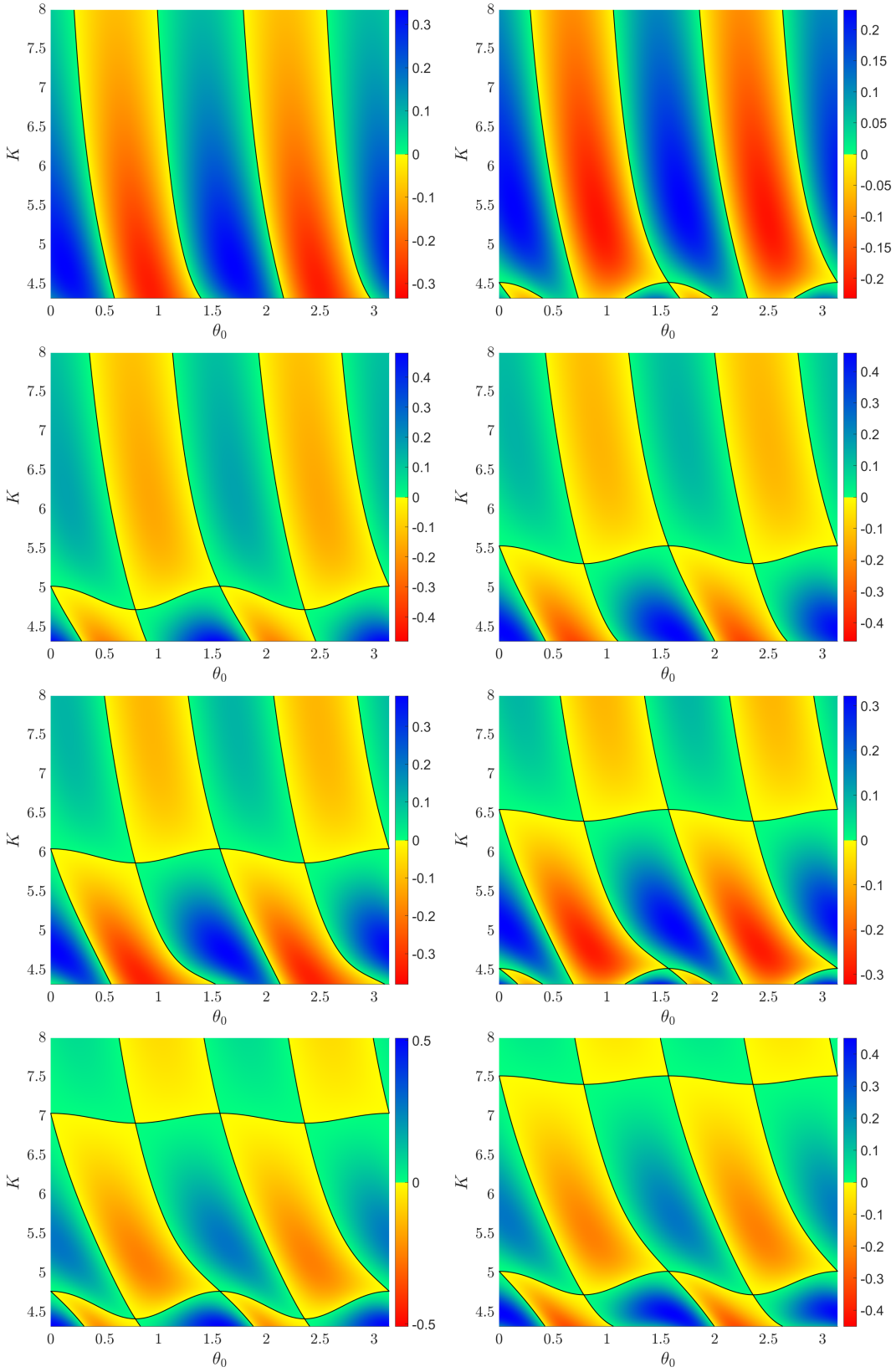

Figure 5.3: Value of the angular momenta of the ejection orbits at the n intersection with Σ_m for $K \in [K_{L_1}, 8]$ and $n = 3, ..., 10$. In black the values corresponding to an n-EC orbits.

Similarly, if we introduce $K = Ln^{2/3}$, that is, we consider the change

$$\begin{cases} u_h = \dfrac{\sqrt{2}}{\sqrt{L}n^{1/3}}\mathcal{U}_h, \\ v_h = \dfrac{\sqrt{2}}{\sqrt{L}n^{1/3}}\mathcal{V}_h, \\ \hat{\mathcal{T}} = \dfrac{2\sqrt{L}}{n^{2/3}}s, \end{cases} \tag{5.75}$$

we obtain the same system of equations as (5.28) putting $\mu = 1$ and considering $\xi = 1/\sqrt{L}$. In this way we can obtain the following corollary of Theorem A:

Corollary 5.5.2. *There exists a $\hat{L}$ such that for $L \geq \hat{L}$ and for any value of $n \in \mathbb{N}$ and $K = Ln^{2/3}$, there exist exactly four n-EC orbits, which can be characterized in the same way as the previous corollary.*

In this way, if we do the numerical exploration to compute the n-EC orbits that exist for values of $K \geq K_L$ (see Figure 5.3) we see that, as expected by the Corollary 5.5.2 the value of $\hat{K}$ grows with n.

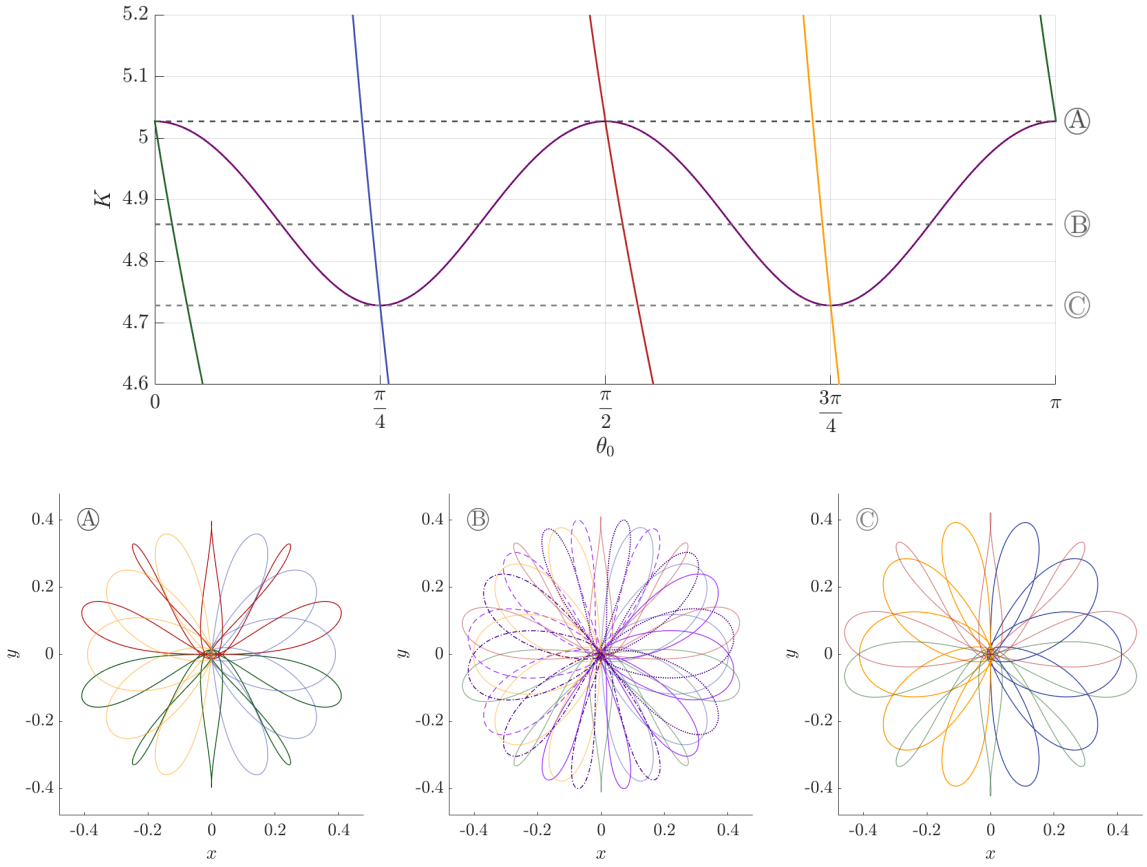

Figure 5.4: Top. Initial conditions for the 5-EC orbits corresponding to the families α_n (yellow), β_n (green), γ_n (blue), δ_n (red) and the new families of orbits (purple) as function of K. Bottom. The trajectories of the orbits (in correspondence with the previous color) that exists for the values of K denoted previously. The values of K correspond to the value of the bifurcation $K \approx 5.02714993$ (left), a value where we have eight 5-EC orbits $K = 4.86$ (middle) and the value of collapse $K \approx 4.72835275$.

Before going into more detail on the value of $\hat{K}$ let us make a few comments about Figure 5.3. It is important to note that thanks to the extra symmetry we could only study the ejection orbits with $\theta_0 \in [0, \pi/2)$, but in order to visualize the evolution of the n-EC orbits we will consider the interval $\theta_0 \in [0, \pi)$ in Figure 5.3. In this figure we observe how at least the first new families of n-EC orbits that appear are born from two of the original families (α_n and γ_n, or β_n and δ_n) when the angle of ejection θ_0 is 0 and $\pi/2$ respectively (i.e. $\vartheta_0 = 0, \pi$) and collapse into the two other original families when the value of θ_0 is $\pi/4$ and $3\pi/4$ (i.e. $\vartheta_0 = \pi/2, 3\pi/2$) (see for example Figure 5.4).

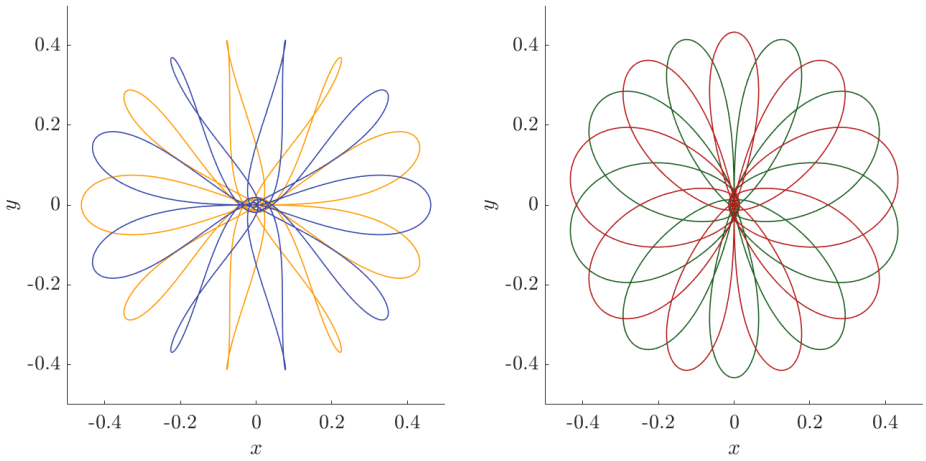

Figure 5.5: Trajectories of 9-EC periodic orbits associated with α_9 (yellow) and γ_9 (blue) for $K \approx 4.77318771$ (left) and β_9 (green) and δ_9 (red) for $K \approx 4.42215362$ (right).

These respective values are very particular, since when these bifurcations take place we have that the n-EC orbits are periodic or are part of a periodic EC orbit. In particular we have:

- If the θ_0 of β_n is 0 or $\pi/2$ (therefore θ_0 of δ_n is $\pi/2$ or 0) then we have periodic EC orbit formed by β_n and δ_n (see Figure 5.4 left). Analogously, if the θ_0 of α_n is $\pi/4$ or $3\pi/4$ (therefore θ_0 of γ_n is $3\pi/4$ or $\pi/4$) then we have periodic EC orbit formed by α_n and γ_n (see Figure 5.4 right).

- If the θ_0 of β_n is $\pi/4$ or $3\pi/4$ (therefore θ_0 of δ_n is $3\pi/4$ or $\pi/4$) then β_n and δ_n are periodic *EC* orbits (see Figure 5.5 right). Analogously, if the θ_0 of α_n is 0 or $\pi/2$ (therefore θ_0 of γ_n is $\pi/2$ or 0) then α_n and γ_n are periodic EC orbits (see Figure 5.5 left).

Regarding the value of $\hat{K}(n)$, it is important to remark that the numerical value of $\hat{K}(n)$ obtained has the same shape as the analytical bound of the Corollary 5.5.2. In particular, if we draw the curve $Ln^{2/3}$ with $L = 2^{2/3}$ we can see how it practically matches the value of the numerical bound obtained for $\hat{K}$ (see Figure 5.6).

To conclude, we have seen how not only does the value of $\hat{K}(n)$ follow the curve $Ln^{2/3}$ with $L = 2^{2/3}$, but also the successive bifurcations (the values of K where appear new EC orbits) are closely related to the curves $Ln^{2/3}$ with $L = (2/p)^{2/3}$ being p a natural number. In particular, in Figure 5.7 we can see how the value of the successive bifurcations coincides with the curves $Ln^{2/3}$ with $L = (2/p)^{2/3}$ and $p = 1, ..., 10$.

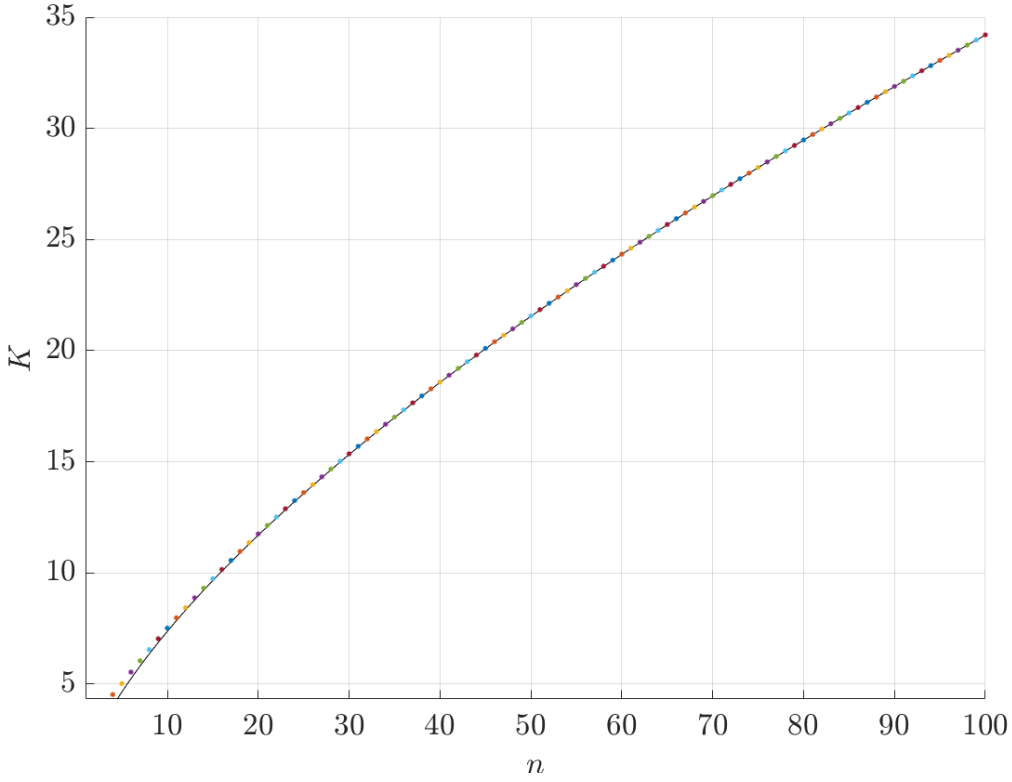

Figure 5.6: Dots: Values of $\hat{K}(n)$. Black line, curve $Ln^{2/3}$ with $L = 2^{2/3}$.

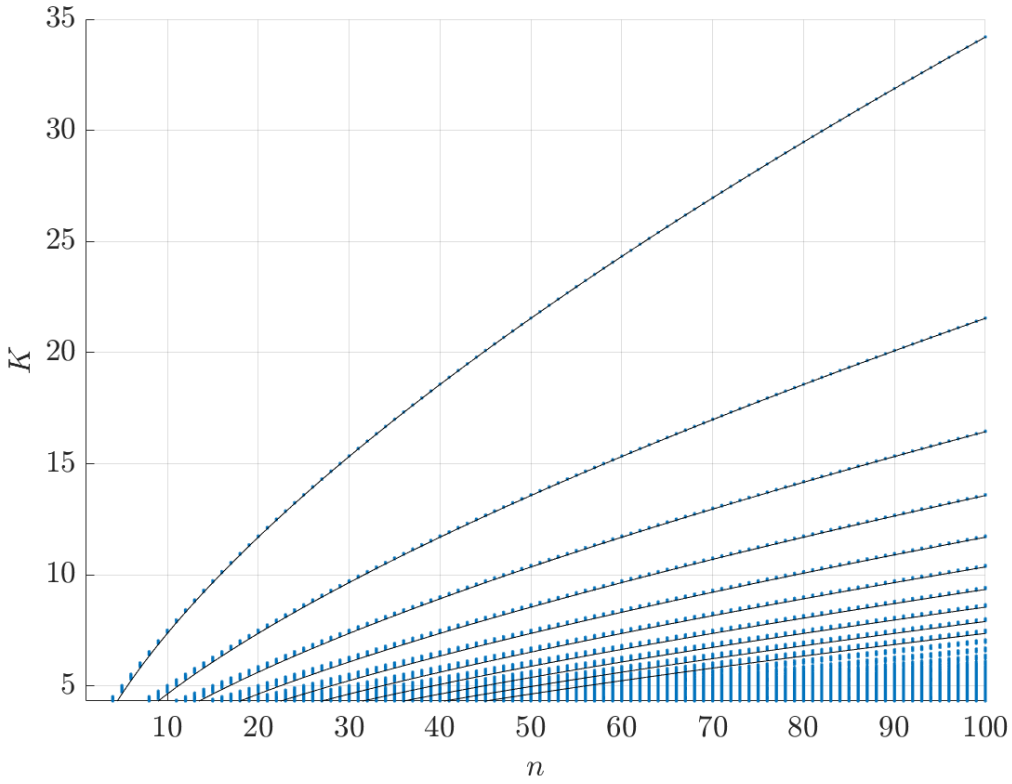

Figure 5.7: In color values of K where exists more than 4 n-EC orbits for $n = 1, .., 100$. The black lines correspond to the curves $Ln^{2/3}$ with $L = (2/p)^{2/3}$ and $p = 1, ..., 10$.

Chapter 6

Transit regions and ejection/collision orbits

In this chapter, we want to analyse numerically the behaviour (evolution) of the whole set of ejection orbits, which can be EC orbits or not, for a finite range of time, for a $\mu \in (0,1)$ given and a value of the Jacobi constant C. So the starting initial condition is always ejection from the first primary.

As we have seen in Chapter 3, the dynamics of the EC orbits is very rich as we consider smaller C values (i.e. less restrictive Hill regions). In particular, we will focus on a phenomenon observed in the previous mentioned section, the role of the Lyapunov periodic orbit around L_1 (LPO_1).

We will take $C \in [C_{L_{2,3}}, C_{L_1})$, recall that $C_{L_{2,3}}$ refers to C_{L_2} if $\mu \in (0, 0.5]$ (the equilibrium point L_2 is located on the left hand side of the small primary on the negative x-axis) and to C_{L_3} if $\mu \in [0.5, 1)$ (the equilibrium point L_3 is located on the right hand side of the small primary on the positive x-axis). The reasons for that choice are the following: for bigger values of C, the bounded Hill's regions of motion (where the motion of the particle is possible) are simply two close circle-like shaped regions, each one around each primary, so no possible interaction or transit from the region around one primary and the region around the other primary is possible, and the ejection orbits are "pretty" simple (see Figures 1.3e 1.3f). However, for any $C \in [C_{L_{2,3}}, C_{L_1})$, the Hill's region allows to move from a region around one primary to a region around the other one, and for these values of C, the role of LPO_1 in the transit (or not) is fundamental (see Figures 1.3c 1.3d). This periodic orbit and its invariant stable and unstable manifolds will play an essential role, not only to explain transition between the two regions, but also, to find an infinity number of heteroclinic orbits connecting the ejection and the periodic orbit, on one hand, to compute also an infinity number of EC orbits, on the other hand, and moreover, an infinity number of homoclinic orbits to the LPO_1. The interaction among these infinities, and the effects on the ejection orbits result in a chaotic classification of the dynamical behavior of the ejection orbits. We also remark that other periodic orbits in this same level of fixed C exist and do interfere with the ejection orbits. For smaller values of $C < C_{L_{2,3}}$, the Hill's region allows to connect the ejection with the infinity and there appear other Lyapunov and other kind of periodic orbits and, therefore, the dynamics gets much more complicated.

So, focussed on the description of the behaviour of the ejection orbits, our main goal on this chapter is threefold: *first*, to describe big sets of ejecting orbits from one primary that transit to the region around the other primary. A key role in this transition is played by the heteroclinic connections between one primary and the LPO_1, denoted by $P_i - LPO_1$, $i = 1$ or 2. Two main important consequences are explained: such heteroclinic connections act as barriers of transition regions and, moreover, allow to classify the geometrical trajectory of the ejection (collision) orbits. *Second*, although in principle the classification seems clear to apply, we show that this is not the case at all, due to the existence

of a chaotic infinity of heteroclinic connections $P_i - LPO_1$. We explain how this chaotic infinity is generated. *Third*, for a $\mu > 0$ given and C fixed, we want to visualize the trajectory that an ejection orbit will describe for a finite range of time. That is, the key point is that this description will be done by means of 2D colour code diagram plots, which contain the global dynamics of the whole set of individual ejection orbits. All the ingredients described before appear in these meaningful 2D plots that provide a global perspective.

Before proceeding we note that the contents of this chapter have been extracted from [ORS21b].

6.1 Transit Regions

A main goal in this Section is to study *big* regions of ejection-transit orbits. This means big sets of orbits where the particle ejects from one primary and, in a natural way, *crosses* a Poincaré section Σ (defined by $x = const$) and goes to the region where the other primary is located. In order to somewhat classify the ejecting orbits, we will distinguish among the ejection orbits that, after describing n *close passages* around the primary P_i (from which the orbit started) cross the section Σ. Numerically, the condition of close passage means that, in the suitable Levi-Civita coordinates (depending on the primary we are regularizing), a minimum in the (square) distance u^2+v^2 is achieved so the conditions $f(\boldsymbol{u}) = uu' + vv' = 0$ and $f'(\boldsymbol{u}) > 0$ where $\boldsymbol{u} = (u, v, u', v')$, are satisfied.

In Figure 6.1 left, and for $\mu = 0.5$, $C = C_{L_2}$, we show in red big regions (the (x, y) projection) of ejection orbits from P_1 that after n close passages around P_1 (for $n = 0, 1, 2, 3$) cross Σ defined by $x = 0.1$.

A natural question arises: how do we find such big regions? The answer is through the heteroclinic connections between a primary and the LPO_1, denoted by $P_i - LPO_1$, $i = 1, 2$. We will call a *heteroclinic connection* $P_i - LPO_1$, $i = 1$ or 2, the orbit that ejects from P_i, $i = 1$ or 2, and ends asymptotically in the LPO_1.

So, first of all, let us compute those possible heteroclinic connections between a primary and the LPO_1, such that the particle, after ejecting from a primary, describes n close passages around it and goes directly to the LPO_1 where it ends asymptotically.

We describe how to compute a heteroclinic connection $P_1 - LPO_1$, (we proceed similarly for the other case, $P_2 - LPO_1$). Since a heteroclinic connection $P_1 - LPO_1$ is an orbit that belongs to $W^e(P_1) \cap W^s(LPO_1)$, where $W^e(P_i)$ denotes the manifold of the ejection orbits of P_i (similarly we will use $W^c(P_i)$ for denoting the manifold of collision orbits of P_i) and $W^s(LPO_1)$ denotes the stable manifold associated with LPO_1, the numerical strategy to compute such connections, given $\mu > 0$ and for a fixed value of C, consists, roughly speaking, in the following steps: to compute the 2D manifold $W^s(LPO_1)$ (one of the two possible branches) up to a given Poincaré section Σ, giving rise to a curve denoted by γ_s (see for example [BMO13] for more details and references therein); to compute the 2D manifold $W^e(P_1)$ up to Σ, giving rise to a curve denoted by γ_e and to look for intersection points between both curves. Each intersection point belongs to a heteroclinic connection, since the solution at this intersection point, integrated forward in time, tends asymptotically to the LPO_1 and backwards in time to the primary P_1.

In order to be more precise, and consider not only the first intersection but the i-th intersection with Σ, to take into account the number n of close passages around the primary, to distinguish between the stable or unstable manifold $W^{s,u}(LPO_1)$ and the branch $+, -$ (recall Chapeter 1), and the possibility of ejection/collision (we will use a subscript e/c), we now provide the detailed description of the notation we will use at the same time as the steps involved to compute heteroclinic orbits. We remark that all the notation introduced is the necessary one to distinguish among the different properties we

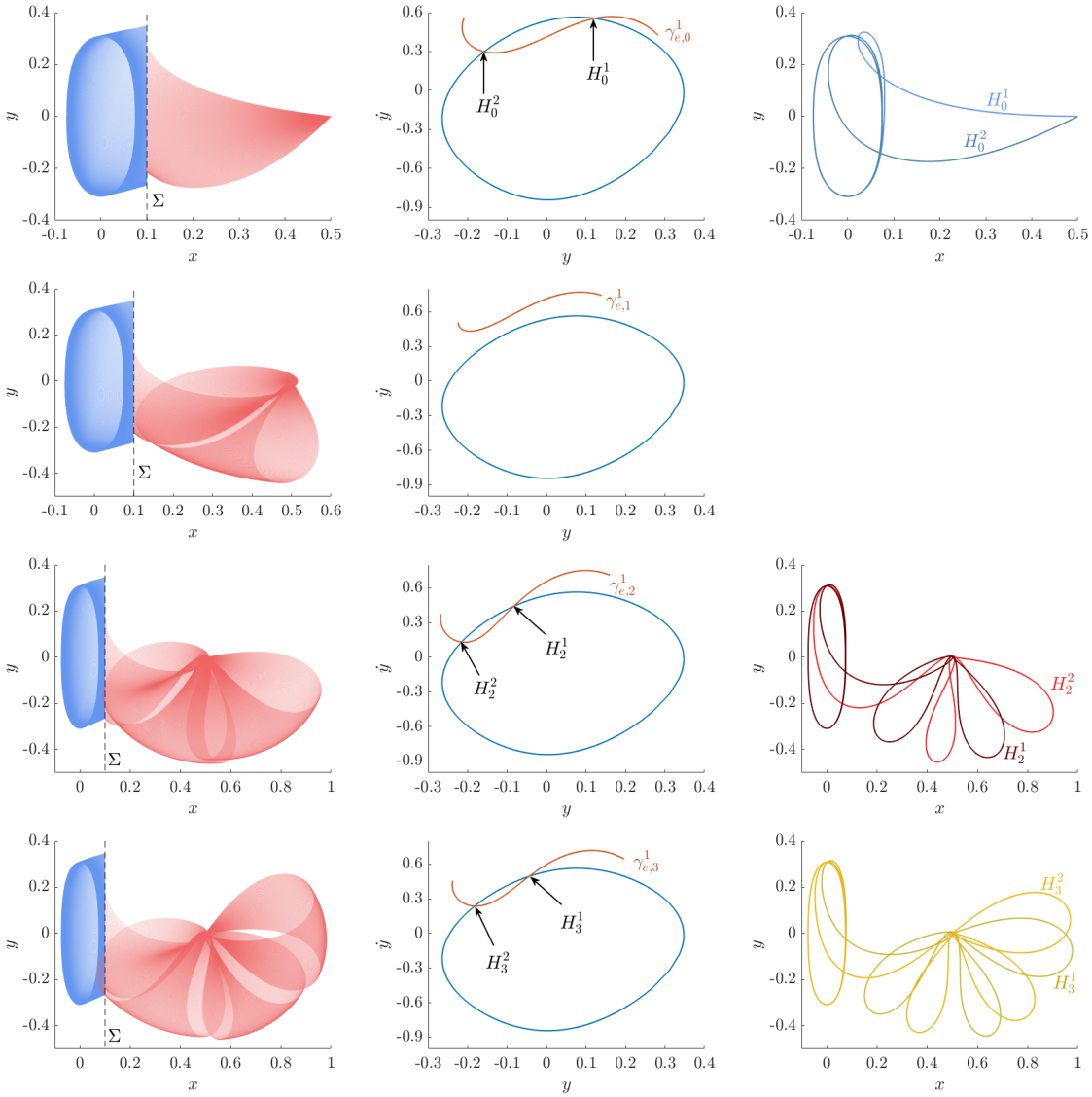

Figure 6.1: $\mu = 0.5$, $C = C_{L_2}$. Left. (x, y) projection. A set of ejection orbits of $W^e(P_1)$ (in red) such that after n close passages around P_1 reach Σ. ($n = 0$ first row, $n = 1$ second row, $n = 2$ third row, $n = 3$ fourth row). Also the orbits of $W^{s,+}(LPO_1)$ (in blue) up to Σ^+ are plotted. Middle. (y, y') projection of curves $\gamma_s^{+,1}$ (in blue) and $\gamma_{e,n}^1$ (in red). Right. (x, y) projection of two heteroclinic connections, H_n^1 and H_n^2, ejecting from P_1 and tending to the LPO_1. We remark that for $n = 1$ figure right does not appear since there are no heteroclinic orbits in this case as shown on the middle plot.

want to take into account.

(i) The first step to obtain a heteroclinic orbit from P_1 to the LPO_1 is to compute the corresponding orbit LPO_1 and its 2D positive stable manifold branch ($W^{s,+}(LPO_1)$) backwards in time up to a given Poincaré section Σ^+ defined by $x = x_{L_1} + d$ (for a suitable $d > 0$), giving rise to a $1D$ closed curve $\gamma_s^{+,1}$. In Figure 6.1 we take $\mu = 0.5$, $C = C_{L_2}$ and $d = 0.1$ so Σ^+ defined by $x = 0.1$; we show $W^{s,+}(LPO_1)$ ((x, y) projection in blue) on the left figures, and the curve $\gamma_s^{+,1}$ ((y, y') projection in blue) on the middle ones. In order to obtain an heteroclinic orbit from the LPO_1 to P_1, we will consider the intersection curve $\gamma_u^{+,1}$ obtained from $W^{u,+}(LPO_1) \cap \Sigma^+$ (integrating forward in time).

Similarly, taking into account the Poincaré section Σ^- defined by $x = x_{L_1} - d$ and the branch

$W^{s,-}(LPO_1)$ or $W^{u,-}(LPO_1)$, we obtain the curve $\gamma_s^{-,1}$ from the intersection $W^{s,-}(LPO_1) \cap \Sigma^-$, or the curve $\gamma_u^{-,1}$ from the intersection $W^{u,-}(LPO_1) \cap \Sigma^-$.

We generalise the notation for the curve $\gamma_{u/s}^{\pm,j}$ when considering the j-th crossing of the manifold of the LPO_1 with $\Sigma^\pm$.

So, roughly speaking, we consider the orbits that leave the LPO_1 asymptotically backwards in time up to the Poincaré section, giving rise to one curve.

(ii) The second step is to compute the 2D manifold of the orbits ejecting from (colliding to) the primary P_i, $i = 1$ or 2, $W^{e/c}(P_i)$, describing n *close passages* around the primary P_i (from which the orbit started) and crossing Σ (which will be a chosen Σ^+ or Σ^-). We will denote $\gamma_{e,n}^1$ ($\gamma_{c,n}^1$) the corresponding curve if the ejecting (colliding) body is P_1 and $\bar{\gamma}_{e,n}^1$ ($\bar{\gamma}_{c,n}^1$) if the ejecting (colliding) body is P_2. Due to the restriction of the n close passages around the primary for fixed n, only a piece of curve, not a closed one, for $\gamma_{e/c,n}^1$ or $\bar{\gamma}_{e/c,n}^1$ is obtained. We plot the (y, y') projection of the curves $\gamma_{e,n}^1$, for $n = 0, 1, 2, 3$ in Figure 6.1 middle, for $\mu = 0.5$, $C = C_{L_2}$.

We generalise the notation for the curve $\gamma_{e/c,n}^j$ (or $\bar{\gamma}_{e/c,n}^j$) when considering the 2D manifold of orbits that eject/collide with a primary, describe n close passages around it and cross Σ at the j-th time.

So, roughly speaking, we consider the orbits that eject from the primary, forward in time, describe n close passages to that primary and reach the Poincaré section, giving rise to another curve.

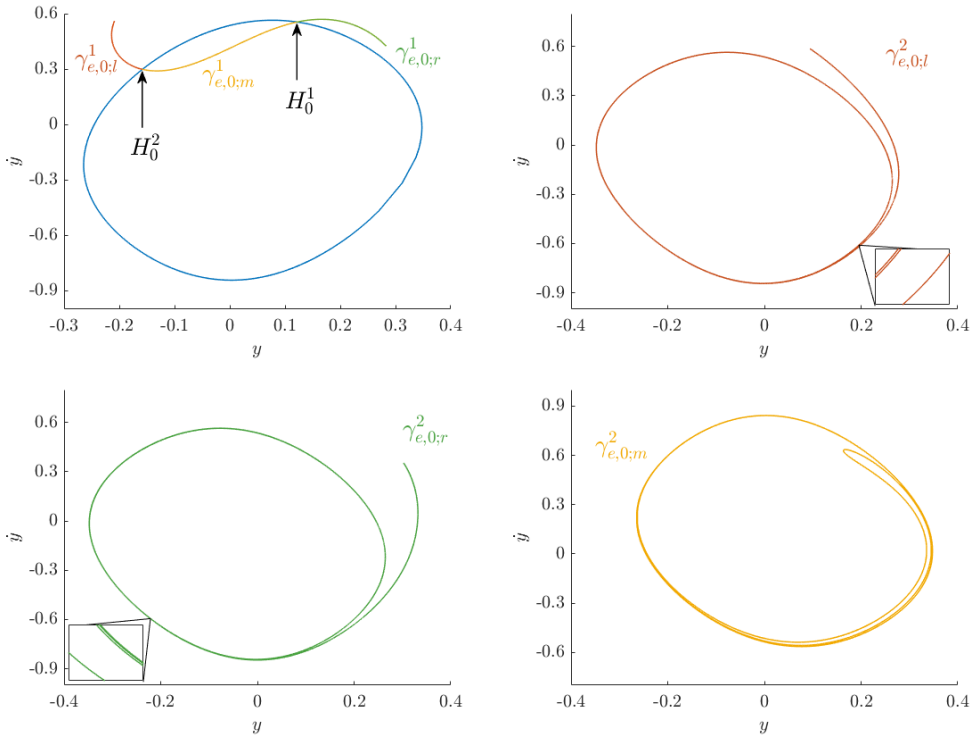

Figure 6.2: $\mu = 0.5$, $C = C_{L_2}$. $(y, \dot{y})$ projection. Top left. Curve $\gamma_s^{+,1}$ in blue and $\gamma_{e,0}^1$ as the union of the piece $\gamma_{e,0;l}^1$ (in red), $\gamma_{e,0;m}^1$ (in yellow) and $\gamma_{e,0;r}^1$ (in green). The points in $\gamma_{e,0;l}^1 \cup \gamma_{e,0;r}^1$ belong to non transit orbits and the points in $\gamma_{e,0;m}^1$ belong to transit ones. The spiralling curves $\gamma_{e,0;l/m/r}^2$ are obtained following the flow, forward in time, of points in $\gamma_{e,0;l}^1$ (top right), $\gamma_{e,0;r}^1$ (bottom left), up to Σ^+; and $\gamma_{e,0;m}^1$ (bottom right), up to Σ^-.

(iii) Last step is to compute the intersection points between both curves obtained in (i) and (ii). In

order to fix ideas, let us consider heteroclinic orbits $P_1 - LPO_1$. Each intersection point belonging to $\gamma_s^{+,1} \cap \gamma_{e,n}^1$ gives rise to a heteroclinic connection between P_1 (integrating backward in time) and the LPO_1 (integrating forward in time). We will label such heteroclinic connection by H_n (and abusing notation, also the intersection points will be labelled the same way). We point out that for $n = 0, 2, 3$, there exist typically two heteroclinic connections, labelled by H_n^1 and H_n^2, and there are no heteroclinic connections for $n = 1$. See Figure 6.1 middle and also both heteroclinic orbits (the (x, y) projection) in the right plots (for $n = 0, 2, 3$ at the first, third and fourth rows respectively).

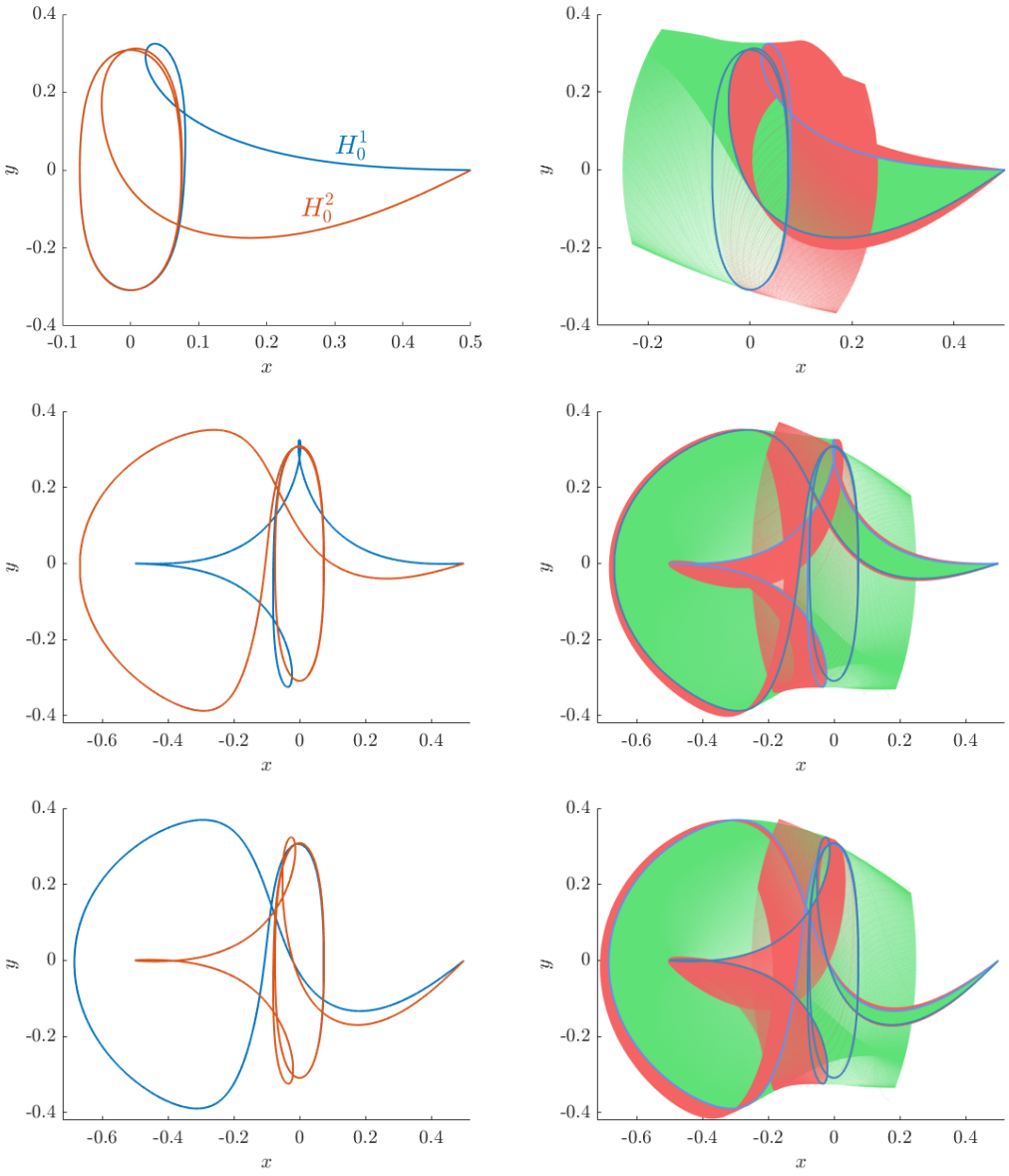

Figure 6.3: $\mu = 0.5$, $C = C_{L_2}$, (x, y) projection. Top. The two heteroclinic connections $P_1 - LPO_1$, H_0^1 and H_0^2, with $n = 0$ close passages around P_1 with initial angles θ_0^i, $i = 1, 2$ (left). These angles are the end points of the transit interval $I_0 = (\theta_0^1, \theta_0^2)$. Right, orbits that after ejecting from P_1, either transit to the region around P_2 (in green) or do not transit (in red). Transit orbits (in green) follow $W^{u,-}(LPO_1)$; non-transit ones (in red) follow $W^{u,+}(LPO_1)$. Middle and bottom. Left. Two new heteroclinic orbits with angles θ_0 close to θ_0^1 (middle), and close to θ_0^2 (bottom). Right. In green orbits ejecting from P_1, pass close to the LPO_1, transit to the region around P_2, pass near the LPO_1 and either transit to the region around P_1 (in green) or bounce back to the region around P_2 (in red).

The location of these heteroclinic connections is relevant for our purpose of determining transit regions. We have just shown that fixed n, we obtain points H_n^1 and H_n^2. So there is a set of points (located on the red curve $\gamma_{e,n}^1$) of Figure 6.1 middle –first, third and fourth rows–) between H_n^1 and H_n^2. Such points belong to ejection orbits, each one characterized by a value of θ_0 as already described in subsection 3.1.2. Moreover such points are located inside the blue curve in Figure 6.1 middle. This means that any such point comes (backwards in time) from ejection and goes (forward in time) to the region around P_2, that is each such point belongs to a transit orbit. So regarding the set of initial angles of these transit orbits, we have an interval that we denote by $I_n = (\theta_n^1, \theta_n^2)$, called *transit interval* such that for any $\theta_0 \in I_n$, the associated ejecting orbit, with initial angle θ_0, is a transit orbit, since it will be inside $W^{s,+}(LPO_1)$ (i. e. the intersecting point of the orbit with Σ_+ will be a point on $\gamma_{e,n}^1$ –the red curve– inside $\gamma_s^{+,1}$ –the blue one–). More specifically, the particle will be ejected from the primary P_1, will describe a trajectory such that will have n close passages around the primary P_1, afterwards will cross Σ and will visit the region around the other primary P_2. The set of points in the curve $\gamma_{e,n}^1$ belonging to transit orbits will be denoted by $\gamma_{e,n;m}^1$ (m stands for middle). See Figure 6.1 and Figure 6.2 top left. We show the set of transit orbits in green Figure 6.3 top for $n = 0$ right. We neatly see the two heteroclinic orbits (in red and blue on the left plot) H_0^1, H_0^2 and the whole set of transit orbits in between on the right plot. An interesting remark here that will be relevant later on is that all such orbits are transit orbits, but notice that the closer θ_0 is to θ_n^i, $i = 1, 2$, the closer the ejecting trajectory passes near the LPO_1 describing some rounds around it before transiting to the region around P_2.

Interestingly, while the piece $\gamma_{e,n;m}^1$ contains points belonging to transit orbits, we wonder what happens with the remaining part of the curve $\gamma_{e,0}^1 - \gamma_{e,0;m}^1$ in Figure 6.2 top left. As foreseen, since such points are outside the curve $\gamma_s^{+,1}$ (the blue one on the top left figure), they belong to non transit orbits. Let us label the two pieces as $\gamma_{e,n;l}^1$ and $\gamma_{e,n;r}^1$ (l and r stand for left and right respectively). See Figure 6.2 top left for $n = 0$. For any point in $\gamma_{e,0;l}^1 \cup \gamma_{e,0;r}^1$, the corresponding orbit, that is outside $W^{s,+}(LPO_1)$, will be a non transit orbit with the initial θ_0 outside I_n (but close to it): the particle, after ejecting from P_1, having n close passages around P_1 and going close to Σ, will return to the same region around P_1 (where it came from). We plot in Figure 6.3 top right the set of ejection orbits from P_1 that become non-transit orbits and *bounce back* to the region around P_1, in red.

In summary, we have $\gamma_{e,n}^1 = \gamma_{e,n;l}^1 \cup \gamma_{e,n;m}^1 \cup \gamma_{e,n;r}^1$. A point in $\gamma_{e,n;l}^1 \cup \gamma_{e,n;r}^1$ belongs to an ejecting orbit which is a non-transit orbit, whereas a point in $\gamma_{e,n;m}^1$ belongs to a transit one; and the end points of $\gamma_{e,n;m}^1$ belong to heteroclinic connections acting as barrier between the two kinds of motions.

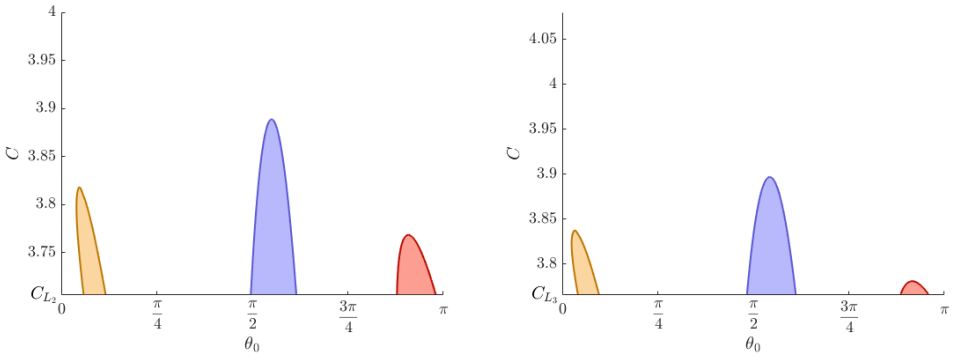

Figure 6.4: $\mu = 0.5$ and $\mu = 0.7$, primary transition intervals when varying C. The corresponding transition regions are in blue for $n = 0$, in red for $n = 2$, and in brown for $n = 3$. For each value of C given, an interval of ejection orbits (each one identified by its value θ_0) which are transit orbits is obtained. The interval depends on the value of n.

The discussion about the role of the transition interval to distinguish between transit and non transit ejection orbits is based on the existence of such transition interval I_n. However the existence of

the transition interval I_n depends on n, μ and C, that is, for n given, the presence of heteroclinic connections $P_i - LPO_1$ is not guaranteed for all μ and $C \geq C_{L_{2,3}}$. We show in Figure 6.4, the transition intervals for $\mu = 0.5$ and $\mu = 0.7$ for $C \geq C_{L_{2,3}}$ (in blue for $n = 0$, in red for $n = 2$ and in brown for $n = 3$). We can see, that fixed μ and n, for each suitable value of C (on the y axis) there is an interval I_n of initial angles θ_0 (on the x axis) of ejecting-transit orbits and the points on the boundary of the transition interval correspond to the two specific values of θ_0 of heteroclinic connections $P_1 - LPO_1$. However, there is a maximum value of C where the two curves $\gamma_s^{+,1}$ and $\gamma_{e,n}^1$ become tangent and there is a single heteroclinic connection $P_1 - LPO_1$. For higher values of C there are no heteroclinic connections.

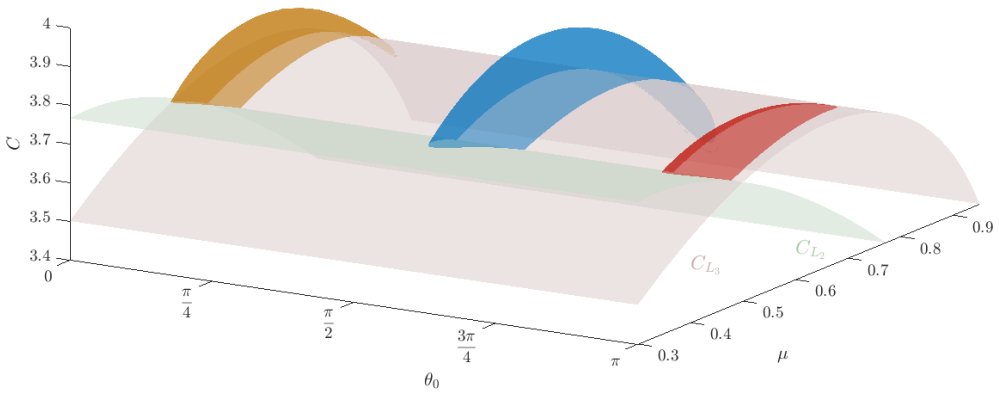

Figure 6.5: 3D plot of heteroclinic connections between the primary of mass μ and the LPO_1 when varying $\mu \in (0, 1)$, $C \in [C_{L_{2,3}}, C_{L_1})$, taking $n = 0, 2, 3$. The corresponding transition regions are in blue for $n = 0$, in red for $n = 2$, and in brown for $n = 3$. This figure is the generalization of Figure 6.4 varying μ.

So far we have shown the heteroclinic connections $P_1 - LPO_1$ with $n = 0, 2, 3$ close passages around P_1 as well as the transition interval I_n, just for single values of μ ($\mu = 0.5$ and 0.7). We have done massive computations in order to obtain the transition interval for any value of $\mu \in (0, 1)$, any value of $C \in [C_{L_{2,3}}, C_{L_1})$ (recall the location of L_i, $i = 1, 2, 3$ for any μ), and for $n = 0, 1, 2, 3$. See Figure 6.5. The blue, red and brown surfaces provide the transition intervals (θ_0 values on the x axis) respectively for any μ on the y axis, and a suitable range of values of C on the z axis. Several comments must be done concerning this figure: (i) We remark that for $n = 1$, neither varying $C \in [C_{L_{2,3}}, C_{L_1})$ nor $\mu \in (0, 1)$, we have not found any heteroclinic connection ejecting from P_i ($i = 1$ or 2), describing 1 close passage around P_i and tending asymptotically to the LPO_1. (ii) Heteroclinic connections $P_i - LPO_1$ do not exist for all μ and $C \geq C_{L_{2,3}}$. For n given, there exist minimum and maximum values of μ for which the heteroclinic connections exist. These extreme values correspond to tangencies between the curves $\gamma_s^{+,1}$ and $\gamma_{e,n}^1$. Just before (after) the tangency, the curves $\gamma_s^{+,1}$ and $\gamma_{e,n}^1$ do not intersect (intersect) in two points, which provide the transition interval (any slice in Figure 6.5 with μ fixed). (iii) Another important remark is that, given μ, such heteroclinic connections only exist for values of C in a suitable interval for $C \geq C_{L_{2,3}}$ and such interval depends on μ. We showed the particular cases $\mu = 0.5$ and $\mu = 0.7$ in Figure 6.4.

So, from the previous exploration we conclude that the two heteroclinic connections H_n^1 and H_n^2 (given n) –or equivalently the transition interval $I_n = (\theta_n^1, \theta_n^2)$– determine a barrier that allows to distinguish between ejection orbits that (after describing n close passages to the primary) are transit orbits or non transit. That is we have a *first* classification on the dynamical behaviour of the ejection orbits regarding its transit/non transit character. This is the simple part of the story we have seen

so far. The story line goes on when we ask ourselves what happens if there are other heteroclinic connections $P_i - LPO_1$. The answer is that we can use *other* heteroclinic connections, in general, to know which region (around the big primary or around the small one) the ejection orbit will visit along its trajectory, and therefore such heteroclinic connections will provide an additional way to classify the dynamical behaviour of the ejection orbits.

So, next, in this Section we just want to discuss an example of the consequences of the appearance of two heteroclinic orbits *close* to the heteroclinic connection H_0^1 (and similarly the appearance of two heteroclinic orbits *close* to the heteroclinic connection H_0^2). In the next Section, a deeper analysis is carried out when there appear not two but infinitely many heteroclinic orbits. So it is worthwhile understanding, first, what happens in this simple situation.

Let us describe the plots in Figure 6.3 (all the plots contain the projection in (x, y) variables). As mentioned, we show on the top left figure, the two heteroclinic connections H_0^i, $i = 1, 2$, with initial angles $\theta_0^1 = 1.558674225724$ and $\theta_0^2 = 1.932752613334$ respectively and in the top right figure the set of ejection and transit orbits (in green) and two sets of ejection and non-transit orbits (in red). As previously discussed, the two heteroclinic connections provide the barriers between transit and non-transit orbits. Now we consider two new heteroclinic orbits $P_1 - LPO_1$, with initial θ_0 close to θ_0^1; more specifically, we denote the new values by $\theta_0^{1,1} = 1.584919597063$ and $\theta_0^{1,2}$ (the superscripts being $1, 1$ and $1, 2$ because they are close to $\theta_0^1 = 1.702359169703$). Notice that $(\theta_0^{1,1}, \theta_0^{1,2}) \subset (\theta_0^1, \theta_0^2)$.

The first remark is that we can clearly see that the two new heteroclinic connections behave differently from H_0^1 in the sense that after ejecting from P_1, do visit a region around P_2 and end asymptotically in the LPO_1 (see Figure 6.3 middle) whereas H_0^1 does not visit any region around P_2. The key point is that such two heteroclinic connections provide new barriers of transit and non transit, and therefore determine an additional *second* classification of the ejecting orbits in the previous bigger set of ejecting orbits in the top figure. More precisely, for the set of ejection orbits with $\theta_0 \in (\theta_0^1, \theta_0^2)$ we can distinguish two kinds of behaviour: first, the ejection orbits in the thinner set determined by the two new heteroclinic orbits (that is, whose $\theta_0 \in (\theta_0^{1,1}, \theta_0^{1,2})$); they eject from P_1, transit to the region around P_2 (since $\theta_0 \in (\theta_0^1, \theta_0^2)$, i. e. first classification), and transit again towards the region around P_1 (since $\theta_0 \in (\theta_0^{1,1}, \theta_0^{1,2})$, i. e. second classification). See the green set of orbits in Figure 6.3, middle right. Second, the ejection orbits with $\theta_0 \in (\theta_0^1, \theta_0^2)$ but outside the thinner set (that is, whose $\theta_0 \notin (\theta_0^{1,1}, \theta_0^{1,2})$). Such orbits eject from P_1, transit to the region around P_2 (since $\theta_0 \in (\theta_0^1, \theta_0^2)$, i. e. first classification) but are non transit orbits and bounce back and remain on the same region around P_2 (second classification). See the red set of orbits in Figure 6.3, middle right.

A similar behaviour concerning transit/non transit (first classification) and transit/non transit (second classification) can be described for the two new heteroclinic orbits, with initial $\theta_0^{2,1} = 1.867534417000$, $\theta_0^{2,2} = 1.925408730327$, respectively close to θ_0^2, that can be seen in the bottom Figure 6.3. Notice that $(\theta_0^{2,1}, \theta_0^{2,2}) \subset (\theta_0^1, \theta_0^2)$.

So far, we have discussed the dynamical behaviour of the ejection orbits, transit/non transit, taking into account the effect of the LPO_1 and the heteroclinic connections $P_1 - LPO_1$. Now, we may add a new ingredient to be even more precise in the classification of the ejection orbits, taking into account the number of turns that the ejection orbit (whether it is transit or non transit) describes around the LPO_1, when it passes close to it. To clarify this idea, let us consider first the points on $\gamma_{e,n;l}^1$ and $\gamma_{e,n;r}^1$ (that belong to non-transit orbits) and for each such point we follow the corresponding trajectory (that started ejecting from P_1) by the flow up to the Poincaré section Σ^+. In a natural way we denote the corresponding curves by $\gamma_{e,n;l}^2$ and $\gamma_{e,n;r}^2$. Since the points on $\gamma_{e,n;i}^1$, $i = r, l$ are very close to a point that belongs to a heteroclinic orbit $P_1 - LPO_1$, the resulting orbits are very close to the manifold branch $W^{u,+}(LPO_1)$, so such orbits describe a trajectory that surrounds the LPO_1 several times and follow the manifold $W^{u,+}(LPO_1)$; therefore the resulting curves, $\gamma_{e,n;l}^2$ and $\gamma_{e,n;r}^2$, spiral on and on towards the curve $\gamma_u^{+,1}$. More precisely, the set of points of every spiral turn of the curve $\gamma_{e,n;l/r}^2$ correspond to points that, on the section Σ, track the whole LPO_1 (sort to speak). So the infinitely many spiral turns of the curve $\gamma_{e,n;l/r}^2$ are intrinsically related to the number k of

turns (k from 0 to infinity) that the ejection orbit does around the LPO_1. We plot in Figure 6.2 the resulting spiralling curves for $\mu = 0.5$, $C = C_{L_2}$ and $n = 0$.

Second we reason analogously with the points in the curve $\gamma^1_{e,n;m}$. Since they belong to ejecting transit orbits, we follow the curve by the flow up to Σ^- (instead of Σ^+) giving rise to a double spiral, $\gamma^2_{e,n;m}$ that spirals on and on towards the curve $\gamma_u^{-,1}$. See Figure 6.2 right. In the three plots the spiral curves look fastly 'glued' (although always infinitely spiralling) to the corresponding curve $\gamma_u^{\pm,1}$.

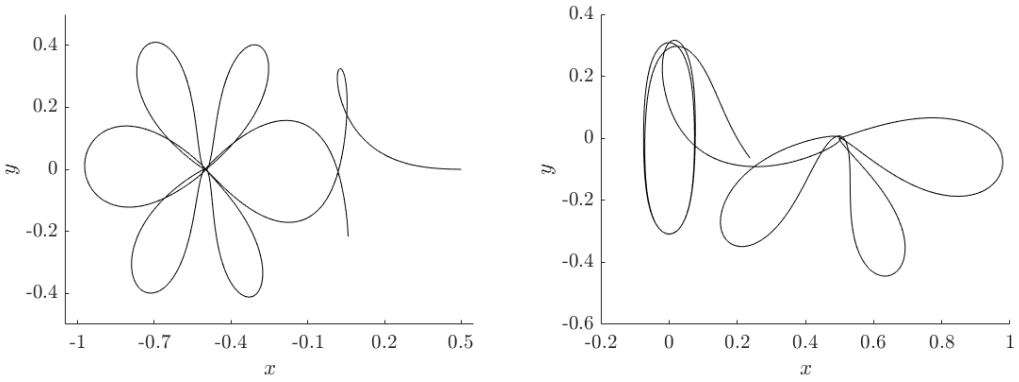

Figure 6.6: $\mu = 0.5$, $C = C_{L_2}$. (x, y) projection. Ejection orbit $E^0_1 - PO^0 - P^6_2 - ....$ (left) and $E^3_1 - PO^2 - ....$ (right).

In accordance with the aforementioned considerations, the natural code we are going to use in order to classify an ejecting orbit will be the following:

$$E^n_i - PO^k - P^j_l - ...$$

which stands for: an ejecting orbit from the primary P_i ($i = 1$ or 2), describes n close passages around this primary before going close to the LPO_1, surrounds k times the LPO_1, and visits the region around P_l ($l = 1$ or 2), describing j close passages around this primary,... Therefore, this code determines the geometrical trajectory the ejection orbit is actually doing. See Figure 6.6 for two particular examples of ejection orbits. It is clear that symbolic dynamics might be introduced.

In the particular case that the orbit is an EC orbit, the code will be

$$E^n_i - PO^k - C^j_l$$

where now C^j_l means that, after j close passages around the primary P_l, the particle ends at collision with it.

Just summarizing, so far we have described the role of the two simple heteroclinic connections $P_1 - LPO_1$ (providing a first classification), given by θ^1_0, θ^2_0 and the couple of new heteroclinic connections $\theta^{1,1}_0$, $\theta^{1,2}_0$ and $\theta^{2,1}_0$, $\theta^{2,2}_0$ (providing an additional second classification). We know that the two simple heteroclinic connections come from the requirement that the ejection orbit has $n = 0$ close passages to P_1 and reaches the Poincaré section Σ matching with a point belonging to $W^{s,+}(LPO_1)$. But at this point we would like to know where the other new heteroclinic orbits come from. The answer involves the existence of homoclinic orbits to the LPO_1, that is orbits that asymptotically tend to the LPO_1 forward and backward in time.

Actually the situation is much more involved, because there appear infinitely many homoclinic orbits and as a consequence infinitely many heteroclinic connections $P_1 - LPO_1$, giving rise to a chaotic behaviour. Thus, once we have described the simple, or *regular* situation in this Section, let us analyse the effects of the existence of infinitely many homoclinic and heteroclinic connections. This is one purpose of the next Section.

6.2 Regular motion vs chaos. The role of the LPO_1

In the previous Section we have described a *regular* kind of motion in the sense that the transition interval provides a barrier to distinguish between transit and non transit ejection orbits, which becomes a *first* classification for the ejection orbits. That is the dynamical behaviour of the ejection orbits is related to the heteroclinic connections. However, we have also described an example to show that the appearance of two new heteroclinic orbits close to H_0^1 (or H_0^2) provide an additional *second* classification of the ejection orbits: the orbits eject from the primary, are transit orbits (first classification), and once they are on the region around the other primary, they can be classified as transit or non transit orbits (second classification). One purpose of this Section is to show that, actually, there are infinitely many heteroclinic connections between the primary and the LPO_1. This infinity is related to the existence of homoclinic orbits to the LPO_1 so this orbit plays a key role here. Moreover the heteroclinic connections are very close to each other. Thus, an immediate consequence is that if we take all of them into account, we have infinitely many ways of classifying an ejection orbit, which results in a chaotic classification.

A second and interesting purpose of this Section is focussed on another chaotic infinity, now related to the EC orbits. We will discuss the mechanism to generate infinitely new EC orbits taking into account the presence of LPO_1.

6.2.1 Infinitely many heteroclinic orbits $P_i - LPO_1$

In the previous Section we have shown *big* transition intervals of values of θ_0, that is big sets of ejection orbits that can be classified as transit or non-transit when they pass close to the LPO_1. We have also remarked that the barriers of such intervals are the heteroclinic orbits $P_i - LPO_1$.

However, the determination of such transition intervals, whose end points are initial angles for heteroclinic connections $P_i - LPO_1$, is not that simple: we will show that there are infinitely many heteroclinic connections $P_i - LPO_1$. A crucial point to understand where this infinity comes from is the existence of homoclinic orbits of the LPO_1.

Let us discuss this complexity just taking into account two homoclinic orbits (later on we will consider infinitely many homoclinic orbits). The simulations are done for $\mu = 0.5$ and $C = C_{L_2}$.

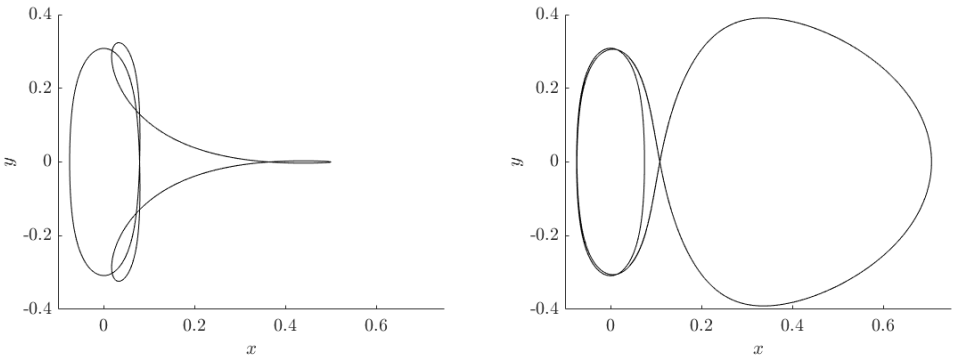

Figure 6.7: $\mu = 0.5$, $C = C_{L_2}$. Two different homoclinic orbits to the LPO_1, HO^1 (left) and HO^2 (right). (x, y) projection.

Let us start with two simple homoclinic orbits of the LPO_1, shown in Figure 6.7, and called HO^1 (on the left) and HO^2 (on the right). Roughly speaking the shape of HO^1 ((x, y) projection) is composed of a curved triangular shape plus the asymptotic shape to the LPO_1, whereas HO^2 ((x, y) projection) is composed of a big loop (close to circular) shape plus the asymptotic shape to the LPO_1.

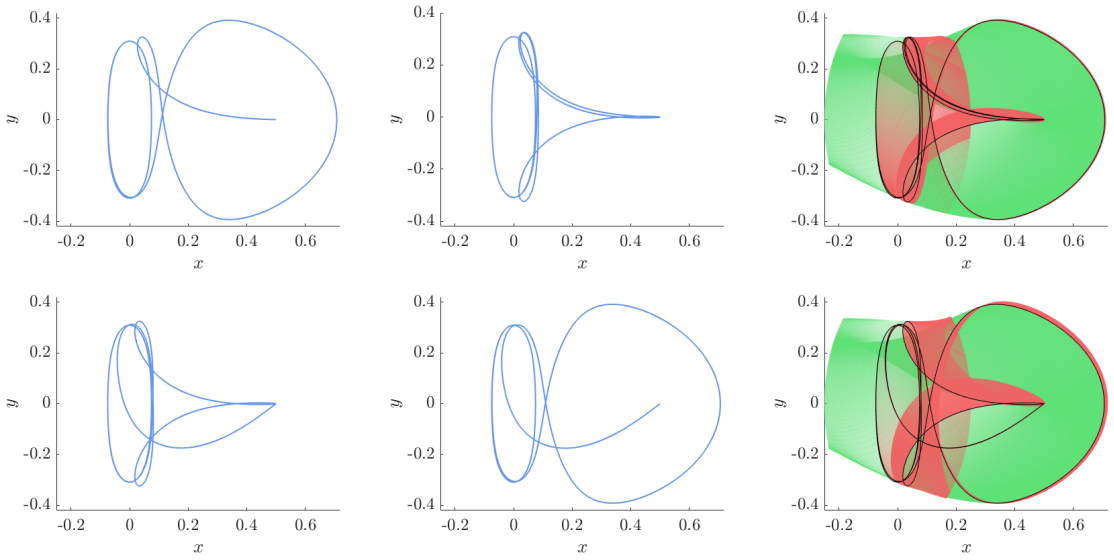

Figure 6.8: $\mu = 0.5$, $C = C_{L_2}$, (x, y) projection. Left and middle. Two heteroclinic orbits with values of θ_0 equal to $\tilde{\theta}_0^{i,1}$ and $\tilde{\theta}_0^{i,2}$ near near θ_0^i ($i = 1$ in top figure, $i = 2$ in bottom figure). Right. The set of transit orbits (in green) and non-transit ones (in red) are shown.

A main consequence of such homoclinic orbits is that there exist infinitely many heteroclinic connections $P_1 - LPO_1$ with an initial angle θ_0 *very close* to θ_0^1 such that the associated heteroclinic connections $P_1 - LPO_1$ are rather different. More precisely, let us describe how these infinitely many appear. First, look just at three (not infinite but just three) simple heteroclinic connections which have a *quite similar path from ejection to (near) the* LPO_1 (the piece of trajectory from ejection up to the first small loop of the three orbits is almost the same), that is with values of θ_0 very close to each other: the first one, H_0^1 (in Figure 6.3 top left), just ends asymptotically at the LPO_1. The second one with $\theta_0 = \tilde{\theta}_0^{1,1} = 1.553258226788$ (in Figure 6.8 top left), when the particle is near the LPO_1, does not surround the LPO_1 but follows the path of the big loop of the homoclinic orbit HO^2 once and ends asymptotically at the LPO_1. The third heteroclinic orbit with $\theta_0 = \tilde{\theta}_0^{1,2} = 1.557995153267$ does not surround the LPO_1 but follows the path of the curved triangular piece of the homoclinic orbit HO^1 and ends asymptotically at the LPO_1. See Figure 6.8 top middle. Notice that all of them describe 0 turns along the first piece of trajectory (from ejection up to the first small loop). We call them three basic heteroclinic connections.

Therefore, we have the same phenomenon described in the Figure 6.3 as far as the classification of the trajectory of ejection orbits is concerned, we obtain a very thin interval of values of θ_0 near θ_0^1 that separates transit of non-transit orbits. This is shown in Figure 6.8 top right. However now the range of the transition interval $(\tilde{\theta}_0^{1,1}, \tilde{\theta}_0^{1,2})$ is remarkably thinner.

We have a similar situation when we consider the homoclinic orbits HO^i, $i = 1, 2$ and the heteroclinic connection H_0^2. There are two heteroclinic connections with $\theta_0 = \tilde{\theta}_0^{2,1} = 1.932919335638$ and $\theta_0 = \tilde{\theta}_0^{2,2} = 1.934043834973$, respectively, values very close to θ_0^2. The three of them describe (almost) the same path from ejection up to the first big loop (see Figure 6.3 top left and Figure 6.8), however afterwards one goes directly to the LPO_1, another one describes a path close to the curved triangular piece before ending to the LPO_1 (see Figure 6.8 bottom left) and the other one describes a piece of the big circular loop before ending to the LPO_1 (see Figure 6.8 bottom middle). Notice that all of them describe 0 turns along the first piece of trajectory (from ejection up to the first big loop). We call them three basic heteroclinic connections (one of them does not involve a homoclinic orbit, and two of them do involve either one or the other homoclinic orbit). Again a remarkably thin transition interval appears very close to θ_0^2.

So far we have shown the two simplest (or basic) heteroclinic connections involving HO^1, with an initial $\tilde{\theta}_0^{1,1}$ and $\tilde{\theta}_0^{1,2}$ (respectively) quite close to each other and near θ_0^1. And similarly for $\tilde{\theta}_0^{2,1}$ and $\tilde{\theta}_0^{2,2}$ involving HO^2.

But this is the *simple version* of the description of heteroclinic connections involving the homoclinic orbits HO^1 and HO^2. From the above discussion we want to emphasize that we have considered six heteroclinic connections, all of them sharing a common property: each one describes its own path but all of them describe zero turns before ending asymptotically to the LPO_1. We will say that the number of turns is $k = 0$.

We mentioned above that the situation is much more complex. Actually there are infinitely many heteroclinic connections $P_1 - LPO_1$. Let us explain how they appear.

A first mechanism is the following. We can obtain new heteroclinic connections $P_1 - LPO_1$ just with the same kind of trajectory as the four heteroclinic orbits described in Figure 6.8 top and bottom, left and middle, but with one difference: the first piece is the same as before, now the trajectory describes k turns around the LPO_1, and afterwards describes the *same* path (of course almost the same) as the previous ones. So we have four new heteroclinic orbits for $k = 1$, four new ones for $k = 2$,...., four new ones for each number of k turns given. In that way, we obtain infinitely many heteroclinic orbits. Or equivalently, we have shown three plus three heteroclinic connections, with $k = 0$, the basic ones. For any k, we have a new triplet of heteroclinic connections which share (almost) the same first piece of trajectory (from ejection to the first loop), then describe k turns to the LPO_1 and then each one follows (almost) the same path as each of the three basic heteroclinic connections. In Figure 6.8, we have just considered the simplest ones ($k = 0$).

The second mechanism is a generalization of the previous one. Of course, there are other infinitely many families of heteroclinic orbits, not only playing with the number k of turns around the LPO_1, but also playing with two homoclinic orbits. More specifically, above we have considered two ternaries of heteroclinic connection: for the first triplet, one does not involve any homoclinic orbit, the second one involves one homoclinic orbit and the third one involves another (different) homoclinic orbit. And similarly for the second triplet. Let us describe, for example a new heteroclinic connection: we take the heteroclinic connection in Figure 6.8 top left. We might construct a new heteroclinic connection (with θ_0 extremely close to $\tilde{\theta}_0^{1,1}$) as follows: the first piece from ejection to the first small loop (almost) the same, then k turns around the LPO_1, then the path of the big circular loop (of HO^2), then m turns around the LPO_1, then the path of the curved triangle, then tending asymptotically to the LPO_1. Another different one would be (almost) the same but before ending to the LPO_1, the trajectory might follow the curved triangle piece, the j turns around the LPO_1, then follow the big circular loop, then l turns around the LPO_1, then ..., before ending to the LPO_1, where the dots ... stand for any pre-desired combination of turns around the LPO_1, the big circular loop and/or the curved triangle.

So, in conclusion, for values of θ_0 extremely close to θ_0^1 or θ_0^2, a chaotic behaviour, that is infinitely many heteroclinic connections $P_1 - LPO_1$, show up.

But the complexity procedure does not end here. Why? Because there are, not only two (HO^1 and HO^2), but infinitely many homoclinic orbits of the LPO_1 involving other invariant objects. So we may apply the previous mechanisms playing with any (one or more) of this infinity of homoclinic orbits to obtain a new *chaotic* infinity of heteroclinic connections $P_1 - LPO_1$.

So now, quite naturally, we want to talk about the homoclinic orbits to the LPO_1, how to compute them and how many of them the RTBP has in the range of C considered.

First, let us show a systematic way to find the infinity of homoclinic orbits to the LPO_1. Just consider the first crossing of $W^{s,+}(LPO_1)$ with Σ^+, that is $\gamma_s^{+,1}$ which is a nice S^1 shaped curve (see Figure 6.9 top left in blue), and the second crossing of $W^{u,+}(LPO_1)$ with Σ^+, $\gamma_u^{+,2}$ which is now a very intricated set of curves (see Figure 6.9 top in red). Each intersection point between both curves corresponds

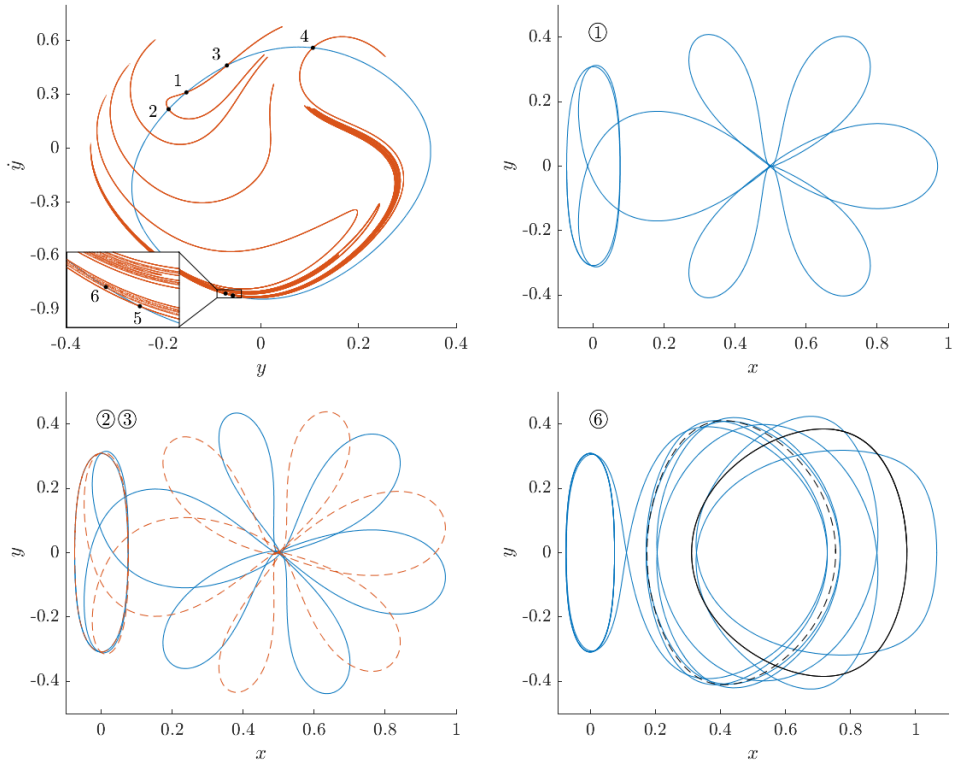

Figure 6.9: $\mu = 0.5$, $C = C_{L_2}$. Top left. $(y, \dot{y})$ projection. Intersection curve $W^{s,+}(LPO_1) \cap \Sigma^+$ at the first crossing (in blue) and the intersection $W^{u,+}(LPO_1) \cap \Sigma^+$ at the second crossing (in red). Examples of homoclinic orbits: the ones labelled by 1,2,3 and 6. 4 and 5 are shown in Figure 6.7. The homoclinic orbit 6 involves two periodic orbits, one stable (discontinuous black line) and one unstable (continuous black line).

to a homoclinic orbit of the LPO_1. We can see that there are 'clean' intersections but also 'tongues' concentrated in some area. We have labelled $1, 2, 3, 4$ four clean points and 5 (a not so clean point). See Figure 6.9 top left. The corresponding homoclinic orbits are shown as follows: 1 in the top right figure, 2 and 3 in the bottom left figure, and 4, 5 are the ones shown in Figure 6.7. As we can see the role of the path close to collision with the primary P_1 is essential here. But not only the collision plays a role; there are other simple periodic orbits (apart from the LPO_1) that are also involved and that is a reason for the infinity of homoclinic orbits. Just to show an example, we have chosen point 6 in the top left figure which has an associated homoclinic orbit shown in the same figure, bottom right. We have also plotted two periodic orbits involved in the shape of the homoclinic orbit. One periodic orbit is stable (in discontinuous black line) and another one is unstable (in continuous black line). It is clear that the homoclinic orbits is sensitive to the effect of both periodic orbits; in particular the particle surrounds the stable one several times and follows its trajectory to visit the unstable one, then surrounds again the stable one and finally goes towards the LPO_1. In general there are infinitely many periodic orbits which can be stable or unstable, each one potentially playing a role in the homoclinic orbits. The deep analysis of such role is left for a future work.

Second, we want to emphasize that we can obtain other infinite family of homoclinic orbits of the LPO_1 just taking into account not only the intersection of $W^{u,+}(LPO_1)$ with Σ^+ at the *second* crossing, curve $\gamma_u^{+,2}$, but also the $2k$-*th* crossing, curve $\gamma_u^{+,2k}$. In order to illustrate the richness of this curve, we consider the curve $\gamma_u^{+,2}$ (see Figure 6.10) and we just take the *small* (darker red) piece of curve ending at point 4 and external to $\gamma_s^{+,1}$ (the blue one). Let us denote it by $\bar{C}$. We follow the flow of such points, integrating forward in time, up to the fourth crossing with Σ^+ (that is we take a suitable small range of values of θ_0 for ejection orbits, such that at the second crossing with Σ^+ they

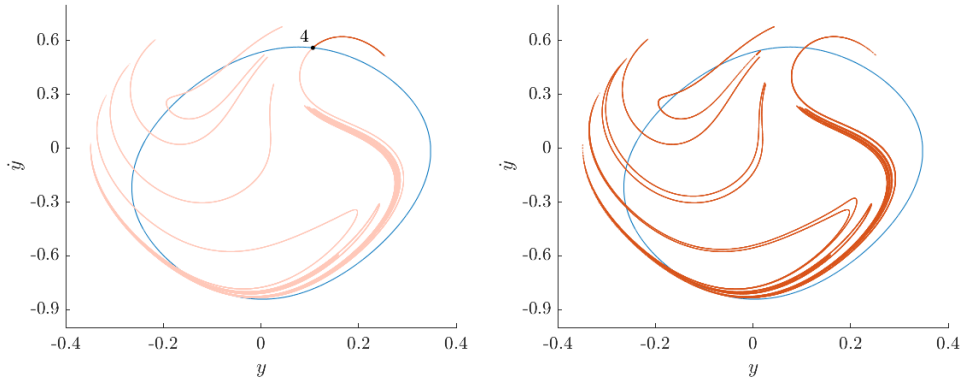

Figure 6.10: $\mu = 0.5$, $C = C_{L_2}$. $(y, \dot{y})$ projection. Left. Curves $\gamma_u^{+,2}$ and $\gamma_s^{+,1}$. Right. From curve $\gamma_u^{+,2}$, we take the *small darker red piece* external to $\gamma_s^{+,1}$ (the blue one) and ending at point 4. The fourth crossing of such small piece with Σ^+ gives rise to the infinite foliation of replications of the second crossing curve $\gamma_u^{+,2}$ shown on the plot.

define the points on the small piece of curve $\bar{C}$, and follow these orbits up to the fourth crossing with Σ^+. Actually if we took a very small sub-piece of such curve $\bar{C}$, we would obtain a replication of the Figure 6.10 left: the closer the sub-piece of curve is to the intersection point (between the blue curve $\gamma_s^{+,1}$ and $\gamma_u^{+,2}$), the similar replication to the Figure 6.10 left will be obtained. Since the corresponding orbits pass very close to the LPO_1, turning k times the LPO_1, the trajectories from the second to the fourth crossing with Σ^+ will be (almost) a replication of those going from $W^u(LPO_1)$ to the second crossing with Σ^+. Therefore varying k (that is, taking smaller and smaller sub-pieces of the small piece $\bar{C}$) we obtain a foliation of (almost) replications of the curve $\gamma_u^{+,2}$. This foliation is shown in Figure 6.10 right. Due to the closely packed foliation, the plot apparently looks like the left one but it is not exactly equal.

So we conclude that the structure of homoclinic orbits is amazingly rich.

6.2.2 Generation of infinitely many EC orbits

This subsection is focussed on describing a mechanism that explains how a chaotic infinity of EC orbits are obtained taking into account the role of the LPO_1. We will distinguish two cases: EC orbits to the same primary and ejection orbits from one primary and collision with the other one.

EC orbits from/to P_1 involving the LPO_1

An EC orbit is a trajectory that belongs to $W^e(P_1) \cap W^c(P_1)$ (recall the notation introduced previously). So actually we just need to compute such intersection on a Poincaré section. However, such intersection is very intricate, due in particular to the role of the LPO_1, as we shall show.

In order to simplify the exposition, let us start with the simplest EC orbits at P_1, involving the LPO_1. This means a trajectory that ejects from P_1, goes directly to the LPO_1 (that is, has $n = 0$ close passages around the primary), is a non transit orbit and turns back to collide with P_1 (after $j = 0$ close passages around the primary).

In order to find numerically such EC orbits, and guarantee the implication of the LPO_1, we just need to take into account a suitable set of initial angles θ_0 close to θ_0^1 and θ_0^2, that is ejection orbits passing close to the LPO_1, which are, moreover, non transit orbits (to guarantee the return towards P_1). This requirement leads us to take into account the heteroclinic connections H_0^1 and H_0^2.

More specifically we must intersect the curves $\gamma^1_{c,0}$ (collision orbits, integrated backward in time with $n = 0$, up to the first crossing with the section Σ^+) and either $\gamma^2_{e,0;l}$ or $\gamma^2_{e,0;r}$ (ejection orbits, integrated forwards in time with $n = 0$, and which we know they pass close to the LPO_1 and are *non transit*, up to the second crossing with the section Σ^+). We remark that we precisely select the pieces of $\gamma^2_{e,0;l/r}$, since we know they are non transit.

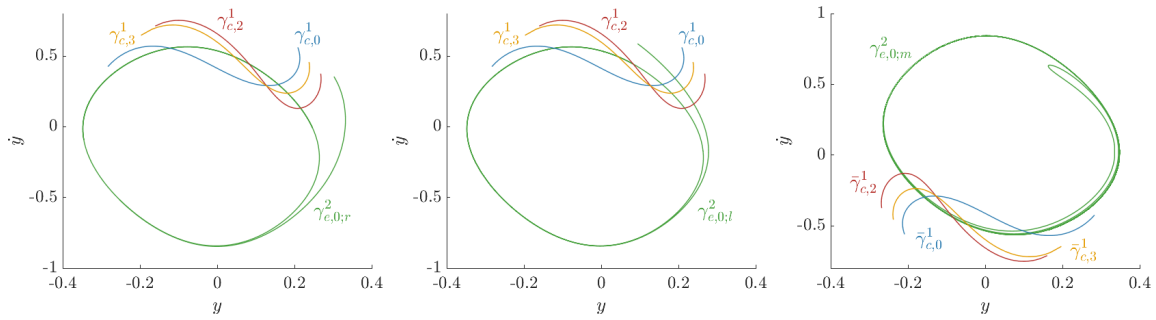

Figure 6.11: $\mu = 0.5$, $C = C_{L_2}$. (y, y') projection. Curves $\gamma^2_{e,0;i}$ (green) and $\gamma^n_{c,0}$, for $n = 0$ (blue), $n = 2$ (red), $n = 3$ (orange). Left. $i = r$. Middle. $i = l$. Each intersection point between the green curve and another one is a point of an EC orbit with P_1. Right. Curves $\gamma^2_{e,0;m}$ (green) and $\bar{\gamma}^1_{c,j}$, for $j = 0$ (blue), $j = 2$ (red), $j = 3$ (orange). Each intersection point between the green curve and another one is a point of an EC orbit (ejects from P_1 and collides with P_2).

Let us focus on the intersection $\gamma^2_{e,0;r} \cap \gamma^1_{c,0}$. See Figure 6.11 left ($(y, \dot{y})$ projection): the spiralling curves are plotted in green and $\gamma^1_{c,0}$ in blue. Each point belonging to the intersection of the green and blue curves is a point that belongs to an EC orbit (forward in time collides with P_1 and backward in time ejects from it and along its trajectory visits the LPO_1). So from the left plot, we see *apparently* two intersection points, that is two EC orbits. Let us denote by E_1 and E_2 these two *apparent* points that correspond (integrating forward in time) to collision orbits with initial angles $\theta^1_{0,c}$ and $\theta^2_{0,c}$, respectively. In Figure 6.11, E_1 and E_2 are the apparent intersection points with lower and higher value of $\dot{y}$ respectively. However, due to the heteroclinic connections H^1_0 and H^2_0, the green curve is an infinitely spiralling one, and this means that the *apparent* two points are actually a *double infinitely countable* set of intersection points, corresponding to a double infinitely countable set of values of initial angles θ_0 very close to an apparent value $\theta^1_{0,c}$ and $\theta^2_{0,c}$, respectively. Let us denote by C^1_∞ and C^2_∞ both sets of initial angles. Each infinity has to do with the infinity of spiral turns of the curve $\gamma^2_{e,0;l}$, and recall that this infinity of turns is related to the number of k turns (k from 0 to infinity) that the ejection orbit does around the LPO_1 (as discussed in the previous Section).

Considering $\gamma^2_{e,0;r} \cap \gamma^1_{c,0}$, a double infinitely countable set of EC orbits is obtained. We observe that all these EC orbits share a common property: the ejection angle is very close to θ^1_0, so the initial path from ejection to (near) the LPO_1 looks quite the same as the path of H_1. Roughly speaking we will say that all these EC orbits have an "ejection road" type 1. Concerning the collision path, we will distinguish between those EC orbits with an intersection point, in $\gamma^2_{e,0;r} \cap \gamma^1_{c,0}$, near E^1 or E^2. We will say that the EC orbit has a "collision road 1" or "collision road 2", respectively. So depending on the intersection point considered, we will have an infinity of EC orbits leaving from P_1 following the ejection road 1 and going to collision following the collision road 1 (if the intersection point belongs to C^1_∞); and an infinity of EC orbits leaving from P_1 following the ejection road 1 and going to collision following the collision road 2 (if the intersection point belongs to C^2_∞). For each infinity, the distinction between two EC orbits is simply the number of turns, k, around the LPO_1 after the ejection and before the collision.

Similarly we can think about $\gamma^2_{e,0;l} \cap \gamma^1_{c,0}$. See Figure 6.11 middle with the same colour code. Now it is the heteroclinic orbit H^2 which plays a role. Roughly speaking we will say that all these EC orbits have an "ejection road" type 2, because the initial angle is close to θ^2_0. Again we distinguish the two collision roads 1 and 2, in accordance with the intersection point (see middle plot of Figure 6.11). So we obtain an infinity, $\tilde{C}^1_\infty$, of EC orbits leaving from P_1 following the ejection road 2 and collision

road 1; and an infinity, $\tilde{C}^2_\infty$, of EC orbits leaving from P_1 following the ejection road 2 and collision road 2. Again, in both cases, the infinity appears because of the number k of turns around the LPO_1.

Therefore these four roads are the responsible for the existence of infinitely many EC orbits just choosing one "ejection road" and one "collision road", on the one hand, and taking into account the number of turns around the LPO_1, on the other hand. For each choice of the "ejection road" and "collision road" selected, we have an infinity of EC orbits with $n = 0$ close passages around P_1.

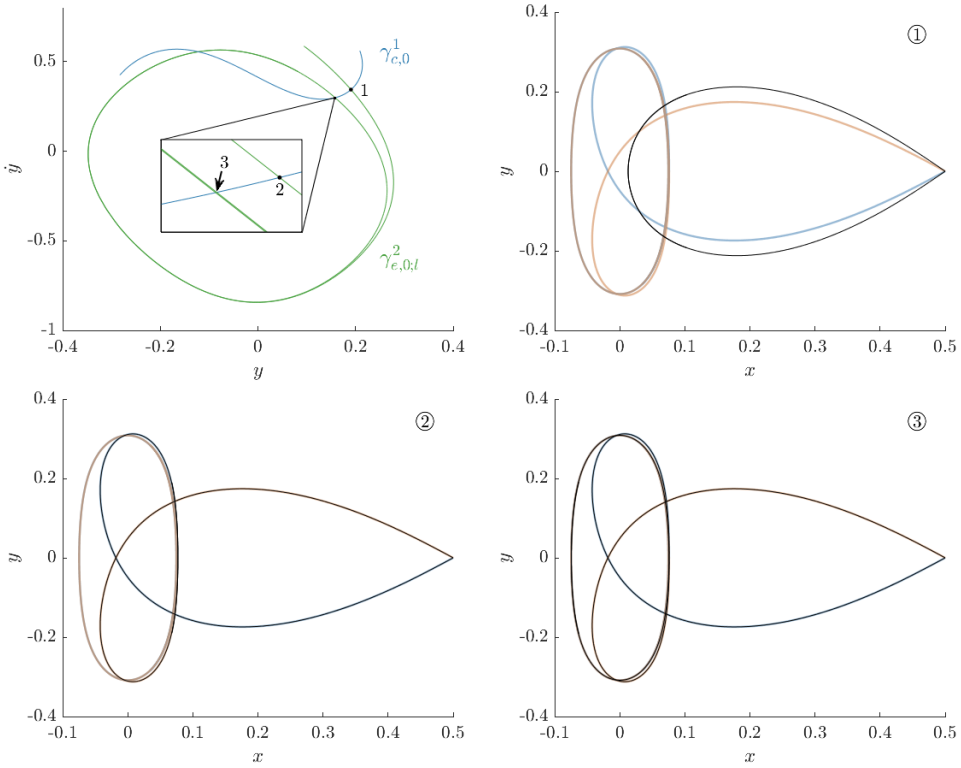

Figure 6.12: $\mu = 0.5$, $C = C_{L_2}$. Top left. $(y, \dot{y})$ projection. Curves $\gamma^2_{e,0;l}$ and $\gamma^1_{c,0}$. We choose three intersection points corresponding to $k = 0, 1, 2$ turns around the LPO_1. The three of them take the "ejection road 2" and the "collision road 1". We plot the associated EC orbits (black path) with $k = 0$ (orbit 1, top right), $k = 1$ (orbit 2, bottom left) and $k = 2$ (orbit 3, bottom right). (x, y) projection. The blue and red orbits correspond to the heteroclinic connections H_1 and H_2 respectively.

To illustrate some particular EC orbits, in Figure 6.12, we take three specific intersection points in $\tilde{C}^1_\infty$ that is in $\gamma^2_{e,0;l} \cap \gamma^1_{c,0}$, corresponding to $k = 0, 1, 2$ turns around the LPO_1. The three of them take the "ejection road 2" and the "collision road 1" (see the top middle figure). We plot the associated EC orbits in the top right figure (orbit 1 with $k = 0$, bottom left figure (orbit 2 with $k = 1$) and bottom right figure (orbit 3 with $k = 2$). According to the code defined in the previous Section, such orbits are coded by: $E^0_1 - PO^0 - C^0_1$, $E^0_1 - PO^1 - C^0_1$ and $E^0_1 - PO^2 - C^0_1$, respectively.

Going on with some examples, taking $k = 0$ and the possible ejection road and collision road, we have four EC orbits shown in Figure 6.13. First row: two orbits with choice of ejection road 1 (left, due to $\gamma^2_{e,0;r}$), and either collision road 2 (orbit A in the middle) or collision road 1 (orbit B in the right). Second row: two orbits with choice of ejection road 2 (left, due to $\gamma^2_{e,0;l}$), and either collision road 2 (orbit C in the middle) or 1 (orbit D in the right, which coincides with Figure 6.12 bottom left). All of them coded by $E^0_1 - PO^0 - C^0_1$.

We want to emphasize that, so far, we have shown these four mechanisms (2 choices for the ejection road and 2 for the collision road) to explain the existence of the simplest EC orbit involving the LPO_1

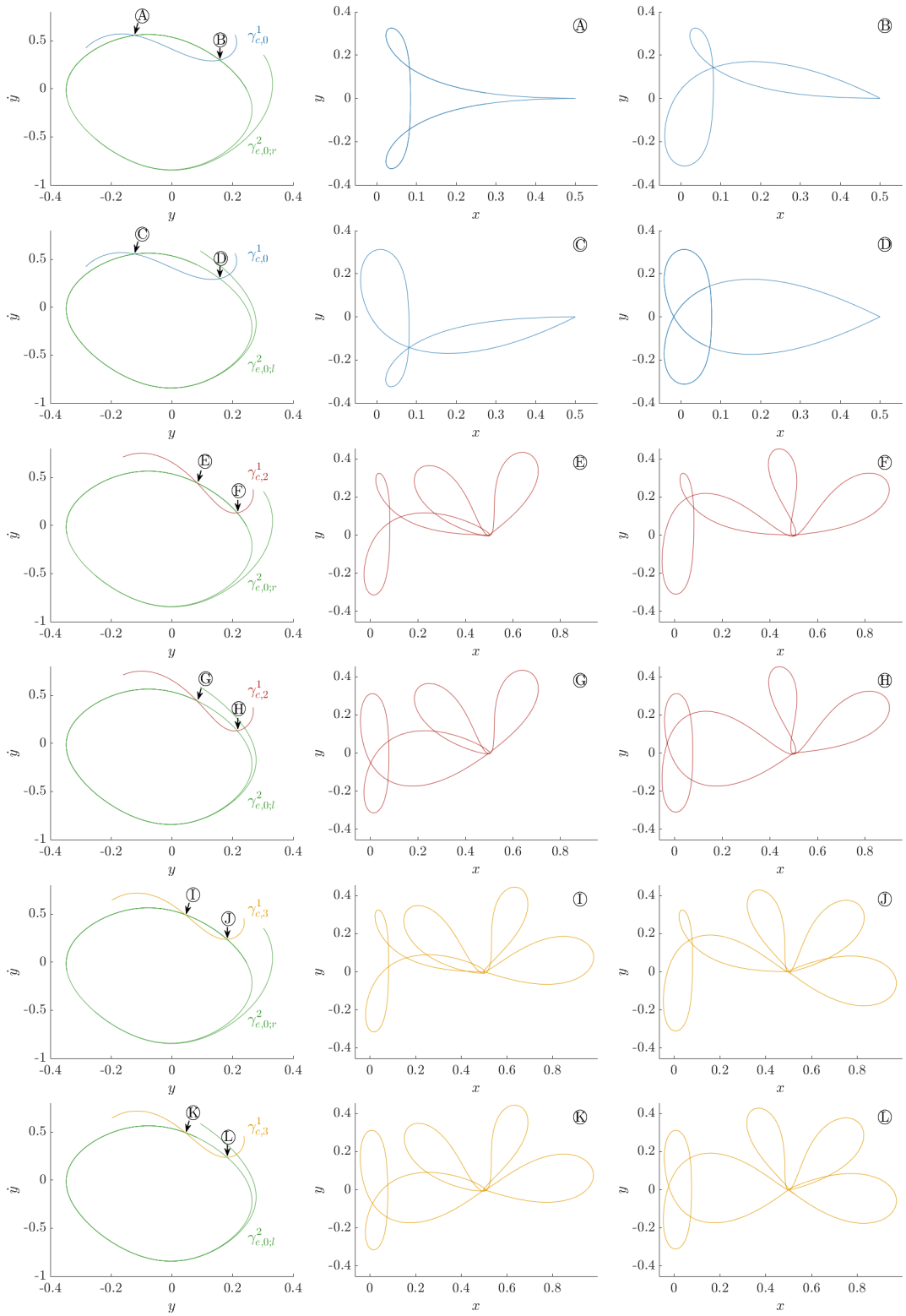

Figure 6.13: $\mu = 0.5$, $C = C_{L_2}$. Left. Curves $\gamma^2_{e,0,r/l}$ and $\gamma^1_{c,n}$ (left column) $(y, \dot{y})$ projection. Middle and right columns, (x, y) projection. $n = 0$, first and second rows. Orbits $E^0_1 - PO^0 - C^0_1$. $n = 2$, third and fourth rows. Orbits $E^0_1 - PO^0 - C^2_1$. $n = 3$, fifth and sixth rows. Orbits $E^0_1 - PO^0 - C^3_1$.

with $n = 0$ (close passages from ejection to the LPO_1) and $j = 0$ (from the LPO_1 to collision arriving at collision after j close passages).

Of course, we can repeat the same kind of description for each given value of n and j. Regarding the number j, we plot in Figure 6.11 the curves obtained from collision with P_1, backwards in time up to Σ^+, for $l = 2$ (in red) and for $l = 3$ (in orange). The same four mechanisms apply again. For each ejection road and collision road chosen, we obtain an infinity of EC orbits (regarding the k turns around the LPO_1). Some particular examples are shown in Figure 6.13. We take $n = 0$ and $j = 2$ (third and fourth rows): orbit E (with ejection road 1, collision road 2), orbit F (with ejection road 1, collision road 1), orbit G (with ejection road 2, collision road 2), orbit H (with ejection road 2, collision road 1). All these orbits are coded as $E_1^0 - PO^0 - C_1^2$. Similarly we take $n = 0$ and $j = 3$ (fifth and sixth rows), EC orbits I, J , K and L, coded as $E_1^0 - PO^0 - C_1^3$.

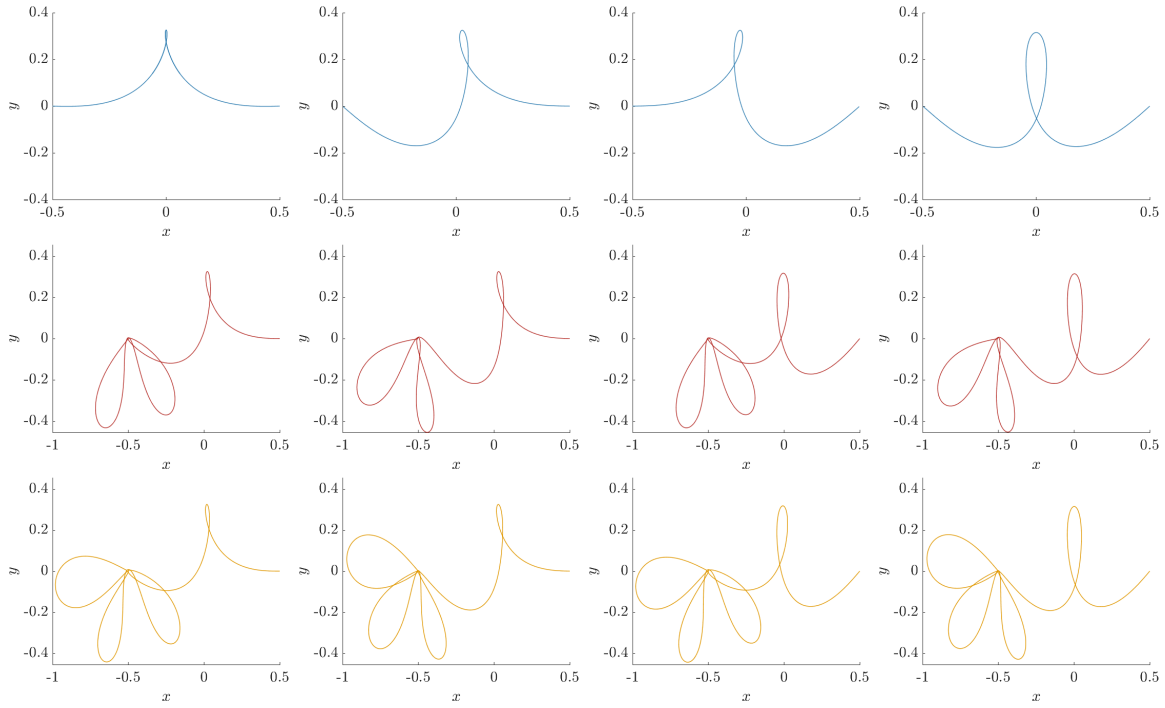

Figure 6.14: $\mu = 0.5$, $C = C_{L_2}$. Some orbits ejecting from P_1 and colliding with P_2. (x, y) projection. First row: orbits coded as $E_1^0 - PO^0 - C_2^0$. Second row: $E_1^0 - PO^0 - C_2^2$. Third row: $E_1^0 - PO^0 - C_2^3$.

EC orbits ejecting from P_1 involving the LPO_1 and colliding with P_2

An EC orbit ejecting from one primary (P_1 for instance) and colliding with the other primary (P_2) is a trajectory that belongs to $W^e(P_1) \cap W^c(P_2)$. So we will proceed in a similar way as in the previous subsection. In this case we will consider the intersection between the curve $\bar{\gamma}_{c,j}^1$ (the bar denoting collision orbits to P_2, integrated backward in time with j close passages around P_2, up to the first crossing with the section Σ^-) and $\gamma_{e,0;m}^2$ (ejection orbits from P_1, integrated forwards in time with $n = 0$, and that we know that pass close to the LPO_1 and are *transit* orbits, so we follow the orbits up to the second crossing with Σ_+). We remark that we precisely select the piece of $\gamma_{e,0;m}^2$, since we know they are transit orbits. We can see in Figure 6.11 right the curve $\gamma_{e,0;m}^2$, which is a double infinite spiral (in green) and $\bar{\gamma}_{c,j}^1$, for $j = 0$ (in blue), $j = 2$ (in red) and $j = 3$ (in orange). So, fixed n, the curve $\bar{\gamma}_{c,j}^1$ intersects $\gamma_{e,0;m}^2$ (the green one) in four infinitely countable sets of points (versus two infinite sets in the EC orbits to the same primary, as discussed in the previous subsection). Thus, we obtain four infinitely countable sets of ejecting orbits from P_1 and colliding with P_2. Similarly as before, the geometry of these orbits is determined through two ejection roads 1 and 2 (due to

the double spiral) and two collision roads 1 and 2 (due to the intersection points). We show some particular examples ((x, y) projection) in Figure 6.14. First row: orbits coded as $E_1^0 - PO^0 - C_2^0$. Second row: $E_1^0 - PO^0 - C_2^2$. Third row: $E_1^0 - PO^0 - C_2^3$.

As above, these are the simplest orbits. We might take a value of n, a value of j and a value of k, to find a zoo of ejecting orbits from P_1 and colliding with P_2. However, in all the cases the geometrical mechanism is always the same.

6.3 Global evolution and detection of EC orbits

Our main goal in this Section is to provide a plot that contains the description of the dynamics of any ejection orbit, for a given finite range of time. That is, we provide a plot containing the dynamics of the set of ejection orbits from a global point of view. Thus, naturally, we should present a 3D-plot containing the dynamical information in the variables x, y and time. But this turns out to generate very heavy loaded plots. Instead, we will use lighter 2D plots with colours containing 3D information. We call them *colour diagram plots*. Roughly speaking, the whole motivation and goals of the chapter are provided in these colour diagram 2D plots in Figures 6.18 and 6.19. We will discuss the effect that the variation of C has on the dynamics on the ejection orbits, and, of course, we will recover the information described in the previous Sections concerning transition intervals I_n and chaos.

So, for a value of $\mu \in (0, 1)$ given, the particle ejects from the big ($\mu \in (0, 0.5]$) or small primary ($\mu \in (0.5, 1)$) and we fix a value of C. Since we are particularly interested in the influence of the LPO_1 and their manifolds on ejection orbits, we will consider (as in the previous sections) values of $C \geq C_{L_{2,3}}$.

But before providing directly such diagram plots and their description, we discuss first two items which should be understood independently and that afterwards, will appear as part of the diagram plots. We think they will help the reader to easier interpret and understand the meaning of such 2D plots.

(i) *Time to reach the successive minima distances to a primary*. We want to illustrate the effect of decreasing C (for μ fixed) on the time needed to make an excursion from ejection until the next passage at minimum distance with respect to a primary. To do so we compute the normalized time to reach the k-th close approach to the primary as a function of the initial ejection angle, that is, for a given μ and C fixed, we compute

$$T_k^N(\theta_0) = k\frac{T_k(\theta_0)}{\bar{T}_k},$$

where $T_k(\theta_0)$ is the necessary time to reach the k-th minimum distance to the primary for that θ_0 and $\bar{T}_k$ is the mean value obtained from all the values of T_k varying θ_0, that is, the mean time that the ejection orbits need to reach the k-th minimum distance.

We plot in Figure 6.15 top the curves obtained for $T_k^N(\theta_0)$ for $k = 1, ..., 10$ and different values of C. On the x-axis we put the k-th close approach, and on the y-axis the initial ejection angle θ_0. The green curve corresponds to $C = 10$, the blue one to $C = 5$, the black one to $C = 4.2$ and the red one to $C = 3.8$. Two aspects should be mentioned. First, as expected, for an ejection angle θ_0 close to $\pi/2$, since the ejection velocity points towards the other primary, the influence of this other primary is apparent, not only for big values of $k \geq 4$ but also for small ones. For small values of k, we see almost vertical curves with a clear deviation (maximum in time) for θ_0 near $\pi/2$. See Figure 6.15 (top) for $k = 1, 2, 3$. In particular, for $k = 1$, we plot in the figure a zoom area and by a dot we remark the time to reach the maximum time of the curves $T_1^N(\theta_0)$, for the four different values of C.

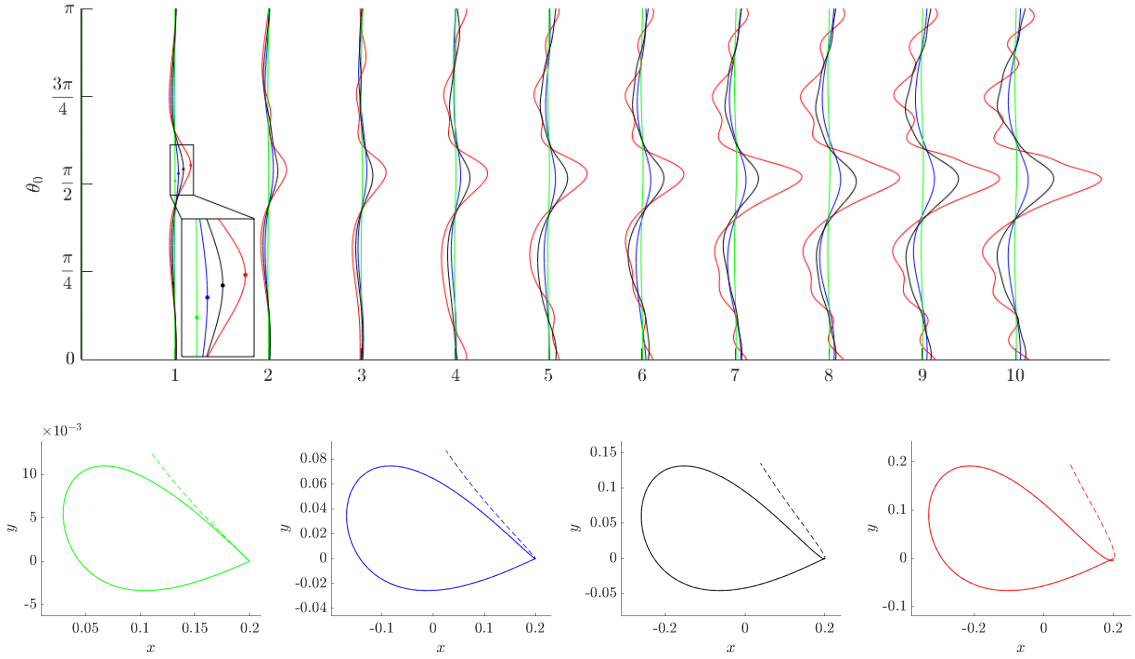

Figure 6.15: $T_k^N(\theta_0)$ at the k-th minimum distance with the primary for $\mu = 0.2$. The green curve corresponds to $C = 10$, the blue one to $C = 5$, the black one to $C = 4.2$ and the red one to $C = 3.8$.

In the bottom figure, we plot the corresponding ejection orbits (for the four particular values of θ_0), in the (x, y) variables, for the range of time that it takes to reach the first minimum (in continuous line) and a bit more (in discontinuous line). We observe how the shape of the ejection curve changes close to the minimum when decreasing C. For bigger values of k, the deviation, when θ_0 is near $\pi/2$, is clearly more visible and the time to reach the k-th minimum distance gets longer. See the top figure for $k \geq 7$. Second, when C decreases and k increases, the curves for each k look like waves with several ripples. It is clear that as C decreases, the amplitude of the LPO_1 gets bigger, and its stable and unstable manifolds play also some role on the trajectory of the ejecting orbits giving rise to such ripples. Actually this is consistent with the description done in the previous sections.

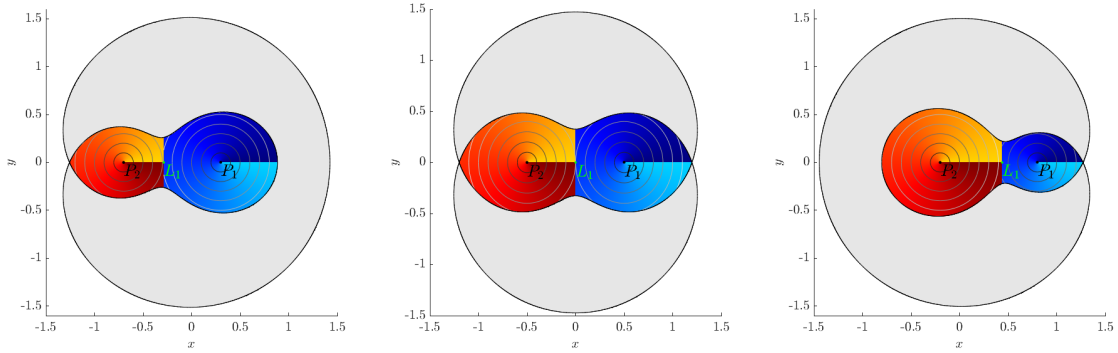

Figure 6.16: Bounded Hill region and identification of the two separate regions, one around each primary. $C = C_{L_2}$ and $\mu = 0.3$ (left), $\mu = 0.5$ (middle). $C = C_{L_3}$ and $\mu = 0.8$ (right).

(ii) *System of coordinates used and particular examples.* In order to understand the system of coordinates used, we divide the bounded Hill region in two regions separated by the line $x = x_{L_1}$. We use polar coordinates (r, θ) (instead of cartesian ones (x, y)) at each region around the corresponding primary which is at the origin of this system of coordinates. Each region has a colour, blue for the region around the right primary and red for the one around the left primary. Actually we will use a

shaded gradual colour to identify the angle θ, and the contour level curves also in a shaded gradual colour will identify the distnace r to the primary. In Figure 6.16 we show an image for $C = C_{L_2}$ and $\mu = 0.3$ (left), $\mu = 0.5$ (middle) and for $C = C_{L_3}$ and $\mu = 0.8$ (right). As shown in the plots, an angle of θ near 0 (near 2π) corresponds to dark blue (light blue), in the region around P_1. Similarly we use orange (dark red) in the region around P_2. On the other hand, the darker (lighter) the contour lines are, the closer (further) the particle is from the corresponding primary.

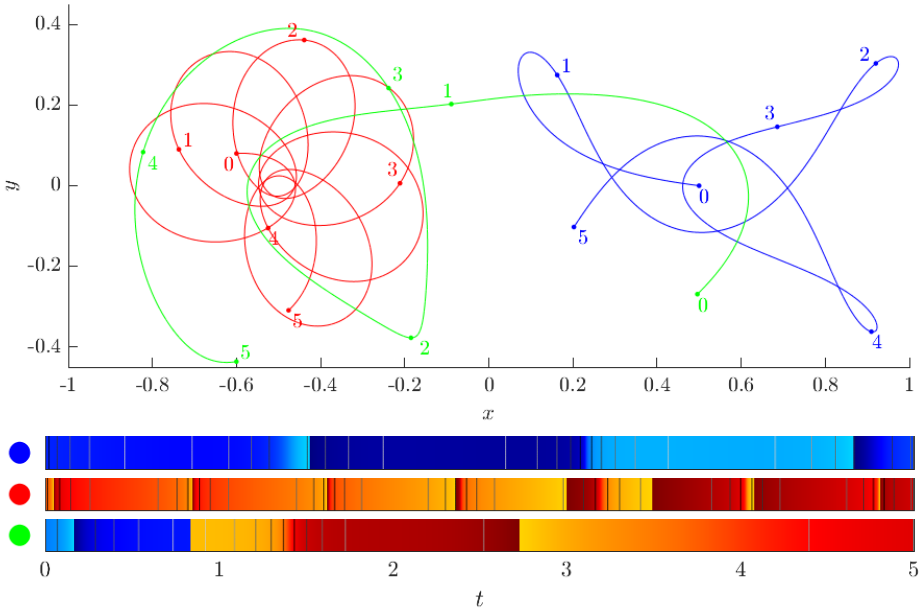

Figure 6.17: Three different examples of orbits in (x, y) coordinates (top) and the associated colour code (bottom), for $t \in [0, 5]$. Number labels are added to identify easily the actual geometrical path with the colour in the diagrams.

So the important point is to visualize the dynamical behaviour of an orbit (and particularly an ejection orbit), along time, through colours. In Figure 6.17 we show three different examples of orbits and its evolution in the range of time $[0, 5]$, both in cartesian coordinates and the corresponding colour code band. The first example corresponds to an ejection orbit (in blue). In (x, y) coordinates the trajectory is self explanatory. The number labels on the trajectory correspond to the location of the particle at the precise instants of time $t = 1, 2, 3, 4, 5$. When regarded according to the colour code band (first one in the bottom figure), we observe the following: since the colour is always blue, the ejecting particle from P_1 remains in that region; from $t = 0$ to $t = 2$, and from $t = 4$ to $t = 5$ the angle crosses the line $\theta = 0$, and the vertical lines provide information about the distance from the particle to P_1. We see vertical darker lines when the particle is closer to the primary, and the bands with a similar intensity of blue correspond to the upper or lower half plane. Regarding the second example, the red orbit in (x, y) coordinates lives in the region around P_2. We can see the close and far passages around P_2 through the vertical lines and the successive passages of the angle through $\theta = 0$, from the sudden changes from lightest orange to darkest red. Finally, the third example corresponds to an orbit that transits from the region around P_1 to the region around P_2. This is clearly seen on the third colour code band, from $t = 0$ to close to $t = 1$:we infer the behaviour of the particle on the region around P_1, from the blue colour and its varying intensity. Then the sudden change from blue to orange corresponds to a transition from one region to the other one. From now on, the intensity in red and the vertical lines describe the trajectory of the particle in that region as time passes by.

Now, let us proceed to an important point of the chapter and that somewhat collects and reflects the results discussed in the previous sections: the *description of the colour diagram plots*. After explaining the colour code to follow the actual trajectory of any particular ejection orbit (as done in the previous item (ii)), we have done massive simulations in order to obtain the complete colour code diagrams for different values of $\mu \in (0, 1)$ and varying C.

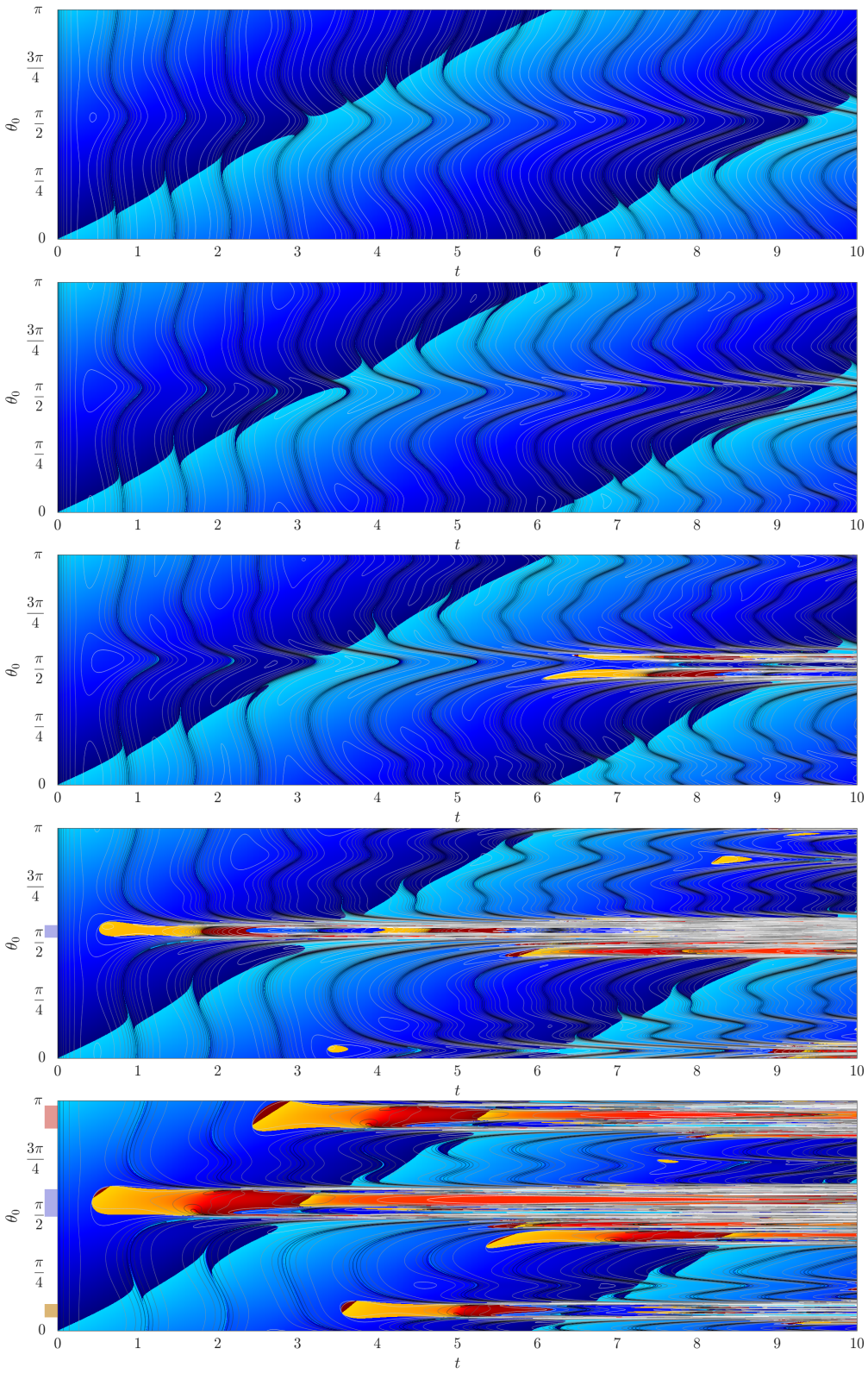

Figure 6.18: Colour code diagrams for $\mu = 0.5$ and $C = C_{L_1}, 4.1, 4, 3.85, C_{L_2}$ (from top to bottom). On the y-axis, we add the transition intervals I_n: blue, red and brown for $n = 0$, $n = 2$ and $n = 3$ ejection orbits, respectively. See more explanation in the text.

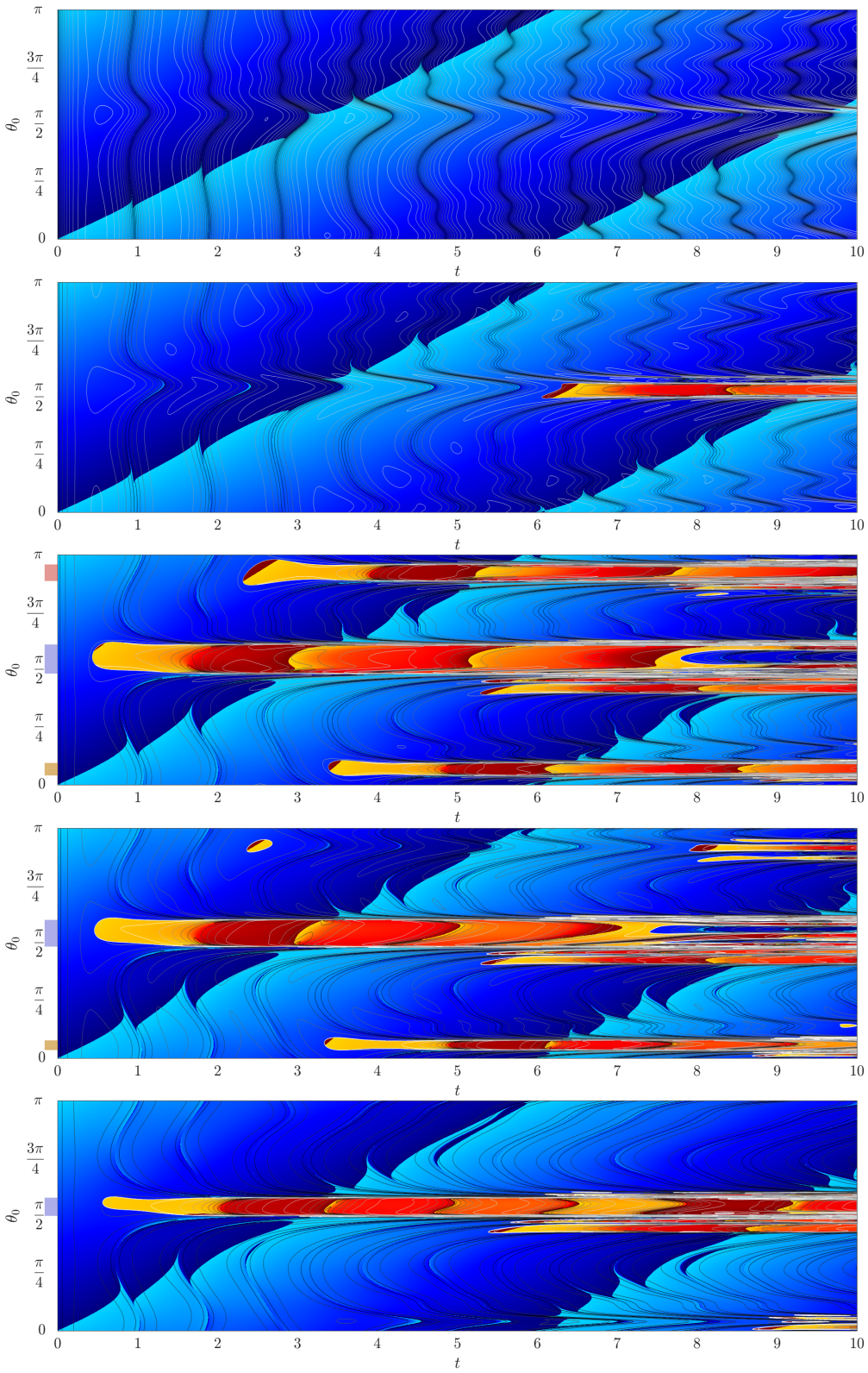

Figure 6.19: Colour code diagrams for $C = C_{L_2}$ and $\mu = 0.2$, 0.3, 0.7, 0.8 and 0.9 (from top to bottom). On the y-axis, we add the transition intervals I_n: blue, red and brown for $n = 0$, $n = 2$ and $n = 3$ ejection orbits, respectively. See more explanation in the text.

For example, we provide the colour code diagrams in Figure 6.18 for $\mu = 0.5$, and different values of C to see the effect of varying C for a μ given; and in Figure 6.19 for $C = C_{L_2}$ and different values of μ to see the effect varying μ for $C = C_{L_2}$ given. In all cases the range of time $t \in [0, 10]$.

Let us start with Figure 6.18. We show the colour code diagrams obtained for $\mu = 0.5$ and $C = C_{L_1} = 4.25, 4.1, 4, 3.85, C_{L_2} = 3.7067962240861525$ and range of time $t \in [0, 10]$ (from top to bottom). Notice that on the y-axis, we also add the transition intervals I_n (range of values of θ_0 for which there is transition from one region to the other one), discussed in Section 6.1. We keep the same colour used in Figures 6.4 and 6.5: blue, red and brown for $n = 0$, $n = 2$ and $n = 3$ ejection orbits, respectively. Recall that n allows to classify the ejection orbits since it is the number of close passages that the ejection orbit describes after ejection, and the endpoints of each interval (that give rise to heteroclinic connections $P_i - LPO_1$ are the frontier between two regimes, transit to the region around the other primary or remaining in the same region the particle ejected from. As discussed in Section 4, such transition intervals appear depending on μ and C, for n given. That is the reason why in the figure only such intervals appear in the last two plots. Now let us explain each plot in the Figure 6.18.

For $C = C_{L_1} = 4.25$, the bounded motion takes place in each independent Hill region around the primary, so any ejection orbit remains on this region for ever. See Figure 6.18 first row. For a given θ_0, the particle ejects form P_1, does the successive far and close passages around the primary P_1 (visible by the darker successive curves). This first plot is related to the top one of Figure 6.15. If we decrease the value of C just a bit, for example $C = 4.1$, there is a very narrow channel that communicates the region around P_1 and the region around P_2. Although there exists the LPO_1 with a small amplitude as well as its invariant stable and unstable manifolds, their influence has no apparent effect for this range of time (we would see its effects for longer ranges of time). So we do not see yet any ejecting orbit that transits to the region around P_2. See Figure 6.18 second row. For $C = 4$, the channel is wider and so is the LPO_1. So now the transit passage from one region from one region to the other one is more feasible. We observe in Figure 6.18 third row the two thin tongues of transit orbits that have appeared, clearly seen by the change of colour from blue to orange. Now for a value of θ_0 in between these two tongues, we can easily describe the corresponding ejection orbit. For example, if we take θ_0 in the first tongue (values of $\theta_0 < \pi/2$), we see that the particle, after ejecting from P_1 and describing six close passages around this primary (seen as six darker blue wave deformed vertical curves), transits to the region around P_2 (entering through the region $x < 0, y > 0$, –orange colour–), describes one turn around P_2 (colour changes from orange to red) and transits again to the region around P_1 (blue colour).

For $C = 3.85$, see Figure 6.18 fourth row, the channel gets wider now and there is a tongue of transit orbits, which appears for t less than the unity (see the orange tongue in the figure). For such orbits, the particle ejects from the primary P_1, has $n = 0$ close approaches to P_1 and transits to the region around P_2 (look at the change of colour from blue to orange approximately in the central part of the plot). The blue transition interval (on the y axis) $I_0 = (\theta_0^1, \theta_0^2)$ (for $n = 0$) (according to the notation of Section 3) is also plotted. We know that for the values of θ_0^1 and θ_0^2 endpoints of I_0 we have heteroclinic connections which are responsible for the chaotic motion if we take values of θ_0 close to both of them (due to the existence of many heteroclinic connections $P_1 - LPO_1$). This can be checked on the plot where many changes of colour are clearly visible. For values of θ_0 in the central part of interval, the path of the trajectories can still be distinguished (for $t \in [0, 7]$), whereas for values of θ_0 near θ_0^i, $i = 1, 2$, we see chaotic behaviour (that is, very thin tongues non distinguishable).

Finally for $C = C_{L_2}$, the channel is yet wider, and there appear new sets of transit orbits, clearly visible from the change of blue colour to red/orange in the plot. See Figure 6.18 last row. Of course, these transitions are in accordance with the intervals I_n, for $n = 0, 2, 3$, also plotted on the y-axis. Remark that simply looking at the plot (the deformed darker vertical waves), we can count the number n of close approaches before the transition ($n = 0$ for the blue interval, $n = 2$ for the red one and $n = 3$ for the brown one).

Now let us move to the next figure and discuss the global evolution of the ejection orbits, not in

terms of variation of C, for μ fixed, but with respect to μ, for a C fixed. We will consider $C_{L_{2,3}}$ (see Figure 6.16) where both the channel between the regions around each primary and the amplitude of the LPO_1 are maxima. We remark, however, that the size of the channel and the amplitude increase with μ. In Figure 6.19 we plot the colour diagrams for the values of $\mu = 0.2, 0.3, 0.7, 0.8, 0.9$ (from top to bottom plots). It is clear from the pictures that for moderate values of μ ($\mu = 0.2$ on the first row plot) the particle that ejects from the big primary P_1 does not feel enough attraction from the small primary and the LPO_1 is also small, so the particle, for this range of time, remains on the region around P_1. However, when μ increases, as expected, the particle feels the attraction of the other primary, and since the LPO_1 is bigger, it is easier to have ejection orbits that transit to the other region. In a natural way, there appears a main tongue of transit orbits for θ_0 near $\pi/2$. Again we have plotted the transition intervals I_n, $n = 0, 2, 3$ on the y-axis, as particular examples. A final remark is that just looking at these diagrams, not only we recognise the I_n intervals, for $n = 0, 2, 3$, but we easily identify other transition intervals. For example see the interval I_5 (not labelled on the y-axis) on second row plot: we can see the horizontal tongue on the approximate central part of the plot for an interval of time $[0, 6]$; for each value of θ_0 in this interval, the corresponding ejection orbit crosses five deformed darker vertical curves, each one associated to a close passage to P_1.

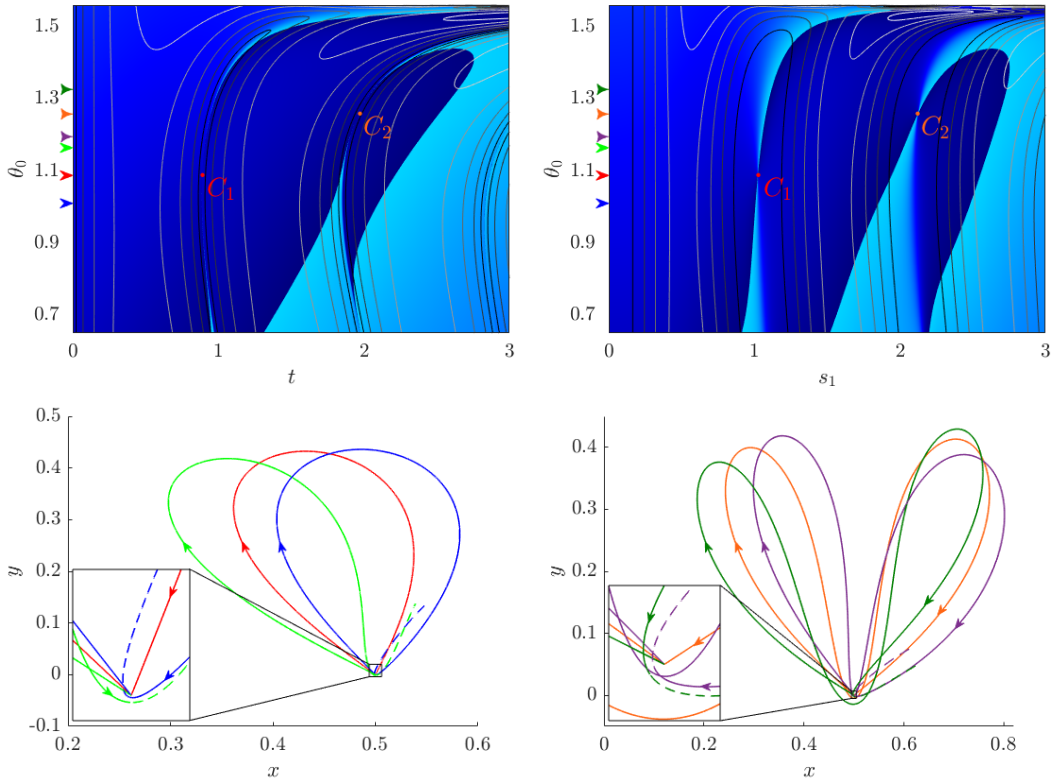

Figure 6.20: Top. Zoom of a colour code diagram to visualize two different EC orbits, the collision taking place at C_1 and C_2 respectively. On the x axis, the usual time t (left) and Levi-Civita time s_1 (right). Bottom. (x, y) variables. We plot the two EC orbits and two orbits nearby to show the path close and at collision. Increasing θ_0 compare the blue and green ejection orbits, with the red EC orbit C_1 in between; and similarly, the purple and dark green orbits with the orange EC one C_2 in between. The values of θ_0 for these orbits are indicated, with the same colour, in the ordinate axis of the top figures.

Just to end this Section, and after the above discussion of the evolution of the ejection orbits, from the ejection instant up to $t = 10$, focussing on successive transitions and close passages to one primary, let us concentrate on a particular type of ejection orbits: the *Ejection-collision orbits*. More specifically, let us explain how to visualize two cases: first, ejection-collision orbits with a primary and, second, ejection from one primary and collision to the other one.

So first, let us focus on the EC orbits with a primary. We show in Figure 6.20 a zoom area for $t \in [0, 5]$ and $\theta_0 \in [0.7, 1.5]$, $\mu = 0.5$ and $C = C_{L_2}$ where we distinguish two values of θ_0 for which we obtain two EC orbits with the big primary. We label the collision points by C_1 and C_2 on the diagram. Of course, concerning the two top plots, we have the same information taking into account the usual time t or the local Levi-Civita time s_1. However, we remark the advantage of using s_1 instead of t: the thin transition of blue colour using t (the left plot) is widened taking the time s_1 and therefore the transition is more clearly visible. Let $\theta_{0,c}$ be the specific value for the EC orbit that collides at C_1. We know that $d\theta/ds$ will be zero at the instant of collision. Moreover, for two different values of θ_0, one bigger and the other one smaller than $\theta_{0,c}$, we know that $d\theta/ds$ will change sign, at the minimum distance to the primary. This change of sign is precisely what we show in the plot: for the three orbits, blue, red (EC orbit) and green (in the bottom left figure), we see this change of sign close to the collision, that is the particle passes on one side (for the blue orbit) or the other one (for the green orbit) with respect to the primary. Similarly, in the top figure, we take the three initial values of θ_0 labelled by the same small colour arrows, and we follow for each θ_0 the corresponding ejection orbit along time. For a range of time s_1 near the time of collision at C_1, we see the degradation of blue colour that goes from dark blue to light one for $\theta_0 < \theta_{0,c}$ and from light blue to dark one for $\theta_0 < \theta_{0,c}$. In between we take the $\theta_{0,c}$ value and on the same range of time, we see that the orbit after and before the collision remains on the same colour region (dark blue in the top figure). A completely analogous behaviour is observed for the collision at C_2. Now the orbits are coloured purple, orange and dark green.

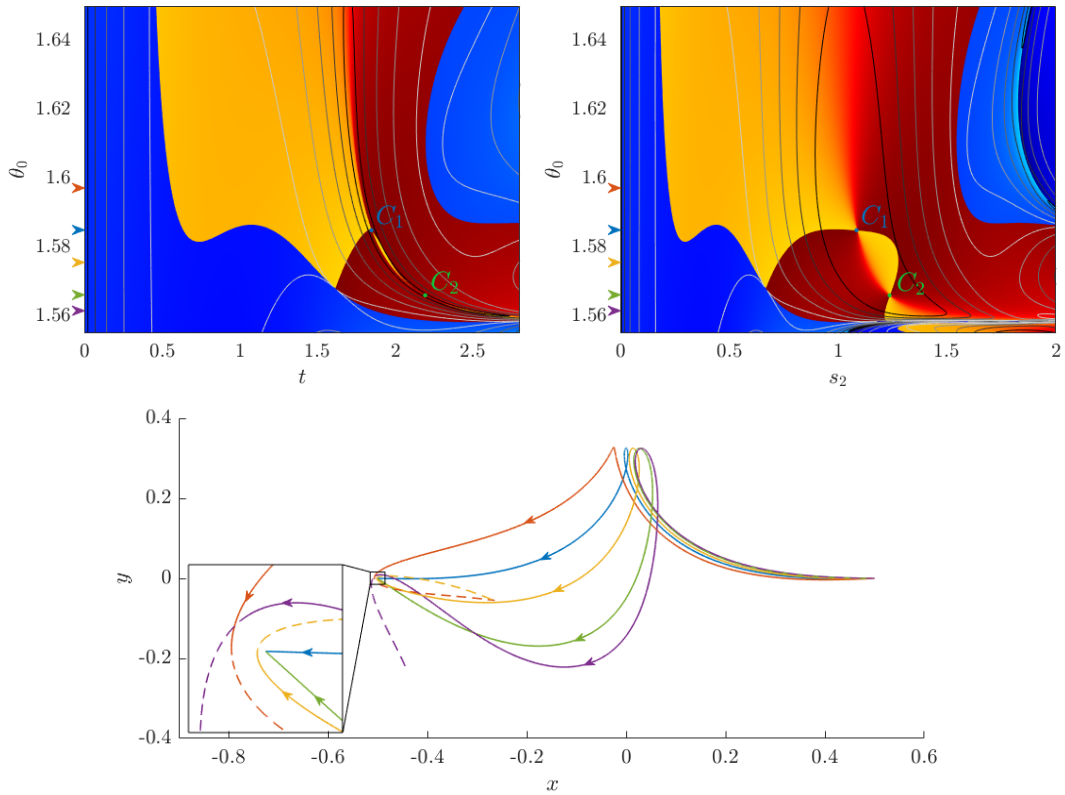

Figure 6.21: Top. Zoom of a colour code diagram to visualize two different orbits, that eject from P_1 and collide with P_2, the collision taking place at C_1 and C_2 respectively. On the x axis, the usual time t (left) and Levi-Civita time s_1 (right). Bottom. (x, y) variables. We plot five ejection orbits to show the path close and at collision. Decreasing θ_0 compare the orange and yellow ejection orbits, with the blue EC orbit in between; and similarly, the yellow and purple orbits with the green EC one in between. The values of θ_0 for these orbits are indicated, with the same colour, in the ordinate axis of the top figures.

Second and finally, concerning the EC orbits that eject from one primary and collide to the other one, a similar description is obtained. In Figure 6.21, we consider $\mu = 0.5$ and $C = C_{L_2}$, and show the evolution of five ejection orbits, purple, green (EC orbit), orange, blue (EC orbit) and red. Of course, in the colour code diagram, the ejection orbits start at the blue region (because they eject from P_1), but move to the other region (change of colour from blue to orange or dark red). We can distinguish the collision because if we take a small box containing on its center C_1 (and not containing C_2) on the right plot, then varying θ_0 on this box from top to bottom, we see the degradation from orange to red above C_1 (look at the orange orbit that describes an increasing angle –in polar coordinates– close to the collision); we observe a degradation from red to orange under C_1 (look at the yellow orbit that describes a decreasing angle –in polar coordinates– close to the collision). Therefore, necessarily there must exist a collision in between (look at the blue EC orbit at C_1). A similar reasoning applies to a small box containing C_2 (and not C_1). Now we can consider the yellow, green (collision) and purple orbits.

Chapter 7

Ejection-Collision orbits in the spatial case

In this last chapter we will make a first approach to the spatial problem and we will focus solely on studying the ejection orbits up to the first minimum at the distance from the first primary and, in particular, on the 1-EC orbits.

As we have seen in the planar RTBP, there are several regularization options, from local ones (removing a collision with one primary but not with the other one) to global ones (regularizing both singularities). The McGehee's local choice is the easiest one from the point of view of the physical meaning of the regularizing variables considered (which are essentially polar coordinates); moreover, the system of ODE has a simple expression and one can analyse the collision manifold. However, ejection or collision orbits, in the McGehee variables and time, become asymptotic solutions to equilibrium points and this is a drawback when doing numerical simulations. By contrast, Levi-Civita local regularization results more suitable from the numerical point of view, since the path through collision is a regular point, but the expression of the resulting ODE is more intricate and a double covering of the phase space intrinsically appears.

A similar situation occurs in the spatial problem. The McGehee's 3D local choice is the easiest one from the point of view of the physical meaning (which are essentially spherical coordinates); but the ejection/collision become asymptotic in time. By contrast, the Kustaanheimo-Stiefel regularization (which is the generalization of Levi-Civita's regularization) results more suitable from the numerical point of view, since the path through collision is a regular point, but it requires and extra dimension (from 3D to 4D, i.e. obtaining a nonlinear system of 8 ODE of first order) making the physical meaning even more complicated.

For that reason, we will consider in this chapter the McGehee's 3D local regularization.

Before proceeding we note that the contents of this chapter have been extracted from [ORS21a].

7.1 McGehee regularization in the 3D case

In this chapter, as we said previously, we want to analyse the McGehee regularization, which is local in the sense that, after applying some changes of variables and time, we obtain a new system of ODE which is regular at $r_1 = 0$ but singular at $r_2 = 0$ (or regular at $r_2 = 0$ and singular at $r_1 = 0$). In the

sequel, we describe the different steps to regularize the collision $r_1 = 0$.

The first step is to move the primary P_1 to the origin, by means of a translation: $\bar{x} = x - \mu, \bar{y} = y, \bar{z} = z, \bar{p}_x = p_x = \dot{x} - y = p_x, \bar{p}_y = p_y = \dot{y} + x = \dot{y} + \bar{x} + \mu, \bar{p}_z = p_z$. We obtain a new Hamiltonian, we abuse the notation and skip the bar notation and denote by (x, y, z, p_x, p_y, p_z) the new variables. The Hamiltonian of the 3D RTBP is:

$$H(x, y, z, p_x, p_y, p_z) = \frac{1}{2}(p_x^2 + p_y^2 + p_z^2) + yp_x - xp_y - \frac{1-\mu}{r_1} - \frac{\mu}{r_2} - \mu p_y - \frac{1}{2}\mu(1-\mu), \tag{7.1}$$

where $r_1 = \sqrt{x^2 + y^2 + z^2}$ and $r_2 = \sqrt{(x+1)^2 + y^2 + z^2}$ with

$$\begin{cases} p_x = \dot{x} - y, \\ p_y = \dot{y} + x + \mu, \\ p_z = \dot{z}. \end{cases}$$

The next step is to consider the symplectic change to spherical variables given by

$$\begin{cases} x = r\cos\theta\cos\varphi, \\ y = r\sin\theta\cos\varphi, \\ z = r\sin\varphi, \end{cases} \tag{7.2}$$

with the longitude $\theta \in [0, 2\pi)$ (on the (x, y) plane) and the inclination (or latitude) $\varphi \in [-\frac{\pi}{2}, \frac{\pi}{2}]$. We will call this change *spherical variables with respect to the z axis*.

Let us recall that the symplectic change of variables $(\boldsymbol{q}, \boldsymbol{p})$ to $(\boldsymbol{Q}, \boldsymbol{P})$ in $\mathbb{R}^{2n}$, when we know $\boldsymbol{q} = \boldsymbol{f}(\boldsymbol{Q})$ comes from:

$$\boldsymbol{p} = \left[D\boldsymbol{f}(\boldsymbol{Q})^T\right]^{-1} \boldsymbol{P}.$$

So, we have

$$\begin{pmatrix} p_x \\ p_y \\ p_z \end{pmatrix} = \begin{pmatrix} \cos\varphi\cos\theta & -\dfrac{\sin\theta}{r\cos\varphi} & -\dfrac{\cos\theta\sin\varphi}{r} \\ \cos\varphi\sin\theta & \dfrac{\cos\theta}{r\cos\varphi} & -\dfrac{\sin\theta\sin\varphi}{r} \\ \sin\varphi & 0 & \dfrac{\cos\varphi}{r} \end{pmatrix} \begin{pmatrix} p_r \\ p_\theta \\ p_\varphi \end{pmatrix},$$

and the Hamiltonian (7.1) becomes:

$$\begin{aligned} H(r, \theta, \varphi, p_r, p_\theta, p_\varphi) = &\frac{1}{2}\left(p_r^2 + \frac{p_\theta^2}{r^2\cos^2\varphi} + \frac{p_\varphi^2}{r^2}\right) - p_\theta - \frac{1-\mu}{r} - \frac{\mu}{r_2} \\ &- \mu\left(p_r\sin\theta\cos\varphi + \frac{p_\theta\cos\theta}{r\cos\varphi} - \frac{p_\varphi\sin\theta\sin\varphi}{r}\right) - \frac{1}{2}\mu(1-\mu), \end{aligned} \tag{7.3}$$

with $r_2 = \sqrt{r^2 + 2r\cos\theta\cos\varphi + 1}$.

The associated system of ODE is given by

$$\begin{cases} \dot{r} = p_r - \mu \sin\theta \cos\varphi, \\ \dot{\theta} = \dfrac{p_\theta}{r^2 \cos^2\varphi} - \dfrac{\mu \cos\theta}{r \cos\varphi} - 1, \\ \dot{\varphi} = \dfrac{p_\varphi}{r^2} + \dfrac{\mu \sin\theta \sin\varphi}{r}, \\ \dot{p}_r = \dfrac{p_\varphi^2}{r^3} - \dfrac{1-\mu}{r^2} + \dfrac{p_\theta^2}{r^3 \cos^2\varphi} - \mu \left(\dfrac{r + \cos\theta\cos\varphi}{r_2^3} + \dfrac{p_\theta \cos\theta}{r^2 \cos\varphi} - \dfrac{p_\varphi \sin\theta \sin\varphi}{r^2} \right), \\ \dot{p}_\theta = \mu \left(\dfrac{r \sin\theta \cos\varphi}{r_2^3} + p_r \cos\theta\cos\varphi - \dfrac{p_\theta \sin\theta}{r\cos\varphi} - \dfrac{p_\varphi \cos\theta \sin\varphi}{r} \right), \\ \dot{p}_\varphi = -\dfrac{p_\theta^2 \sin\varphi}{r^2 \cos^3\varphi} + \mu \left(\dfrac{r\cos\theta\sin\varphi}{r_2^3} - p_r \sin\theta\sin\varphi + \dfrac{p_\theta \cos\theta \sin\varphi}{r\cos^2\varphi} - \dfrac{p_\varphi \sin\theta\cos\varphi}{r} \right). \end{cases} \tag{7.4}$$

Next let us consider the variables $(r, \theta, \varphi, v_r, v_\theta, v_\varphi)$ where $(v_r, v_\theta, v_\varphi)$ are the spherical components of the velocity:

$$v_r = \dot{r}, \qquad v_\theta = r\dot{\theta}\cos\varphi, \qquad v_\varphi = r\dot{\varphi}. \tag{7.5}$$

From (7.4) and (7.5) we have:

$$\begin{cases} v_r = p_r - \mu \sin\theta\cos\varphi, \\ v_\theta = \dfrac{p_\theta}{r\cos\varphi} - \mu\cos\theta - r\cos\varphi, \\ v_\varphi = \dfrac{p_\varphi}{r} + \mu \sin\theta \sin\varphi, \end{cases} \quad \text{or similarly} \quad \begin{cases} p_r = v_r + \mu \sin\theta\cos\varphi, \\ p_\theta = (v_\theta + \mu\cos\theta)\, r\cos\varphi + r^2\cos^2\varphi, \\ p_\varphi = r v_\varphi - \mu r \sin\theta\sin\varphi, \end{cases}$$

and system (7.4) becomes:

$$\begin{cases} \dot{r} = v_r, \\ \dot{\theta} = \dfrac{v_\theta}{r\cos\varphi}, \\ \dot{\varphi} = \dfrac{v_\varphi}{r}, \\ \dot{v}_r = \dfrac{v_\theta^2 + v_\varphi^2}{r} + 2v_\theta\cos\varphi + r\cos^2\varphi - \dfrac{1-\mu}{r^2} + \mu\left(\cos\theta\cos\varphi - \dfrac{r + \cos\theta\cos\varphi}{r_2^3} \right), \\ \dot{v}_\theta = -\dfrac{v_r v_\theta}{r} - 2v_r\cos\varphi + 2v_\varphi \sin\varphi + \dfrac{v_\theta v_\varphi \sin\varphi}{r\cos\varphi} - \mu\sin\theta\left(1 - \dfrac{1}{r_2^3}\right), \\ \dot{v}_\varphi = -\dfrac{v_\theta^2 \sin\varphi}{r\cos\varphi} - \dfrac{v_r v_\varphi}{r} - 2v_\theta\sin\varphi - r\cos\varphi\sin\varphi - \mu\cos\theta\sin\varphi\left(1 - \dfrac{1}{r_2^3}\right). \end{cases} \tag{7.6}$$

Next, and as it is done in the 2D case, we introduce the variables:

$$v = r^{1/2} v_r, \qquad u_\theta = r^{1/2} v_\theta, \qquad u_\varphi = r^{1/2} v_\varphi, \tag{7.7}$$

and system (7.6) becomes:

$$\begin{cases} \dot{r} = \dfrac{v}{r^{1/2}}, \\ \dot{\theta} = \dfrac{u_\theta}{r^{3/2}\cos\varphi}, \\ \dot{\varphi} = \dfrac{u_\varphi}{r^{3/2}}, \\ \dot{v} = \dfrac{v^2}{2r^{3/2}} + \dfrac{u_\theta^2+u_\varphi^2}{r^{3/2}} - \dfrac{1-\mu}{r^{3/2}} + 2u_\theta\cos\varphi + r^{3/2}\cos^2\varphi + \mu r^{1/2}\left(\cos\theta\cos\varphi - \dfrac{r+\cos\theta\cos\varphi}{r_2^3}\right), \\ \dot{u}_\theta = -\dfrac{u_\theta v}{2r^{3/2}} + 2u_\varphi\sin\varphi - 2v\cos\varphi + \dfrac{u_\varphi u_\theta\sin\varphi}{r^{3/2}\cos\varphi} - \mu r^{1/2}\sin\theta\left(1-\dfrac{1}{r_2^3}\right), \\ \dot{u}_\varphi = -\dfrac{u_\varphi v}{2r^{3/2}} - \dfrac{u_\theta^2\sin\varphi}{r^{3/2}\cos\varphi} - 2u_\theta\sin\varphi - r^{3/2}\cos\varphi\sin\varphi - \mu r^{1/2}\cos\theta\sin\varphi\left(1-\dfrac{1}{r_2^3}\right). \end{cases} \tag{7.8}$$

At this point, we want to emphasize that if we follow the same strategy as in the 2D case and introduce a rescaling in time through the relation $dt/d\tau = r^{3/2}$, we still have a problem: the resulting system of ODE is not defined for $\varphi = \pm\pi/2$, i.e. all the points on the z axis are singular. This situation did not happen in the 2D case and it is precisely the reason why the regularization of Kustaanheimo-Stiefel requires an extra dimension (see [SS71] for details). With this change of time the previous system becomes

$$\begin{cases} r' = vr, \\ \theta' = \dfrac{u_\theta}{\cos\varphi} \\ \varphi' = u_\varphi, \\ v' = \dfrac{v^2}{2} + (u_\theta^2+u_\varphi^2) - (1-\mu) + 2u_\theta r^{3/2}\cos\varphi + r^3\cos^2\varphi + \mu r^2\left(\cos\theta\cos\varphi - \dfrac{r+\cos\theta\cos\varphi}{r_2^3}\right), \\ u_\theta' = -\dfrac{u_\theta v}{2} + 2u_\varphi r^{3/2}\sin\varphi - 2vr^{3/2}\cos\varphi + \dfrac{u_\varphi u_\theta\sin\varphi}{\cos\varphi} - \mu r^2\sin\theta\left(1-\dfrac{1}{r_2^3}\right), \\ u_\varphi' = -\dfrac{u_\varphi v}{2} - 2u_\theta r^{3/2}\sin\varphi - \dfrac{u_\theta^2\sin\varphi}{\cos\varphi} - r^3\cos\varphi\sin\varphi - \mu r^2\cos\theta\sin\varphi\left(1-\dfrac{1}{r_2^3}\right), \end{cases} \tag{7.9}$$

where $' = d/d\tau$. This rescaling in time was applied in [LMA85], and the authors proceeded not taking into account this whole set of singularities. In order to deal with this set of singularities on the z axis, we now consider the following rescaling in time $dt/d\hat{\tau} = r^{3/2}\cos\varphi$. The resulting system of ODE is now

$$\begin{cases} r' = vr\cos\varphi, \\ \theta' = u_\theta, \\ \varphi' = u_\varphi\cos\varphi, \\ v' = \dfrac{v^2}{2}\cos\varphi + (u_\theta^2+u_\varphi^2)\cos\varphi - (1-\mu)\cos\varphi + 2u_\theta r^{3/2}\cos^2\varphi + r^3\cos^3\varphi, \\ \qquad + \mu r^2\cos\varphi\left(\cos\theta\cos\varphi - \dfrac{r+\cos\theta\cos\varphi}{r_2^3}\right), \\ u_\theta' = -\dfrac{u_\theta v}{2}\cos\varphi + 2u_\varphi r^{3/2}\cos\varphi\sin\varphi - 2vr^{3/2}\cos^2\varphi + u_\varphi u_\theta\sin\varphi - \mu r^2\sin\theta\cos\varphi\left(1-\dfrac{1}{r_2^3}\right), \\ u_\varphi' = -\dfrac{u_\varphi v}{2}\cos\varphi - u_\theta^2\sin\varphi - 2u_\theta r^{3/2}\cos\varphi\sin\varphi - r^3\cos^2\varphi\sin\varphi - \mu r^2\cos\theta\cos\varphi\sin\varphi\left(1-\dfrac{1}{r_2^3}\right), \end{cases} \tag{7.10}$$

where $' = d/d\hat{\tau}$. Let us remark that we have removed the (local) singularity $r_1 = r = 0$ and the z axis and now only the singularity $r_2 = 1$ persists; however two consequences of such a rescaling are (i) the

whole set $\cos\varphi = 0$, $u_\theta = 0$ is composed of equilibrium points, and (ii) the z axis ($\cos\varphi = 0$) –on the configuration space– is invariant. This is a main difference between the McGehee regularization for the planar and for the spatial RTBP.

We also remark that the first integral (the Jacobi constant or the Hamiltonian itself) is not defined neither on $r = 0$ nor on $r_2 = 0$. However if we multiply the relation $H = \mathfrak{H}$ by r we obtain

$$0 = -\mathfrak{H} r + \frac{1}{2}\left(u_\varphi^2 + u_\theta^2 + v^2\right) - (1-\mu) - \frac{r^3\cos^2\varphi}{2} - \frac{\mu r}{2} - \frac{\mu r}{r_2} - \mu r^2\cos\theta\cos\varphi, \tag{7.11}$$

which is valid on each energy level $H = \mathfrak{H}$ constant.

7.1.1 Local charts

From the above system it is clear that one drawback appears: this system is not a suitable one to deal with numerically if we want to consider trajectories with high inclinations (that is passing close to the invariant z axis), since the time of integration may become very large.

Our approach to deal with this inconvenience consists in taking three different local charts in such a way that, for each chart we only consider inclinations in the interval $[-\pi/4, \pi/4]$ –and the numerical integrations work perfectly fine–, and the union of the local charts recover the whole space.

More precisely, we consider a first chart taking into account system (7.10), that is using the McGehee variables from the spherical variables with respect to the z axis. We avoid high inclinations just taking into account values of $\varphi \in [-\pi/4, \pi/4]$. Similarly we introduce a second local chart using the McGehee variables from the spherical variables with respect to the x axis. We avoid high inclinations just taking into account inclination values in $[-\pi/4, \pi/4]$. Finally we introduce a third local chart using the McGehee variables from the spherical variables with respect to the y axis. We avoid high inclinations just taking into account inclination values in $[-\pi/4, \pi/4]$.

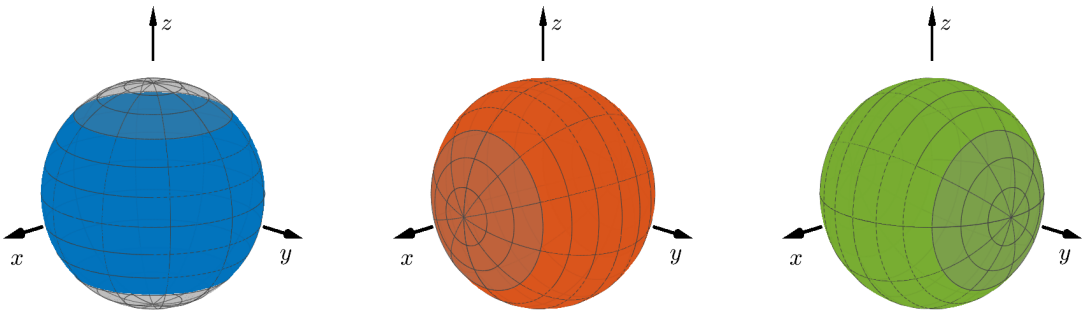

Figure 7.1: Local charts considered avoiding the z axis (left), x axis (middle) and y axis (right). The inclination considered for each local chart is always in the interval $[-\pi/4, \pi/4]$.

In Figure 7.1, we plot explicitly the 3 different local charts considered, only regarding the values of the longitude and latitude: on the left plot we avoid the z axis, on the middle one we avoid the x axis, and on the right one we avoid the y axis. For every local chart we will consider only inclinations (in the corresponding angular variable) in the interval $[-\pi/4, \pi/4]$. We also plot in Figure 7.2 the spherical caps which are avoided for each local chart. It is clear that taking any pair of local charts we recover the whole sphere S^2.

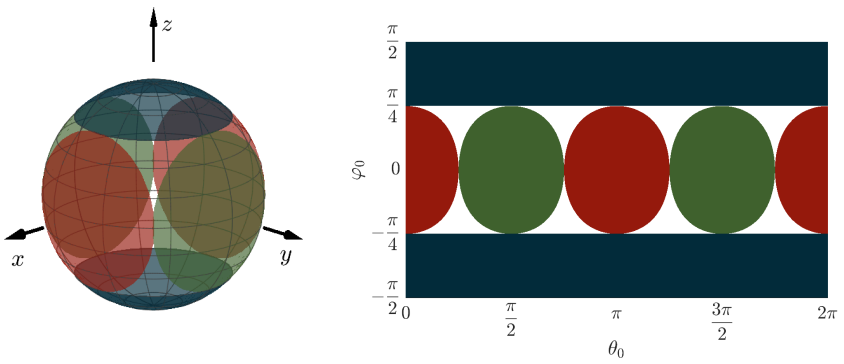

Figure 7.2: Spherical caps not parametrized with the different local charts. Any pair of local charts recovers the whole sphere S^2.

In a similar way as we have explained how to obtain the regular system of ODE (7.10), from the spherical variables (r, θ, φ), we consider the other two changes of spherical variables and proceed to obtain the corresponding systems of regularised ODE. Their outcome expressions are the following.

Spherical variables with respect to the x axis

We consider the symplectic change of variables to spherical variables with respect to the x axis, that is

$$\begin{cases} x = r \sin \widehat{\varphi}, \\ y = r \cos \widehat{\theta} \cos \widehat{\varphi}, \\ z = r \sin \widehat{\theta} \cos \widehat{\varphi}. \end{cases}$$

A similar procedure, with $' = d/d\hat{\tau}$ where now $dt/d\hat{\tau} = r^{3/2} \cos \widehat{\varphi}$, leads to the system

$$\begin{cases} r' = vr \cos \widehat{\varphi}, \\ \widehat{\theta}' = u_{\widehat{\theta}}, \\ \widehat{\varphi}' = u_{\widehat{\varphi}} \cos \widehat{\varphi}, \\ v' = \dfrac{v^2}{2} \cos \widehat{\varphi} + (u_{\widehat{\theta}}^2 + u_{\widehat{\varphi}}^2) \cos \widehat{\varphi} - (1-\mu) \cos \widehat{\varphi} - 2r^{3/2}(u_{\widehat{\theta}} \sin \widehat{\theta} \sin \widehat{\varphi} + u_{\widehat{\varphi}} \cos \widehat{\theta}) \cos \widehat{\varphi} \\ \qquad + r^3 \cos \widehat{\varphi}(\cos^2 \widehat{\theta} + \sin^2 \widehat{\theta} \sin^2 \widehat{\varphi}) + \mu r^2 \cos \widehat{\varphi} \left(\sin \widehat{\varphi} - \dfrac{r + \sin \widehat{\varphi}}{r_2^3} \right), \\ u'_{\widehat{\theta}} = u_{\widehat{\varphi}} u_{\widehat{\theta}} \sin \widehat{\varphi} - \dfrac{u_{\widehat{\theta}} v}{2} \cos \widehat{\varphi} + 2r^{3/2}(u_{\widehat{\varphi}} \cos \widehat{\varphi} + v \sin \widehat{\varphi}) \sin \widehat{\theta} \cos \widehat{\varphi} - r^3 \cos \widehat{\theta} \sin \widehat{\theta} \cos^2 \widehat{\varphi}, \\ u'_{\widehat{\varphi}} = -\dfrac{u_{\widehat{\varphi}} v}{2} \cos \widehat{\varphi} - u_{\widehat{\theta}}^2 \sin \widehat{\varphi} - 2r^{3/2}(u_{\widehat{\theta}} \cos \widehat{\varphi} \sin \widehat{\theta} - v \cos \widehat{\theta}) \cos \widehat{\varphi} + r^3 \sin^2 \widehat{\theta} \cos^2 \widehat{\varphi} \sin \widehat{\varphi} \\ \qquad + \mu r^2 \cos \widehat{\varphi}^2 \left(1 - \dfrac{1}{r_2^3} \right), \end{cases} \tag{7.12}$$

where $r_2 = \sqrt{r^2 + 2r \sin \widehat{\varphi} + 1}$.

Spherical variables with respect to the y axis

We consider the symplectic change of variables to spherical variables with respect to the y axis, that is,

$$\begin{cases} x = r\sin\bar{\theta}\cos\bar{\varphi}, \\ y = r\sin\bar{\varphi}, \\ z = r\cos\bar{\theta}\cos\bar{\varphi}. \end{cases}$$

A similar procedure, with $' = d/d\hat{\tau}$ where now $dt/d\hat{\tau} = r^{3/2}\cos\bar{\varphi}$, leads to the system

$$\begin{cases} r' = vr\cos\bar{\varphi}, \\ \bar{\theta}' = u_{\bar{\theta}}, \\ \bar{\varphi}' = u_{\bar{\varphi}}\cos\bar{\varphi}, \\ v' = \dfrac{v^2\cos\bar{\varphi}}{2} + (u_{\bar{\theta}}^2 + u_{\bar{\varphi}}^2)\cos\bar{\varphi} - (1-\mu)\cos\bar{\varphi} + 2r^{3/2}(u_{\bar{\varphi}}\sin\bar{\theta} - u_{\bar{\theta}}\cos\bar{\theta}\sin\bar{\varphi})\cos\bar{\varphi} \\ \qquad + r^3\cos\bar{\varphi}(1-\cos^2\bar{\varphi}\cos^2\bar{\theta}) + \mu r^2\cos\bar{\varphi}\left(\cos\bar{\varphi}\sin\bar{\theta} - \dfrac{r+\cos\bar{\varphi}\sin\bar{\theta}}{r_2^3}\right), \\ u_{\bar{\theta}}' = u_{\bar{\varphi}}u_{\bar{\theta}}\sin\bar{\varphi} - \dfrac{u_{\bar{\theta}}v}{2}\cos\bar{\varphi} + 2r^{3/2}(u_{\bar{\varphi}}\cos\bar{\varphi} + v\sin\bar{\varphi})\cos\bar{\theta}\cos\bar{\varphi} + r^3\cos\bar{\theta}\sin\bar{\theta}\cos^2\bar{\varphi} \\ \qquad + \mu r^2\cos\bar{\theta}\cos\bar{\varphi}\left(1 - \dfrac{1}{r_2^3}\right), \\ u_{\bar{\varphi}}' = -u_{\bar{\theta}}^2\sin\bar{\varphi} - \dfrac{u_{\bar{\varphi}}v}{2}\cos\bar{\varphi} - 2r^{3/2}(u_{\bar{\theta}}\cos\bar{\varphi}\cos\bar{\theta} + v\sin\bar{\theta})\cos\bar{\varphi} + r^3\cos^2\bar{\theta}\cos^2\bar{\varphi}\sin\bar{\varphi} \\ \qquad - \mu r^2\sin\bar{\theta}\cos\bar{\varphi}\sin\bar{\varphi}\left(1 - \dfrac{1}{r_2^3}\right), \end{cases} \tag{7.13}$$

where $r_2 = \sqrt{r^2 + 2r\sin\bar{\theta}\cos\bar{\varphi} + 1}$.

Remark 11. *It is clear now that using systems* (7.10), (7.12) *and* (7.13), *we can integrate any orbit, with the exception that it passes very close to the second primary. In such a case we can proceed in a similar way with the same kind of regularization around the second primary.*

7.2 The collision manifold

The collision manifold, called from now on Λ, is the invariant manifold by the flow of system (7.10) (or (7.12) or (7.13)) when we take $r = 0$. We will analyse the collision manifold in variables $(r, \theta, \varphi, v, u_\theta, u_\varphi)$. A similar study can be done when taking the other set of variables introduced for the different local charts.

A first observation is that the energy relation (7.11) on Λ becomes $u_\varphi^2 + u_\theta^2 + v^2 = 2(1-\mu)$ for arbitrary θ and φ, so the manifold Λ is a four-dimensional manifold diffeomorphic to $S^2 \times S^2$ and is defined on the boundary of each fixed level of the Jacobi integral (or the Hamiltonian). Moreover the system of ODE (7.10) on Λ is

$$\begin{cases} \theta' = u_\theta, \\ \varphi' = u_\varphi\cos\varphi, \\ v' = \dfrac{v^2}{2}\cos\varphi + (u_\theta^2 + u_\varphi^2)\cos\varphi - (1-\mu)\cos\varphi = \dfrac{u_\theta^2 + u_\varphi^2}{2}\cos\varphi, \\ u_\theta' = -\dfrac{u_\theta v}{2}\cos\varphi + u_\varphi u_\theta\sin\varphi, \\ u_\varphi' = -\dfrac{u_\varphi v}{2}\cos\varphi - u_\theta^2\sin\varphi, \end{cases} \tag{7.14}$$

which describes the internal dynamics on the manifold.

In particular, on Λ there exist two spheres $S^2_\pm$ of equilibrium points defined by

- $S^2_+ = \{(r = 0, \theta, \varphi, v = v_0, u_\theta = 0, u_\varphi = 0)\}$,
- $S^2_- = \{(r = 0, \theta, \varphi, v = -v_0, u_\theta = 0, u_\varphi = 0)\}$,

with $v_0 = \sqrt{2(1-\mu)}$. In order to determine their stability as equilibrium points in R^6, we proceed to the linearization of system (7.10) on any point belonging to S^2_+ and we obtain the Jacobian matrix:

$$M^+ = \begin{pmatrix} \lambda & 0 & 0 & 0 & 0 & 0 \\ 0 & 0 & 0 & 0 & 1 & 0 \\ 0 & 0 & 0 & 0 & 0 & \cos\varphi \\ 0 & 0 & 0 & \lambda & 0 & 0 \\ 0 & 0 & 0 & 0 & -\lambda/2 & 0 \\ 0 & 0 & 0 & 0 & 0 & -\lambda/2 \end{pmatrix}, \tag{7.15}$$

with $\lambda = v_0 \cos\varphi$. Similarly we obtain the linearization of the system on each point of S^2_-, that is M^-, simply interchanging λ by $-\lambda$. M^+ has eigenvalues λ, λ, $-\lambda/2$, $-\lambda/2$, 0, 0.

The corresponding eigenvectors are:

$$\begin{array}{lll} \boldsymbol{v}_1 = (1,0,0,0,0,0), & \boldsymbol{v}_2 = (0,0,0,1,0,0), & \boldsymbol{v}_3 = (0,-2,0,0,v_0\cos\varphi,0), \\ \boldsymbol{v}_4 = (0,0,-2,0,0,v_0), & \boldsymbol{v}_5 = (0,1,0,0,0,0), & \boldsymbol{v}_6 = (0,0,1,0,0,0). \end{array} \tag{7.16}$$

Let us denote by $W^{u,s}(P)$ the unstable and stable invariant manifolds of an equilibrium point P, and $W^{u,s}(S^2_\pm)$ the unstable and stable invariant manifolds of the whole sphere S^2_+ or S^2_-. Concerning the dimensions of these invariant manifolds and the internal dynamics on Λ, Llibre and Alfaro in [LMA85] proved the following result.

Proposition (i) Fixed an energy level we have

$$\begin{aligned} \dim W^s(S^2_+) &= \dim W^u(S^2_-) = 4, \\ \dim W^u(S^2_+) &= \dim W^s(S^2_-) = 3. \end{aligned} \tag{7.17}$$

(ii) For the flow on the collision manifold Λ, the unstable invariant manifold associated with the equilibrium point $P_- = (\theta = \theta^*, \varphi = \varphi^*, -v_0, 0, 0) \in S^2_-$, $W^u(P_-)$, coincides with the stable invariant manifold of the equilibrium point $P_+ = (\theta = \theta^*, \varphi = \varphi^*, v_0, 0, 0) \in S^2_+$, $W^s(P_+)$. Therefore

$$W^s(S^2_+) = W^u(S^2_-) = \Lambda - \{S^2_+ \cup S^2_-\}. \tag{7.18}$$

7.3 Computation of candidates to EC orbits. Numerical approach

Concerning our purposes on this Section, we distinguish three types of orbits: (i) ejection, (ii) collision and (iii) ejection-collision orbits. More specifically, as in the planar case we have:

(i) The set of ejection orbits –those for which the particle ejects from a primary– is the set of orbits on the unstable manifold $W^u(P_+)$, for any $P_+ = (0, \theta, \varphi, v_0, 0, 0) \in S^2_+$. So each ejection orbit may be

regarded as an orbit such that $r > 0$ for all finite time τ and asymptotically tends to an equilibrium point $P_+ \in S^2_+$ as $\tau \to -\infty$.

(ii) The set of collision orbits –those for which the particle arrives at collision with a primary– is the set of orbits on the stable manifold $W^s(Q_-)$, for any $Q_- = (0, \theta, \varphi, -v_0, 0, 0) \in S^2_-$. So each collision orbit may be regarded as an orbit such that $r > 0$ for all finite time τ and asymptotically tends to an equilibrium point $Q_- \in S^-$ as $\tau \to +\infty$.

(iii) The set of ejection-collision orbits –those for which the particle ejects from/arrives at collision with the same primary– is the set of orbits obtained from the intersection $W^u(S^2_+) \cap W^s(S^2_-)$. So they may be regarded as heteroclinic orbits between $P_+ \in S^2_+$ and $Q_- \in S^2_-$.

Recall that in the Chapter 5 we prove analytically that there exits a constant $\hat{L}$ such that for $L \geq \hat{L}$ and for any value of $\mu \in (0, 1)$, $n \in \mathbb{N}$ and $C = 3\mu + Ln^{2/3}(1-\mu)^{2/3}$, there exists exactly four n-EC orbits in the planar problem. Furthermore, focusing on the particular case of the 1-EC orbits we have seen in Chapter 3 that we can extend this result numerically for less restrictive values of C.

Recall also that, in the planar case fixed a value of μ and C, two 1-EC orbits are such that each one itself is symmetrical with respect to the x axis and the other two 1-EC orbits are such that one is symmetrical with respect to the other one with respect to the x axis.

Our purpose is to provide numerical evidence that for a fixed value of μ and a value of $C \geq C_{L_1}$, the two planar EC orbits that are one symmetrical with respect to the other one, seem to be continued to a family of spatial EC orbits; however the two planar EC orbits which are themselves symmetrical are not continued in the spatial case. So next, we explain how to compute EC orbits in the spatial RTBP and afterwards we describe the continuation of the EC orbits from the planar to the spatial case.

7.3.1 Numerical strategy to compute candidates of EC orbits

A first remark at the very beginning of this Subsection is that, whereas in the planar RTBP, the strategy to detect EC orbits is numerically very satisfactory (due to a transversal intersection that can be detected very well), in the spatial RTBP, the method does not apply so clearly as will be shown. So from now on we will talk about candidates to EC orbits (instead of EC themselves).

In order to compute candidates to EC orbits numerically, our strategy follows different steps: (i) computation of initial conditions for the whole set of ejection (collision) orbits; (ii) detection of the existence of candidates to EC orbits.

Computation of initial conditions of ejection (collision) orbits

As we have said previously, the set of EC orbits is the set of orbits that belong to the intersection $W^u(S^2_+) \cap W^s(S^2_-)$, that is the set of heteroclinic connections between the points of S^2_+ and S^2_-. Therefore, the first step is the computation of the ejection (collision) orbits, that is, we need to compute $W^u(P_+)$ ($W^s(P_-)$) of any equilibrium point $P_+ \in S^2_+$ ($P_- \in S^2_-$).

The procedure follows the ideas of the computation of ejection (collision) orbits for the planar RTBP (see Section 3.1.1) but adapted to the spatial case. Recall that fixed a value of the mass parameter $\mu \in (0, 1)$ we will consider always that the particle ejects from the primary P_1 which is the big one if $\mu \in (0, 1/2]$, and the small one if $\mu \in [1/2, 1)$.

For any fixed value $H = \mathfrak{H}$ and for each equilibrium point $P_+ = (0, \theta_0, \varphi_0, v_0, 0, 0) \in S^2_+$, (with

$v_0 = \sqrt{2(1-\mu)}$) parametrized by two angles θ_0 and φ_0, the associated unstable manifold reduces to a single orbit, which is an ejection orbit. As in the planar case, we know that the 2D $W^u(P_+)$ is tangent to the plane passing through P_+ generated by the eigenvectors $\boldsymbol{v}_1$ and $\boldsymbol{v}_2$ defined in the previous section, i.e. vectors like $\boldsymbol{v} = (\alpha, 0, 0, \beta, 0, 0)$, with α, $\beta \in \mathbb{R}$. Furthermore, we recall that the energy level $H = \mathfrak{H}$ is defined implicitly by (7.11) and the normal vector to this level of energy at point P_+ is given by $\boldsymbol{n} = (-\mathfrak{h} - \frac{3}{2}\mu, 0, 0, v_0, 0, 0)$. Therefore, the vectors $\boldsymbol{v}$ tangent to $W^u(P_+)$ at P_+ must be perpendicular to $\boldsymbol{n}$, i.e. they must satisfy the same relation than in the planar case

$$\alpha(-\mathfrak{h} - \frac{3}{2}\mu) + \beta v_0 = 0.$$

In this way, the normalized vector tangent to $W^u(P_+)$ for $H = \mathfrak{h}$ is given by

$$\boldsymbol{w}_1 = \frac{1}{\sqrt{(\mathfrak{h} + 3\mu/2)^2 + v_0^2}} \left(v_0, 0, 0, \mathfrak{h} + \frac{3\mu}{2}, 0, 0 \right). \tag{7.19}$$

As in the planar case, if we want to consider the linear approximation to $W^u(P_+)$ we will take the initial condition of an ejection orbit associated with the point $P_+ = (0, \theta_0, \varphi_0, v_0, 0, 0)$ as

$$(0, \theta_0, \varphi_0, v_0, 0, 0) + s\boldsymbol{w}_1 \tag{7.20}$$

with $s > 0$ a small quantity (typically ranging from 10^{-8} to 10^{-6}). This has the main advantage of being very simple but it has a clear disadvantage: for obtaining a small error we must use a sufficiently small s and therefore we will need more integration time, which will cause numerical error to accumulate. To avoid this problem we will use the parameterization method as in the Section 3.1.1 in order to compute approximations of high order.

The procedure to compute this approximation of high order is exactly the same described in Section 3.1.1, and the first terms of the parameterization $\boldsymbol{W}(s)$ of the manifold $W^u(P_+)$ are given by

$$\begin{aligned}
\boldsymbol{W}(s) = &\begin{pmatrix} 0 \\ \theta_0 \\ \varphi_0 \\ v_0 \\ 0 \\ 0 \end{pmatrix} + \begin{pmatrix} v_0 \\ 0 \\ 0 \\ \hbar \\ 0 \\ 0 \end{pmatrix} \frac{s}{B} - \frac{v_0^{1/2}}{3B^{3/2}} \begin{pmatrix} 0 \\ 2 \\ 0 \\ 0 \\ 3v_0 \cos\varphi_0 \\ 0 \end{pmatrix} s^{3/2} + \frac{\hbar}{2v_0 B^2} \begin{pmatrix} 2v_0 \\ 0 \\ 0 \\ \hbar \\ 0 \\ 0 \end{pmatrix} s^2 \\
&- \frac{3\hbar}{10 v_0^{1/2} B^{5/2}} \begin{pmatrix} 0 \\ 2 \\ 0 \\ 0 \\ 5v_0 \cos\varphi \\ 0 \end{pmatrix} s^{5/2} + \frac{1}{28 v_0^2 B^3} \begin{pmatrix} 21 v_0 \hbar^2 \\ -4\mu v_0^3 \sin(2\theta_0) \\ -4\mu v_0^3 \cos^2\theta_0 \sin(2\varphi_0) \\ 7\hbar^3 - 14\mu v_0^4 [1 - 3\cos^2\theta_0 \cos^2\varphi_0] \\ -12\mu v_0^4 \sin(2\theta_0) \cos\varphi_0 \\ -12\mu v_0^4 \cos^2\theta_0 \sin(2\varphi_0) \end{pmatrix} s^3 \\
&- \frac{3\hbar^2}{14 v_0^{3/2} B^{7/2}} \begin{pmatrix} 0 \\ 2 \\ 0 \\ 0 \\ 7v_0 \cos\varphi_0 \\ 0 \end{pmatrix} s^{7/2} + \mathcal{O}(s^4),
\end{aligned}$$

where $\hbar = \mathfrak{h} + 3\mu/2$ and $B = \sqrt{\hbar^2 + v_0^2}$.

It is important to note that $s \geq 0$, since $r \geq 0$ and that we have the 2D parameterization of the manifold $\boldsymbol{W}$ in terms of $(\mathfrak{h}, s)$. We have implemented this procedure to calculate the approximation of

the manifold up to the desired order, but in practice we have usually worked with the approximation of order 5-10.

So with this procedure we obtain the whole set of ejection orbits, $W^u(S^2_+)$. Similarly we can compute the whole set of collision orbits, $W^s(S^2_-)$.

An important remark at this point is that, using the local charts described in the previous Section, the whole set of initial conditions of ejection (collision) orbits (that is for all value of the longitude $\theta_0 \in [0, 2\pi)$ and latitude $\varphi_0 \in [-\pi/2, \pi/2]$) can be considered.

7.3.2 Detection of candidates to collision orbits

Assume a value of μ fixed and C (or equivalently H) given. Take a small neighborhood centered at the origin and of radius $\epsilon > 0$ small. Then the method to detect collision orbits is based on this statement: the conditions

$$\begin{cases} r' = 0, \\ r'' > 0, \\ \boldsymbol{m} = \mathbf{0}, \\ r \neq 0, \end{cases} \tag{7.21}$$

where $\boldsymbol{m}$ is the angular momentum vector, are not compatible. Indeed, from the two first conditions the particle reaches a point $Q = (x, y, z)$ or (r, θ, φ) which is a minimum in distance with respect to the origin. If $\epsilon > 0$ is small enough, the motion of the particle will be essentially the motion of a two body problem and the velocity will be a non zero vector (the modulus of the velocity can be obtained from (1.26) $(2\Omega(x, y, z) - C = ||(\dot{x}, \dot{y}, \dot{z})||^2)$ and the point Q is far from the zero velocity surface). At Q, with $r \neq 0$, the position velocity and vector velocity will be orthogonal vectors, and therefore it is impossible for the angular momentum vector to be equal to zero.

Therefore, for $\epsilon > 0$ small enough, the requirement of the first three conditions implies that $r = 0$, that is a collision between the particle and the primary. This is precisely the numerical strategy we have implemented to compute collision orbits.

We now discuss how this strategy works very well in the planar RTBP but not in the spatial case.

Detection of EC orbits in the planar RTBP

Note that the strategy described previously is exactly the generalization of the strategy introduced in Section 3.2.2 and also used in Chapter 5.

The great advantage in the planar case is that having $z = \dot{z} = 0$ we know that the angular momentum is of the form $\boldsymbol{m} = (0, 0, m)$ and therefore we only have to find the zeros of a 1-dimensional function. This makes very easy to detect a transversal EC orbit in the plane problem.

An alternative (as explained in Section 3.2.3) is to look at the sign of m because it tells us in which direction the particle surrounds the primary when it approaches (see Figure 3.9 for an intuitive description).

Detection of candidates to EC orbits in the spatial RTBP

Now let us discuss the strategy based on the angular momentum in the spatial RTBP. We recall that on the collision manifold there is a whole sphere S^2_+ of equilibrium points and a whole sphere S^2_- of equilibrium points. Moreover there is an sphere connecting asymptotically the point $P_- =$

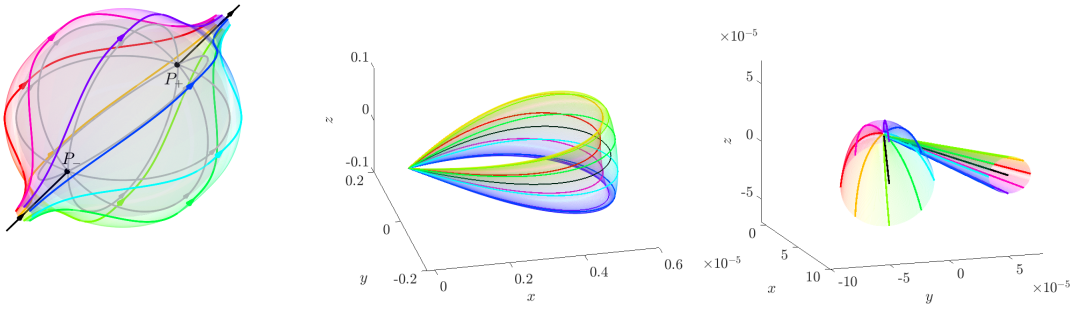

Figure 7.3: Left. Schematic plot close to collision. Middle. A set of ejection orbits integrated up to the first crossing with Σ. The interior black curve is an EC orbit. Right. Zoom region around the origin. Set of ejection orbits and the same set close to collision.

$(0, \theta_0, \varphi_0, -v_0, 0, 0) \in S^2_-$ with the point $P_+ = (0, \theta_0, \varphi_0, v_0, 0, 0) \in S^2_+$, that is, we have an sphere of heteroclinic connections between P_- and P_+. See the grey curves in Figure 7.3 left. We recall that this sphere of grey curves simply becomes the union of two heteroclinic connections in the planar RTBP (see Figure 3.9).

First let us discuss how to detect a collision orbit. Now the geometric picture is the one described in Figure 7.3. Roughly speaking, in the spatial problem we need a circumference of trajectories (instead of two orbits in the planar case) such that *cover the whole grey sphere*, forward in time. In such a case there is an orbit that tends to P_- and thus, is a collision orbit. See Figure 7.3 left and compare with Figure 3.9 right. We also compare the plot in Figure 3.9 middle for the planar case with the ones in Figure 7.3 middle and right. We take now a *cone* of ejection orbits in the (x, y, z) configuration space (plus the interior ejection orbit) and follow the evolution of the orbits up to the first passage to minimum distance (with respect P_1 located at the origin). The whole evolution from ejection to close to collision is globally shown in the middle plot. On the right plot we see a zoom region close to the origin: the cone of ejection orbits (plus the black one inside that will be an EC orbit) and the *kind of umbrella* set close to collision (plus the collision orbit in black inside). The single black orbit is an EC orbit.

Now let us focus on the numerical strategy to detect EC orbits based on the angular momentum vector which now is $\boldsymbol{m} = (m_x, m_y, m_z)$. We take the whole set of initial conditions of ejection orbits whose initial conditions are parametrized by θ_0 and φ_0. In principle $\varphi_0 \in [-\pi/2, \pi/2]$, but as described above, we will consider different local charts. Our goal is to obtain a value (or several values) of (θ_0, φ_0) such that the angular momentum at the crossing with Σ, is equal to zero. Such (θ_0, φ_0) will provide the initial condition of an EC orbit.

So, for each (θ_0, φ_0), we follow the ejection orbit up to Σ. Rather than in $\boldsymbol{m}$, we are interested in its direction defined by two angles (α, δ) through

$$\begin{cases} m_x = m \cos\alpha \cos\delta, \\ m_y = m \sin\alpha \cos\delta, \\ m_z = m \sin\delta, \end{cases} \tag{7.22}$$

where $m = |\boldsymbol{m}|$ and $\alpha \in [-\pi, \pi)$, $\delta \in [-\pi/2, \pi/2]$.

The actual numerical computation of the angles α and δ follows from two steps. First the angular momentum $\boldsymbol{m} = (m_x, m_y, m_z)$ for each ejection orbit at the crossing with Σ is computed taking spherical variables with respect to the corresponding axis considered and in terms of the McGehee variables and time. For example, taking spherical variables with respect to the z axis, we obtain

$$\begin{aligned} m_x &= r^2 \cos\varphi \left[u_\varphi \sin\theta - u_\theta \cos\theta \sin\varphi\right], \\ m_y &= -r^2 \cos\varphi \left[u_\varphi \cos\theta + u_\theta \sin\theta \sin\varphi\right], \\ m_z &= u_\theta r^2 \cos^2\varphi, \end{aligned} \tag{7.23}$$

and

$$m = r^2 \cos\varphi \sqrt{u_\varphi^2 + u_\theta^2}. \tag{7.24}$$

Similarly, we obtain the corresponding expressions if the other sets of spherical variables are used. Second, we compute the associated angles α and δ.

The numerical strategy applied to detect EC orbits is as follows:

(i) varying $\theta_0 \in [0, 2\pi)$ and $\varphi_0 \in [-\pi/2, \pi/2]$, we generate two plots, the surfaces $\alpha(\theta_0, \varphi_0)$ and $\delta(\theta_0, \varphi_0)$.

(ii) Taking into account α, we look for a sudden change of complete direction of the vector $\boldsymbol{m}$ in the (x, y) plane, that is, $\alpha \to \alpha + \pi$. We obtain a curve or set of curves labelled by A.

(iii) Taking into account δ, we look for a sudden change of complete direction of the vector $\boldsymbol{m}$ in the (z) direction, that is, $\delta \to -\delta$. We obtain a curve or set of curves labelled by D.

(iv) The values of (θ_0, φ_0) such that the curves A and D intersect correspond to initial conditions of EC orbits.

7.4 Numerical results on EC orbits

We describe now the numerical results obtained.

For a fixed $\mu \in (0, 1)$ and $C \geq C_{L_1}$ given, we need to compute the two plots $\alpha(\theta_0, \varphi_0)$ and $\delta(\theta_0, \varphi_0)$, the corresponding curves A and D and the intersection points belonging to $A \cap D$, as mentioned above.

To do so, we compute the whole set of ejection orbits. This implies to take for each local chart, the whole set of ejection orbits parametrized by $\theta_0 \in [0, 2\pi)$ and $\varphi_0 \in [-\pi/4, \pi/4]$, using the spherical variables with respect to the z axis, $\hat{\theta}_0 \in [0, 2\pi)$ and $\hat{\varphi}_0 \in [-\pi/4, \pi/4]$, using the spherical variables with respect to the x axis, and $\bar{\theta}_0 \in [0, 2\pi)$ and $\bar{\varphi}_0 \in [-\pi/4, \pi/4]$, using the spherical variables with respect to the y axis. We integrate the set of ejection orbits up to the first crossing with the Poincaré section Σ. We simply plot the values of α and δ of the angular momentum vector $\boldsymbol{m}$, obtained in the corresponding set of variables. We will call them the *local parametrization of* α and δ, respectively.

In Figure 7.4 we plot the resulting local parametrizations for $\mu = 0.1$ and $C = 4$. We plot the value of $\alpha(\theta_0, \varphi_0)$ on the top plots and the value of $\delta(\theta_0, \varphi_0)$ on the bottom ones. For clearer visualization, we also plot the values of α and δ on the sphere S^2 with the usual variables (x, y, z) and the usual longitude and latitude θ and φ. See Figure 7.5.

In Figure 7.6 we plot the whole composition plot $\alpha(\theta_0, \varphi_0)$ and $\delta(\theta_0, \varphi_0)$. This corresponds to step (i).

Now we proceed with steps (ii) and (iii). We plot the resulting curves A and D. The changes $\alpha \to \alpha + \pi$, result in two curves A_1 and A_2, that is $A = A_1 \cup A_2$; and the changes of sign in δ result in two curves D_1 and D_2, that is $D = D_1 \cup D_2$. They are shown in blue and red respectively in Figure 7.7 top.

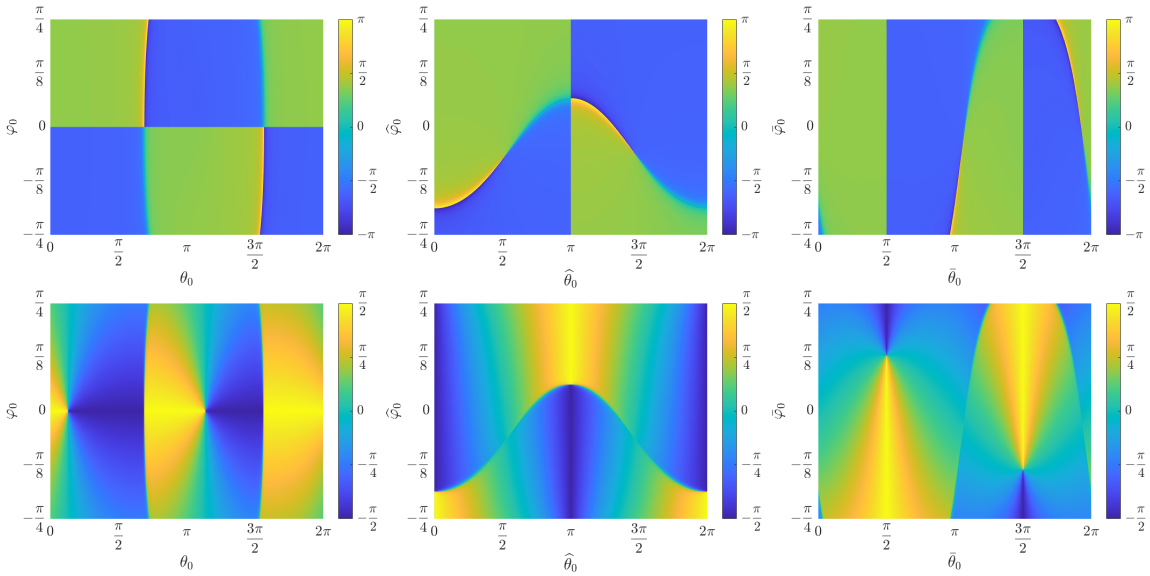

Figure 7.4: $\mu = 0.1$, $C = 4$ (equivalently $H = -2$). Local parametrizations of α (top) and δ (bottom) (that is , values of α (top) and δ (bottom) according to the gradual colour of the angular momentum vector at the first crossing of the ejection orbits using the spherical variables with respect to the z axis (left), x axis (middle) and y axis (right). The initial conditions of the corresponding ejection orbits are parametrized by (θ_0, φ_0) (left), $(\hat{\theta}_0, \hat{\varphi}_0)$ (middle), $(\bar{\theta}_0, \bar{\varphi}_0)$ (right).

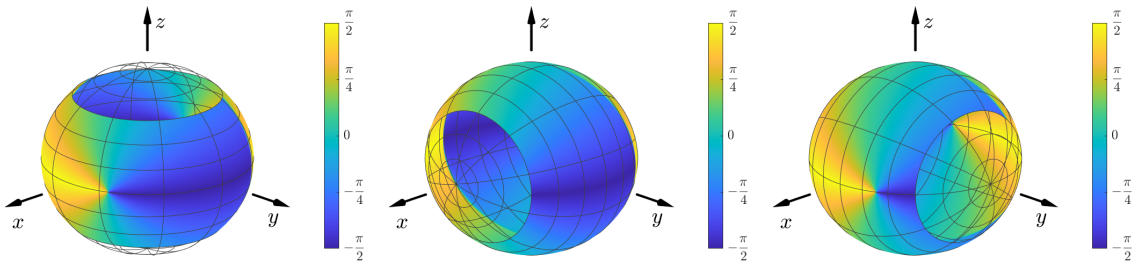

Figure 7.5: $\mu = 0.1$, $C = 4$ (equivalently $H = -2$). Local parametrizations of δ on the sphere S^2 (with the usual variables θ, φ).

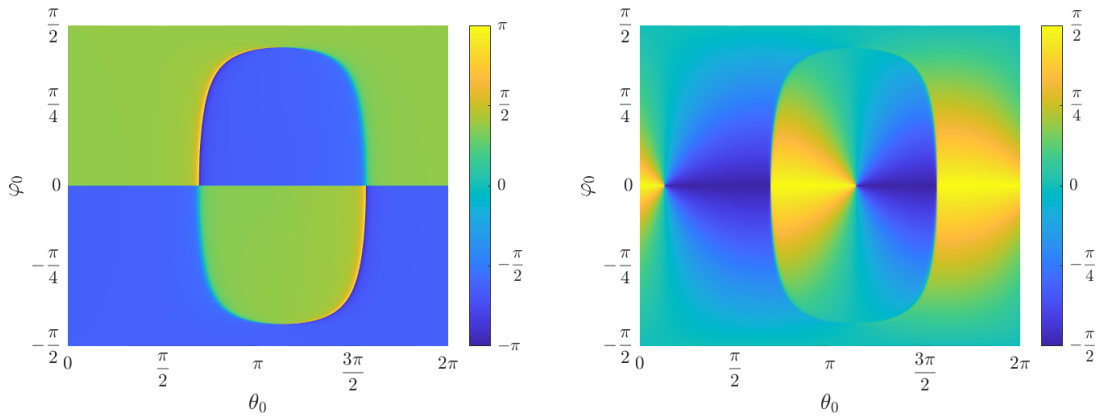

Figure 7.6: $\mu = 0.1$, $C = 4$ (equivalently $H = -2$). Global parametritzations: α (left) and δ (right).

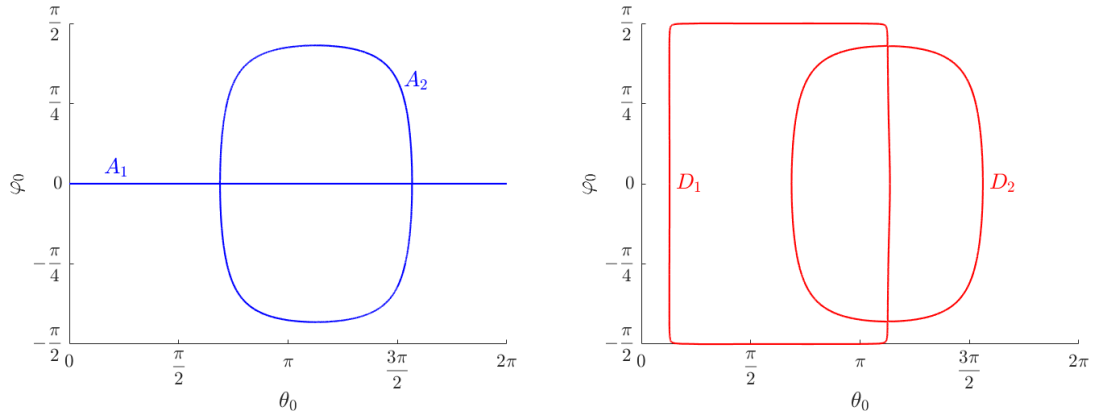

Figure 7.7: $\mu = 0.1$, $C = 4$ (equivalently $H = -2$). In blue the curves A_1 and A_2 obtained from the change $\alpha \to \alpha + \pi$. In red the curves D_1 and D_2 obtained from the change $\delta \to -\delta$.

Finally step (iv) requires the intersection points belonging to $(A_1 \cup A_2) \cap (D_1 \cup D_2)$.

Concerning the intersection of both sets of curves, we distinguish:

- Four transversal intersection points with $\delta_0 = 0$. See the two blue points and two red ones in Figure 7.7. The associated values of θ_0 provide the initial conditions of four EC orbits which are planar. These four planar EC orbits were expected in accordance with the analytical results proved in Chapter 5. he two blue points in Figure 7.8 provide the initial conditions of the two EC orbits which are symmetrical with respect to the x axis. The two red points in Figure 7.8 provide the initial conditions of the two EC orbits which are non symmetrical, but symmetrical one of the other one with respect to the x axis.

- Two transversal intersection points with $\delta_0 \neq 0$. The associated values of (θ_0, φ_0) provide the initial conditions of two EC orbits which are non planar. See the green dots in Figure 7.8. Each EC orbit is symmetrical itself with respect to plane xz, and one of the other with respect to the plane xy.

- Apparently there appears a whole continuous family of intersection points that belong to $A_2 \cap D_1$ (see Figure 7.7, plotted in grey discontinuous line in Figure 7.8. We cannot guarantee numerically that the curves A_2 and D_1 coincide so we can claim that there appears a continuous family of candidates to non planar EC orbits. However, we emphasize that this continuous family would be a real family of non planar EC orbits if both curves were coincident.

Summarizing, for $\mu > 0$ and $C \geq C_{L_1}$ fixed, our results are the following:

- there are two planar EC orbits which are symmetrical. Their initial conditions are provided by the values (θ_0, φ_0), with $\varphi = 0$, in blue in Figure 7.8 for $\mu = 0.1$ and $C = 4$.

- There are two planar EC orbits which are non symmetrical, but symmetrical one of the other one with respect to the x axis. Their initial conditions are provided by the values (θ_0, φ_0), with $\varphi = 0$, in red in Figure 7.8.

- There are two spatial EC orbits, symmetrical themselves symmetrical with respect to the (x, z) plane, and symmetrical one of the other one with respect to the (x, y) plane. Their initial conditions are provided by the values (θ_0, φ_0) in green in Figure 7.8.

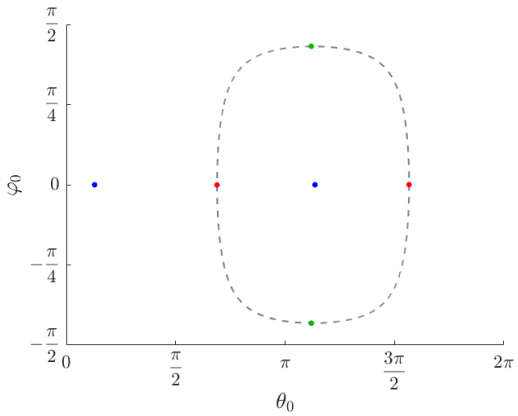

Figure 7.8: $\mu = 0.1$, $C = 4$ (equivalently $H = -2$). The blue and red points ($A_1 \cap D_1$) provide initial conditions of the two planar symmetrical and the two planar non symmetrical EC orbits, respectively. The green points ($A_2 \cap D_1$) provide initial conditions of spatial EC orbits. The grey points provide initial conditions of candidates to EC orbits.

We have computed both the apparently coincident curves and the four points (that provide the initial conditions of EC orbits) varying both C and μ. We plot the results obtained in Figure 7.9 for $\mu = 0.1$ (top) and for $\mu = 0.5$ (bottom), taking values of $C = C_{L_1}, 4, 6, 8, 10, 20, 50, 100$. For μ fixed, we plot the curve and the four points corresponding to EC orbits with the same colour. We observe that when C goes increasing, the values of θ_0 tend to 0, $\pi/2$, π and $3\pi/2$ for the planar EC orbits. These results are in concordance with the known properties of planar EC orbits (see Chapter 5). Concerning the two spatial EC orbits, we observe that as C increases, (θ_0, φ_0) tends to $(\pi, \pm\pi/2)$.

From the numerical results obtained, we can claim that, for μ fixed and varying $C \geq C_{L_1}$, we obtain four families of planar EC orbits (as already known) and two *new* families of spatial EC orbits. Moreover, for μ fixed and $C \geq C_{L_1}$ fixed, a continuous family of candidates to EC orbits also does exist.

At this point we make a remark about the paper [LMA85]. In that paper the authors claim there exist, for small $\mu > 0$ and fixed $C > C_{L_1}$, two families of spatial, symmetric (with respect to the xz-plane) EC orbits, parameterized by the angle ϕ. For $\mu = 0$ every ejection orbit ends in collision and an argument based on the symmetries of the problem is used to show that some of them survive when $\mu > 0$. It can be easily seen that this is indeed the case for two planar ($\phi = 0$) EC orbits. The symmetry argument given in [LMA85] to show the existence of a family of spatial EC orbits (parameterized by ϕ) is, however, unclear. Furthermore, our numerical results contradict the existence of such a family or families: the planar symmetric EC orbits are isolated and do not continue to a family of spatial EC orbits.

Finally, and as expected for μ fixed, as far as C increases, the maximum distance of the candidates to EC orbits decreases, since the bounded Hill regions of possible motion around each primary (for $C \geq C_{L_1}$) decrease. This effect is clearly shown in Figure 7.10, comparing the left plot for $C = C_{L_1} = 3.68695322987989$ (left) and $C = 6$ (right) where the grey cloud represents the whole set of candidates to EC orbits in the (x, y, z) configuration space, apart from the EC orbits plotted in red, blue and green.

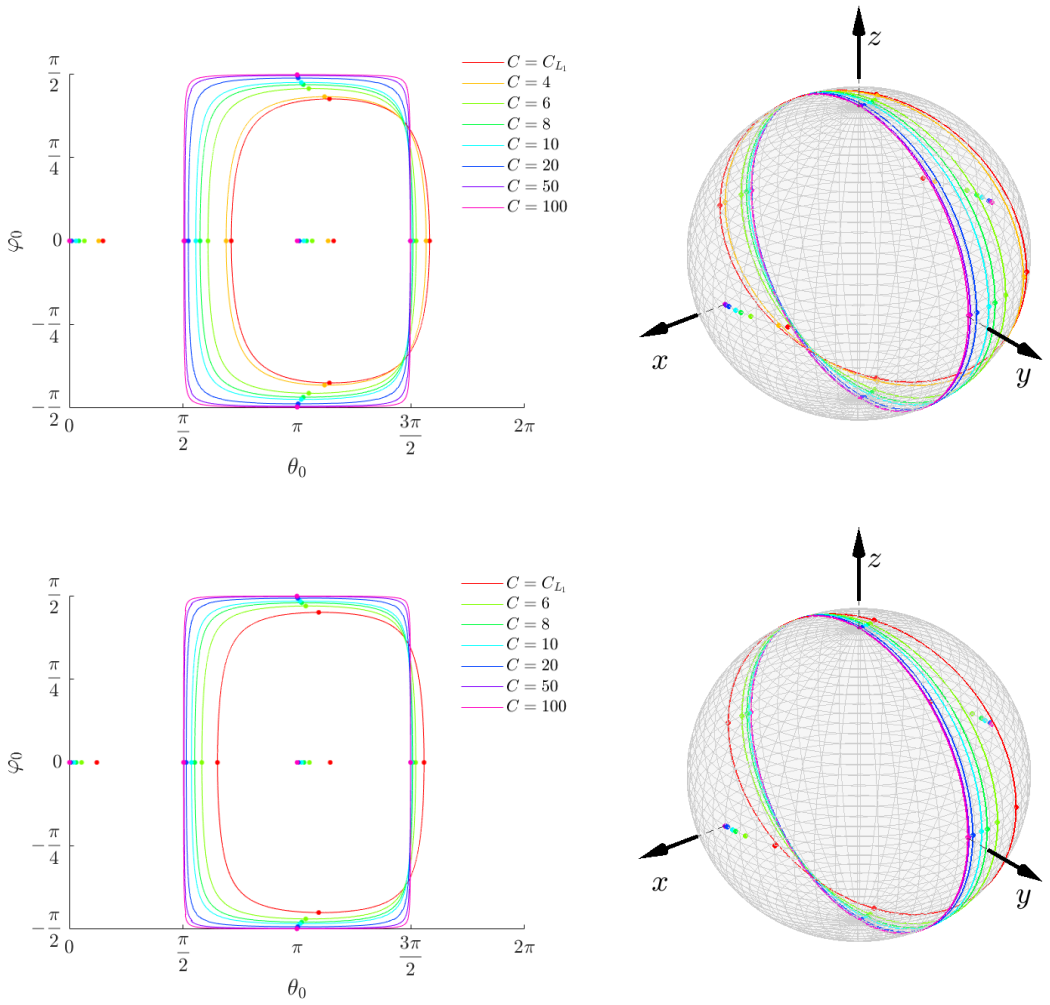

Figure 7.9: Initial conditions of candidates to EC orbits for $\mu = 0.1$ (top) and $\mu = 0.5$ (bottom) taking different values of C.

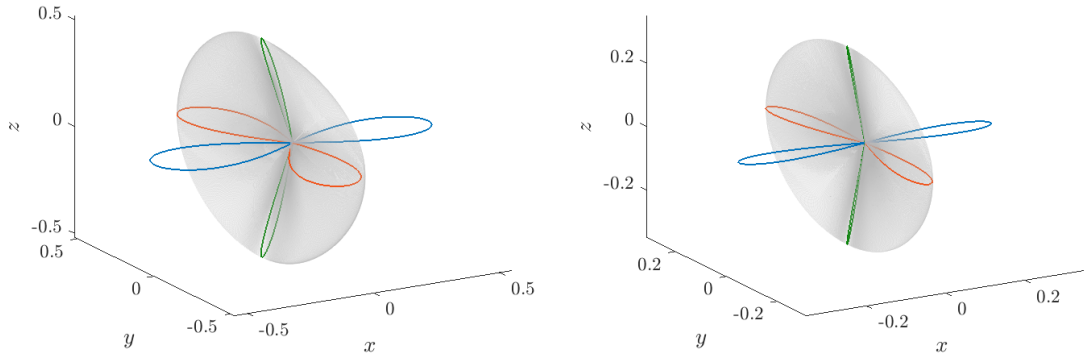

Figure 7.10: $\mu = 0.1$. Configuration space (x, y, z). The two planar symmetrical EC orbits in blue. The two non symmetrical planar ones in red. The spatial ones in green. The candidates to EC orbits in grey. $C = C_{L_1}$ (left) and $C = 6$ (right).

Conclusions and future work

Throughout each chapter we have been drawing different conclusions, therefore our goal in this section is not to make a complete list of all of them, but we aim at briefly highlighting some of the results obtained in order to explain and motivate the mainly future work that we want to carry out.

First, it is important to note the generalization of the concept of EC orbits that can be found in the literature to the definition of n-EC orbits. During this thesis we have made an exhaustive analysis, both numerical and analytical, of these kind of orbits. In this dissertation, we have proved that there exists a value of the Jacobi constant $\hat{C}(\mu, n)$ such that for all $C \geq \hat{C}(\mu, n)$ there exist exactly four n-EC orbits for any value of $\mu \in (0, 1)$ and $n \in \mathcal{N}$ with the specific characterization given in Theorem A. Besides, we have seen that the shape of the expression of $\hat{C}(\mu, n)$ obtained analytically coincides with the value obtained numerically. This result is not something that we consider 100% closed, since, on the one hand, it may be interesting to try to compute the radius of convergence of the solution obtained and, on the other, to try to understand why the successive bifurcations of the Hill problem occur (see Figure 5.7).

In this dissertation, we have analyzed the advantages and disadvantages of the McGehee and Levi-Civita regularizations and of the different techniques in order to prove the existence of exactly four n-EC orbits and to detect them. In such a way, we have developed an optimal process to prove the Theorem A. This process can be generalized to other problems with a Newtonian potential. This is because by regularizing the position of the object (from which the particle ejects –and then collides with it–) with the coordinate change introduced in Chapter 5, we can always rewrite the problem as a two-body problem plus perturbation. It is clear that the result on the number of n-EC orbits that will exist and its characterization may differ depending on the potential considered, but the process to obtain it is the same. In this way, in the future we would like to generalize these results as much as possible and explore the case where non-Newtonian potentials also appear.

Furthermore, we have seen how the dynamics of the ejection (and ejection-collision) orbits is very rich when we consider less restrictive Hill regions. In particular, we have focused on the evolution of the ejection orbits for values of the Jacobi constant $C \geq C_{L_{2,3}}$ (which implies that these orbits are bounded) and on the role of the family of Lyapunov periodic orbits associated with L_1 in the transit and generation of new EC orbits. This leads us to wonder about the different invariant objects that interact with ejection orbits if less restrictive values of C are considered. In particular, we want to study the interaction with the invariant objects associated with the other equilibrium points (we have already seen in Chapter 3 how L_4 and L_5 also influence the evolution of the original four families of n-EC orbits) and the relation with the manifold of the infinity. We also want to study in more depth the periodic EC orbits

Finally, we would like to study the 3D case in more detail. In Chapter 7 we have made a first approach to the spatial problem using the generalization of the McGehee regularization and considering only the case of 1-EC orbits. In this way, we want to study in more detail the general case of n-EC orbits. As we have seen in detail in the planar case, the McGehee regularization has its limitations and, therefore, our intention is to use the Kustaanheimo – Stiefel regularization in the future explorations.

It is clear the spatial problem also offers a much richer dynamics, but for the moment our next step in this direction will be to restrict ourselves to the study of the n-EC orbits since, as we have seen for the case $n = 1$ this is already challenging.

Bibliography

[ABWF03] S.A. Astakhov, A.D. Burbanks, S. Wiggins, and D. Farrelly. Chaos-assisted capture of irregular moons. *Nature*, 423:264–267, 2003.

[ALF05] S.A. Astakhov, E.A. Lee, and D. Farrelly. Formation of Kuiper-belt binaries through multiple chaotic scattering encounters with low-mass intruders. *Mon. Not. R. Astron. Soc.*, 360:401–415, 2005.

[ARMO19] E. Alvarez-Ramírez, M.and Barrabés, M. Medina, and M. Ollé. Ejection-collision orbits in the symmetric collinear four–body problem. *Communications in Nonlinear Science and Numerical Simulation*, 71, 06 2019.

[ARV13] M. Alvarez-Ramírez and C. Vidal. Behavior of the binary collision in a planar restricted (n+1)-body problem. *Physica D: Nonlinear Phenomena*, 254:1–11, 2013.

[Bir15] G.D. Birkhoff. The restricted problem of three bodies. *Rend. Circ. Mat. Palermo*, 39:265, 1915.

[BMO13] E Barrabés, J.M. Mondelo, and M. Ollé. Numerical continuation of families of heteroclinic connections between periodic orbits in a Hamiltonian system. *Nonlinearity*, 26, 10 2013.

[Boz70] G. Bozis. Sets of collision periodic orbits in the restricted problem. In G.E.O. Giacaglia, editor, *Periodic orbits, stability and resonances*, pages 176–191. Springer, 1970.

[Bro65] R. Broucke. Regularizations of the plane restricted three-body problem. *Icarus*, 4, 1965.

[BUF97] A.F. Brunello, T. Uzer, and D. Farrelly. Hydrogen atom in circularly polarized microwaves: Chaotic ionization via core scattering. *Phys Rev A*, 55:3730–3745, 1997.

[Bur06] C. Burrau. Über einige in Aussicht genommene Berechnung, betreffend einen Spezialfall des Dreikörperproblems. *Vierteljahrsschrift Astron. Ges.*, 41:261, 1906.

[CFdlL03a] X. Cabré, E. Fontich, and R. de la Llave. The parameterization method for invariant manifolds I: Manifolds associated to non-resonant subspaces. *Indiana University Mathematics Journal*, 52, 2003.

[CFdlL03b] X. Cabré, E. Fontich, and R. de la Llave. The parameterization method for invariant manifolds II: regularity with respect to parameters. *Indiana University Mathematics Journal*, 52, 2003.

[CFdlL05] X. Cabré, E. Fontich, and R. de la Llave. The parameterization method for invariant manifolds III: overview and applications. *Journal of Differential Equations*, 218, 2005.

[CL88] A. Chenciner and J. Llibre. A note on the existence of invariant punctured tori in the planar circular restricted three-body problem. *Ergodic Theory and Dynamical Systems*, 8:63–72, 1988.

[Con63] C. Conley. On some new long periodic solutions of the plane restricted three body problem. *Communications on Pure and Applied Mathematics*, 16, 1963.

[DF89] J. Delgado Fernández. Transversal ejection-collision orbits in Hill's problem for C»1. *Celestial Mechanics and Dynamical Astronomy*, 44:299–307, 1988-1989.

[DP05] J.R. Dormand and J.P. Prince. A familiy of embedded Runge-Kutta formulae. *J. Computat. App. Math.*, 6:19–26, 2005.

[EL68] R.H. Estes and E.R. Lancaster. Power series solutions of the Thiele-Burrau regularized planar restricted three-body problem. Technical report, Goddard space flight center, 1968.

[Feh68] E. Fehlberg. Classical fifth, sixth, seventh and eighth order Runge-Kutta formulas with stepsize control. Technical report, NASA, R-287, 1968.

[GLM89] G. Gómez, J. Llibre, and J. Masdemont. Homoclinic and heteroclinic solutions in the restricted three-body problem. *Celestial Mechanics and Dynamical Astronomy*, 44, 1988-1989.

[HCF+16] À. Haro, M. Canadell, JL. Figueras, A. Luque, and J.M. Mondelo. *The Parameterization Method for Invariant Manifolds: From Rigorous Results to Effective Computations.* Applied Mathematical Sciences 195. Springer International Publishing, 1 edition, 2016.

[Hén65] M. Hénon. Exploration numérique du problème restreint I. Masses égales. *Annales d'Astrophysique*, 28:499–511, 1965.

[Hén69] M. Hénon. Numerical exploration of the restricted problem v. Hill's case: Periodic orbits and their stability. *Astron. Astrophys.*, 1:223–238, 1969.

[HTP02] J.R. Hurley, C.A. Tout, and O.R. Pols. Evolution of binary stars and the effect of tides on binary populations. *Mont. Not. of the Roy. Astr. Soc.*, 329:897–928, 2002.

[JZ05] A. Jorba and M. Zou. A software package for the numerical integration of ODE's by means of high-order taylor methods. *Exp. Maths.*, 14:99–117, 2005.

[LC03] T. Levi-Civita. Sur les trajectoires singulières du problème restreint des trois corps. *C. R. Hebd. Acad. Sci. Paris*, 136:82–84, 1903.

[LC04] T. Levi-Civita. Traiettorie singolari ed urti nel problema ristretto dei tre corpi. *Annal. Mat. Pura Appl.*, 9:1–32, 1904.

[LC06] T. Levi-Civita. Sur la résolution qualitative du problème restreint des trois corps. *Acta Mathematica*, 30:305–327, 1906.

[LC20] T. Levi-Civita. Sur la régularisation du problème des trois corps. *Acta Mathematica*, 42:99–144, 1920.

[Lem55] G. Lemaître. Regularization of the three-body problem. *Vistas in Astronomy*, 1:207–215, 1955.

[LL88] E.A. Lacomba and J. Llibre. Transversal ejection-collision orbits for the restricted problem and the Hill's problem with applications. *Journal of Differential Equations*, 74:69–85, 1988.

[Lli82] J Llibre. On the restrited three-body problem when the mass parameter is small. *Celestial Mechanics and Dynamical Astronomy*, 28:83–105, 1982.

[LMA85] J Llibre and J. Martínez Alfaro. Ejection and collision orbits of the spatial restricted three-body problem. *Celestial Mechanics and Dynamical Astronomy*, 35:113–128, 1985.

[LP90] J. Llibre and C. Piñol. On the elliptic restricted three-body problem. *Celestial Mechanics and Dynamical Astronomy*, 48:319–345, 1990.

[McG74] R. McGehee. Triple collision in the collinear three-body problem. *Inventiones mathematicae*, 27:191–227, 1974.

[McG78] R. McGehee. Singularities in classical celestial mechanics. *Proceedings of the International Congress of Mathematicians Helsinki*, pages 827–834, 1978.

[MK80] J.L. Modisette and Y. Kondo. Mass transfer between binary stars. *Symposium - International Astronomical Union*, 88, 1980.

[ML98] D.L. Maranhão and J. Llibre. Ejection–collision orbits and invariant punctured tori in a restricted four-body problem. *Celestial Mechanics and Dynamical Astronomy*, 71:1–14, 1998.

[MO17] K.R. Meyer and D.C. Offin. *Introduction to Hamiltonian Dynamical Systems and the N-Body Problem*. Springer, 2017.

[MS82] K.R Meyer and D.S. Schmidt. Hill's lunar equations and the three-body problem. *Journal of Differential Equations*, 44:263–272, 1982.

[MSORS21] T. Martínez-Seara, M. Ollé, O. Rodríguez, and J. Soler. Generalised analytical results on n-ejection-collision orbits in the rtbp. analysis of bifurcations. *Preprint*, 2021.

[Nag04] J. Nagler. Crash test for the copenhaguen problem. *Phys. Rev. E*, 69:066218, 2004.

[Nag05] J. Nagler. Crash test for the restricted three-body problem. *Phys. Rev. E*, 71:026227, 2005.

[Oll18] M. Ollé. To and fro motion for the hydrogen atom in a circularly polarized microwave field. *Commun Nonlinear Sci Numer Simulat*, 54:286–301, 2018.

[ORS18] M. Ollé, O. Rodríguez, and J. Soler. Ejection-collision orbits in the RTBP. *Commun Nonlinear Sci Numer Simulat*, 55:298–315, 2018.

[ORS20a] M. Ollé, O. Rodríguez, and J. Soler. Analytical and numerical results on families of n-ejection-collision orbits in the RTBP. *Commun Nonlinear Sci Numer Simulat*, 90:105294, 2020.

[ORS20b] M. Ollé, O. Rodríguez, and J. Soler. Regularisation in ejection-collision orbits of the RTBP. *Recent Advances in Pure and Applied Mathematics*, pages 35–47, 2020.

[ORS21a] M. Ollé, O. Rodríguez, and J. Soler. Mcgehee regularization in the 3d restricted three-body problem. application to ejection-collision orbits. *Prepint*, 2021.

[ORS21b] M. Ollé, O. Rodríguez, and J. Soler. Transit regions and ejection/collision orbits in the RTBP. *Commun Nonlinear Sci Numer Simulat*, 94:105550, 2021.

[Pai97] P. Painlevé. Leçons sur la théorie analytique des équations différentielles professées à Stockholm (Septembre, Octobre, Novembre 1895) sur l'invitation de s.m. le Roi de Suède et de Norvège. *Librairie scientifique A. Hermann*, 1897.

[PG20] R.I. Paez and M. Guzzo. A study of temporary captures and collisions in the circular restricted three-body problem with normalizations of the Levi-Civita Hamiltonian. *International Journal of Non-Linear Mechanics*, 120:103417, 2020.

[Piñ95] C. Piñol. Ejection-collision orbits with the more massive primary in the planar elliptic restricted three body problem. *Celestial Mechanics and Dynamical Astronomy*, 61:315–331, 1995.

[PW85] J.E. Pringle and R.A. Wade. *Interacting Binary Stars*. Cambridge Univ. Press, 1985.

[SS71] E. L. Stiefel and G. Scheifele. *Linear and Regular Celestial Mechanics*. Springer-Verlag, 1971.

[Sun07] K.F. Sundman. Recherches sur le problème des trois corps. *Acta Soc. Sci. Fenn.*, 34:1–43, 1907.

[Sun09] K.F. Sundman. Nouvelles recherches sur le problème des trois corps. *Acta Soc. Sci. Fenn.*, 35:1–27, 1909.

[Sun13] K.F. Sundman. Mémoire sur le problème des trois corps. *Acta Mathematica*, 36:105–179, 1913.

[Sze67] V. Szebehely. *Theory of Orbits: The Restricted Problem of Three Bodies*. Academic Press, 1967.

[Thi95] T. N. Thiele. Recherches numériques concernant des solutions périodiques d'un cas spécial du problème des trois corps. *Astron. Nachr*, 138:1, 1895.

[Ver78] J.H. Verner. Explicit Runge–Kutta methods with estimates of the local truncation error. *SIAM J. on Numer. Anal.*, 15:772–790, 1978.

[WDT95] R.A. Witjers, M.B. Davies, and C. Tout. Evolutionary processes in binary stars. *Proceedings of the NATO ASI on evolutionary processes in binary stars*, July 10-21, 1995.

[Win30] A. Wintner. Zur effektiven stabilität des mondes. *Mathematische Zeitschrift*, 32, 1930.